Methoden zur Zustandserkennung von Lithium-Ionen-Batterien

Dissertation zur Erlangung des naturwissenschaftlichen Doktorgrades der Julius-Maximilians-Universität Würzburg

Vorgelegt von

Lukas Gold

Aus Thüngersheim

Fraunhofer-Institut für Silicatforschung ISC

Würzburg, 2021

Fraunhofer ISC

Eingereicht bei der Fakultät für Chemie und Pharmazie am

_____

Gutachter der schriftlichen Arbeit

1. Gutachter: Prof. Dr. Gerhard Sextl

2. Gutachter: Prof. Dr. Henning Heuer

Prüfer des öffentlichen Promotionskolloquiums

1. Prüfer: Prof. Dr. Gerhard Sextl

2. Prüfer: Prof. Dr. Henning Heuer

3. Prüfer: _____

Datum des öffentlichen Promotionskolloquiums

_____

Doktorurkunde ausgehändigt am

_____

Methods for the state estimation of lithium-ion batteries

Doctoral Thesis to obtain the degree of
“Doktor der Naturwissenschaften” (Dr. rer. nat.)
Awarded by the Julius-Maximilians-Universität Würzburg

Submitted by

Lukas Gold

From Thüngersheim

Fraunhofer Institute for Silicate Research ISC

Würzburg, 2021

Fraunhofer ISC

Submitted to the Faculty of Chemistry and Pharmacy on

_____

Evaluators of the written Dissertation (Thesis)

Supervisor - 1. Evaluator: Prof. Dr. Gerhard Sextl

2. Evaluator: Prof. Dr. Henning Heuer

Examiners of the Public Defense

1. Examiner: Prof. Dr. Gerhard Sextl

2. Examiner: Prof. Dr. Henning Heuer

3. Examiner: _____

Date of the Public Defense

_____

Doctoral Certificate awarded on

_____

Statement

I hereby affirm that I have independently prepared the dissertation entitled ""Methods for the state estimation of lithium-ion batteries"" and have not used any sources and aids other than those mentioned.

I also declare that this dissertation has not already been submitted in the same or any other form in any other examination process.

I have not previously earned or attempted to earn any academic degrees other than those submitted with the application for admission.

I am aware that an untrue statement regarding the assurance of independent performance may have legal consequences.

Würzburg, _____ _____

Lukas Gold

Erklärung

Hiermit versichere ich, dass ich die Dissertation mit dem Titel „Methoden zur Zustandserkennung von Lithium-Ionen-Batterien“ selbständig angefertigt und keine anderen als die von mir angegebenen Quellen und Hilfsmittel benutzt habe.

Ich erkläre außerdem, dass diese Dissertation weder in gleicher oder in anderer Form bereits in einem anderen Prüfungsverfahren vorgelegen hat.

Ich habe früher außer den mit dem Zulassungsgesuch urkundlich vorgelegten Graden keine weiteren akademischen Grade erworben oder zu erwerben versucht.

Ich bin mir bewusst, dass eine unwahre Erklärung zur Versicherung der selbständigen Leistungserbringung rechtliche Folgen haben kann.

Würzburg, den _____ _____

Lukas Gold

List of abbreviations

ADC ..... Analog to Digital Converter

AE ..... Acoustic Emission

AEKF ..... Adaptive Extended Kalman Filter

ASE ..... Autoregressive Spectral Estimation

BEV ..... Battery Electric Vehicle

BMS ..... Battery Management System

BoL ..... Beginning of Life

CC ..... Coulomb Counting

CoM ..... Center of Mass

CPE ..... Constant Phase Element

DC ..... Direct Current

DFT ..... Discrete Fourier Transform

DFunT ..... Density Functional Theory

DL ..... Deep Learning

DSP ..... Digital Signal Processing

EC ..... Energy Content

ECC ..... Enhanced Coloumb Counting

EChM ..... ElectroChemical Model

ECM ..... Equivalent Circuit Models

EIS ..... Electrochemical Impedance Spectroscopy

EKF ..... Extended Kalman Filter

EMA ..... Experimental Modal Analysis

EMF ..... ElectroMotive Force

EoL ..... End of Life

FBG ..... Fiber Bragg Grating

FFT ..... Fast Fourier Transform

FIR ..... Finite Impulse Response

GEP ..... Generalized Elastic Parameter

GMA ..... Generalized Additive Model

HFR ..... High-Frequency Resistance

ICP-OES ..... Inductively Coupled Plasma-Optical Emission Spectrometry

IR ..... Internal Resistance

IS ..... Impedance Spectroscopy

KF ..... Kalman Filter

LCO ..... Lithium Cobalt Oxide

LFP ..... Lithium Iron Phosphate

LIB ..... Lithium-Ion Battery

LIBs ..... Lithium-Ion Batteries

LTI ..... Linear Time-Invariant

LTO ..... Lithium Titanate

ML ..... Machine Learning

NCA ..... Lithium Nickel Cobalt Aluminum Oxide

NDE ..... Non-destructive Evaluation

NEP ..... Negative Electrode Potential

NMC ..... Lithium Nickel Manganese Cobalt Oxide

NN ..... Neural Network

NU ..... Normalized Units

OBE ..... Observer-Based Estimation

OCV ..... Open-Circuit Voltage

PDE ..... Partial Differential Equation

PEP ..... Positive Electrode Potential

POM ..... Poly-Oxy-Methylene

PSD ..... Power Spectral Density

RBF ..... Radial Basis Function

RC ..... Resistor-Capacitor

RCn ..... Raised Cosine with n oscillations

RMSE ..... Root Mean Square Error

ROI ..... Region of Interest

RUL ..... Remaining Useful Life

SBR ..... Styrene-Butadiene Rubber

SEI ..... Solid Electrolyte Interface

SH ..... Horizontally polarized Shear wave

SHM ..... Structural Health Monitoring

SMO ..... Sliding Mode Observer

SNR ..... Signal-to-Noise Ratio

SoC ..... State of Charge

SoE ..... State of Energy

SoH ..... State of Health

STD ..... STandard Deviation

SV ..... Vertically polarized Shear wave

SVM ..... Support Vector Machine

SVR ..... Support Vector Regression

TIE ..... Transversely Isotropic Equivalent

ToA ..... Time of Arrival

ToF ..... Time of Flight

US-NDE ..... Ultrasonic Non-Destructive Evaluation

List of symbols

Remarks

Variables that are marked with an arrow above, e.g., $\vec{v}_{ector}$, denote a vector. A dot over a variable implies its derivative with respect to time, e.g., $\dot{x}$. An asterisk * in the exponent of a variable or quantity denotes its complex conjugate. The midline dot $\cdot$ denotes the multiplciation operator. The six-pointed star $*$ denotes the convolution operator. The five-pointed star $\star$ denotes the cross-correlation operator. Vertical bars around a variable denote its absolute value, e.g., $|Z|$. $\mathrm{Re}(Z)$ and $\mathrm{Im}(Z)$ indicate the real and imaginary part of a variable (here Z), respectively. As common in computer science, sampled, discrete signals and quantities are denoted with square brackets around the index n, as in $x[n]$.

Symbol	Description / explanation
A_S, B_S, C_S	Matrices, expressing the relation of the measured quantities and the state variable $x_S(t)$ of a system in the context of linear time invariant systems
A_{GEP}	Generalized elastic parameter
$\alpha(f)$	Frequency dependent attenuation on a medium
b_0	Viscous damping factor
$b(\lvert\vec{z}\rvert)$	Propagation length $\lvert\vec{z}\rvert$ dependent dampening constant
B_{abs}	Absolute bandwidth of a frequency spectrum
B_{rel}	Relative bandwidth of a frequency spectrum
β	Porosity
β_{eff}.	Effective porosity
β_i	Angle of incident
c	General propagation velocity, e.g., of a wave
c_k	Discrete Fourier transform coefficient of index k
c_l	Phase velocity of a longitudinal (compressional) sound wave
c_t	Phase velocity of a transversal (shear) sound wave
c_0	Speed of sound; sound velocity
c_{P1}, c_{P2}	Phase velocity of fast and slow pressure sound wave in a fluid-saturated porous medium
$c_{P,dry}$	Phase velocity of a pressure or compressional sound wave in a dry porous medium

c_R	Propagation velocity of a Rayleigh wave
c_S	Phase velocity of a shear sound wave in a fluid-saturated porous medium
$c_{S,dry}$	Phase velocity of a shear sound wave in a dry porous medium
$c_*(t)$	Convolution of two continuous signals, a function of the index variable t
$c_*[n]$	Convolution of two discrete signals; a function of the index variable n
$c_\star(\tau)$	Cross-correlation of two continuous signals; a function of the shift variable τ
$c_\star[m]$	Cross-correlation of two discrete signals; a function of the shift variable m
C	Regularization parameter of a support vector regression (SVR)
$C_{DC}(t)$	Available discharge capacity of a battery cell at a given time t
C_{ijkl}	Stiffness tensor (a fourth-order tensor), mapping stress to strain
C_{max}	Maximum available electrochemical capacity of a battery cell in a given cycle
C_n	Nominal electrochemical capacity of a battery cell at its beginning of life
C_x	Constant modelling the depth-dependent amplitude of a Rayleigh wave, depth in x-direction
$C_*[k]$	Fourier transform of the discrete convolution $c_*[n]$
$C_\star[k]$	Fourier transform of the discrete cross-correlation $c_\star[n]$
d_m, Δd_m	Thickness, change of thickness of a material under stress or strain
d_p	Pore diameter
d_l	Spatial period of layering
d_{PE}	Piezoelectric proportionality constant
d_{plate}	Thickness of a plate
d_{xdr}	Dimension of the active element of a piezo transducer along a given axis
D_F	Electric displacement field
D_{xdr}	Diameter of the active element of a piezo transducer (abbreviated “xdr”)
δ_{ik}	Kronecker delta; equals 1 for $i = j$, otherwise 0
$\delta[n]$	Discrete Dirac delta function; equals 1 for $n = 0$, otherwise 0

$\delta(t)$	Continuous Dirac delta function; equals 1 for $t = 0$, otherwise 0
E	Young's modulus; elastic modulus
E_F	Electric field strength
$E(t)$	Envelope of a continuous signal
$\in$	Element of; as in $x \in \{1,2,3\}$
$\epsilon(f)$	Frequency dependent dispersion in a medium
ε	Maximum acceptable error or margin of a SVR
ε_{ij}	Strain tensor in a solid (a second-order tensor)
η_{batt}	Efficiency of the charging and discharging process, accounting for loss reactions
$\eta[n]$	Additive noise in a discrete measurement process
f	Frequency of an oscillation
$f(t)$	Arbitrary time dependent function
f_a, f_b	Frequencies at the -3 dB to the left and the right of the center frequency within a frequency spectrum
f_B	Folding frequency
f_c	Center frequency of a frequency spectrum
f_p	Peak frequency of a frequency spectrum
f_s	Sampling frequency of a signal
f_{sk}	Skewness of a frequency spectrum
f_t	Transition frequency (Biot theory)
f_0	Resonance frequency
F	Physical force
$F(\omega)$	Fourier transform of $f(t)$
G	Shear modulus
γ	Weighing factor of an SVR, regulating the penalty on values outside of the margin ε
$h[n]$	Discrete impulse response
$H_{ae}(f)$	Acoustic-electrical transfer function
$H_{ea}(f)$	Electric-acoustical transfer functions
$H_e(f)$	Electrical transfer function
$H_r(f,z)$	Transfer function of the propagation path z
$H[k]$	Fourier transform of the impulse response
i	A natural number, used as index
$\hat{\imath}$	Imaginary number, defined by $\hat{\imath}^2 = -1$

I_r, I_i	Refracted and incident intensities of a sound wave at an interface between two media with acoustic impedances Z_1 and Z_2
$I(t)$	Instantaneous electrical current at a given time t
$\hat{\mathrm{I}}(t)$	Complex electrical current at a given time t
∞	Infinity
j	A natural number, used as index
k	A natural number, used as index
$\vec{k}$, k_i	Wavenumber, three-dimensional; vectorial and indicial notation
k_x, k_y, k_z,	Wavenumber, one-dimensional; subscript denotes direction of propagation or
$\bar{k}$, k_1, k_2	Wavenumber, one-dimensional, subscript according to single wave in superposition
k_p	Permeability of a medium
K_b	Bulk modulus of a dry porous matrix
K_f	Bulk modulus of a fluid
K_G	Gain vector of the KF, regulating the correction of the state variable $x_S(t)$
K_p	Constrained modulus of a dry porous matrix
K_s	bulk modulus of a solid,
l	A natural number, used as index
l_m, Δl_m	Length, change of length; of a material under stress or strain
λ	Wavelength of a sound wave
λ_t	Wavelength of the transversal sound wave
m	A natural number, used as index
m_{th}	Number of points exceeding the threshold τ_{th} of the sliding-window
M	Stiffness or constrained modulus M of a material; P(ressure)-wave modulus
μ_d	Dynamic viscosity
n	A natural number, used as index or as the number of oscillations in a raised cosine pulse
N	A natural number, used as maximum value of an index or as the length of a signal
$N[k]$	Fourier transform of the additive noise
N_F	Near field length
N_S	Shear modulus

N_{th}	Length of the sliding-window (double threshold method)
ν	Poisson's ratio
ν_k	Kinematic viscosity
ω	Circular frequency of an oscillation
$d\omega$	Integration variable for circular frequency
P_{GEP}	Generalized elastic parameter
ϕ_k, ϕ_1, ϕ_2	Phase angle of a complex quantity, e.g., voltage
$\Delta\phi$	Phase shift between complex quantities, e.g., voltage and current
π	The mathematical constant, defined as the ratio of a circle's circumference to its diameter
$\psi(t)$	Analytical signal, derived from a signal $y(t)$
$\Psi(f)$	Fourier transform of the analytical signal
Q_{GEP}	Generalized elastic parameter
Q^2_{Wiener}	Wiener regularization parameter or "noise desensitizing factor"
$\vec{r}$	location vector
$r[n]$	Discrete reflectivity
R	Reflectance
R_{GEP}	Generalized elastic parameter
R_{lw}	Ratio of wavelength and pore diameter d_p for long wave approximation
ρ	Density of a material / medium
ρ_f	Density of the fluid
ρ_s	Density of the solid
S_D	Deformation
$S_{\mathrm{N}}[k]$	Power spectral density of the additive noise $\mathrm{N}[k]$
$S_X[k]$	Power spectral density of the input signal $x[n]$
$SoC(t)$	State of charge of battery cell at a given time t
SoH	State of health of a battery cell
σ	Standard deviation of the noise of a digital signal
σ_{ij}	Stress tensor (a second-order tensor)
t	Time
dt	Integration variable for time, taking values in the interval $[t_1, t_2]$
t_0	Time of flight of a signal, or specific delay of a sent and received signal
T	Period of an oscillation

T_M	Mechanical tension
τ	Delay
τ_{th}	Threshold
$\Theta(f)$	Heaviside or Theta step function, as a function of frequency f, which is 0 for $f < 0$ and 1 for $f \geq 0$
$\vec{u}(\vec{r}, t)$	Local displacement in a solid, in vector notation
u_i	Local displacement in a solid, in indicial notation, $i \in \{1,2,3\}$ indicates one of the directions in a Cartesian coordinate system
$u(x, t)$	Local displacement in a solid in one direction x and time t, one-dimensional
$u_S(t)$, $y_S(t)$	Measured quantities of the system at a given time t
$U(f)$	Electrical excitation of a sending transducer
$\vec{U}(\vec{r}, t)$	Local displacement in a fluid, three-dimensional
$\hat{\mathrm{U}}(t)$	Complex voltage at a given time t
v	Velocity of, e.g., a particle
v_p	Phase velocity of a sound wave
v_g	Group velocity of a sound wave
w_j	Weighing factor of a neural network (NN)
x_i	Location vector in indicial notation; $i \in \{1,2,3\}$
x_{obs}, y_{obs}	Observable quantities of an arbitrary system
$x_S(t)$	Variable describing the inner state of a system at a given time t, not directly observable
$x[n]$	Discrete, sampled signal; input signal
$x(t)$	Continuous, time dependent signal
$X[k]$	Fourier transform of the discrete signal $x[n]$
$X'[k]$	Estimate of the Fourier transform of the original discrete input signal
$X(\omega)$	Fourier transform of the continuous signal $x(t)$, as a function of the circular frequency ω
$X(f)$	Fourier transform of the continuous signal $x(t)$, as a function of frequency f
ξ	Error or deviation of a data point outside of the margin of a SVR
$y[n]$	Discrete, sampled signal; output signal
$y(t)$	Continuous, time dependent signal
$\hat{y}(t)$	Hilbert transform of the signal $y(t)$

$\hat{y}_S(t)$	Estimate of the measured quantity of a system, output of a Kalman Filter (KF)
$\hat{y}_{err}(t)$	Deviation of the estimate $\hat{y}_S$ from the measured quantity $y_S(t)$
$Y(f)$	Fourier transform of the signal $y(t)$
$Y[k]$	Fourier transform of the discrete signal $y[n]$
$\vec{z}$	Propagation path in a medium
Z	Electrical impedance
$Z_{acoustic}$, Z_1, Z_2	Acoustic impedance

Table of contents

1 Introduction & aim of the thesis

1.1 Motivation

With the events of 2020 and 2021, the climate change and the necessary countermeasures, to prevent the further rise of the mean global temperature, are more present in the public consciousness than ever before. Thanks to technical advances, the question isn't any more if sourcing energy from 100% renewable sources is possible [1], but when it will be achieved. One energy sector that makes up for a big share of global greenhouse gas emissions is transport and mobility. With almost every car manufacturer having a battery electric vehicle (BEV) program announced or in execution, lithium-ion batteries are at the moment the best energy storage solution at hand. Even though the technology has advanced rapidly in the past three decades since the introduction to the global market by Sony in 1991, lithium-ion batteries remain inherently un-save and require continuous monitoring to ensure compliance with a very narrow operating range. Otherwise, they are prone to premature unexpected failure, a shortened lifespan, or might pose a safety hazard to the environment or the user of the battery-powered product [2]. Today's battery management systems, that handle the task of monitoring the battery cell condition, rely on terminal voltage, current, and temperature measurements. The hereby provided estimate is known to inaccurately describe the state of the battery cells, as the electrically measurable features are partially unable to represent the battery's internal conditions, especially when the progressed aging plays a significant role. The omitting of the mechanical behavior, physical properties, and their change during regular battery operation and changes resulting from aging, in design considerations had detrimental effects on the public perception of the safety of lithium-ion batteries and caused enormous economic damage, e.g., in the case of the Samsung Galaxy Note 7 [3,4]. Since the physical properties of the battery cells correlate with the battery state, the integration of the sensing and the designing for those property changes does not only provide the opportunity to avoid future catastrophe but also offers an improvement of the state estimation accuracy [2]. Thereby two of the most critical inhibitors in public opinion for the switch from internal combustion engine-powered mobility to sustainable mobility provided by BEVs can be combatted: safety concerns and even more important, the fear of too short and unreliable driving range – the so-called range anxiety or German "Reichweitenangst". Ultrasound is one of the most promising candidates to sense those physical properties, as sensors can be attached on the surface, without interfering with battery operation, but are still able to access the properties of the bulk volume of the battery cell. Ultrasonic non-destructive evaluation (NDE) or structural health monitoring

(SHM) usually involves expensive measurement equipment and is therefore often limited to the monitoring of expensive structures or testing that involves the reversible attachment of ultrasonic probes to the device under test (DUT). This thesis aims to achieve improved state estimation capabilities by utilizing low-cost off-the-shelf piezo elements that are fitted to the surface of the battery cells, whose state is to be estimated, acting as ultrasonic probes of the physical properties.

1.2 Scope of the thesis

This thesis is supposed to serve two purposes. First, it is meant as an introduction to the complex fields of state estimation for lithium-ion batteries (LIBs), and ultrasonic nondestructive evaluation of LIBs for current and future activities. Both were untapped topics at Fraunhofer ISC at the beginning of this work in 2016. Second, this thesis aims to demonstrate the feasibility of state of charge (SoC) estimation with a data-driven machine learning approach, based on ultrasonic data.

To establish the described two topics, the theory section gives an overview of the relevant technologies and theoretical frameworks. This includes information on today's most relevant battery technology regarding production, the principle of operation, and state estimation. Furthermore, the generation, reception, and propagation of ultrasound in solids and fluid-saturated porous media are covered. The latter is the class that LIBs can be counted to. To establish the base for the analysis of the results, the fundamentals of digital signal processing and impedance spectroscopy are introduced as well. The experimental methods and instrumentation are described in the third chapter. The results and discussion chapter demonstrates the implementation of a data-based SoC estimation, correlating ultrasonic signal features with the SoC by employing modern concepts of signal processing and machine learning. Finally, a conclusion is drawn and the quality of SoC estimation is compared with the state of the art and a prospect on the future of the application of ultrasound to lithium-ion batteries is given.

2 State of the art & theoretical background

2.1 The object of investigation: the lithium-ion battery

This section gives a brief overview of lithium-ion batteries (LIBs) and aims to state all information relevant for understanding the interaction of ultrasound with the structure of LIBs. This includes the working principle and associated reversible changes to their mechanical properties, a description of the components, the manufacturing process, and the aging phenomena. Finally, methods for the state estimation of LIB are reviewed.

2.1.1 Working principle of lithium-ion batteries and reversible changes

A lithium-ion battery (LIB) cell usually consists of several galvanic cells, connected in parallel. A galvanic cell contains two composite electrodes and a separator in between. The structure of the three is wetted with an electrolyte that acts as the medium for lithium-ion transport. The structure and the basic working principle are depicted in Figure 2.1. During charging of the battery, lithium in the positive electrode is oxidized and deintercalated. The lithium-ion is then solvated when passing to the electrolyte and migrates to the negative electrode. On the electronic conduction path, electrons reach the negative electrode, where they reduce lithium-ions to neutral lithium atoms which are desolvated and intercalated into the host structure. What makes lithium-ion batteries unique is the high reversibility of this process during discharge [5].

Because the (de-)intercalation reaction takes place on the interface of active material and electrolyte, a concentration gradient within the active material particles exists which is subsequently slowly reduced by diffusion processes. The change of lithium concentration within the particles is accompanied by a change in crystal lattice structure, which in turn causes changes in Young's modulus and volume. Lattice parameters can be measured in-situ by neutron or X-ray diffraction [6–10] and Young's moduli can be calculated lithium concentration-dependent by density functional theory (DFunT) [11–13]. Table 2.1 lists a selection of common active materials in the delithiated and lithiated phase, as well as the volume change at lithiation and the change in Young's modulus.

While some materials undergo drastic changes, e.g., graphite and silicon, others such as lithium titanate (LTO) do not show that strong dependence of their mechanical behavior on lithium concentration and are therefore considered zero strain materials.

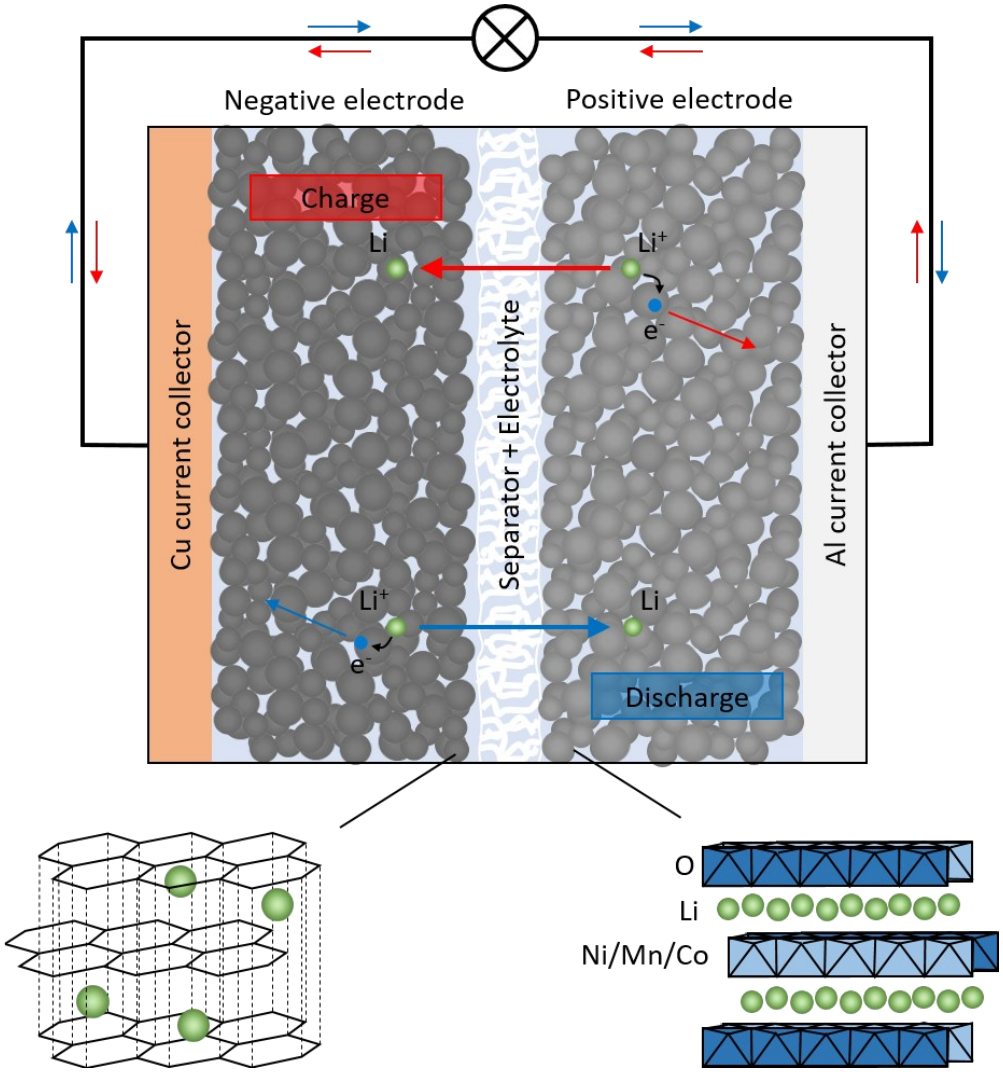

Figure 2.1: Components and working principle of a lithium-ion battery. For this example, a graphite negative electrode and a lithium nickel manganese cobalt oxide positive electrode were chosen. Both electrodes are prepared as a porous layer on the current collector foil and are separated by a porous separator. The pores of the three are soaked with electrolyte. The rocking chair mechanism, employed by lithium-ion batteries utilizes the (de-)intercalation of lithium-ions in the host structure of the active materials. During battery charging, lithium-ions are deintercalated from the positive electrode and intercalated into the negative electrode. During discharge, the process is reversed. Graph after [14].

For most active materials, DFunT calculations are only available at two distinct phases, either fully lithiated or delithiated. In electrochemical applications, for, e.g., lithium cobalt oxide (LCO) the full range of lithium content from $x = 0$ to $x = 1$ in Li_xCoO_2 is not utilized. Therefore, a more realistic estimation can be established by interpolating between the two available data points in [11], yielding a Young's modulus increase of approximately 34% from 197 GPa to 264 GPa in the utilized range of lithium concentration. Another source using instrumented nano-indentation to estimate the elastic modulus [15] states different values for LCO from 89 GPa ($Li_{0.5}CoO_2$) to 178 GPa ($LiCoO_2$). From neutron and X-ray

diffraction data, the volume change in this range can be estimated to be around 1% to 2% [6–10,16]. When considering a state-of-the-art lithium-ion battery, it can be concluded that the change in volume (up to 10%) and Young's moduli (up to 275%) of the carbonaceous negative active material outweigh the changes of the lithium transition metal oxide positive active material.

Table 2.1: Selected active materials, their composition of fully lithiated and delithiated phase, volume change, and Young's modulus. The arrow represents the change in Young's modulus from delithiated to lithiated phase. Where available, practically utilized compositions are stated. According to [12] and [17].

Delithiated phase	Lithiated phase	ΔV	Young's Modulus / GPa	Ref.
Typical positive electrodes				
CoO_2	$LiCoO_2$	2%	59.8 → 264 (calculated)	[12,16]
$Li_{0.5}CoO_2$	$Li_{0.9}CoO_2$	n.a.	89 → 85	[15,17]
	$Li_{0.95}CoO_2$	n.a.	96	[15,17]
	$LiCoO_2$	n.a.	178 (nano-indentation)	[15,17]
Mn_2O_4	$LiMn_2O_4$	6.8%	190 → 194	[12]
$FePO_4$	$LiFePO_4$	5%	125 → 124	[18–20]
$Li_{0.45}(NiMnCo)O_2$	$Li(NiMnCo)O_2$	1%	n.a.	[9,21]
Typical negative electrodes				
C (graphite)	1/18 LiC_{18} (dilute stage 2L)	5.8%	32 → 29	11
	1/18 LiC_{18} (stage 3)	3.6%	29	[11]
	1/12 LiC_{12} (stage 2)	4.6%	58	[11]
	1/6 LiC_6 (stage 1)	10%	109	[11]
$Li_4Ti_5O_{12}$	$Li_7Ti_5O_{12}$	0.3%	181 → 209	[20,22,23]
Si	$Li_{3.75}Si$	263%	96 → 41	[13]

Recently, it was shown that even though active material particles account for up to 97% of the solid electrode, the electrode's mechanical behavior is dominated by the properties of the binder and by being soaked with electrolyte [24]. Therefore, the magnitude of change of the mechanical properties of lithium-ion batteries during operation, as a result of (de-)intercalation, is still under discussion. Methods of ultrasonic non-destructive evaluation were already applied to address this question [25]. The herein calculated effective elastic

modulus of the studied battery cell increases about 10% during a cycle from fully discharged (5.09 GPa) to fully charged state (5.54 GPa) [25].

2.1.2 Components of lithium-ion batteries

Both, negative and positive electrodes are porous structures, made up of active material particles, a binder, and a conductive additive. The negative electrode, or anode, is typically composed of a carbonaceous active material coated onto a copper current collector foil. The positive electrode, or cathode, usually contains lithium transition metal oxides or phosphates as active material coated onto an aluminum current collector foil. Cobalt, manganese, and nickel oxides are most commonly found and are used either in pure form, e.g., $LiCoO_2$ (LCO), or in combination in varying compositions, e.g., lithium nickel manganese cobalt oxide (NMC). Besides those two very common positive active materials, aluminum-doped nickel cobalt oxide (NCA) is also often found in applications with a demand for high energy density [26,27]. Even though the specific energy density of the carbonaceous negative electrode is higher than the energy density of available positive active materials, its ability to store energy can be further improved by adding silicon. With the introduction of silicon to the lithium-ion battery, the cycling stability is reduced, mostly by detrimental mechanical effects caused by the comparably large volume change of Si during lithiation of up to 310% [28]. Therefore, only a small percentage, e.g., up to 10% [29], of the negative active material in modern-day batteries is made up of silicon. Where energy density is not a top priority but high charging and discharging rates are important, lithium titanate (LTO) is used as a negative active material, and lithium iron phosphate (LFP) is used as a positive active material. Typically, the separator is a porous polymer film, often made from a polyolefin such as polypropylene or polyethylene, with a composition varying depending on application and safety concerns. To increase battery safety by inhibiting thermal runaway through increased thermal stability the separator is often coated with a ceramic layer, such as Al_2O_3 [30]. The aforementioned electrolyte consists of a mixture of polar and non-polar organic solvents such as organic carbonates, a conducting salt such as $LiPF_6$, and additives [31].

Lithium-ion batteries are, besides active materials, further distinguished by the housing that seals the stack of galvanic cells off from the surrounding and provides electrical contact. There are three types of battery cell designs today: pouch, cylindrical and prismatic [32]. For pouch cells, the housing is constructed of a weld-able barrier film, made from a multilayer polymer-metal foil compound. Cylindrical cells are similar in design to primary alkaline batteries, having a rather rigid tubular housing made from stainless steel. Prismatic

cells have an often even stronger housing, constructed from steel or aluminum. With the accompanying ability to withstand high internal cell pressure and external loads, prismatic cells are today preferred by some manufacturers for automotive applications [32].

2.1.3 Battery assembly, filling, and formation

Battery cell production is a complex and cost-competitive process that can be divided into three major sections: *electrode manufacturing, cell assembly,* and *cell finishing* as depicted in Figure 2.2. The following description follows the overview of the production process in [33]. *Italic* font marks the most significant process steps.

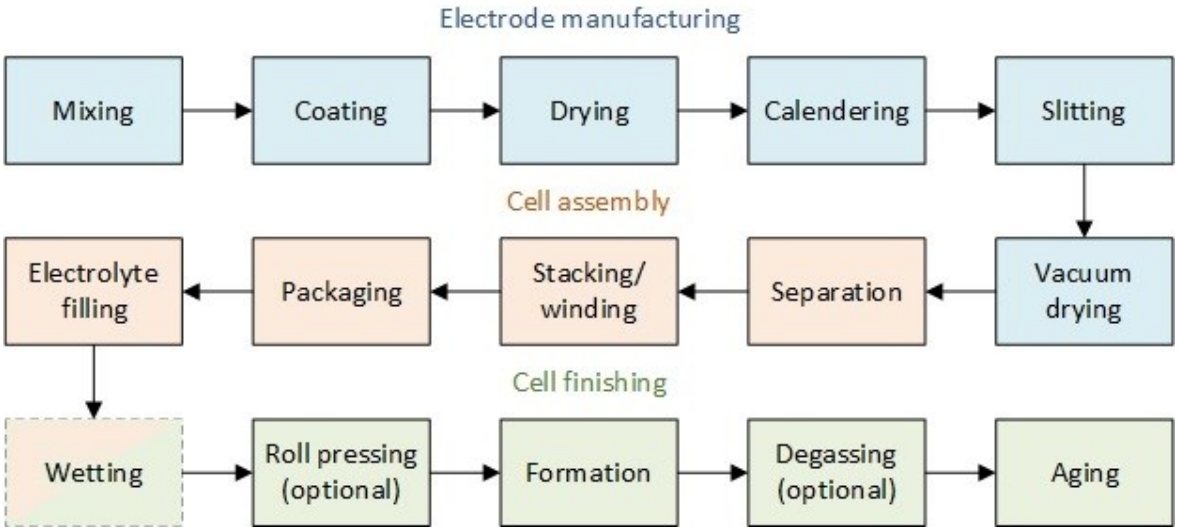

Figure 2.2: Li-ion battery cell production process, divided into three major sections. Solid line frames mark active processes, while the passive process wetting is marked with a dashed line frame.

Electrode manufacturing includes the slurry preparation by *mixing* the components, which is followed by the *coating* of the slurry on current collector foils. The wet film is then dried and solvents are removed. During the subsequent *calendering* the layers are compressed by rotating rollers. Thereby the porosity of the electrodes is defined which influences cell performance and wettability of the electrodes in a later step. Subsequently, the electrode foils are *slit*, cleaned and *vacuum dried* to remove residues from preceding steps and humidity [33].

Cell assembly is usually performed in a dry room atmosphere, with the *separation* of electrode rolls into single sheets being the first step. After punching out single sheets, those are again cleaned and fed into the *stacking* process, which combines electrode sheets and separator into one assembly. Depending on cell design, the stacking process can either be single-sheet stacking, Z-folding or winding. Subsequently, tabs are *welded* onto the blank

parts of the current collector foils. During *packaging,* the stack is *inserted* into a preformed housing and partially sealed. Now, the electrolyte is *filled* into the battery housing. As soon as the electrolyte makes contact with the porous structure of the electrodes and separator, the capillary force starts to suck it into the pores and the *wetting* begins. The penetration into the porous network is affected by the polarity of the electrolyte and the binder/electrode composition as well as the pore structure. Thus, the wetting process can take a long time and is often aided by additional steps. The number of dosing steps, electrolyte temperature, atmospheric pressure in the filling chamber, and timings may vary depending on the design and size of the battery cell. The latter is then *sealed* and the filling chamber is flooded with air, concluding the cell assembly [33].

Cell finishing can be divided into several steps. *Roll pressing* is the first but optional step to improve electrolyte distribution by rolling over the sealed pouch cell. Before the *formation* can start, all pores and cavities within the battery cell should ideally be saturated with electrolyte. This slowly advancing process is called *wetting*. “To date, there are no industrial established measuring methods to determine the wetting state of the cell.” [34] (A3249) Therefore, the estimate of the waiting time to proceed is a result of experience and cell tests [34]. The linked need for available storage space, temperature control, process time, and safety monitoring make the wetting/waiting step costly and poses a big chance for improvement. During the subsequent *formation* process, the battery cells are initially charged and discharged according to precisely defined procedures that usually remain under the discretion of the manufacturers. Hereby, the solid electrolyte interface (SEI) is formed. The composition, the stability and the homogenous distribution of the SEI on the surface of the negative electrode are important quality criteria that strongly effect cycle stability and performance. Pouch cells require an additional step, called *degassing*, where gas that evolved during the formation process is removed from the cell body and the cell is finally sealed. *Aging* is the final step of cell production and acts as a quality assurance during which the cell characteristics and the cell performance are monitored. When no significant change in the cell properties occur, the cells passed the check [33].

2.1.4 Battery aging: irreversible changes

The term *battery aging* describes the process of degradation of available capacity and available power of a lithium-ion battery during operation (cycle aging) and during storage or non-operating conditions (calendar aging) [35]. Analogically to the state of charge (SoC), the state of health (SoH) can be defined as:

$$\boldsymbol{SoH = \frac{C_{max}}{C_n} \cdot 100\%,} \quad \textbf{(1)}$$

with C_{max} being the maximum available capacity at a given cycle and C_n being the nominal capacity of the battery at its beginning of life (BoL) [36]. The end of life (EoL) of a lithium-ion battery is commonly defined by the point at which the SoH reaches 80% [36] but is also associated with the doubling of the internal impedance of the battery cell [37–39] since at that point the available battery power is cut in half. In-depth reviews of aging mechanisms can be found for example in [40–44].

2.1.5 Lithium-ion battery state estimation methods

Lithium-ion battery cells do not inhibit an inherent over-charge or over-discharge safety mechanism. The electrolyte is thermodynamically not stable at the potentials, at which the negative electrode operates in non-abusive conditions, and at the potentials, at which the positive electrode may operate in highly delithiated states. Besides electrolyte decomposition, there are several other abusive scenarios, e.g., lithium plating and short circuits through dendrites or thermal runaway, which have to be prevented and, therefore, require permanent monitoring of the cell and the battery. Monitoring, state estimation, and charging/discharging are the main tasks of the battery management system (BMS) [45] that ensure a safe and reliable operation.

The SoH, defined in Equation (1), the SoC, and the internal temperature of a battery cell cannot be measured directly and have to be estimated [45]. The $SoC(t)$ at a given time t is defined by:

$$\boldsymbol{SoC(t) = \frac{C_{DC}(t)}{C_n} \cdot 100\%,} \quad \textbf{(2)}$$

with $C_{DC}(t)$ being the available discharge capacity of the battery at given time t. Especially in mobile applications, where LIBs act as power sources, the state of energy (SoE) is of equal importance as it states the remaining available energy until the end of discharge voltage (also known as cut-off voltage) is reached. The course of SoC and SoE development during battery operation depend highly on operation conditions such as ambient temperature and applied/extracted current or power, as the cell voltage and the internal temperature depend on those factors and act as ultimate cut-off criteria.

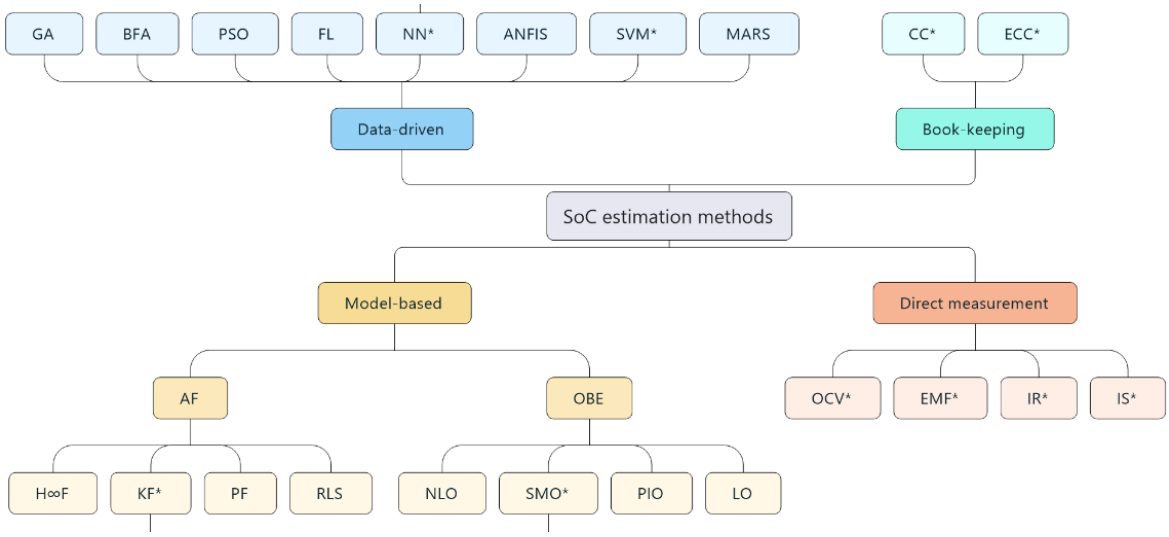

Figure 2.3: Classification of SoC estimation methods. Methods marked by * are detailed in the text. The listed methods are divided into four groups that differ fundamentally in the principle of operation. Abbreviations are defined as follows. AF: Adaptive filters, ANFIS: Adaptive neuro-fuzzy inference system, BFA: Bacterial foraging algorithm, CC: Coulomb counting, ECC: Enhanced coulomb counting, EMF: Electromotive force, FL: Fuzzy logic, GA: Genetic algorithm, H∞F**:** H infinity filter, IR: Internal resistance, IS: Impedance spectroscopy, KF: Kalman filter, MARS: Multivariate adaptive regression splines, LO: Luenberger-based observer, NLO: Non-linear observer, NN: Neural network, OBE: Observer-based estimation, OCV: Open circuit voltage, PF: Particle filter, PIO: Proportional integral observer, PSO: Particle swarm optimization, RLS: Recursive least square filter, SVM: Support vector machine, SMO: Sliding mode observer. Graph according to [46].

SoC estimation methods were reviewed extensively in the past [2,39,45–52]. Those methods can be classified into four categories [46], as shown in Figure 2.3. Those groups differ fundamentally in the principle of operation. Book-keeping methods basically keep track of the battery state by counting the charge transported in and out of the battery cell through charging and discharging currents. Direct measurement-based methods rely on the measurement of a quantity that correlates with the state of the battery cell and often involve lookup tables, serving as a reference to estimate the SoC from said quantity. Model-based methods deploy methods to abstract the working principle of the battery to a certain extent and thereby link the measurable quantities, e.g., cell voltage, to the not directly measurable SoC. The last group, the data-driven methods rely on the correlation of measurable quantities and SoC. They employ a data-basis containing the two to train a machine learning model to fit this correlation. The resulting model can then, at a way lower computational cost than the training, be employed to estimate the SoC. SoC estimation methods are generally judged according to estimation accuracy, computational efficiency, and how well they fit the requirements of a certain application [53].

2.1.5.1 Book-keeping methods

The methods requiring the smallest computational power are *book-keeping methods*. The simplest and most widespread method is the Coulomb counting (CC) or Ampere-hour counting technique which calculates the SoC based on the integration of the current flowing in and out of the battery [49]. With a known initial $SoC(t_1)$, the $SoC(t_2)$ at any time t_2 can be estimated based on the formula [45,53]

$$\boldsymbol{SoC(t_2) = SoC(t_1) + 1/C_n \int_{t_1}^{t_2} \eta_{batt} I(t) dt,} \quad \textbf{(3)}$$

where C_n is the nominal capacity and η_{batt} is the efficiency of the charging and discharging process, accounting for loss reactions. $I(t)$ is the instantaneous, electrical current, having a positive sign for charging and a negative sign for discharging. The accuracy of this method depends highly on accurate knowledge of the initial SoC and on the measuring accuracy of the current. Besides the accumulation of errors from inaccuracy in the technical implementation of current measurement and integration, the coulombic efficiency of the system contributes to the inaccuracy [45,48] and is, therefore, obtained from the average value of several tested batteries [53]. The accuracy of the basic Coulomb counting method can be enhanced (enhanced Coulomb counting, ECC) by several measures: The initial SoC can be estimated based on open-circuit voltage (OCV) or from the cell voltage under load, requiring a look-up table. Instead of the nominal capacity, the maximum achievable discharge capacity can be used, which has to be obtained by dynamic recalibration, simultaneously evaluating the SoH of the battery [53].

2.1.5.2 Direct measurement-based methods

The second group of direct estimation methods rely on *direct measurement-based methods*, including the OCV, the electromotive force (EMF), the internal resistance (IR), and the impedance spectroscopy (IS) approaches. They are all based on the relationship between a measurable quantity and the SoC. As these quantities are also a function of temperature but also depend on battery health, these effects have to be considered as well. The cell voltage in absence of a current is called open-circuit voltage. After sufficient resting time, following a current interrupt, the battery reaches equilibrium and the OCV equals the EMF which describes the capability of an electrochemical system to deliver energy. SoC and EMF are closely related. Therefore, the OCV of a battery can be used to estimate the SoC after sufficient resting time [46,49]. The load profiles commonly found in mobile applications

make the OCV method unsuitable for online estimation but allow for a precise initialization of the SoC [48] – $SoC(t_1)$ in Equation (3). Models, including equivalent circuits, can be used to estimate the EMF under load using the load current and the terminal voltage [54] or using the terminal voltage alone after the current interrupt [55]. The calculated EMF allows then for an estimate of the SoC. The internal resistance (IR) method also uses the battery current and a change in terminal voltage, estimating the direct current (DC) resistance. The terminal voltage delta, measured at a high sampling frequency, with a change in current is used to calculate the IR [46], which is related to the SoC. Since the value of the resistance is very small, therefore challenging to measure [56,57], and is also a function of multiple other parameters besides the SoC, this method is not preferred. For the impedance spectroscopy method, the voltage response to a small signal current excitation of a broad frequency spectrum is analyzed to calculate the internal impedance and estimate the SoC. The current excitation requires external instrumentation, making the IS method difficult to implement in a BMS and thus less relevant for online estimation [57]. Still, the impedance and derivable/deducible parameters of a battery may be online measured at selected frequencies and under laboratory conditions to initialize battery models.

2.1.5.3 Model-based methods

Although the approaches described above already rely on modeling to some extent, *model-based estimation methods* present a distinct third group. Before detailing specific approaches, it is useful to establish an overview of various battery models. Models that are used in BMS today, can be categorized as the battery-electric model, the battery thermal model, and the battery coupled model [45]. Future BMS systems may also include modeling of mechanical behavior and mechanical properties of the battery [39].

The *battery-electric models* include electrochemical models, reduced-order models, equivalent circuit models, and data-driven models. The electrochemical models (EChM) describe the battery dynamics with partial differential equations (PDE) [49], accounting for electrode potentials, ion concentration, and Butler-Volmer kinetics [45]. These full-order battery models provide a high accuracy but also require a large set of parameters and high computational power. With suitable assumptions, reduced-order models can be established that have lower requirements and thus are more practical for real-life applications. In equivalent circuit models (ECM), the battery dynamics are described by a series of resistances, capacities or constant phase elements (CPE) and voltage sources [45,49,57], as illustrated in Figure 2.4.

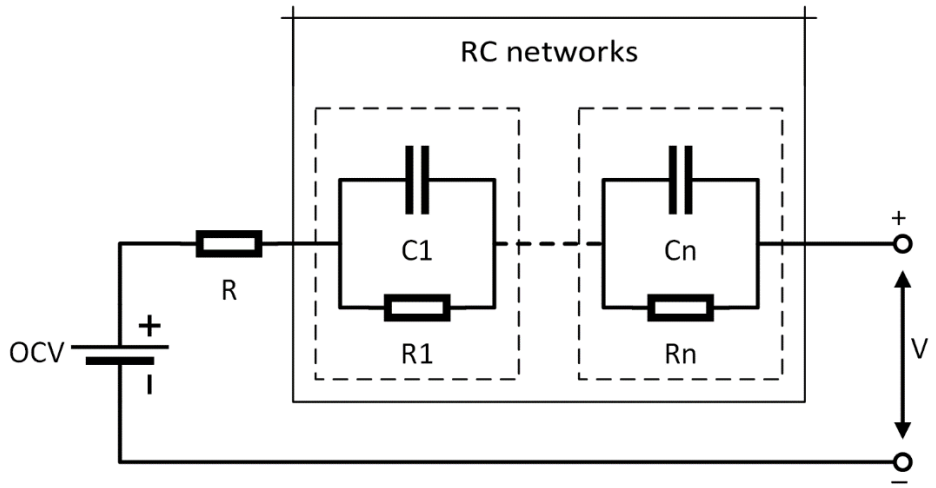

Figure 2.4: Equivalent circuit model of a battery. Electrical and ionic conduction, as well as different electrochemical processes, are represented by circuit elements. The complexity of employed models may vary with the number of circuit elements but is generally kept as simple as possible to avoid an over-parametrization of the system. This circuit diagram adapted from [45]

Depending on available computing power and demanded accuracy, the number of resistor-capacitor (RC) networks may differ. Commonly used are first and second-order models, with one or two RC networks, respectively [49]. Due to their simplicity and good accuracy, especially for SoC estimation and power prediction, ECMs are widely adopted in applications [37,49].

The *battery thermal model* has to account for heat generation and heat transfer. Entropic heat, as of electrochemical reactions, or Joule's heat, as a result of ohmic losses, contribute to heat generation within a battery. Very often, heat generation is assessed by the power loss due to the internal resistance, the power loss caused by over-potentials, and by the entropy change during chemical reactions [58–61]. Heat transfer models describe heat dissipation by heat conduction, heat convection, and heat radiation. Full-scale models with three-dimensional geometry allow for the highest accuracy, but also require the highest computing power. Therefore, reduced-order models and data-driven models are also applied to thermal modeling and battery thermal management [45]. Heat conduction, being the dominant heat transfer mechanism, allows establishing a reduced-order thermal model - the popular two-stage model, which assumes that the temperature within the battery is uniformly distributed [45].

The *battery coupled model* combines electric and thermal models to account for the strong interplay of thermal and electric behavior of a battery [45]. Especially transport properties within the electrolyte and the active materials are highly temperature-dependent. Therefore,

coupled models also play an important role in developing charging strategies [62], estimating available power [37], and state of safety considerations.

The aforementioned models are required for *model-based* estimation *methods*. Especially, ECM and EChM are used for adaptive filters, like the Kalman filter (KF) or the extended Kalman filter (EKF), and for observer-based estimation (OBE), like the sliding mode observer (SMO) [45,46]. All model-based estimation methods are based on the objective to estimate an inner state $x_S(t)$ by measured quantities $u_S(t)$ and $y_S(t)$. Assuming linearity, such a system can be expressed by

$$\dot{\boldsymbol{x}}_{\boldsymbol{S}}(\boldsymbol{t}) = \boldsymbol{A}_{\boldsymbol{S}}\boldsymbol{x}_{\boldsymbol{S}}(\boldsymbol{t}) + \boldsymbol{B}_{\boldsymbol{S}}\boldsymbol{u}_{\boldsymbol{S}}(\boldsymbol{t}), \quad \textbf{(4)}$$

$$\boldsymbol{y}_{\boldsymbol{S}}(\boldsymbol{t}) = \boldsymbol{C}_{\boldsymbol{S}}\boldsymbol{x}_{\boldsymbol{S}}(\boldsymbol{t}), \quad \textbf{(5)}$$

with A_S, B_S and C_S being matrices, expressing the relation of the measured quantities and the state variable [63].

The most prominent model-based estimation method is the Kalman filter [52] (working principle depicted in Figure 2.5) which, in general, can be used to achieve an estimate $\hat{x}_S$ of the inner state x_S of any dynamic system. The history of the Kalman filter dates back to the age of the space race when it was applied to circumlunar navigation problems for the Apollo Project as early as 1961 [64]. Regarding the application to LIBs, the basic idea is to model the battery as a system including an unknown quantity, like the SoC, in the filter's state description [53]. The estimation and correction workflow of such a filter is depicted in Figure 2.5. Here its working principle is described for the example of SoC estimation. A common BMS often measures the electrical current, voltage, and temperature of a battery. The KF uses current and temperature as input variables $u_S(I,T)$ to the battery model and estimates the battery voltage $\hat{y}_S(t)$ as response to this input with the aid of a SoC dependent function for the battery voltage. The output error or discrepancy between the modelled voltage and the measured battery voltage $\hat{y}_{err}(t)$ is then used as a feedback to reiterate the process with a corrected value for the SoC, aiming to reduce the discrepancy until a certain threshold is reached. Thereby the KF observes the not accessible state variables of the system, in this case the SoC. The correction of the state variable is tuned by a gain vector K_G that enable tuning of the dynamic and performance of the filter [53]. An important feature of the KF is the ability to filter disturbances (noise), uncertainties, and high variations of measurements by weighted averaging of measured and predicted values and therefore to estimate the inner state of the system accurately [46]. The diverse variations of the KF, like the extended KF (EKF) and the adaptive extended Kalman filter (AEKF), improve the

estimation result by considering nonlinearities of the system, e.g., in the EMF over SoC curve. With the KF approach, combinations with other estimation methods like the OCV [65–67] and Coulomb counting (CC) [68,69] method are feasible and several battery models can be used [65,66,70].

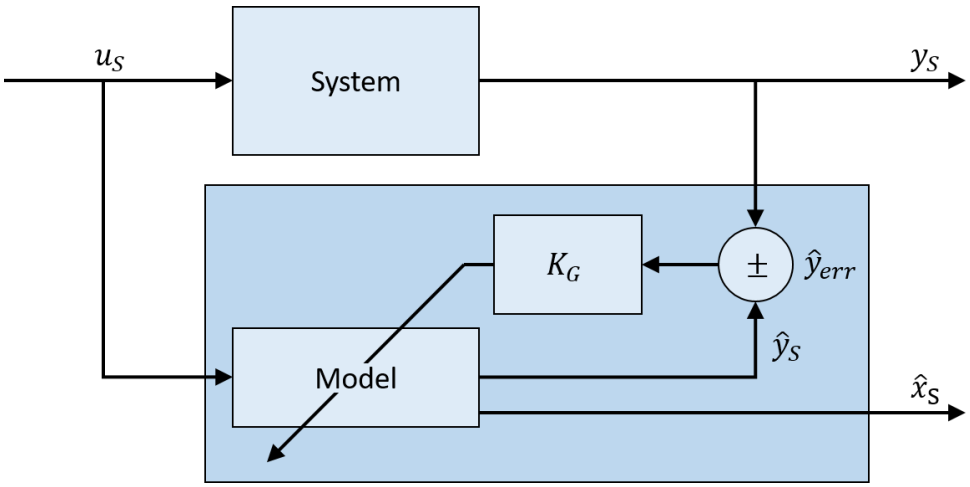

Figure 2.5: Kalman filter (KF) working principle. A KF feeds the input variables u_S of the system, whoms state is to be estimated, to a model. This model describes an output variable $\hat{y}_S$ as a function of a state variable. The model output is iteratively compared to the output of the actual system. If a deviation of model and system $\hat{y}_{err}$ exists, the estimate of the state variable $\hat{x}_S$ is tuned by a gain vector K_G to achieve a smaller deviation. Thereby the KF observes the not accessible state variable x_S of the system indirectly. Graph adapted from [53].

The sliding mode observer (SMO) is one example of observer-based estimation (OBE) methods. The concept was first published by Utkin [71] in 1981. The main difference between an SMO and KF is that instead of feeding back the output error linearly, modified by the gain vector K_G, the output error is fed back via a discontinuous switched signal [63]. Through this switched-mode and sliding observation, SMOs become resilient to noise and can reduce estimation error to next-to-zero in a finite time period [63].

2.1.5.4 Data-driven methods

Data-driven estimation approaches are not capturing the dynamic of the battery in a physicochemical model, they are built on empirical observations [49] and represent battery behavior as a relation of input and output signals of a battery. Therefore, in contrast to model-based approaches, the model parameters are determined by self-learning algorithms [72]. Data-driven approaches very often rely on the use of machine learning (ML) concepts to obtain parameters and relations of the model [49]. Because the model employed by these methods is generated from real training data, it is very flexible, and matches non-linearity well, and exhibits strong adaptability. Establishing a generic model based on data makes

the approach also very dependent on the quality of the data [45]. Therefore, a careful selection of a sufficiently large dataset and eventual pre-processing is necessary. Depending on the optimization method, to which the resulting model is very sensitive, over-fitting of the data may occur and thus an application of the model to other datasets than the training data may lead to high inaccuracy [39,45].

Artificial neural networks (NN) are inspired by biological neural networks in the human brain [46]. The basic structure of a three-layer NN for SoC estimation is sketched in Figure 2.6. The input layer is formed by the vector of instantaneous voltage, current, and temperature values, and the output layer is the instantaneous SoC value [49,57]. The hidden layer contains a non-linear map that can capture the relationship of input and output without prior knowledge of the battery's internal structure or processes [49]. The hidden layer is constructed from a suitable number of neurons and an activation function [49]. By feeding training data in the form of input-output pairs and tuning the weighing factors w_j, the model of the NN is optimized. Following the universal approximation theorem, NNs are capable of approximating any continuous function [73], e.g., $SoC(V, I, T)$, which can be exploited to accurately estimate the SoC [74–77]. Neural networks with more than two hidden layers are often considered "deep" and are therefore counted among the deep learning (DL) algorithms.

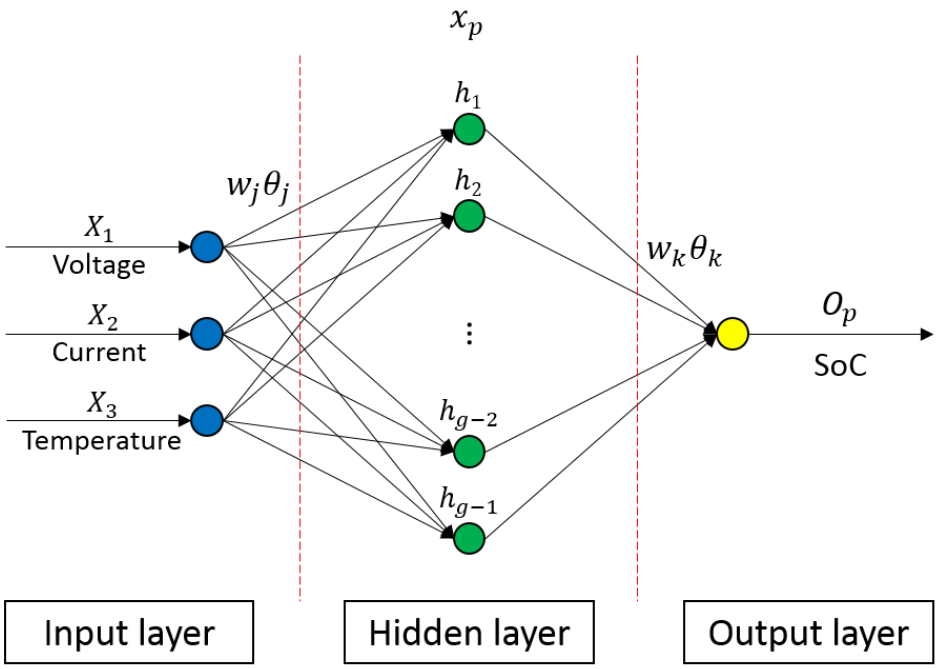

Figure 2.6: Structure of a three-layer neural network for SoC estimation, consisting of input, output, and hidden layer. The hidden layer captures the relationship between input and output in a map. This map is constructed from a number of neutrons and trained with input-output pairs to tune the weighing factors w_j. Graph according to [74].

The support vector machine (SVM) is a machine learning technique (ML), often employed to solve classification and regression tasks [49,57]. SVMs were first conceptually presented by Vladimir Vapnik and his colleagues in 1992 [78]. The working principle of SVMs can be explained for a two-dimensional case with the aid of Figure 2.7. Here, data points of two different classes also called training instances with two observables, x_{obs}, and y_{obs}, are plotted in a two-dimensional space. In this simple example, the data points are linearly separable. Several lines are plotted as grey lines, representing possible decision boundaries, separating the data points into two groups. The grey spur around these lines represents the margin ξ, marking the maximum distance to the closest data point, called a support vector. Support vectors are identified by the effect of their removal or repositioning on the position of the decision boundary – removing a support vector moves the decision boundary. Thus, the support vectors are considered critical elements of the dataset.

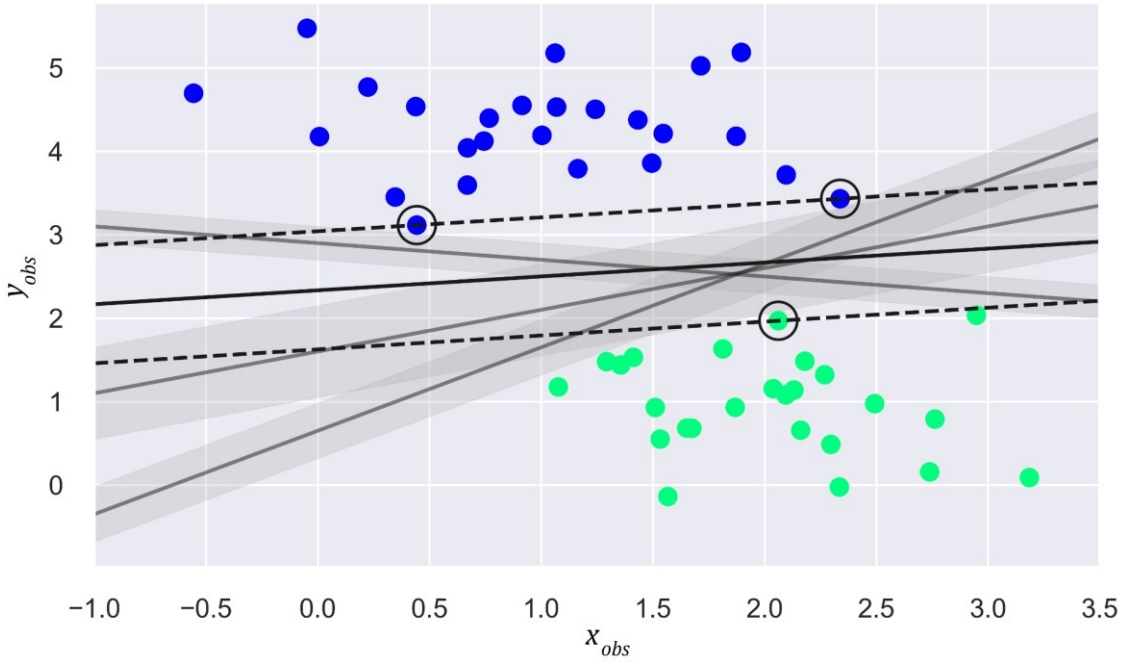

Figure 2.7: Example for a classification problem in two dimensions, solved with a support vector machine. Four lines, representing possible decision boundaries, are plotted along with respective margins. The margin describes the distance of the decision boundary to the closest point of both datasets. The SVM solves an optimization problem by maximizing these margins, resulting in the decision boundary, represented by the solid black line with the dashed lines marking the corresponding margin. Data points that limit the expansion of the margin are called support vectors, here marked with a black circle. This graph was created according to [79] with an adaptation of the python code available under MIT license at [80].

The SVM is used to optimally choose a decision boundary that maximizes the margin. In this two-dimensional example, the solid black line and the dashed lines represent the decision boundary and the margin, respectively. In any case, involving more than two observables and thus more than two dimensions, the decision boundary becomes a hyperplane. Support vectors are used to represent this hyperplane [81]. Even if the data points are not separable linearly in two dimensions by a line, classification is possible with an SVM by employing kernel tricks [79]. To achieve such classification, the data is projected into higher dimensional space, referred to as kernel space, where separation by a hyperplane and thus linear classification becomes feasible again. An analogous procedure is possible in higher-dimensional cases, making SVMs incredible useful and efficient, especially for cases in which the number of observables exceeds the number of samples. SVMs are special in the way that they solve a convex optimization problem, resulting in a unique solution – a set of hyperplane parameters – and thus do not rely heavily on the initialization and termination criteria in contrast to genetic algorithms [81].

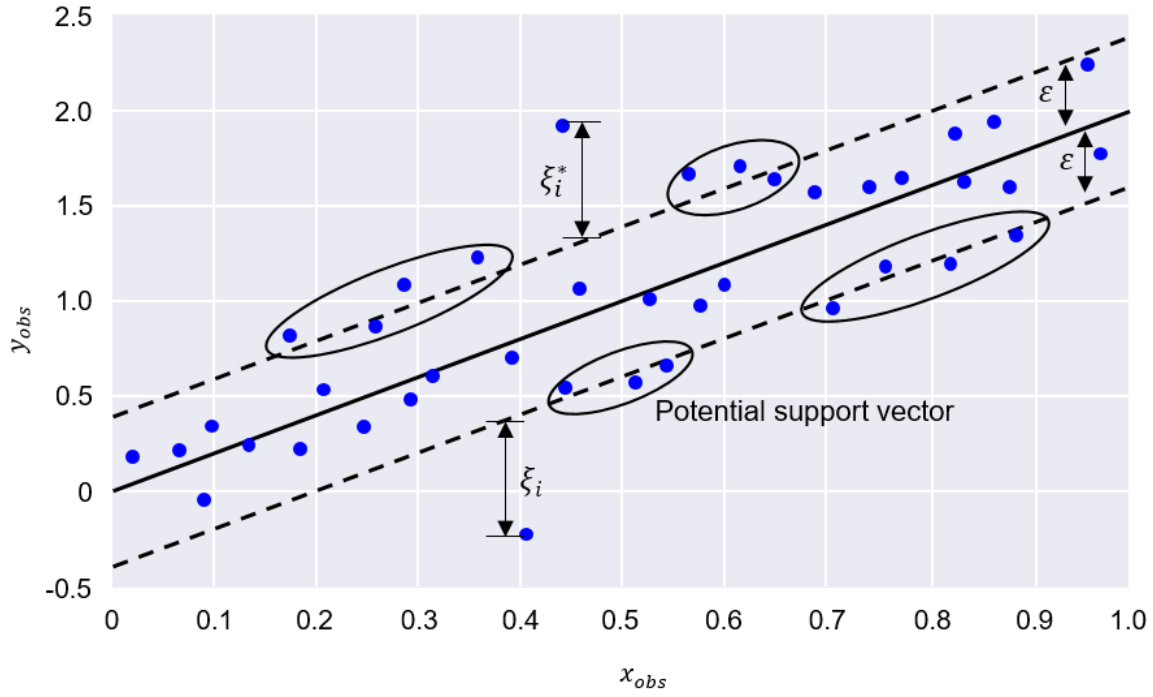

Figure 2.8: Example for a one-dimensional linear support vector regression (SVR). The SVR represents an advanced way of linear regression, applicable to more than two dimensions. Here the two-dimensional case is shown. The fitting process relies largely on the selection of potential support vectors that lie outside of an ε-tube around the estimated function. ε describes the acceptable error of the fit. The hereby generated fit is iteratively optimized to reduce the value of a loss function while maintaining the simplicity of the estimated function. The points outside the ε-tube are penalized according to their distance ξ_i to the tube by said loss function. The tradeoff between complexity and values the loss function is allowed to take is regulated by the regularization parameter C. Graph according to [81].

Support vector machines can be generalized to make them applicable to regression problems. The so-called support vector regression (SVR) is an effective tool in real-value function estimation [81]. Instead of looking for an optimal solution with a minimum number of mismatches lying within the margin, the SVR's output is a continuous-valued, multivariate function surrounded by an ε-tube to contain most of the data points, as pictured in Figure 2.8. The SVR is flexible in the way that one can select the extent of maximum acceptable error ε. The quality of regression is judged from a symmetrical loss function, penalizing mismatches outside of the ε-tube, below or above the estimated function, deviating from that margin ε by ξ_i. As in SVM, the support vectors in SVR are the data points that affect the shape of the tube the most, e.g., lie outside of the ε-region and, thus contribute to the value of the loss function [81]. Given a certain margin and a weighing factor γ to penalize values outside of that margin, the SVR aims to minimize the complexity of the output function while maintaining an as low as possible value of the loss function, being the result of a convex optimization problem with a unique solution [82]. The tradeoff between

complexity and the number of penalized values, retuned by the loss function, is regulated by the regularization parameter C, where regularization is inversely proportional to C. This means that high C leads to a low regularization and thus might lead to an over parametrization or overfitting of the training data. Support vector regression (SVR) can be employed for SoC estimation in a multidimensional space spanned by voltage, current, and temperature [83,84]. The non-linear relationship of SoC with the input measures is transferred to a high dimensional space by the SVM [49], thus enabling estimation of the SoC based on the input values. Similar to other data-driven approaches for SoC estimation, SVM requires large computational power [46], when compared to other solutions like the Kalman filter, and achieves an accuracy comparable to that of NN approaches.

Besides being proposed to be the SoC estimation of choice for the future [46], data-driven approaches have paved the way for the utilization of measured signals other than voltage, current, and temperature to estimate SoC and SoH. ML allows for state estimation of a system, even if this system is not fully understood and a model is not readily available. Since ultrasonic interrogation of LIBs is a new field of research, such models, especially with comparably small complexity such as ECMs, are not yet developed. Therefore, published studies utilizing ultrasound to estimate the state of a battery are relying on ML concepts. The feasibility of ultrasonic-based state estimation was first demonstrated in 2015 by Hsieh, Bhadra, *et al.* [85,86]. The authors showed that acoustic time of flight (ToF) experiments can measure SoC and SoH of a battery because the distribution of density within a battery and the bulk modulus of the battery's electrodes change during cycling. Ultrasound propagation is sensitive to changes in both properties, which can be measured through the ToF. Their pulse[1]-echo and through-transmission experiments at 2.25 MHz unveiled that, besides ToF, attenuation also changes depending on the battery's state. In 2017, Ladpli *et al.* [87,88] showed that the application of guided waves at frequencies between 100 kHz and 200 kHz also allows for the exploitation of the mechano-electrochemical coupling in battery cells for SoC and SoH estimation. Gold, Bach *et al.* [89] demonstrated that with an excitation at a frequency of 200 kHz acoustic interrogation of

[1] The word „pulse“ is used in this work in the context of digital signal processing. Therefore, it refers to the change of a signal's amplitude from baseline to a higher value, followed by the return to baseline. Common pulse shapes include the rectangular pulse, the raised cosine, the Morlet wavelet, and the Gaussian pulse. It is not synonymous with the word „impulse“, which refers to the impulse function, a short input signal, e.g., the Dirac delta function.

batteries for SoC estimation is possible with low-cost off-the-shelf piezo buzzers as transducers. SoH monitoring [25,90,91] and detection of abusive conditions [92] based on ultrasound were demonstrated. Several patents [93] and publications [17,94] claim the enhanced SoC and SoH estimation capability of ultrasound in combination with machine learning. In [17], supervised ML in the form of support vector regression was applied. Incorporating ToF and amplitude data improved the SoC estimation accuracy to 1% compared to 3% resulting from using the voltage signal as input alone. For SoH estimation, the complete waveform was used and an estimation accuracy of 1% could be achieved. In this first attempt, three identical batteries were cycled at the same conditions, training data from two battery cells was used and the resulting model was tested on the remaining, independent cell. In [94], guided waves were used to probe the LIB's state. The received signals were decomposed into "atoms" by the matching pursuit technique. The descriptive parameters of these atoms were mapped as a function of SoC and SoH. These maps were then fed to a generalized additive model (GMA) for state prediction. The authors demonstrated that prediction based on voltage data alone could be augmented with the atom's parameters to achieve a two-fold better SoC and twenty-fold better SoH estimation.

2.1.5.5 Mechanical methods for state estimation

Popp *et al.* have reviewed the various state estimation methods based on the mechanical property changes of lithium-ion batteries in [20]. Those methods can be roughly divided into four groups: expansion-based methods, experimental modal analysis (EMA), ultrasonic probing, and acoustic emission (AE). The expansion-based methods have mostly been used to study the active materials in regard to their volume change upon lithiation and delithiation [95–97]. The involved studies focused mostly on the effect of different C-rates along with temperature dependence [98–100], which are closely linked, and the spatial distribution of the expansion of a battery cell [101,102]. Dilatometry can also be used to detect the reversible and irreversible expansion, associated with lithium plating [96,102–104], beyond the swelling common to a cycle at non-plating conditions. When the battery cell under test is geometrically constrained, the volume expansion due to (de-)intercalation leads to the build-up of force against the constraining structure. For any battery cell type, the casing acts as some sort of constrain, which experiences strain as a consequence of the expansion. This link of expansion, force, and strain in turn can be used to estimate the state of the battery cell [105–108]. The pressure build-up during the lifetime is often associated with the SEI evolution and thus a good indicator for the SoH of a battery cell, operated under constraint conditions [109]. Battery cells can be instrumented with resistive

foil strain gauges (RFSG) or with fiber Bragg grating (FBG) to measure their surface strain, which correlates with the SoC and SoH [20,110–112]. It is possible to even insert FBG into battery cells, between layers, or integrate them into the electrode coating [113], as they can be made from inert materials [20,114]. It was even shown that by employing an integrated FBG for SoC estimation an error of less than 2.5% can be achieved [115,116].

Especially in automotive applications, the response of battery cells to mechanical loads such as vibrations and shocks is of interest. The experimental modal analysis (EMA) allows studying physical properties such as the natural frequencies and the level of dampening [20]. Natural frequencies are the frequencies at which the frequency response function peaks. The latter is defined as the response of a battery cell to a point force, which acts as mechanical excitation [20]. Research applying EMA to LIBs shows varying results. In most of them, a shift of natural frequencies with SoC [117–119] and SoH [117,119,120] could be demonstrated, which would in principle allow an application of this measurement technique for state estimation. Other studies couldn’t find a correlation between battery state and natural frequencies [120,121]. It was described that the influence of temperature on mechanical properties, sensed by EMA, outweighs the changes to those properties, introduced by SoC and SoH [117,121]. The experimental conditions needed for EMA, e.g., the decoupling of the battery from its surrounding by attaching it to strings or placing it on a low-density foam, make an application in online state estimation very unlikely. Nevertheless, EMA might be a valid choice for the analysis of battery cells, returned from first life application, regarding suitability for second life applications or recycling.

Acoustic emission (AE) is a completely different technique. It does not rely on the active excitation of the battery cell under test but relies on the passive detection of acoustic events [20,122]. Those acoustic events originate from the release of mechanical stress, usually a result of degradation mechanisms in the active materials of lithium-ion batteries. It is in the nature of AE that these events solely occur during operation and thus the method is purely in-operando, which allows estimating the level of stress the active materials experience under certain cycling conditions [123–125]. Even though the working principle seems to predestine the method for the monitoring of battery cells, it was shown in [126] that an estimation of the SoH and remaining useful life (RUL) is feasible with the aid of advanced signal processing and machine learning tools.

Ultrasonic probing techniques utilize that the propagation of sound depends on the mechanical properties of the medium it passes through. As those properties change with the state of the battery cell, ultrasound allows indirect access of its state. Several signal

properties are affected by mechanical property changes, but most studies in this field focus on the time of flight and amplitude of the transmitted or reflected signal. The time of flight is a measure of the time between the sending and reception of the signal, and allows the calculation of propagation speed [20]. The amplitude of the transmitted signal can be taken as a measure of the attenuation of the sound wave passing through the medium [20]. Different placements of transmitter and receiver are possible. Depending on geometry the propagation through the battery cell [17,85,127,128] or along its surface [94,129,130] can be measured [20]. Several publications demonstrate the suitability of ultrasonic probing for SoC and SoH estimation. In a first attempt, Ladpli *et al.* showed the correlation of the signal amplitude and ToF of surface waves (guided waves) with SoC and estimated with means of statistical analysis that the achievable SoC and SoH estimation might be below 1% [129]. In a subsequent publication [94], the authors decomposed the surface waves into atoms, resulting in a number of features, that if combined with the cell voltage enable an even better estimation accuracy of 0.36% and 0.05% for SoC and SoH, respectively. In this publication, the tested cells were cycled at 0.82 C at 45 °C and a five-peak Gaussian-windowed tone burst (a modulated sine wave function) with center frequencies between 100 kHz and 200 kHz was used to excite the surface-mounted piezo disc transducers. An iterative multi-stage algorithm was used to identify the atoms within a transmitted signal, serving as reference, and to subsequently track the changes in the signal as SoC and SoH evolve. The atoms of a signal at a certain state are estimated based on the preceding state [94]. Therefore, the potential parameter space for the atom extraction is reduced and the extracted information at a certain state translates information from the preceding states. Thus, even if the subsequent statistical analysis solely perceives instantaneous measurements and does not take cycling history into account, the accuracy of the model benefits from the reduced parameter space.

In [17], Davies *et al.* placed commercial 2.25 MHz transducers as transmitters and receivers on opposing sides of battery cells with different chemistries and used the amplitude, ToF, and cell voltage to train an SVR for SoC estimation. For cells with graphite and LCO electrodes, they were able to reduce the mean estimation error in 0.05 C cycles from about 3% (voltage alone) to 1% (voltage, ToF, and amplitude). For cells with graphite and LFP electrodes that exhibit a very flat voltage curve, being very challenging for accurate state estimation, the estimation error in 0.5 C cycles could be reduced from about 6% to 1% when including information extracted from the ultrasonic signals [17]. The described model was even applicable to SoH estimation and was robust to a damaging event like an external short-circuit with a mean estimation error of about 1% when training the SVR with the

complete waveform. Davies *et al.* [17] claim that high-frequency transducers, realized as MEMS piezoelectric transducers, could allow a small packaging and thus a real-world application of the presented technique. It remains a question of cost if an ultrasound-based state estimation will be realized in a future BMS, especially if the employed technique requires high sampling rates and linked high-frequency electronics. In [131], Popp *et al.* demonstrated that this can be overcome by utilizing frequencies in the range of 25 kHz to 40 kHz and achieved a mean estimation error of 16.85% SoC under challenging conditions, which is a rather poor accuracy compared with other state of the art methods, that achieve around 5% accuracy [50]. Therefore, designing a cost-efficient and accurate SoC estimation that achieves increased accuracy based on ultrasonic measurements or other mechanical property sensing techniques remains an open task.

2.2 Ultrasonic non-destructive evaluation (US-NDE)

Using sound for the detection of flaws, e.g., in metal parts, is as old as the craft of blacksmithing. Craftsmen could tell from their experience and the ringing resulting from hammering an object if the latter was flawless. It then took until the discovery of the piezoelectric effect and the reverse piezoelectric effect by Pierre and Paul Jaques Currie in 1880 and 1881 [132] to pave the way for the development of ultrasonic non-destructive evaluation in the early 20th century. Ultrasound is defined as sound above the audible frequency range of 16 Hz to 20 kHz and extends up to the GHz range [133] (p 130). The first applications emerged in the 1930s, marked by the patent of Mülhauser in 1931, already utilizing two ultrasonic transducers to detect flaws in solids [134]. Ultrasonic non-destructive evaluation (US-NDE) benefited from the technological demands of World War II and was subsequently developed for medical diagnostic purposes aside from flaw detection [135]. The 1970s are generally recognized as a leap forward within NDE as new technologies made the detection of smaller flaws and details possible [136]. Since then, several new approaches such as the concept of guided waves have emerged. Even though its long history and ultrasound seeming to be an old field of research, not all equations are yet written nor all effects are understood as new applications require increasingly challenging monitoring solutions and, therefore, open new subfields of ultrasound research [137].

Even though many experiments have been conducted to gain insight on the dominant ultrasonic propagation in the setup, used within this work, the verification could not be provided yet. Therefore, the possible propagation modes in question are reviewed on the following pages.

This section is designed as an introduction to the field of ultrasonic non-destructive evaluation. To serve this purpose, it begins with the description of how a distortion of a system or a displacement in a lattice can propagate through matter as a sound wave. For simplicity, the case of isotropic media is treated first. Succeeding the representation of sound waves in the time domain, the interpretation of sound waves in the frequency domain is discussed. Then, boundaries are introduced to the medium and the therefrom-arising modes of propagation are discussed. Subsequently, the wave propagation in anisotropic media is treated, leading to theoretical considerations about fluid-saturated layered media, such as a lithium-ion battery. Finally, the more technical aspects such as generation and reception of sound and the characterization of ultrasonic probes according to their resonant behavior are discussed.

2.2.1 Representation of sound waves and propagation in isotropic media

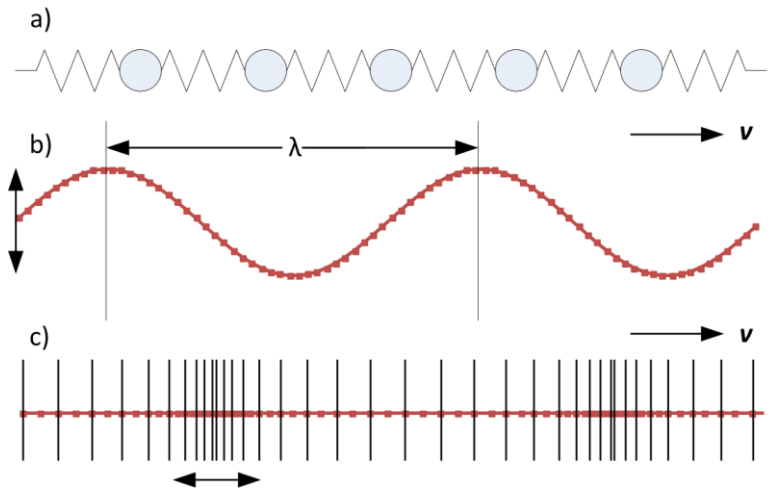

Figure 2.9: Chain of elastically coupled masses, a) and a snapshot of wave propagation along such a chain. b) Shows transversal propagation mode, where mass points are displaced transversal, c) shows longitudinal propagation mode, where particles oscillate in propagation direction such that fluctuations in density occur as illustrated by vertical lines. The distance between two points of equal phase is called wavelength λ and equals the distance covered in a period T at phase velocity v_p. According to [133].

Sound propagation on the micro-scale can be described as the displacement of particles from their resting position. This motion is transferred to adjacent particles through elastic coupling with a delay in time. Consequently, the motion propagates as a wave through the media, assembled from those particles, with a characteristic velocity v. A solid medium can be depicted as a chain of elastically coupled masses in the simplest, one-dimensional case, as shown in Figure 2.9 a). The wave modes can be categorized into longitudinal or pressure waves and transversal or shear waves [133]. In longitudinal waves, particles are oscillating in the direction of wave propagation, therefore density fluctuations occur along the path of

the wave, as shown in Figure 2.9 c). On the contrary, in transversal waves, particles are oscillating vertically to the direction of propagation, as shown in Figure 2.9 b). To communicate the vertical displacement of adjacent particles and, therefore, allow transversal wave propagation, a coupling is required. Hence, transversal waves can only be found in solid media and do not propagate in gas or fluid [133].

For longitudinal waves, the occurring density fluctuations result in local stress and strain forces. The phase velocity c_l of propagating equally compressed or decompressed areas can be related to the stiffness or constrained modulus M and the density ρ of the material by

$$\boldsymbol{c_l = \sqrt{\frac{M}{\rho}}}. \tag{6}$$

M is also known as P-wave modulus and can be related to Young's modulus E via the Poisson's ratio ν by [138,139]

$$\boldsymbol{M = \frac{E(1-\nu)}{(1+\nu)(1-2\nu)}}. \tag{7}$$

The Poisson's ratio is characteristic for a certain material and describes the ratio of relative thickness to relative length change at stress or strain [140]

$$\boldsymbol{\nu = -\frac{\frac{\Delta d_m}{d_m}}{\frac{\Delta l_m}{l_m}}} \tag{8}$$

For solids, ν takes values between zero and 0.5. Similarly, the phase velocity c_t, at which a transversal wave propagates through a material, communicated by shear forces, can be related to the shear modulus G of the material by

$$\boldsymbol{c_t = \sqrt{\frac{G}{\rho}} = \sqrt{\frac{E}{\rho}\frac{1}{2(1+\nu)}}}. \tag{9}$$

Therefore, the sound velocities of longitudinal and transversal waves can be set in relation by

$$\boldsymbol{c_t = c_l\sqrt{\frac{1-2\nu}{2(1+\nu)}}}. \tag{10}$$

For commonly probed solids, the transversal wave velocity is approximately half of the longitudinal wave velocity.

In general, the propagation of ultrasonic waves in media is influenced by absorption, scattering, and reflection at interfaces. The absorption depends highly on the frequency and the materials constituting the medium. Scattering occurs on inhomogeneities and spatial structures in the range of 0.1λ to 5λ, with wavelength λ, while reflection occurs on interfaces between materials of different acoustic impedance $Z_{acoustic}$ [141], which is defined as

$$\boldsymbol{Z_{acoustic} = \rho \cdot c_0}, \tag{11}$$

with the density of the material ρ and the velocity of sound c_0 in a given material. The reflectance R can be defined analogously as in optics for two refractive indices n_1 and n_2 [141]:

$$\boldsymbol{R = \frac{I_r}{I_i} = \left(\frac{Z_1 - Z_2}{Z_1 + Z_2}\right)^2}, \tag{12}$$

with I_r and I_i are the refracted and incident intensities of the sound wave, respectively, and Z_1 and Z_2 are the acoustic impedances of the adjacent layers [141].

As described above, the interaction of sound waves with media depends on their wavelength and, therefore, on their frequency. This effect, called dispersion, is a property of waves in general and is present in measured quantities such as wave velocity, acoustic impedance, and derived quantities. The relation of wavelength λ and phase velocity v_p at which a certain phase propagates during a period T of oscillation and frequency $f = 1/T$ can be written as [136]

$$\boldsymbol{\lambda = v_p / f}. \tag{13}$$

With the definition of the wavenumber $\bar{k} = 2\pi/\lambda$ and the circular frequency $\omega = 2\pi f$, Equation (13) can be rewritten as $v_p(\omega) = \omega/\bar{k}$, being referred to as the dispersion relation. For monochromatic harmonic waves, exhibiting a single wavelength, dispersion is solely influencing phase velocity [141].

Additional complexity is introduced by superimposing two or more waves of similar frequency, resulting in a group of waves as depicted in Figure 2.10.

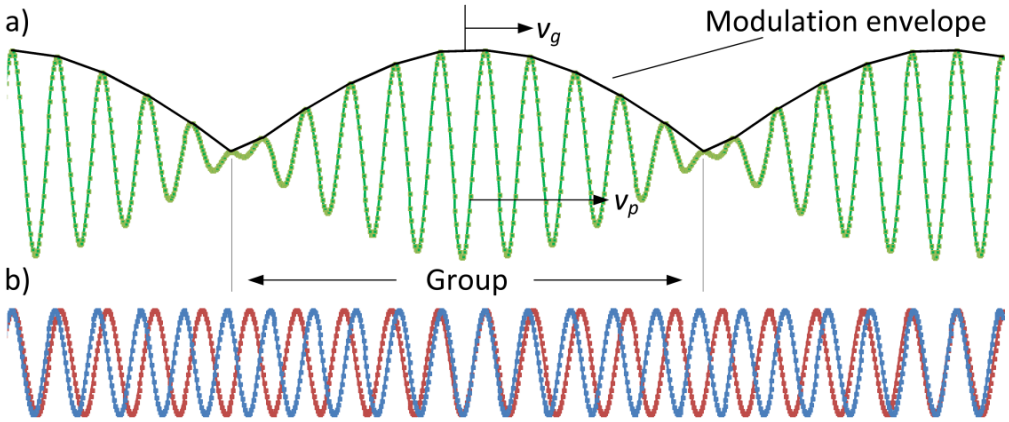

Figure 2.10: Snapshot in time of b) two harmonic waves traveling at phase velocities v_{p1} and v_{p2}, differing 10% in frequencies and a) group of waves or wave packages, resulting from the superposition of these two waves. The modulation envelope highlights the shape of the wave packages. This package travels with the group velocity v_g. According to [136].

This group of waves moves with a group velocity v_g, which smaller than the velocity of the individual waves v_p [136]. The simplest analytical approach considers the summed displacement $u(x,t)$ of a representative volume from rest position within a system, resulting from the superposition of two harmonic waves $u_1(x,t)$ and $u_2(x,t)$, being described by circular frequencies ω_1 and ω_2 and wavenumber $k_1 = \omega_1/c_{p1}$ and $k_2 = \omega_2/c_{p2}$, respectively

$$\boldsymbol{u(x,t) = A \cdot \cos(k_1 x - \omega_1 t) + A \cdot \cos(k_2 x - \omega_2 t).} \tag{14}$$

It can be shown that this equals to

$$\boldsymbol{u(x,t) = 2A \cdot \cos\left(\frac{1}{2}\Delta\bar{k}x - \frac{1}{2}\Delta\omega\right) \cdot \cos(k_m x - \omega_m t).} \tag{15}$$

While the leading low-frequency term describes the envelope of the wave package, traveling at a velocity $v_g = \Delta\omega/\Delta\bar{k} = (\omega_2 - \omega_1)/(k_2 - k_1)$, the high-frequency term, describes a single-phase, traveling at $v_p = \omega_m/k_m$, with ω_m and k_m being the mean values of ω_1 and ω_2, and $k_1$and k_2, respectively. In general, for wave packages, being composed of more than two harmonics, the group velocity is defined through the derivative of circular frequency by wavenumber [141] by

$$\boldsymbol{v_g = \frac{d\omega}{dk}.} \tag{16}$$

A very elegant way to look at wave packages, displacement in a lattice or any distortion propagating in a system, is Fourier analysis. The underlying Fourier theorem states that any

distortion of a system can be described by a superposition of an infinite number of harmonic oscillations. This is a unique feature of waves and serves as a basis for all modern forms of communications. Fourier analysis allows representing wave forms or signals in approximation by decomposing them into their frequency components and allows creating arbitrary waveforms from a finite number of oscillations. The essential tool here is the Fourier transform. To be applicable to a function $f(t)$, the integral

$$\int_{-t_1}^{+t_1} |\mathbf{f(t)}|^2 \, \mathbf{dt} \tag{17}$$

has to converge in the limit $t_1 \rightarrow \infty$ [142]. Then the Fourier transform *F*(*ω*) can be calculated by [143]

$$\mathbf{F(\omega)} = \frac{\mathbf{1}}{\sqrt{\mathbf{2\pi}}} \int_{-\infty}^{+\infty} \mathbf{f(t)} \cdot \mathbf{e}^{-\hat{\imath}\,\boldsymbol{\omega}\mathbf{t}} \, \mathbf{dt}. \tag{18}$$

with $\hat{\imath}$ as the imaginary number. Thereby the function $f(t)$ is transferred from the time domain to the frequency domain. Very often, for example, after processing in the frequency domain, it might be useful to obtain $f(t)$ from the inverse Fourier transform

$$\mathbf{f(t)} = \frac{\mathbf{1}}{\sqrt{\mathbf{2\pi}}} \int_{-\infty}^{+\infty} \mathbf{F(\omega)} \cdot \mathbf{e}^{+\hat{\imath}\,\boldsymbol{\omega}\mathbf{t}} \, \mathbf{d\omega}. \tag{19}$$

The two functions $f(t)$ and $F(\omega)$ make a Fourier couple. In the representation of physical processes, e.g., wave propagation, the real-valued variables t and ω are interpreted as time and (circular) frequency. Since their product has to be dimensionless, their units are reciprocal [142]. Fourier couples have several interesting properties. First, functions that show a very narrow distribution in the time domain, e.g., a Dirac delta-shaped pulse, exhibit a very broad frequency distribution. Therefore, these functions contain many different frequency components. On the other hand, a function with a single frequency component is represented by an infinitely extending harmonic oscillation, e.g., a sine wave. One important consequence of this fact is that a wave package will broaden while it propagates. A typical sound pulse used for non-destructive evaluation has a finite length and therefore contains several frequency components. Due to the dispersion of the speed of sound, different frequency components of a wave package will propagate at different phase velocities. Therefore, with increasing travel distance, the components will separate more and more and the wave package will become wider. Consequently, its group velocity characterizes a wave package. In experiments, the velocity at which a wave package of a

certain frequency propagates is always the group velocity which can be calculated from phase velocity [139].

For an excellent explanation of the phenomenon of wave package broadening due to dispersion, the reader may refer to [144] (85 ff.), which covers this topic on electron wave packages in an easily accessible way that is also transferable to acoustic wave packages.

2.2.2 Propagation of sound waves in half-space geometry

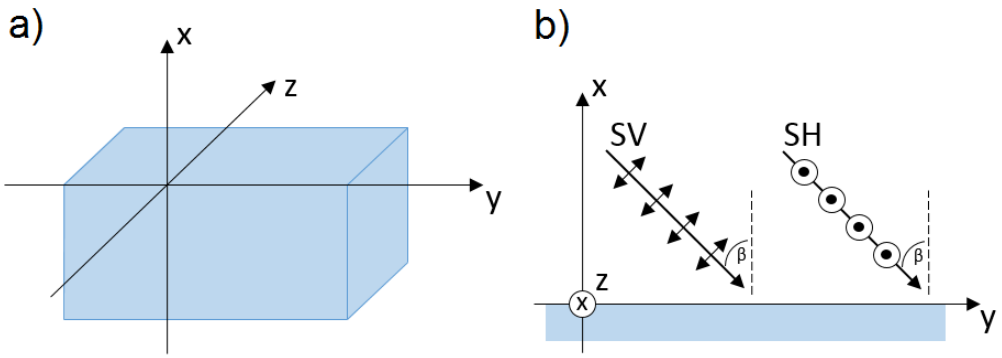

Figure 2.11: a) Half space geometry, b) polarized transversal waves with respect to an interface. The depicted isotropic solid is meant to be infinitely extending in y and z-direction and bordered by an interface in the y-z-plane at $x = 0$. SV and SH stand for vertically and horizontally polarized shear (transversal) waves, respectively. SV and SH waves meet the surface at an incident angle of β.

2.2.2.1 Surface waves: Rayleigh waves

In 1885, Lord Rayleigh published the theoretical description of wave propagation upon the plane free surface of an infinite homogenous elastic solid. He stated that this case can be analogically considered to that of deep water waves, while the potential energy of displacement does not arise from gravity but the elastic coupling of particles within the medium. The so-called *Rayleigh* waves propagate close to the surface, their depth of penetration can be approximated to be one fold to twofold of the wavelength [145].

The modes of propagation in this geometry can be deduced from the general wave equation

$$\Delta\vec{u} = \frac{1}{c^2}\frac{\partial^2\vec{u}}{\partial t^2}, \qquad (20)$$

with $\vec{u}$ being an arbitrary (longitudinal and/or transversal) displacement and c being the propagation velocity of the respective displacement [146]. When introducing the boundary at $x = 0$ (see Figure 2.11) and anticipating a propagation in the y-direction, the solution to

Equation (20) in y-direction can be written as $u(y,t) = f(x,y)\exp[i(\omega t - k_y y)]$, implying a plane wave geometry with a depth depending term $f(x,y)$. Inserting this solution into Equation (20) yields a differential equation for the function $f(x,y)$:

$$\boldsymbol{\partial^2 f(x,y)/\partial y^2 - \left(k_y^2 - \frac{\omega^2}{c^2}\right) f(x,y) = 0.} \quad \textbf{(21)}$$

Here, we can discuss two cases. First, $\omega^2/c^2 > k_y^2$ leads to a sine-shaped plane wave (either longitudinal or transversal) [146]. The solution, specific to this geometry, arises from the second case, where $\omega^2/c^2 < k_y^2$. It is described by an exponential function with the exponent $\pm x\sqrt{k_y^2 - \omega^2/c^2}$. The solution with the negative sign would mean an infinitely increasing intensity towards the body of the solid ($x < 0$) and has no physical relevance [146]. The remainder is the real solution to the wave equation, Equation (20):

$$\boldsymbol{u(y,t) = f_0 \cdot exp(-C_x x) \cdot exp[\hat{\imath}(\omega t - k_y y)],} \quad \textbf{(22)}$$

With f_0 being a constant, independent of time and location, and $C_x = \sqrt{(k_y^2 - \omega^2/c^2)}$. This solution matches a wave, propagating in the y-direction and being dampened along the x-direction with increasing depth [146].

As stated earlier, the general solution $\vec{u}$ contains transversal and longitudinal components. While in the solid body both components can propagate independently of each other, the surface wave does always contain both components [146]. Similar to water waves, the particles within the wave are oscillating elliptically, contrary to the circular oscillation of sine-like wave propagation in the infinite solid [139]. The components of the elliptical movement depend on the ratio of the velocities c_l/c_t and, therefore, on the Poisson's ratio ν. The propagation velocity of the Rayleigh waves c_R also depends on this ratio and is independent of frequency [146]. For solids, with ν lying between 0 and 0.5, c_R can be calculated to take values between $0.862c_t$ and $0.955c_t$, being slightly slower than the pure transversal wave in the solid body [147].

2.2.2.2 Plate waves, Lamb waves, Love waves

When a second boundary surface is introduced to the solid, we have to consider now the geometry of a plate in which a surface wave can only exist as long as its wavelength is small compared to the thickness of the plate [139].

To initiate waves in plates, transversal waves of two kinds have to be considered. Those are depicted in Figure 2.11b. Depending on their polarization with respect to the boundary surface either horizontally polarized shear waves (SH) or vertically polarized shear waves (SV) can propagate in a plate. To form a plate wave the criteria for constructive interference has to be met [148]:

$$\boldsymbol{n\lambda_t = 2d_{plate}\sin(\beta_i)}, \tag{23}$$

with thickness d_{plate} of the plate, angle of incident β_i, n being a natural number and λ_t the wavelength of the transversal wave.

SH plate waves exhibit no component perpendicular to the surface and therefore won't interact with adjacent fluids since transversal waves cannot propagate in fluids and also no mode conversion can occur on the interface. This makes them especially useful in the testing of parts immersed in a fluid [140]. An example of such an SH plate wave is shown in Figure 2.12 a).

SV waves can also initiate plate waves that are referred to as *Lamb* waves and always have a displacement component perpendicular to the surface. Those can be split up into two groups with symmetrical and asymmetrical displacement on the boundary surfaces - see Figure 2.12 b) and Figure 2.12 c). As pointed out by Schoch [149], *Lamb* waves can be interpreted as a superposition of two plain longitudinal or transversal waves, being reflected between the two boundary surfaces.

For the case of a thin, solid layer on another solid, so to say a layer on a half-space, special types of waves can propagate in such a layer. Within those, the *Love* waves represent transversal waves with a displacement parallel to the boundary surface. Similar to *Rayleigh* waves, *Love* waves show little dampening due to being confined to a layer close to the surface of the solid and therefore are able to travel long distances and thus being valuable for the application in structural health monitoring of large structures [146]. Contrary to *Rayleigh* waves, they show dispersive behavior and are purely transversal.

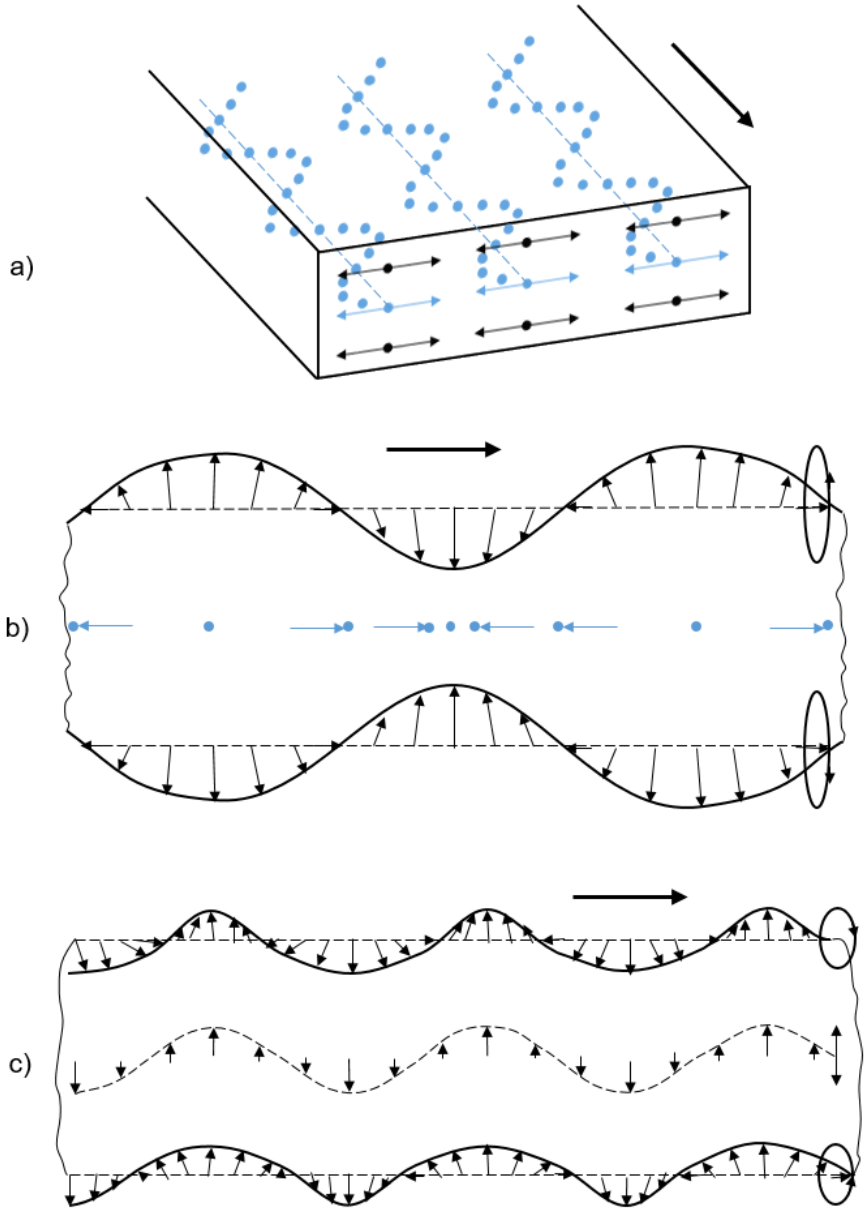

Figure 2.12: Modes of propagation of sound waves in a plate. a) Transversal wave with displacement parallel to the surface, b) and c) Lamb waves, symmetrical and asymmetrical base mode. The graph was reproduced according to [139].

2.2.2.3 Guided waves

When waves travel along a certain structure, close to the surface of a solid (*Rayleigh* waves) or confined to a layer (*Lamb* and *Love* waves), this structure is very often referred to as a *waveguide* and the waves involved are referred to as *guided waves*. Technology revolving around the use of *guided waves* emerged in the 1990s [150] and has developed a lot since. Most structures can act as *waveguides* and include plates (aircraft skin, car body), rods (rails, cylinders), hollow cylinders (pipes, tubing), and multilayer structures as long as the

wavelengths are large enough with respect to the dimensions in the *waveguide* [150]. Guided wave experiments pose huge benefits due to their simplicity in setup and long sonic travel distances that allow the monitoring of large structures.

2.2.3 Propagation of sound waves in anisotropic media

Here, we discuss the basic idea of sound propagation in anisotropic media. For an in-depth discussion of the topic, the reader is referred to [136] and [151].

In the general case of the propagation of small amplitude elastic waves in initially un-deformed, infinite, anisotropic media, the governing equation can be formulated based on three relations [136].

(1) Dynamic equilibrium (Newton's second law), using indicial notation

$$\frac{\partial \sigma_{ij}}{\partial x_j} = \rho \frac{\partial^2 u_i}{\partial t^2}, \tag{24}$$

with the Cauchy stress tensor σ_{ij} (a second-order tensor), the density ρ, and the second derivative after time of the displacement $\partial^2 u_i / \partial t^2$. $i, j \in \{1,2,3\}$ are indicating the directions in a Cartesian coordinate system.

(2) The infinitesimal (linear) strain-displacement relation,

$$\varepsilon_{kl} = \frac{1}{2}\left(\frac{\partial u_k}{\partial x_l} + \frac{\partial u_l}{\partial x_k}\right) = \varepsilon_{lk}, \tag{25}$$

with the strain tensor ε_{kl} (a second-order tensor).

(3) A linear stress-strain relation – the generalized Hooke's law

$$\sigma_{ij} = C_{ijkl}\varepsilon_{kl}, \tag{26}$$

with the stiffness tensor C_{ijkl} (a fourth-order tensor, $3^4 = 81$ components), mapping stress and strain. Eliminating the stress and strain from these equations, leads to the governing equation describing the propagation of a displacement in a linearly elastic, inhomogeneous body [136]:

$$\frac{\partial C_{ijkl}}{\partial x_j}\frac{\partial u_k}{\partial x_l} + C_{ijkl}\frac{\partial^2 u_k}{\partial x_j \partial x_l} = \rho\ \frac{\partial^2 u_i}{\partial t^2} \tag{27}$$

If the body is homogeneous, the elastic constants are independent of their position within the body and the according derivatives vanish. Therefore, the equation simplifies to

$$C_{ijkl}\frac{\partial^2 u_k}{\partial x_j \partial x_l} = \rho\ \frac{\partial^2 u_i}{\partial t^2} \tag{28}$$

One of the many possible solutions of this governing equation is the equation describing plane waves

$$u_i = A_i \mathbf{exp}[\hat{\imath}(k_i \cdot x_i - \omega t)], \tag{29}$$

where A_i denotes the amplitude of the plane wave travelling in direction of index i, with wavenumber k_i, imaginary number $\hat{\imath}$ and location vector x_i (in indicial notation) [136].

In non-polar media σ_{ij} is symmetric, e.g., $\sigma_{ij} = \sigma_{ji}$. By definition, ε_{kl} is symmetric as well, e.g., $\varepsilon_{lk} = \varepsilon_{kl}$. Therefore, a symmetry for the elements of the stiffness tensor C_{ijkl} can always be assumed, e.g., $C_{ijkl} = C_{jikl} = C_{ijlk}$. Given a positive definite strain energy function, there are at most 21 independent elements in C_{ijkl}. Systems are categorized according to the count of symmetry planes with respect to the direction of propagation. For different symmetry classes the number of independent constants is reduced further. For the symmetry class with the least symmetry, the triclinic system, C_{ijkl} has 21 independent elements, for the orthorhombic (or orthotropic) there are nine independent elements, for the hexagonal (or transversely isotropic) system there are five independent elements and for the isotropic system there are two independent elements [136]. It has to be noted that these symmetries, strictly speaking, only apply for single crystals, where the point to point validity of the governing equations is given. Many materials, and especially composites, don't fulfill this requirement and vary from point to point. Composites, by nature, are composed by more than one material, exhibiting different elastic properties. Nevertheless, the sound propagation within many composite materials is described using one of the symmetries [136].

All layered media, like batteries or other composite materials, exhibit at least monoclinic symmetry. Here, the stiffness tensor is constituted by 13 independent components. Orthotropic systems, include one more symmetry plane, which is perpendicular to the first plane and therefore lies in the same plane as the vector of propagation. All unidirectional

layers in a composite exhibit orthotropic symmetry. In a battery this applies to the electrode sheets, at least in the plane parallel to the current collector, but should also apply in the plane perpendicular to the coating direction. With the symmetry in mind, the complexity of the tensor is further reduced to nine independent components. One could even argue that for a layered composite, like a lithium-ion battery, the transversely isotropic symmetry could be applied. Therefore, one had to assume the structure within a layer perpendicular to the stacking axis (and propagation direction) to be isotropic, reducing the number of independent elements in C_{ijkl} to five.

It can be shown, that the constants in C_{ijkl} represent the square wave speed of a plane wave in some directions [152]. For the isotropic case, with two independent constants, it becomes clear, that from the symmetry of the system the number of plane wave modes can be concluded. In isotropic media, those are longitudinal and transversal waves, with their propagation velocities stated in Equation (6) and Equation (9).

2.2.4 Propagation of sound waves in layered, fluid-saturated, porous media – sound propagation in the Lithium-ion battery

Depending on the wavelength of applied ultrasonic waves, different effects within the medium “battery” and different properties have to be considered. As described in Chapter 2.1, a Lithium-ion battery is constituted of several layers of the subset “separator-anode-separator-cathode” and a multilayer pouch housing, with the internal, porous structure being (ideally) saturated by a fluid – the electrolyte. Within this subchapter, we will have a look at the interaction of sound waves with such a medium on certain scales.

2.2.4.1 Theoretical considerations on the interaction of ultrasound with the layered structure and particles in lithium-ion battery cells

For the interaction of sound waves with a medium, the following can be stated in general: Even though many materials, e.g., the battery’s active material particles, are intrinsically anisotropic, “[the] random orientation [of their constituents] gives rise to a material which behaves isotopically when the dominant wavelength of the wave field is long compared to the crystal [or particle] dimensions” [153] (p 245). The underlying principle can also be applied to the periodically layered structure of the sample. When the wavelength λ_0 can be considered large compared to the spatial period of layering d_l, the medium can be replaced by an equivalent transversely isotropic (TIE) medium, also called effective medium. The

properties of the TIE medium are described by the thickness weighted averaged properties of the constituting layers, e.g., density and elastic modulus [153].

Carcione *et al.* [153] showed that this long-wave approximation holds true for the ratio $R_{lw} = \lambda_0/d_l$. By comparison of experimental data and numerical simulations for layered samples composed of two sorts of porous rock at a ratio of 1:1, they showed that R should be at least 5 or 6 in this case. They concluded further, that R_{lw} is highest in this composition ratio and that R_{lw} depends highly on the angle of incidence, especially for shear waves. Experiments on periodically layered samples composed of materials with a higher difference in acoustic impedance of adjacent materials suggest values of R_{lw} between 10 and 100 [154].

Besides the layered structure of the battery, its particular nature has also to be accounted for. As already stated in Chapter 2.2.1, interaction with spatial structures and inhomogeneity in the form of scattering occurs in the range of 0.1λ to 5λ. So for sound waves to interact with singular particles or layers, the wavelength of such waves would have to be in the range of 0.5 µm to 400 µm. At a speed of sound in battery composite material of about 1000 m/s to 1600 m/s [25], this implies the usage of frequencies in the range of 2.5 MHz to 3.2 GHz to achieve interaction.

As this study uses frequencies in the range of 20 kHz to 250 kHz, the medium can be treated as an effective medium, in which little interaction with the particles of the electrode layers and the periodic structure of the battery cells' layers is expected.

2.2.4.2 Biot's theory

In the frequency range, in which the medium "battery" appears as an effective medium and wavelengths are large compared to the periodicity of layers, particles, and pores, Biot's "Theory of Propagation of Elastic Waves in a Fluid-Saturated Porous Solid" [155,156] is applicable. Lithium-ion batteries with their porous electrolyte filled layers, represent a medium described by Biot's theory. While established in the 1950s, this theory remains still valid for many applications, today [157–163]. Even though the theory is not able to accurately predict attenuation in certain porous media [164], it was continuously used to study the wave propagation in natural occurring porous layers, e.g., found in sediment rock formations or sand oil deposits, and therefore was extremely valuable to the field of petro-physics, but was also applied in medical applications such as the monitoring of human bones. A fluid-saturated porous medium is special in the way that solid particle and liquid

movements are coupled through inertia at high-frequency and viscous forces at low frequency [165].

Therefore, Biot split his theory up into two parts, a high frequency, and a low-frequency part, separated by a critical frequency. This so-called transition frequency f_t marks the point at which Poiseuille flow (laminar flow) within the pores breaks down and the behavior is no longer viscosity dominated but is described by inertia-dominated flow [155,165]:

$$\boldsymbol{f_t = \pi \nu_k / 4 d_p^2.} \quad \textbf{(30)}$$

Here, the kinematic viscosity ν_k can be related to the dynamic viscosity μ_d via $\nu_k = \mu_d / \rho_f$, with ρ_f being the density of the fluid [155]. Following the initial definition of the transition frequency, other definitions were established [165,166] that account for the influence of the solid's inertia, compressibility, and frequency-dependent momentum exchange [166] which can only be neglected in cases of low porosity or gas-filled pores. Therefore, Biot's initial Equation (30) often underestimates the transition frequency and can here only serve as the lower limit.

For a typical Lithium-ion battery electrolyte – one molar $LiPF_6$ solution in a mixture of EC and DMC, literature states a dynamic viscosity μ_d = 4.44 mPa·s and a density ρ_f = 1.27 g/cm³ at room temperature [167], leading to a kinematic viscosity of $3.50 \cdot 10^6$ µm²/s. The median pore diameter in electrodes with a median particle diameter of 4.8 µm can be estimated to be 1.3 µm [168]. For particles with a diameter distribution of around 10 µm, the biggest pores have a diameter of approximately 4 µm [89,169]. These two particle size distributions represent two extreme points of electrode geometry well – high power and high energy electrodes. The resulting transition frequency according to Biot's original formula can be calculated to be 1.63 MHz and 0.17 MHz, respectively.

Before we focus on the fluid-saturated case, let us assume a porous, dry solid, described by the density of the solid ρ_s (here the grain density) and the porosity β. Here the velocity of the pressure and shear wave is given by

$$c_{P,dry} = \sqrt{K_p/(1-\beta)\rho_s}, \quad (31)$$

$$c_{S,dry} = \sqrt{N_S/(1-\beta)\rho_s}, \quad (32)$$

With shear modulus N_S, constrained modulus $K_p = K_b + 4N_S/3$ and bulk modulus of the dry porous matrix K_b [165].

2.2.4.3 Low-frequency range

This section will cover Biot's theory for the frequency range $f < f_t$, where the assumption of Poiseuille flow (laminar flow) within the pores is valid. According to Biot, three wave-modes exist in the discussed medium, two pressure waves and one shear wave [155]. The two pressure waves are titled fast wave (P1) and slow wave (P2) and differ in the amplitude of the displacement of solid and fluid. For the P1 wave, the amplitudes of displacement are of the same sign/phase; for the P2 wave, the amplitudes of displacement are of opposite sign/phase [155] (p 174). Though, it was shown by numerical calculations by [161] that the second pressure wave can only be observed when the difference in acoustic impedance of the fluid and the containing porous frame is large enough.

In the following text, the shear wave is abbreviated as (S). For the calculation of the velocities of these waves, we are following the report of Jocker and Smeulders [165]. The basic idea to derive the governing equations for wave propagation and to find a solution to those is sketched as follows. Within a unit cell of the fluid-saturated porous medium, the local displacement is defined separately in the solid and in the fluid. Thereby a simultaneous propagation in both is permitted. In each unit cell, the forces on the solid frame of the porous structure, in the form of stress, and on the fluid, in the form of pressure, are present and communicate the propagation of the displacement through the medium. The wave equations are built on the general idea of sound propagation in anisotropic media, as discussed before. The hereby derived equations account for both forces and contain both displacements, the one on the solid and the one in the fluid, which are coupled.

The solution to these equations can be derived by applying decoupling techniques, yielding the dispersion relations [155] of the three propagation modes. Here, only the result of these techniques is presented. The dispersion relation for the pressure waves is quadratic and therefore it has two roots, one solution being the fast wave and one being the slow wave [165]. The velocities can be represented as a function of the material constants:

$$c_{P1,P2} = \frac{\Delta \pm \sqrt{\Delta^2 - 4(\rho_{11}\rho_{22} - \rho_{12}^2)(P_{GEP}R_{GEP} - Q_{GEP}^2)}}{2(P_{GEP}R_{GEP} - Q_{GEP}^2)}, \quad (33)$$

$$c_S = \sqrt{\frac{N_S \rho_{22}}{\rho_{11}\rho_{22} - \rho_{12}^2}}. \quad (34)$$

Here, we have $\Delta = P_{GEP}\rho_{22} + R_{GEP}\rho_{11} - 2Q_{GEP}\rho_{12}$ and N_S is the shear modulus. The mass coefficients ρ_{11} and ρ_{22} as well as the fluid-solid mass coupling coefficient ρ_{12} can be defined as a function of the tortuosity α, the porosity β, the density of the solid ρ_s and the density of the fluid ρ_f, the effective densities are then given by [165]

$$\rho_{12} = -(\alpha - 1)\beta\rho_f, \quad (35)$$

$$\rho_{11} = (1 - \beta)\rho_s - \rho_{12}, \quad (36)$$

$$\rho_{22} = \beta\rho_f - \rho_{12} = \alpha\beta\rho_f. \quad (37)$$

The generalized elastic parameters (GEP) $A_{GEP}, P_{GEP}, R_{GEP}$, and Q_{GEP} can be derived from Gedanken experiments [170] and related to porosity, bulk modulus of the solid K_s, bulk modulus of the fluid K_f, bulk modulus of the porous drained matrix K_b and shear modulus N_S of both the drained matrix and the composite [165]

$$A_{GEP} = K_b - 2N_S/3 + K_f(1 - \beta - K_b/K_s)^2/\beta_{eff}, \quad (38)$$

$$P_{GEP} = A_{GEP} + 2N_S, \quad (39)$$

$$Q_{GEP} = \beta K_f(1 - \beta - K_b/K_s)/\beta_{eff}, \quad (40)$$

$$R_{GEP} = \beta^2 K_f/\beta_{eff}, \quad (41)$$

where $\beta_{eff} = \beta + K_f/K_s(1 - \beta - K_b/K_s)$. It is important to note that each wave (P1, P2, S) propagates simultaneously in the pore fluid and the frame.

2.2.4.4 High-frequency range

The high-frequency range is defined by $f > f_t$ was described by Biot in 1956 [156]. Here, the breakdown of Poisseuille flow (laminar flow) within the pores is assumed. The presented theory has an upper bond for its validity, which is the frequency at which the wavelength is in the order of the pore size. As in the low-frequency range, two pressure and one shear wave exist in the high-frequency range. The second kind of pressure (P2) wave is extremely attenuated and may not be observable in most cases.

Since in this work, materials with considerably small pore size will be studied at comparatively low frequencies, i.e., below the transition frequency f_t, where the pressure wave of the second kind (P2) is still observable, the high-frequency range of Biot's theory will not be covered here in detail. The interested reader may refer to the original work, published by Biot in 1956 [156].

2.2.5 Attenuation and scattering of sound waves

When waves propagate through any media, energy is removed from the waves by inelastic mechanisms. Attenuation can arise from internal friction or energy absorption in material and may be, as well as propagation velocity, a function of frequency. Thus in dispersive media, magnitude reduction and pulse spreading are observed [136]. Magnitude reduction does significantly originate from scattering. The associated process is considered as a sound wave being reflected from an inhomogeneity within the medium, often called a reflector. Basic scattering theory is built around Huygens's principle that states that a plane wave front can be approximated as an infinite number of spherical waves originating from sources, arranged in a straight line [136] (p 338). Following this idea, scattering on a finitely sized object, often called scatterer, can be approximated by placing an infinite number of point sources on its surface and considering the resulting wave field as a superposition of the incident wave front and the waves originating from the object. The resulting deviation from the incident beam means that some of the energy, originally contained in the beam, is redirected and potentially dissipated in destructive interference.

Besides the before discussed case of a homogenous medium with a single scatterer, much more complex cases of interaction of sound with the medium occur. The attenuation of sound waves has to be considered on different scales, depending on the used frequencies and subsequent wavelengths of the sound waves in relation to the size of structural inhomogeneity and periodicity of the transversed medium.

Let's once again consider the case of a Biot medium. Here, the attenuation mechanism depends highly on pore size, fluid viscosity, and wavelength, therefore frequency. For low frequencies, P1- and S-wave are barely attenuated because both phases (liquid and solid) are coupled [166] (455). "The P2-wave represents a typical relative mode of motion and is completely diffusive [and therefore highly attenuated at] low frequencies due to viscous effects' [166] (455). Another loss mechanism is the squirt flow. Unlike the Biot mechanism, "losses due to squirt flow [...] result from the local flow of viscous fluid into and out of micro cracks during the passage of an acoustic wave" [171]. Dvorkin and Nur [172] studied the

dependency of attenuation on viscosity and frequency in a fluid-saturated, porous medium. In their calculations, the frequencies at which the attenuation due to these two loss mechanisms peaks showed the opposite behavior. It can therefore be concluded that in a given medium and at a certain frequency only one of the two mechanisms is dominant or even in a relevant order of magnitude. Which of the mechanisms is adequate to describe the dispersion of velocity and attenuation depends on the nature of the medium. It was reported that the Biot model is most suitable for porous media with high permeability, while the squirt flow is best for media with a low permeability [171]. Here, permeability refers to the property of a porous medium, allowing gases or liquid to pass through it. At higher frequencies, the attenuation is then dominated by the inertia of the system that couples the movement of solid particles and liquid [165].

2.2.6 Generation and reception of Ultrasound

For the use of sound in non-destructive evaluation, it is necessary to excite and detect sound waves in the specimen. This task is usually performed by a transducer, acting either as an actuator or sensor. Sound waves can be generated in various ways that can be grouped into mechanical, electromechanical (piezoelectric), magnetostrictive [173], and optically induced methods. In today's application, the following are playing an important role:

- Piezoelectric transducer
- Electromagnetic acoustic transducer, e.g., [174]
- Laser ultrasonic, e.g., [175]

2.2.6.1 Piezoelectricity

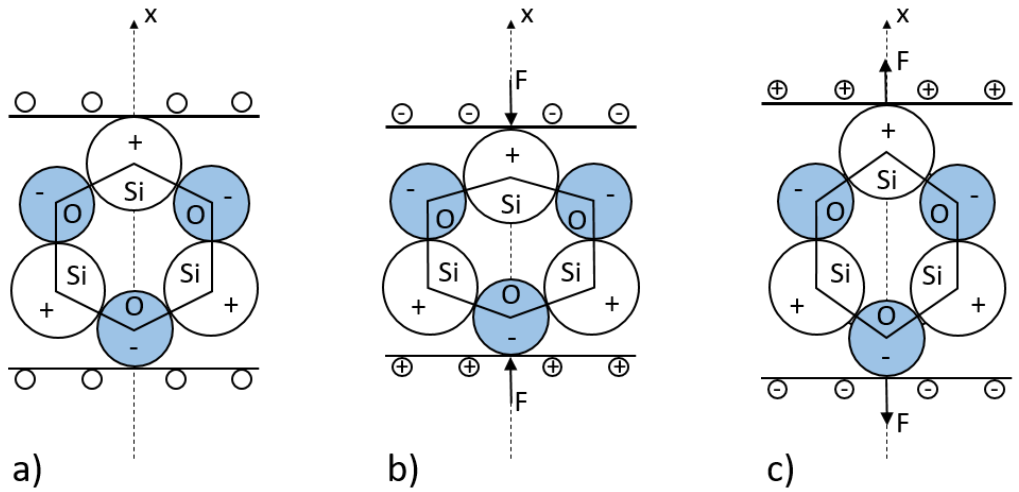

Figure 2.13: On piezoelectricity in Quartz crystal. a) no external load – no charge induced, b) compression due to an external force applied – charge induced, c) expansion due to an electric field. Graph after [176].

The most commonly used among these methods of ultrasound generation is the piezoelectric effect. Piezoelectricity can be translated as “pressure electricity” and describes the occurring charge induced on opposite faces of a crystal, with an asymmetry in its lattice structure, under mechanical pressure. It was originally discovered by J. and P. Curie in 1880 in Quartz crystals [176].

For sound generation, the inverse piezoelectric effect is used: When a piezoelectric material is placed as the dielectric between the two plates of a capacitor, thickness expansion or compression can be observed, depending on the direction of the applied electric field. For the static case, the relation of applied electric field and resulting deformation and vice versa can be expressed by

$$\boldsymbol{S_D = d_{PE} E_F}, \tag{42}$$

$$\boldsymbol{D_F = d_{PE} T_M}, \tag{43}$$

where S_D is the deformation, E_F is the electric field strength, D_F is the electric displacement field, T_M is the mechanical tension, and d_{PE} is the piezoelectric proportionality constant [176]. The dimensional change in thickness is usually accompanied by contraction or expansion in the plane perpendicular to the axis in which the electric field is applied [176]. When an alternating field is applied to a circular piezoelectric plate, thickness and radial oscillations are the results. By bringing the plate in contact with a sample, the oscillation is transferred to the sample and travels as ultrasonic waves through the material [136]. Radial

and thickness oscillation components excite different wave modes and therefore transducer design is usually adjusted to favor the preferred component and frequency. The resonance frequency, at which a piezoelectric element oscillates along a certain axis, depends on the frequency constant and the dimensions d_{xdr} along this axis (the subscript “xdr” stands for "transducer”). The frequency constant correlates directly with the speed of sound c_0 in the piezoelectric material. To achieve resonance at the desired frequency f_0, the dimension d_{xdr} is chosen to fit half a wavelength and is calculated according to $d_{xdr} = \lambda/2 = c_0/(2f_0)$. Therefore, the frequency constant can be estimated to be half the speed of sound (along the given crystal axis of the piezoelectric crystal).

2.2.6.2 Piezoelectric transducers

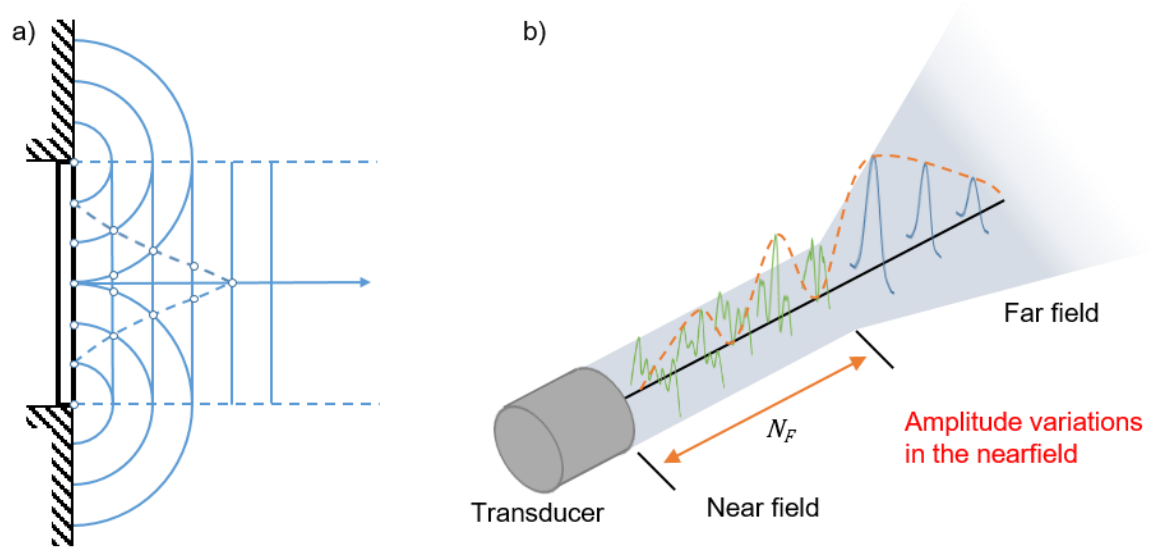

Figure 2.14: (a) Interference of a sound field emitted by an ideal piezoelectric plate between rigid walls according to Huygens’ Principle. For this idealized example, the piezoelectric plate is oscillating in thickness only and therefore moves similarly to a piston. From the interference pattern, the near field length can be obtained. Graph after [139] (p 58). **(b) Profile of the sound pressure at varying distances from the source transducer in the near-field (green) and far-field (blue).** The dotted, orange line shows the pressure at the axis of the transducer as a function of distance. Graph according to [177].

The field emitted by a piezoelectric plate in thickness oscillation mode under continuous excitation can be constructed by applying Huygens’ Principle to an ideal piston oscillator [139]. An exemplary sketch with a ratio of plate diameter D_{xdr} to wavelength λ of $D_{xdr}/\lambda = 6$ is displayed in Figure 2.14 a). The distance N_F at which the field of sound is not any more dominated by the interference effects can be calculated to be [136]

$$N_F = \frac{D_{xdr}^2 - \lambda^2}{4\lambda} \tag{44}$$

and does coincide with the last main maximum of the interference field (not shown). The part of the field that is dominated by this effect is called the near-field, while the interference-free adjacent field is called the far-field. N_F is very often called near field length and can be approximated as [136,150]

$$\lim_{\lambda \ll D_{xdr}} N_F = \frac{D_{xdr}^2}{4\lambda} \tag{45}$$

provided that the wavelength is small compared to the diameter of the piezoelectric plate. For our chosen example in Figure 2.14 a), $N_F \approx 9\lambda$. This value represents a rough approximation and does not represent a sharp border [139].

Depending on the distance to the plate, the sound pressure profile can vary significantly. In the near field, some pressure profiles show a minimum and other a maximum on the axis of transduction (green lines in Figure 2.14 b). While in the far-field, the profile is of bell shape with a maximum on the axis (blue lines). Also, as shown in Figure 2.14 b), the pressure on the axis (orange dashed line) periodically varies in the near field as a function of radial distance from the transducer, and then homogeneously falls off in the far-field [139]. The measured sound pressure in the nearfield range does strongly depend on the lateral and radial distance from the source. Therefore, in most NDT applications, either a section of homogeneous material, a so-called forward member, delay line or wedge, is placed between transducer and sample, or the experiment is designed in such a way that the region of interest (ROI) lies in the far-field range.

To form a transducer, one or more piezo plates are combined with a mounting, eventually braced with an acoustic impedance matching and a backside dampening material in a casing [176]. In NDT, such a transducer is brought in contact with the sample of interest. Very often, it is sufficient to use light pressure to maintain good contact of transducer and sample, but, e.g., surface roughness may require the aid of a coupling agent or couplant [139]. Such might be oil, gel, water, or glue, e.g., an epoxy resin, if a permanent coupling is desired. In manual testing scenarios, a removable coupling agent and, therefore, reversible coupling is preferred. For automated testing, a water or oil bath, in which transducer(s) and the sample are submerged [165], is frequently used. In the case of structural health monitoring (SHM), it is common to permanently mount transducers on the structure of interest or to integrate them [140].

To match the requirements of the desired application, the excitation of the transducer to emit ultrasound may vary [150]. On the one hand, there is single-pulse excitation such as spike pulse, square wave pulse, or step pulse [150] and on the other hand, there are more arbitrary waveforms such as bipolar tone burst, raised cosine, continuous mono-frequency, or frequency sweeping sinusoidal, often called chirp [178]. To match the needs of the application and to allow for fine-tuning of the frequency spectrum, waveforms are also filtered through the application of windowing functions.

To detect ultrasound, in most cases the piezoelectric effect is used. Piezoelectric transducers can be used multipurpose in most applications, acting as actuators and sensors. If the pressure distribution at the surface of a sample is of interest, laser vibrometry can be used to detect the oscillation of a surface at the incident of an ultrasonic wave [175]. To do so, the interferometer principle is used to detect the distance of the detector to a point on a sample surface and the movement thereof.

2.2.6.3 Estimation of bandwidth

The ability of a transducer to both, generate and detect ultrasound, is described by its frequency spectrum. The spectrum allows estimating the resonance frequency and the sensitivity frequency range of the transducer. This range is quantified by the bandwidth. In the time of flight (ToF) estimation, the bandwidth is a limiting factor to the time resolution. Narrow bandwidth transducers emit wide pulses and thus introduce a larger inaccuracy in ToF estimation. In contrast, wideband transducers allow for narrow pulses and high ToF estimation accuracy [139].

The frequency spectrum in question can be calculated by Fourier transformation from a field or energy quantity of a signal, e.g., the pulse-echo or transmission signal through a known sample. In the here discussed case, the voltage present at the electrical connections of a transducer is a result of the pressure applied by the sound wave to the piezoelectric material. Pressure and voltage are considered field quantities. The energy and power transported by the signal are proportional to the square of the amplitude. The energy is calculated by integrating the power of the signal over its duration. Depending on application, it might be beneficial to study the spectra of field or energy/power quantities. Very often, the power spectral density (PSD) of a signal is of special interest. Since spectra are plotted in logarithmic “dB” scale, the squaring of the amplitude to calculate energy and power introduces a factor of two, if the scales of the two quantity types are compared. Generally,

as depicted in Figure 2.15, the -3 dB criteria is taken to estimate the bandwidth [179]. The points within the spectrum where this amplitude criteria is met are denoted frequencies f_a and f_b. Depending on whether it is a spectrum of field quantity or energy / power quantity, frequencies f_2 and f_3 or f_1 and f_4 have to be considered, respectively.

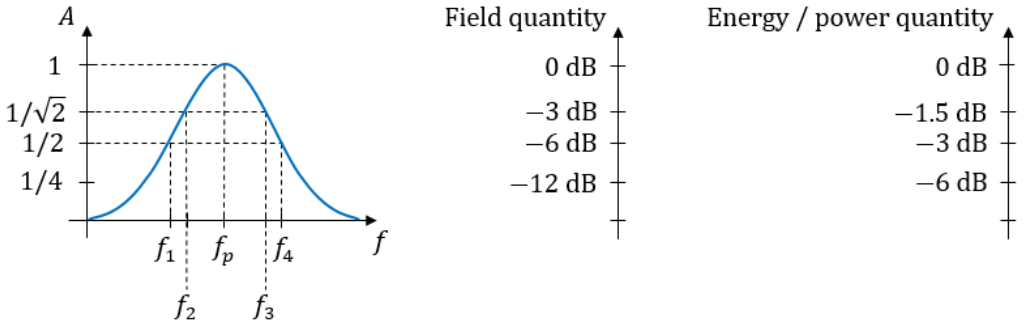

Figure 2.15: A typically bell-shaped spectrum of an ultrasonic transducer. The bandwidth is usually estimated based on the -3 dB criteria. From the spectrum, the peak frequency f_p and the distance of the two intersections with the -3 dB line are taken. When the spectrum is plotted as field quantity (voltage or pressure), this equals $1/\sqrt{2} = 0.7071$ (f_2 and f_3) and in the case of energy or power spectrum, the full width at half the maximum (f_1 and f_4) is taken.

The center frequency f_c is then calculated by arithmetic mean

$$\boldsymbol{f_c = \frac{f_a + f_b}{2}}, \tag{46}$$

as well as the absolute bandwidth [139]

$$\boldsymbol{B_{abs} = f_a - f_b}, \tag{47}$$

and the relative bandwidth

$$\boldsymbol{B_{rel} = \frac{f_a - f_b}{f_c} 100\%}. \tag{48}$$

The dampening of the piezo element within the transducer affects the bandwidth and the shape of the resonance peak. At comparably low dampening, the piezo element's oscillation decays slowly and a narrow resonance peak with comparably high amplitude is observed [139]. The bandwidth is symmetrical around the peak frequency [139]. Therefore, narrowband transducers are best suited for high-sensitivity applications. At comparably high dampening, the opposite effect is observed, e.g., the oscillation decays quickly and a broad

resonance peak is measured. Additionally, the bandwidth tends to become asymmetrical at high dampening, which is described by the skewness

$$f_{sk} = \frac{f_p - f_a}{f_b - f_p}. \tag{49}$$

2.3 Digital signal processing (DSP)

Digital signal processing (DSP) allows a scalable and very flexible approach for the processing of measured data in a digitalized environment. With linear time-invariant systems, DSP also offers a representation and, thereby, a unique angle of access to physical measurement processes. This section aims to give a detailed insight on the basics of digital signal processing, necessary to understand the operations performed on the sampled data in this work. Therefore, the sampling theorem, the concept of frequency representation, and linear time-invariant systems are introduced. The latter is required to obtain the time of flight (ToF) from an ultrasonic signal, which is the time an ultrasonic wave takes to propagate through a sample. The ToF in turn can be used to characterize the state of a sample, as the speed of sound in a given medium can be calculated from it, which depends on the mechanical properties of the sample.

2.3.1 Notation convention used in this chapter

In computer science, it is common to note sampled, discrete signals and quantities with square brackets, as in $x[n]$. For convenience, signals are handled as one-dimensional vectors, where n denotes the index of the sampling point. Commonly, n takes values from the interval $[0, N-1]$, where N is the number of sampling points or the length of the signal in units of the sampling interval.

2.3.2 Sampling theorem

While the world around us is described by continuum physics, its measured representation is mostly discrete. In theory, continuum could be approached, but never reached, with an infinite number of samples. In practice and as a consequence of limited computational and storage capabilities, signals in the time domain are represented by a finite number of sampling points *N*. This conversion of an analog signal to a finite-length sequence of values is performed by an analog to digital converter (ADC). According to sampling theory, the number of points N within a signal of length T_0, thereby the interval $T = T_0/N$ between two points and the sampling frequency $f_s = 1/T$ have to be chosen in a way that any signal ambiguity in the frequency domain is avoided. More precisely, the Nyquist-Shannon

theorem states that a signal containing no frequencies higher than f_B can be completely determined by sampling at $f_s \geq 2f_B$ [180,181]. The frequency f_B is often called folding frequency. If a signal has a frequency content higher than the *folding frequency*, oscillations with those frequencies may appear in the sampled signal as oscillations with lower frequency. This effect is called *aliasing* and is a consequence of the ambiguity of sampled signals in the frequency domain [180]. The signal ambiguity inherent to a sampled signal is illustrated in Figure 2.16. The depicted signal contains seven samples which could either be interpreted to originate from a 1 Hz or 7 Hz sine wave.

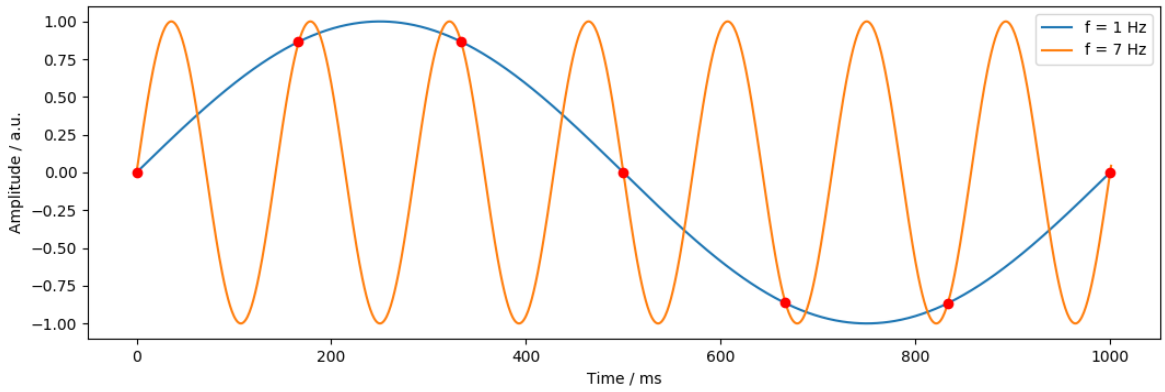

Figure 2.16: Ambiguity of a sampled signal, consisting of seven sampling points. By choosing a sampling rate (6 Hz) lower than the frequency of the sinus in the original signal (7 Hz, orange line), the sampled signal appears with a different frequency (1 Hz, blue line). Graph according to [180].

2.3.3 The discrete Fourier transform

In the case of sampled signals, here represented by squared brackets [ ], the frequency domain representation obtained by the continuous Fourier transform (Equation (18) or (50))

$$\mathbf{X(\omega) = \frac{1}{\sqrt{2\pi}} \int_{-\infty}^{+\infty} x(t)\, e^{-\hat{\imath}\,\omega t}\, dt,} \qquad \textbf{(50)}$$

with a signal $x(t)$ and its Fourier transform $X(\omega)$ can be rewritten as a sum of a finite number of oscillations *N*, the discrete Fourier transform (DFT) [182]

$$\boldsymbol{X[k] = \sum_{n=0}^{N-1} x[n] e^{-\frac{i2\pi kn}{N}}, k = 0, 1, \dots, N-1,} \qquad \textbf{(51)}$$

with $x[n]$ being the amplitude of the signal $x(t)$ at a given sampling point within the discrete time sequence at index *n*, whereas *k* is the frequency index, corresponding to *N* computed DFT coefficients [182]

$$\boldsymbol{c_k = \frac{1}{N}\sum_{n=0}^{N-1} x[n] e^{-\frac{i2\pi kn}{N}}, k = 0, 1, \dots, N-1.} \quad \textbf{(52)}$$

In the frequency domain, the resulting sampling interval becomes $\Delta f = f_s/N$ implying that a higher resolution can be obtained with a longer, sampled signal. Analogically to the continuous case, an inverse discrete Fourier transform can be defined as [182]

$$\boldsymbol{x[n] = \frac{1}{N}\sum_{k=0}^{N-1} X[k] e^{\frac{i2\pi kn}{N}}, n = 0, 1, \dots, N-1.} \quad \textbf{(53)}$$

Besides the amplitude spectrum $X[k]$, the power spectrum $P[k] = |X[k]|^2/N^2$ is of technical relevance and often used [182]. The DFT can be efficiently computed by the fast Fourier transform (FFT) algorithm but requires the sampled signal to have a length equal to a power of 2 [182]. To achieve this, signals are very often cropped or zero-padded. Zero paddings involve adding zeros to the digital signal representation, thereby enlarging the number of sampling points and reducing sampling size Δf. While this equals an interpolation between frequency bins and makes the identification of inherent frequencies of an oscillation easier, it does not involve additional spectral information [182]. For a detailed discussion on the effect of zero paddings, the reader may be redirected to [183]. The application of FFT is based on the validity of the following assumptions for a given signal:

1. The input signal is periodic to itself (repeats itself)
2. The input signal is continuous in itself
3. The input signal does not contain frequencies higher than the folding frequency, equal to half of the sampling frequency

Especially the criterion of continuity is very often violated in non-preprocessed data and results in *spectral leakage*. The effect of spectral leakage shall be illustrated in Figure 2.17 with an example of the cosine of a frequency f_0 = 2 Hz, sampled at f_s = 50 Hz. While we expect the FFT to solely contain the single frequency component f_0, the DFT peaks at the frequency bin of 2 Hz but does also contain other frequency components.

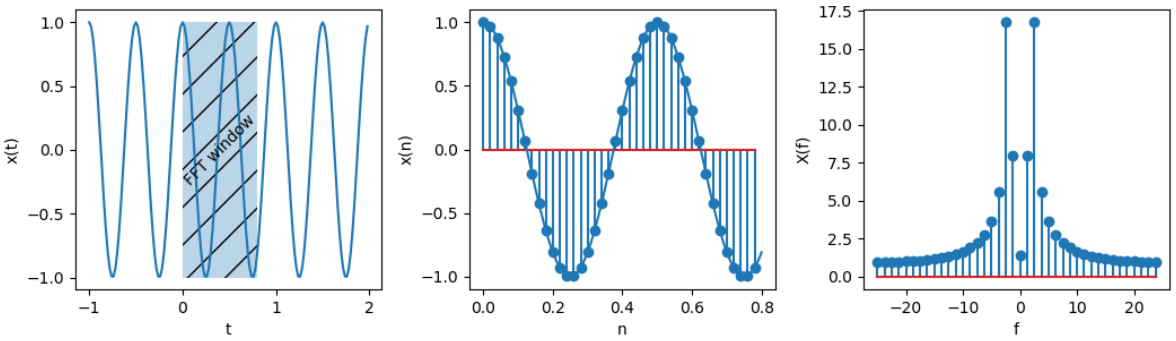

Figure 2.17: Cosine at 2 Hz (left), cosine sampled at 50 Hz (middle), and discrete Fourier transform of a non-continuous section of the cosine (right). The chosen section of the original signal exhibits a discontinuity when connecting the start and end point of the signal, leading to the frequency leakage, displayed on the right. Recreated following an example, published at [184].

This observation can be traced back to the discontinuity of the selected section, exhibiting a big jump from -0.78 to +1.0 under the application of the first assumption that the input signal represents a single period of a periodic signal, and fusing end to start. The resulting step contains a wide distribution of frequencies, similar to a rectangular step function. Therefore, the bigger the discontinuity, the bigger the spectral leakage becomes. Discontinuities in the input signal can be avoided either by choosing a section of the signal equal to a whole period, as shown in Figure 2.18, where the DFT peaks solely at ±2 Hz, as expected. Another option is windowing the input signal in such a way that the first and the last point of the signal can be joint together continuously. Usually, this is performed by a function that smoothly tapers off to zero at both ends [182]. A common example for the application of the DFT is the calculation of the power spectral density of a signal. Here, the squared amplitude of a signal is Fourier transformed to estimate the different frequency components of the signal.

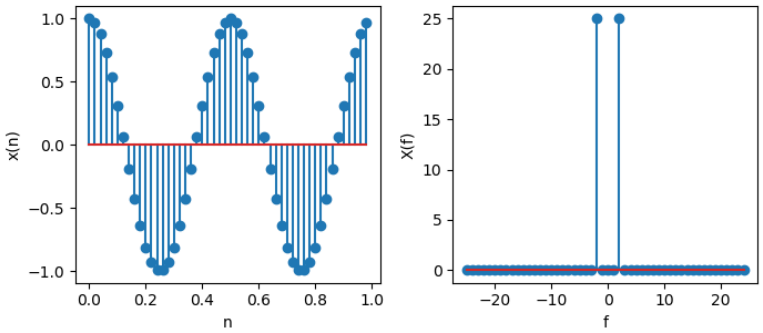

Figure 2.18: Continuous section of a cosine at 2 Hz, sampled at 50 Hz (left) and discrete Fourier transform of this section (right). As expected from a function, containing a single frequency component, the DFT does only peak at 2 Hz. Recreated following an example, published at [184].

2.3.4 Linear time-invariant systems (LTI)

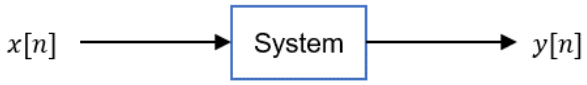

Figure 2.19: Sketch of a simple system interacting with a signal. Passing an input $x[n]$ of n samples results in an output $y[n]$.

Linear time-invariant systems (LTI systems), also called linear systems with shift-invariance, play a very important role in our digital world. They provide the framework for most digital signal processing (DSP) operations and systems since those rely both on the assumption of linearity and time invariance. *Time* or *shift-invariance* refers to a system's property to react in the same way to a disturbance or input at any given time and thus is invariant towards a shift in time. *Linearity* is a bit more difficult to describe. It has several requirements [181] such as homogeneity and additivity. *Homogeneity* means here that a change in the input signal's amplitude yields a corresponding change of the output signal's amplitude [181]. A system inherits *additivity* if two added signals pass through the system without interaction. When considering such a system and two arbitrary signals $x_1[n]$ and $x_2[n]$ resulting in $y_1[n]$ and $y_2[n]$, respectively, passing $x_1[n] + x_2[n]$ through the system results in $y_1[n] + y_2[n]$ [181].

Linearity results in properties, which come in very handy for DSP applications. Some of these properties are commutativity (the order in which a signal is processed by several linear systems is interchangeable and still leads to the same result), linearity on multiplication (depending on the multiplier, multiplication by a constant is linear, multiplication by another signal is not) and superposition. The latter can be seen as the basis for DSP, as the concept of *superposition* implies that a signal can be composed of a sum of other, potentially less-complex signals. So the interaction of a system with a complex signal can be broken down into multiple interactions with simpler signals and thus allowing to understand the system more easily [181].

Examples for linearity are wave propagation, electrical circuits (consisting of R (resistance), C (capacitance), L (inductance) elements), electronic circuits, e.g., amplifiers and filters, signal changes such as echoes, resonance or blurring, convolution, and small perturbations in otherwise non-linear systems [181]. Battery cells can also be understood, depending on magnitude of the perturbation of the system as both, as linear and non-linear systems. The application of a small perturbation to this system is the basis for electrochemical impedance spectroscopy (EIS), where the response of the system can be modeled as the response of

an electrical circuit, consisting of R, C, and L elements. Choosing a too-large perturbation of the system, e.g., during EIS, leads to a non-linear response, thus making the modeling of the system by an electrical circuit inadequate. But also changing the system's state by a too large quantity of charge, yields a non-linear response, often exhibiting hysteresis, e.g., in cell voltage and mechanical properties such as cell thickness. Further examples of non-linearity are hysteresis and saturation [181].

The combination of signals by scaling and addition is called *synthesis*. The inverse operation is called *decomposition*. In DSP two main ways of decomposition exist: *impulse*[1] *decomposition* and *Fourier decomposition*. The topic of Fourier decomposition was already touched in a previous chapter. Impulse decomposition breaks a signal consisting of N samples into N signals, each consisting of a single impulse. Each of these consists of a single non-zero value, and $N-1$ zero values. This allows to study the interaction of a system with a signal one sample at a time, paving the way for the concept of *convolution* [181], which will be discussed next.

2.3.5 Convolution and deconvolution

Mathematically, convolution combines two signals [181] and can be described as a "shift-and-multiply" operation. As represented by Equation (54), one signal $x_1(t)$ is multiplied point-by-point with a shifted version of the second signal $x_2(t)$ and integrated over the signal's length. For convolution the shift variable τ is the integration or summation variable and t the index variable.

[1] The word „impulse" is used in this work in the context of digital signal processing. Therefore, it refers to the impulse function, a brief input signal, e.g., the Dirac delta function. It is explicitly distinguished from the change of momentum of an object in mechanics. It is not synonymous with the "pulse" in digital signal processing, which is defined as the change of a signals amplitude from baseline to a higher value, followed by the return to baseline.

$$\boldsymbol{c_*(t) = (x_1 * x_2)(t) = \int_{-\infty}^{\infty} x_1(\tau)\, x_2(t-\tau) d\tau} \\ \boldsymbol{= \int_{-\infty}^{\infty} x_1(t-\tau)\, x_2(\tau) d\tau.} \quad \textbf{(54)}$$

In the discrete case, this process is then repeated for different shifts [185]. Each point of the convoluted signal is calculated this way [181,186]:

$$\boldsymbol{c_*[n] = (x_1 * x_2)[n] = \sum_{m=-\infty}^{\infty} x_1[m]\, x_2[n-m]} \\ \boldsymbol{= \sum_{m=-\infty}^{\infty} x_1[n-m]\, x_2[m].} \quad \textbf{(55)}$$

Here, m denotes the shift in units of sampling points, and n the index variable. The star $*$ is used as a symbol for the convolution operator. There are two options to calculate the discrete convolution – point-by-point multiplication and summation in the time domain, as stated above, or point-by-point multiplication in the Fourier space [185]. Equation (56) expresses the operation that has to be carried out for all N elements with index k. The calculation in the Fourier space is beneficial regarding computational effort for signals with a large sample size.

$$\boldsymbol{C_*[k] = X_1[k] \cdot X_2[k]} \text{ for all } \boldsymbol{k \in [0, N-1],} \quad \textbf{(56)}$$

with *k* being the frequency index, corresponding to *N* computed DFT coefficients.

2.3.5.1 Representation of measurement processes by convolution

The convolution is such a useful tool, because it describes effects well that occur in scientific measurements [185]. Examples of those effects include the effect of a detector on a measured spectrum in optics or ultrasonics and the interaction of a soundwave with a medium it is passing through. Before detailing how measurement processes are described in this formalism, the concept of *impulse decomposition* is important to mention first. Impulse decomposition refers to the process of splitting a N-sampled signal into N impulses. Those are characterized by $N-1$ zero values and a single non-zero value. The *delta function*, often symbolized by the Greek letter $\delta[n]$, is a prominent case of an impulse, as its first sample has a value of one and all other samples are zero. Therefore, it is also often called the *unit impulse*. To determine the behavior of a system completely, it is sufficient to know its response to the unit impulse [181]. Therefore, the system is characterized by the

impulse response $h[n]$, which is the signal that results from passing the unit impulse through the system. This operation is sketched in Figure 2.20.

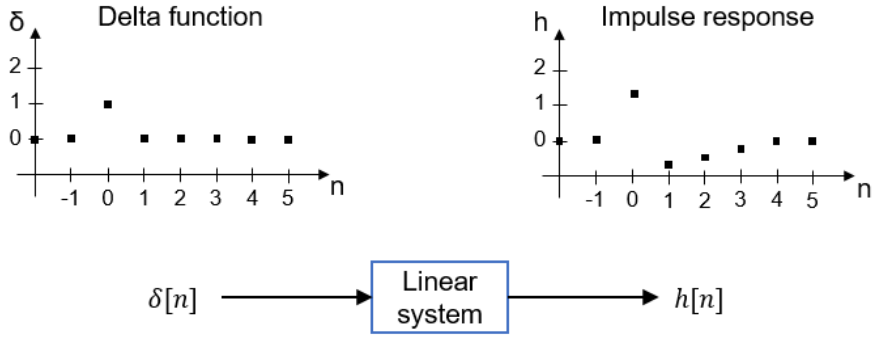

Figure 2.20: Definition of the delta function and the impulse response of a linear system to such an impulse. Graph after [181].

Having the aforementioned properties homogeneity and shift-invariance of an LTI system in mind, one can deduct that the response $y[n]$ of a system to any sampled signal $x[n]$, decomposed into impulses, can be obtained from $h[n]$ as any impulse can be seen as a scaled and shifted delta function [181]. This process is performed by executing the convolution of the input signal $x[n]$ and the impulse response $h[n]$ as depicted in Figure 2.21. Convolution is performed either in the time domain or in the Fourier space as represented in Equations (57) and (58).

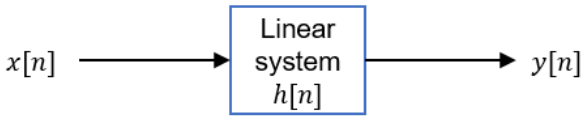

Figure 2.21: Usage of convolution in DSP to represent a measurement process. The output signal is equal to the input signal convolved with the impulse response of the system. This mathematical operation can be performed either by sample-wise multiplication and summation in the time domain or by element-wise multiplication in the Fourier space, as implied by the equations below. Graph after [181].

$$\boldsymbol{x[n] * h[n] = y[n]} \quad \textbf{(57)}$$

$$\boldsymbol{X[k] \cdot H[k] = Y[k]} \quad \textbf{(58)}$$

Here, the capital-letter variables refer to the Fourier transforms of the input signal, impulse response, and output signal, while k is the frequency index, corresponding to N computed DFT coefficients [182]. Depending on the application, several synonyms for the impulse response exist – kernel, filter kernel $f[n]$, convolution kernel or point spread function (in image processing) [181].

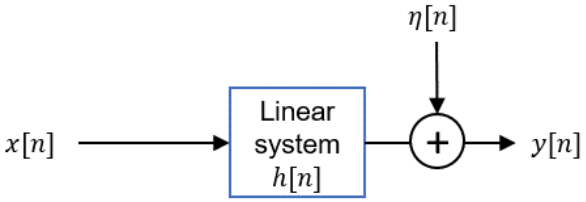

Figure 2.22: Representation of a real measurement process by convolution, including the superposition of additive noise.

In real applications, however, the physical measurement process always involves the superposition of the desired signal with additive noise $\eta[n]$. The general case is depicted in Figure 2.22 and expressed in the following equations for the time and frequency domain [187–190]:

$$\boldsymbol{x[n] * h[n] + \eta[n] = y[n]} \quad \textbf{(59)}$$

$$\boldsymbol{X[k] \cdot H[k] + \mathrm{N}[k] = Y[k]} \quad \textbf{(60)}$$

Convolution can also be used to describe the propagation of sound through a sample. An exemplary case is sketched in Figure 2.23. Any sample has geometric boundaries, at which discontinuities of the acoustic impedance occur. Additional discontinuities may be present within the sample, e.g., at interfaces between layers or sites of manufacturing imperfections. At each discontinuity, the incident wave is partially transmitted and partially reflected, as described by Equation (12). In the ideal case, where the speed of sound is frequency independent and uniform throughout the whole sample, the occurrence of reflection in the transmitted or reflected signal can be directly correlated with the position of discontinuities within the sample [191]. Then it is convenient to define a reflectivity $r[n]$. This reflectivity consists of delta peaks at positions coinciding with the sites of those discontinuities and the time of flight of respective echoes [191] (see Figure 2.23). The measured signal results from the convolution of the reflectivity with the impulse response and subsequent superposition with noise, as sketched in the bottom half of Figure 2.23. This representation can serve as a basic model to simulate acoustic interrogation measurements or as a model for deconvolution, which aims to converse the measurement process and receive an estimate of the reflectivity. In ultrasonic interrogation use cases, the “system” is the whole measurement chain of sending transducer, sample, receiving transducer, and exciting / recording electronic (compare next subchapter). This system generates an impulse response to an input signal, e.g., a needle pulse – mimicking the ideal Dirac delta pulse. The impulse response of the system – the exact waveform – is very often not known and therefore, has first to be estimated from the measured, noisy signal. Then, in a second step, reflectivity can be obtained. This process is called blind deconvolution [192].

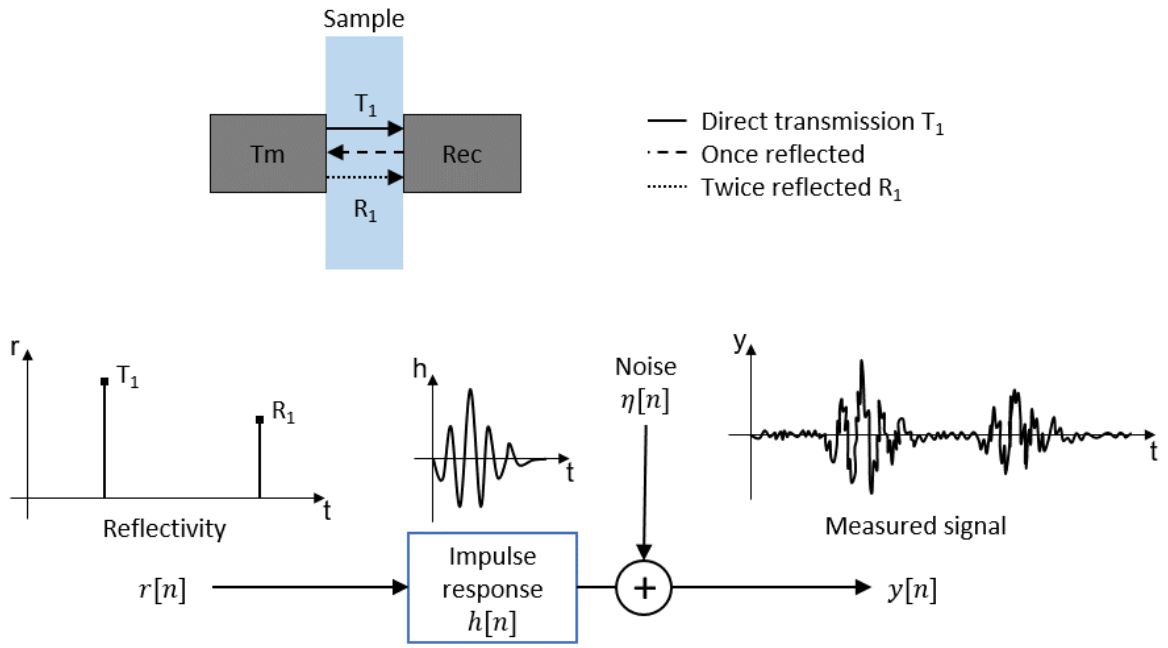

Figure 2.23: Convolution model for acoustic measurement. The top half of the graph shows schematically the transmission of sound waves emitted by the transmitter, traveling through the homogenous sample and detected by the receiver. As discontinuities in acoustic impedance occur at the sample's boundaries, the sound wave is reflected at each boundary. Therefore, one directly transmitted pulse T_1 and subsequent multiple times reflected pulse R_1 can be observed in the transmission signal. The bottom half of the graph shows a sketch of the involved measurement process. It is represented by the convolution of the reflectivity with the impulse response, here being the wave package sent out by the transmitter, and the superposition of noise. Graph after [191].

2.3.5.2 Deconvolution - a method to obtain the input signal of an LTI

In general, *deconvolution* is the inverse of convolution, as division is the inverse of multiplication [185]. Deconvolution is therefore calculated by point-by-point division of the Fourier transforms of the involved signals and then inverse transforming the result [185], while conserving the phase information. In most applications, it is desired to estimate the input signal or reflectivity, e.g., to increase the accuracy of time of flight measurement. The straightforward approach would be to deconvolve the measured signal $Y[k]$ by naïve division of the Fourier transforms [190,192]:

$$\boldsymbol{X'[k] = \frac{Y[k]}{H[k]} = X[k] + \frac{N[k]}{H[k]}.} \qquad \textbf{(61)}$$

This approach relies on the correct representation of the physical convolution by the mathematical convolution model and a good estimate of the impulse response $H[k]$. Noise may be present before and after the physical convolution, while the latter is more detrimental to the result [185]. Referring to the use case of ultrasonic NDT, noise can occur

after the conversion of the acoustic wave package to an electrical signal within the piezoelectric material of the receiving transducer - in the pathway of the signal until its analog-to-digital conversion. In the estimation of the input signal $X'[k]$ by naïve division, the noise $\mathrm{N}[k]$ is greatly amplified, as sketched in Figure 2.24.

Detectors or receivers in real physical measurements are band-limited – they do not possess a uniform frequency distribution like a Dirac delta – and therefore the corresponding impulse response functions are band-limited, e.g., have next-to-zero or zero-valued entries at low and high frequencies. Thus, the division of $Y[k]$ by $H[k]$ leads to an over-amplification of the noise [192], present in the frequency range outside of the bandwidth (compare sections of the spectra in Figure 2.24, marked with red ellipses). The calculation may even fail if some components of the impulse response contain zeros because the zero-point division is not permitted [185]. One has to understand that the exact frequency distribution of $\mathrm{N}[k]$ is unknown for a specific measurement and has to be estimated based on assumptions. Nevertheless, its expectation (in a statistical sense) can be determined by measurement and analyzing the statistical distribution, e.g., to verify the assumptions that the noise is (Gaussian) white and independent of the input signal, which is usually the underlying assumption. “White” in this context refers to a uniform value at all freuqencies.

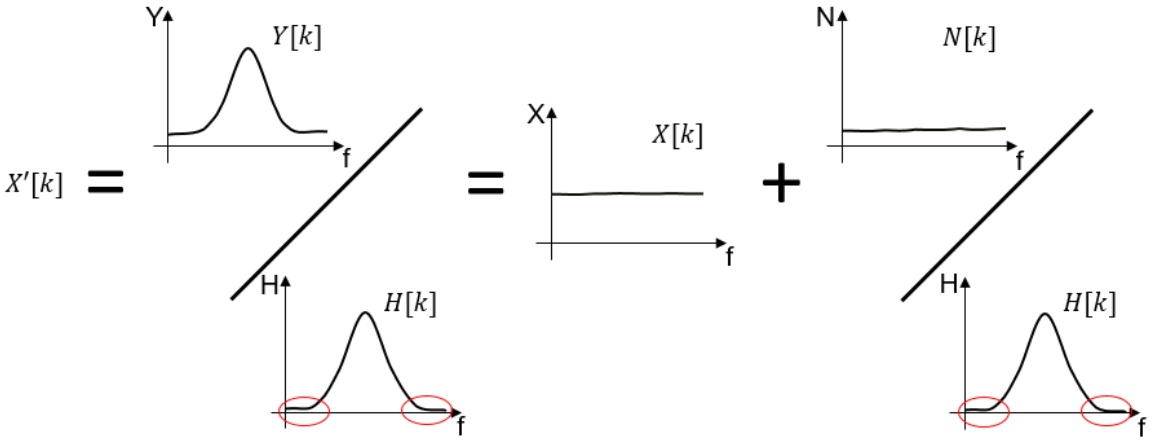

Figure 2.24: Sketch of deconvolution by naïve division, as expressed in Equation (61). The signals from Figure 2.23 are represented in the Fourier domain. In this example, $X[k]$ is a Delta function and has uniform value at all frequencies (is “white”), $Y[k]$ consist of a Gaussian-like shaped peak and an added noise component. The noise $\mathrm{N}[k]$ is assumed white and is therefore uniformly distributed over all frequencies. The impulse response $H[k]$ is also bell shaped and has next-to-zero or zero valued entries outside of the frequencies, contained in the wave package, as marked by the red circles. Therefore, the point-by-point division of $Y[k]$ by $H[k]$ leads to artefacts in the estimate $X'[k]$ caused by an over-amplification of the noise component at indices k, corresponding to high and low frequency, or will lead to failure because zero point division is not permitted [185].

The amplification of noise can be reduced by several measures, a first step usually includes adding a small positive non-zero constant to the impulse response [185]. This eradicates zero or next-to-zero values, especially at higher frequencies, without changing the entries of the impulse response for lower frequencies at large [193]. Smoothing or bandpass filtering can further reduce the amplitude of frequencies that are amplified the most [185]. Another way is to introduce a regularization parameter in the inverse filter, performing the deconvolution of the signal [188]. The most prominent example of such a filter is the Wiener filter [192,194]. It was named after Norbert Wiener and is not to be confused with the Wien filter (a velocity filter for charged particles using perpendicular electric and magnetic fields) or the Wien bridge (a type of bridge circuit, used to measure the capacitance and resistance of a component by comparison to known components). Besides improving the signal-to-noise ratio (SNR), the Wiener filter is used in time of flight estimation application to increase time resolution and is especially useful if echoes in the measured signal are closely spaced. The commonly accepted definition of the filter is [187,190,195]:

$$\boldsymbol{X'[k] = Y[k] \frac{H^*[k]}{|H[k]|^2 + Q^2_{Wiener}}.} \quad \textbf{(62)}$$

Here, $H^*[k]$ denotes the complex conjugate of $H[k]$ and Q^2_{Wiener} denotes the regularization parameter, which is sometimes called the “noise desensitizing factor” [195] and is supposed to stabilize the solution [187]. Note that the complex conjugate of a complex number is that number with the sign of the imaginary part reversed. Originally, the Q^2_{Wiener} parameter is the inverse of the signal-to-noise ratio $1/SNR[k] = S_{\mathrm{N}}[k]/S_X[k]$. Here, $S_X[k]$ and $S_{\mathrm{N}}[k]$ are the power spectral densities of respectively the input signal $x[n]$ and the noise $\mathrm{N}[k]$. Because estimating this parameter in practice is rarely possible, it is commonly replaced by a frequency-independent constant $10^{-2} \cdot |H[k]|^2_{max}$ [195]. Even though the Wiener filter is said to be an optimal filter, the quality of the estimated input signal depends on the bandwidth of the impulse response, or in our example, the estimation of the reflectivity (sharpness/width of the peaks) depends on the bandwidth of the acoustic pulse [187]. The wider the bandwidth in the Fourier domain is, the sharper the pulse can be in the time domain. Frequency content outside of the bandwidth is usually cut and therefore the contained information is lost and cannot be recovered with the Wiener filter [187], which leads to a finite obtainable time resolution.

There are several options to improve the Wiener filter result by integrating a priori information, e.g., on the reflectivity or estimates from the measured signal. A priori information can detail the impulse response function of the LTI or the input signal. In the

case of acoustic interrogation, this can include an estimate of the acoustic pulse or a model for the reflectivity. Reflectivity is often modeled as a sparse spike train in a Bernoulli-Gaussian process [187,196–199], where the count, height, and position of the spikes in the reflectivity are varied to find an optimized deconvolution result. Since using an impulse response that represents the physical convolution operation well yields the best deconvolution result, the acoustic pulse is often estimated from the measured data. This can include the use of higher-order spectral analysis [192] or autoregressive spectral estimation (ASE) [195,200]. The latter builds on the assumption that a part of the measured signal's spectrum, having a high SNR, can be modeled as an autoregressive process. The spectrum is then extrapolated based on this region extending into regions where the SNR is low [195] and used as an estimate for the acoustic pulse's spectrum, effectively increasing the bandwidth of the impulse response. Thereby, even a so-called "blind deconvolution" without a priori knowledge of the impulse response / the acoustic pulse, only using the measured signal, is possible [194,200].

The before mentioned methods, but especially the ones that pick the pulse from the measured signal, rely on the assumption that this pulse represents the pulse used in the physical convolution well. This means in particular, that the pulse remains virtually unchanged in shape and frequency content when passing through the material – being independent in those parameters with respect to propagation distance. This assumption requires the attenuation in the interrogated material to be independent of frequency f, which is especially not true for plastics, composite materials [201] and materials made up from particles, e.g., particle rich suspension (content > 10%) [202] or particle networks. In [201], the authors account for frequency-dependent attenuation and dispersion to achieve a good estimate of the reflectivity in a plastic sample. They describe the whole measurement process as a chain from electrical excitation $U(f)$ of the sending transducer up to the conversion of the acoustic signal to an electrical signal (excluding noise) by

$$\boldsymbol{Y(f,\vec{z}) = U(f)H_{ea}(f)H_r(f,\vec{z})H_{ae}(f).} \quad \textbf{(63)}$$

Here, f denotes the frequency, $H_{ea}(f)$ and $H_{ae}(f)$ are respectively the electric-acoustical and acoustic-electrical transfer functions and can be summed up as the electrical transfer function $H_e(f) = U(f)H_{ea}(f)H_{ae}(f)$. Then, $H_r(f,\vec{z})$ represents the transfer function of the propagation path $\vec{z}$ and accounts for both, frequency-dependent attenuation $\alpha(f)$ and dispersion $\epsilon(f)$, leading to the expression [201]

$$\boldsymbol{Y(f,\vec{z}) = b(|\vec{z}|)H_e(f)e^{-\alpha(f)|\vec{z}|}e^{-\hat{\imath}\epsilon(f)|\vec{z}|}e^{-\hat{\imath}2\pi f|\vec{z}|/c_0}}. \quad \textbf{(64)}$$

Here, $b(|\vec{z}|)$ is a propagation length $|\vec{z}|$ dependent constant, modulating the amplitude of the received signal $Y(f,\vec{z})$, and the exponential functions with $\alpha(f)$ and $\epsilon(f)$ in the exponent accounting for attenuation and dispersion. The last exponential function represents the phase of the acoustic wave with c_0 as the speed of sound [201]. As batteries are in some sense media of alternating layers of particle-rich fluid suspension (electrodes) and solid layers (current collectors), methods that incorporate frequency-dependent attenuation and dispersion are of particular importance.

2.3.6 Time of flight estimation

The time of flight (ToF) is one of the most prominent signal features and allows calculating the speed of sound in the interrogated sample, provided the travel distance of the respective wave package is known. Indirectly, the ToF is linked to the mechanical and therefore electrochemical state of the lithium-ion battery, which this thesis aims to estimate with a higher precision than algorithms relying solely on voltage and current measurement.

As seen in the preceding section, deconvolution can be used to estimate the travel time of ultrasonic pulses or echoes. This travel time is often referred to as the time of flight, time of arrival (ToA) [203], or transit time. Its accurate and reproducible estimation is an important task for DSP in ultrasonic NDT and this work. The ToF is used to calculate the velocity and from this quantity, other quantities like the elastic modulus and the acoustic impedance of a material are determined. Ideally, the ToF clock starts when the acoustic pulse exits the sending transducer and stops when the acoustic pulse reaches the receiving transducer. Because delays within the electronics and the piezoelectric material of the transducer are negligibly small, the time of excitation is often used as zero-point. In ultrasonic NDT, this point is well known since the excitation is triggered. A variety of methods exist to estimate the ToF from a measured signal. Different methods use different reference points of the signal to determine the time at which a pulse is received [204]. To name a few, there is the zero-crossing method, the first detectable deviation from zero (first motion), the threshold method, and the cross-correlation technique. In homogenous media with no absorption present, these techniques yield equivalent results [204]. In contrast, due to pulse broadening in absorptive media different techniques yield different values for the ToF. Pulse-broadening effects are a consequence of frequency-dependent absorption and dispersion, as was discussed in Chapter 2.2.1. Both are linked by the Kramers-Kronig relation and thus always coincide [204].

Within this subchapter, a brief description of the most common ToF estimation methods with respect to their relevance for media with frequency-dependent attenuation, like battery materials, will be given. Comparison of different ToF estimation methods can be found in [204,205]. Some of the well-established ToF estimation methods are sketched in Figure 2.25 for comparison.

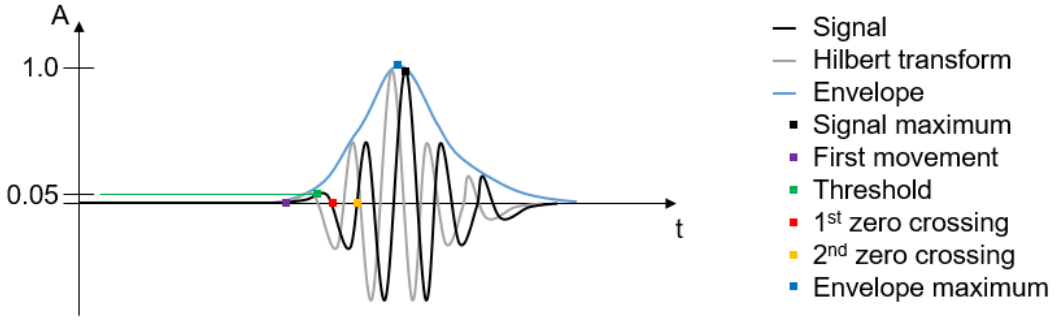

Figure 2.25: Conceptual comparison of several time of flight estimation (ToF) methods, as suggested by the legend. An ultrasonic signal (amplitude vs. time) with a single wave package is sketched (in black). The amplitude is normalized to its maximum. Hilbert transform and envelope are calculated from the signal as described in Subchapter 2.3.6.2. The ToF, as estimated by several different methods, is drawn as colored dots.

2.3.6.1 The first motion, zero-crossing, threshold, and sliding-window method

The *first motion* technique uses the first detectable deviation from zero in the measured signal as a reference point for the ToF [204] (compare the purple dot in Figure 2.25). Unfortunately, noisy signals make this method prone to errors and false positives may yield unreasonably small values for the ToF. These unwanted effects can partially be combated by smoothing or filtering the signal. *Zero crossing* tracks the first or second intercept of the ultrasonic signal with the time axis [204] (see Figure 2.25). With the *threshold* method, the first point of the signal at which, usually, the absolute amplitude is equal or greater than a certain threshold value τ_{th} serves as a reference point [205,206] (see Figure 2.25). The optimum threshold value is often estimated empirically. It can be chosen relative to the maximum of the measured signal, e.g., 5%. Ideally, the maximum of the measured signal lies within one of the transmitted acoustic wave packages. Otherwise more elaborate threshold value picking criteria may be required. Another option is to choose the threshold based on the noise since it should lie above the noise level to avoid false positives. In [207], the threshold was chosen to be eight times the standard deviation of the noise but is usually set to three to five times the background noise level [205]. The background noise level can

either be estimated from a section of the signal containing no acoustic information – before the first arrival, or from collecting statistical noise with the open detector while no pulse is sent. The *sliding-window* method represents a modification of the threshold method, aiming to improve noise robustness. Here, a window of a set length N_{th} is slid through the measured signal and the number of points exceeding the threshold τ_{th} is counted. If this number exceeds a second threshold m_{th} the ToF criteria is met [205], which is why the method is also called double-thresholding and makes it robust towards noise peaks. Another advantage is the comparably low standard deviation of the method. The performance of the method heavily relies on the tuning of τ_{th}, N_{th} and m_{th}. According to [205], both threshold methods are limited by the rise time of the received pulse, which is especially long with narrow-bandwidth transducers. The general problem with the methods above is that the reference point's position within the wave package introduces a delay that is never constant (e.g., due to dispersion) and cannot be accounted for by a known offset [206]. To reduce the occurrence of false positives, the simple threshold method is combined with other methods. Curve fitting and the envelope of the signal can help to uncover the first points of a wave package, potentially buried under noise, thereby reducing or removing the mentioned offset [205,206], as will be explained later.

2.3.6.2 The envelope function and method

The *envelope* is the base for two other ToF estimation methods. For a real-time signal $y(t)$, the envelope $E(t)$ is expressed as the absolute of the analytical signal $\psi(t)$ by

$$\boldsymbol{E(t) = \sqrt{\psi(t)\psi^*(t)} = \sqrt{y^2(t) + \hat{y}^2(t)},} \tag{65}$$

with $\psi^*(t)$ being the complex conjugate of $\psi(t)$ [204]. The analytical signal is calculated from the signal according to

$$\boldsymbol{\psi(t) = y(t) + \hat{\imath}\hat{y}(t),} \tag{66}$$

which in turn is derived from the Hilbert transform [204,208]

$$\boldsymbol{\hat{y}(t) = \frac{1}{\pi t} * y(t),} \tag{67}$$

with the convolution operator $*$. In DSP practice, the analytical signal $\psi(t)$ is calculated by inverse Fourier transforming

$$\boldsymbol{\Psi(f) = 2Y(f)\Theta(f),} \tag{68}$$

with $Y(f)$ being the Fourier transform of $y(t)$ and $\Theta(f)$ denoting the Heaviside or Theta step function, which is 0 for $f < 0$ and 1 for $f \geq 0$ [204]. As depicted in Figure 2.25, the Hilbert transform (grey curve) corresponds to a phase shift of $-\pi/2$ and thus the energy spectra of $y(t)$ and $\hat{y}(t)$ are the same. The peak of the envelope (blue dot) lies between the peaks of signal an Hilbert transform and represent the maximum energy of the analytical signal [204]. As described in [204], the envelope method yields a comparably small estimation error for absorptive and dispersive media, but as we will see later on, the envelope method is best suited for well-separated wave packages, as the neighborhood of wave packages influences the shape of the envelope and thus the position of its maximum. Note that for an accurate estimate the time difference to the maximum of the envelope of the send acoustic pulse has to be available. Studies have shown, that the envelope can be combined, e.g., with the deconvolution by Wiener filter and ASE to further improve ToF estimation and to ease automated peak picking [200].

Besides picking the envelope's maximum, the before mentioned *curve fitting* method can be performed based on the envelope. A parabolic curve of the form $a_0(t - t_0)^2$ fitted to the envelope is according to [206,209,210] a suitable approximation for the rising edge of typical acoustic pulses (compare the course of the blue line in Figure 2.25). An iterative fit can be initialized with values from simple thresholding for a_0 and t_0. The best fit of t_0 is then finally taken as an estimate for the ToF, being free of the above mentioned delay usually associated with the threshold method [205].

2.3.6.3 The cross-correlation function and method

When the signal exhibits a low SNR, *cross-correlation* has proven to be a powerful method for ToF estimation [178] due to its noise reduction property [206]. If used in conjunction with frequency-modulated signals, like a chirp, cross-correlation is often referred to as *pulse compression* [206]. Provided cross-correlation is applied to a single-frequency tone-burst (a modulated sine wave function), another synonym is *matched filtering* [206]. The cross-correlation operation, symbolized by the five pointed star $\star$ operator, is performed on continuous signals $x_1(t)$ and $x_2(t)$, by calculating [208]

$$\begin{aligned} \boldsymbol{c_\star(\tau) = (x_1 \star x_2)(\tau) = \int_{-\infty}^{\infty} x_1^*(t)\, x_2(t+\tau)\, dt} \\ \boldsymbol{= \int_{-\infty}^{\infty} x_1(t-\tau)\, x_2^*(t)\, dt.} \end{aligned} \quad \textbf{(69)}$$

Here $c_\star(\tau)$ denotes the cross-correlation as a function of delay τ. The asterisk * in the exponent denotes the complex conjugate of a variable. The cross-correlation operation is performed on sampled, discrete signals by calculating [17,208]

$$\begin{aligned} \boldsymbol{c_\star[m] = (x_1 \star x_2)[m] = \sum_{n=-\infty}^{\infty} x_1^*[n]\, x_2[n+m]} \\ \boldsymbol{= \sum_{n=-\infty}^{\infty} x_1[n-m]\, x_2^*[n].} \end{aligned} \quad \textbf{(70)}$$

Comparing Equation (70) and (55) unveils the differences between convolution and cross-correlation. They differ in the sign of the shift and the choice of the integration or summation variable. In convolution, the summation is performed over the shift variable (m or τ), while in cross-correlation, the summation is performed over the index variable (n or t). Therefore, the cross-correlation is a function of the shift variable and convolution is a function of the index variable. Therefore, commutativity is not valid for cross-correlation, in detail $x_1[n] \star x_2[n] \neq x_2[n] \star x_1[n]$. In practice, cross-correlation is often performed in the Fourier domain by multiplication of $X_2[k]$ with the complex conjugate of $X_1[k]$, $X_1^*[k]$, and subsequent inverse Fourier transforming [206,208]. The Cross-correlation in the Fourier domain can be calculated by

$$\boldsymbol{C_\star[k] = X_1^*[k] \cdot X_2[k].} \quad \textbf{(71)}$$

The cross-correlation peaks at the delay m where the two signals match best [207]. ToF estimation with cross-correlation is based on the property that a delayed signal's cross-correlation is the auto-correlation (correlation of a signal with itself) of the signal shifted by the delay [208]. This delay corresponds to the ToF of the pulse [202]. To achieve maximum cross-correlation amplitude, the pulse has to be unaltered in shape [205]. Why cross-correlation is also often described as pulse compression can be seen in Figure 2.26. Used on a broadband pulse, like a chirp (frequency modulated sine wave), the cross-correlation allows localizing the reference point for ToF estimation in a narrower peak [206]. The width of this peak is proportional to the inverse of the bandwidth of the sent pulse [206]. The height of the cross-correlation peak increases with the length of the sent pulse for the same bandwidth [211].

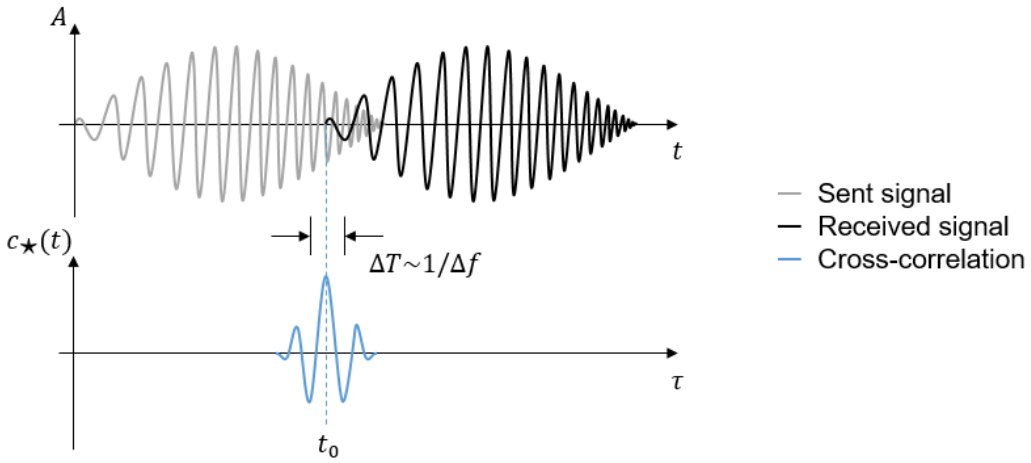

Figure 2.26: Cross-correlation of chirp signals. In the top, two chirp signals are plotted, one starting a $t = 0$ and one shifted by a delay $\tau = t_0$. The cross-correlation, plotted in the bottom row, peaks at exactly this delay τ, where the two signals match best. The width and height of the peak depend on the bandwidth and length of the chirp. Graph after [206]

The ability of the cross-correlation method to enhance the resolution of ToF estimation depends largely on the bandwidth of the utilized transducers and pulses. Therefore, when applied to narrowband pulses, accuracy errors can occur [206]. Especially if the pulses are closely spaced or even overlap, the achieved pulse compression may still be insufficient to separate these pulses. Cross-correlation has one inherent advantage over most other methods, which is that the estimated delay t_0 already equals the ToF (see Figure 2.26). On the contrary, if using, e.g., the envelope for short distance ToF estimation, the position of the envelope's peak (see Figure 2.25) within the sent pulse has to be subtracted from the ToF to avoid a systematic error.

2.4 Impedance spectroscopy

Impedance spectroscopy has many applications in electric circuit design and electrochemistry. In the context of lithium-ion batteries, it has been used to study the degradation phenomena [212,213] and the wetting process of lithium-ion batteries [34], and among others, for the state of health estimation [214–216]. Impedance spectroscopy is also applied to ultrasonic transducers and piezo elements to characterize their properties [217] and interaction (coupling) with the surrounding medium [218–220] or to detect defects [221]. Impedance spectroscopy involves the excitement of the battery cell with a small alternating voltage (potentiostatic) or current (galvanostatic). The amplitude of the excitation has to be small to keep the response in a range, where the assumption of a linear system applies [222]. The impedance Z of the cell is the quotient of complex voltage $\hat{U}(t)$ and complex current $\hat{I}(t)$, as defined by [34,222,223]

$$\boldsymbol{Z = \frac{\hat{U}(t)}{\hat{I}(t)} = \frac{\hat{U}_0 \cdot \sin(\omega t + \phi_1)}{\hat{I}_0 \cdot \sin(\omega t + \phi_2)} = Z_0 \cdot \frac{\sin(\omega t + \phi_1)}{\sin(\omega t + \phi_2)}.} \quad \textbf{(72)}$$

Here, ω describes the radial frequency and ϕ_k the phase angel. It is common to rewrite this formula to describe the impedance as a complex resistance and split the impedance into the real and imaginary parts, as in the Euler representation [34,223,224]

$$\boldsymbol{Z = Z_0(\cos(\Delta\phi) + \hat{\imath} \cdot \sin(\Delta\phi)),} \quad \textbf{(73)}$$

with the phase shift $\Delta\phi = \phi_2 - \phi_1$, the absolute value of the impedance $|Z| = \sqrt{\mathrm{Re}(Z)^2 + \mathrm{Im}(Z)^2}$ and complex number $\hat{\imath}$. The real part of the impedance $\mathrm{Re}(Z)$ describes the ability of the system under investigation to resist the flow of electrical current while the imaginary part of the impedance $\mathrm{Im}(Z)$ describes the ability to store energy [34], e.g., in an electric or magnetic field. The interaction of the system with the alternating voltage or current can be modeled by equivalent circuits, composed of resistors, capacitors, inductors and constant phase elements [34,223].

When studying an electrochemical cell, the complex impedance allows to qualitatively identify and describe processes [34,224,225]. These processes involve different time scales. Therefore, the frequencies at which there are the most prominent differences in the electrochemical impedance spectra differ [34,226]. At low SoC, the impedance spectrum of a lithium-ion battery cell can be schematically represented as in Figure 2.27. The spectrum can be divided into three sections. The first section, with the highest frequency, accounts for the fastest processes such as ionic conduction in the electrolyte. The impedance in this section is shifted by the inductance, associated with the porous and tortuous structure of the electrodes, the wiring and other metallic components of the battery cell, along the imaginary axis [34]. The intersection of the curve with the real axis is referred to as the high-frequency resistance (HFR) and is contributed to by the ohmic resistance of the electrically conductive materials inside the cell and the ionic resistance of the electrolyte [34,227]. The second section is composed of two semi-circles. One of which is assigned to ion migration through layers covering the surface of the active material particles of the electrodes, such as the SEI [34,228]. The other is assigned to the charge transfer between the electrodes and the electrolyte, and the associated double layer capacity [34,229]. The third section spans the lowest frequencies and thus represents the slowest process in the battery cell, which is the diffusion of lithium in the active material of the electrodes [34,230].

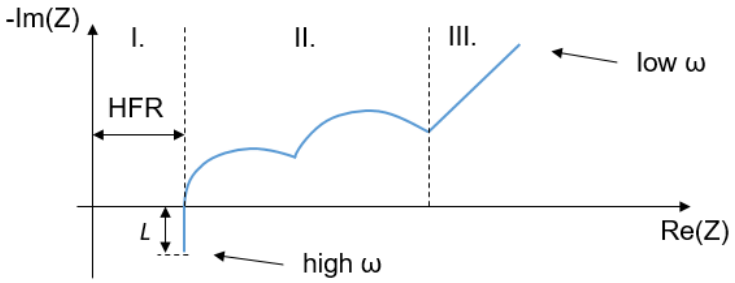

Figure 2.27: Schematic representation of the impedance spectrum of a lithium-ion battery cell. The Nyquist plot is divided into three sections. The first section with the highest frequency accounts for the fastest processes such as ion diffusion in the electrolyte. The second section spans the frequency range in which migration processes through the SEI and the charge transfer are situated. The third section is characterized by the lowest frequencies and represents the diffusion of lithium ions in the active materials. The Graph after [34].

Ultrasonic transducers, consisting of piezo elements, can also be studied by impedance spectroscopy. Commonly their geometry includes two plates with a piezoelectric as the dielectric in between, basically a capacitor. Therefore, equivalent circuit models representing piezo elements, include at least one capacitance, usually in parallel with a resistor and an inductance and sometimes in series with a ZARC element [217,219,220]. The name ZARC element was established by Macdonald and denotes the combination of a constant phase element (CPE) and a resistor in parallel [231]. Resistors and inductances are included to account for the dielectric, elastic and piezoelectric losses [220] and the mechanical inertia of the system, introduced by its mechano-electrical coupled mass. It was shown that impedance spectroscopy can be instrumented to test piezo elements for defects [221] and to characterize the coupling of the oscillation with the surrounding medium [218], and thus the quality of bonding of the piezo element to the object of interest. It is possible to estimate the resonance frequency of a piezo element from an impedance spectrum [218]. Plotting the real part of the impedance versus frequency allows identifying resonant behavior because the piezo elements dissipate energy by mechanical oscillation at the characteristic frequencies and thus show a higher impedance at resonance. The Nyquist plot (imaginary part vs. real part of the impedance) allows, as described in [221], to qualitatively estimate the symmetry of the oscillation of a piezo element. The more symmetric the shape of a piezo disc, the more spherical appears the circle, made up from the measurement points around one of the resonant frequencies.

3 Experimental methods & instrumentation

This chapter describes the experimental methods employed in this work to enable the reproduction and confirmation of the presented results.

3.1 Battery cells under investigation

A battery cell type with graphite and lithium cobalt oxide as active materials and designed for high energy density and high power density was selected. This ensures the relevance and transferability of the results of this work. A battery cell of the selected type “Conrad energy Rechargeable Polymer Li-Ion Battery 3.7 V, 1200 mAh” (Conrad Electronic International GmbH) is depicted in the state “as delivered” in Figure 3.1. A detailed safety data sheet [232] and technical data sheet [233] inform on the components and specifications of the battery cell. Their content is summarized in Table 3.1 and Table 3.2.

Figure 3.1: Studied cell as delivered by the supplier Conrad. The outer blue and dark polymer film can be removed to access the surface of the pouch foil directly.

Table 3.1: Selected specification of the studied battery cell "Conrad energy Rechargeable Polymer Li-Ion Battery 3.7 V, 1200 mAh, Item no.: 517990" – according to [232,233].

Parameter	Value	Parameter	Value
Nominal capacity	1.2 Ah	End of discharge voltage	3.0 V
Nominal voltage	3.7 V	Width	36 mm
Max. charging current	2.4 A	Length	67 mm
Max. discharging current	24 A	Thickness	7 mm
End of charge voltage	4.2 V	Weight	33.3 g

Table 3.2: Components of the studied battery cell "Conrad energy Rechargeable Polymer Li-Ion Battery 3.7 V, 1200 mAh, Item no.: 517990" according to safety datasheet [232]. Horizontal lines group the components into constituents of the positive electrode, negative electrode, electrolyte, and contact material.

	Common chemical name	Concentration / %
Positive electrode	Lithium Cobalt Oxide ($LiCoO_2$)	35.5
	Aluminum Foil (Al)	9
	Poly(vinylidene fluoride) (PVDF)	1
Negative electrode	Graphite (C)	18
	Copper Foil (Cu)	15
	Styrene-butadiene polymer (SBR)	1.5
Electrolyte	Lithium hexafluorophosphate ($LiPF_6$)	2.8
	Ethylene carbonate (EC)	5
	Dimethyl carbonate (DMC)	5
	Ethyl methyl carbonate (EMC)	5
Contact material	Nickel (Ni)	2.2

3.2 Electrochemical tests & post-mortem analysis

All electrochemical tests were conducted within a controlled environment at a constant temperature of 25 °C. Depending on space requirements and duration of the experiment, a Vötsch VT^3 4018-S, a Vötsch VT 4021-S, a Weiss WKL 34/70, or a Memmert IPP 260^{PLUS} were used to control ambient conditions. A Maccor Series 4000 galvanostat was used to perform cycling tests. For electrochemical impedance spectroscopy, a BioLogic VMP-300 potentiostat was employed.

Post-Mortem experiments, involving cell opening and lab cell construction were carried out under argon atmosphere. A glove box (MB200MOD, M. Braun Inertgas-Systeme GmbH) ensured a low content of water and oxygen below 1 ppm.

Three-electrode electrochemical tests were carried out in ECC-PAT-Core test cells, supplied by EL-CELL GmbH. From a battery cell opened at discharged state, the electrodes were harvested. To achieve electrical contact from the backside, the coating was removed from one of the sides of the electrode sheets, and discs were punched out. Besides the electrodes, a lithium reference electrode, integrated into a glass fiber 260 µm separator, a

200 µm plunger, and 150 µl of the electrolyte LP57 (1M $LiPF_6$ in EMC/EC solution, with a weight ratio of 7:3, supplied by BASF) was used to build a test cell. Thereby, the individual electrodes' potentials became accessible for investigation.

From the negative and positive electrodes, two samples at each SoC with a weight of about 1 g were cut and individually dissolved in 30 ml of *aqua regia* - a mixture of nitric acid and hydrochloric acid. The resulting solutions were analyzed by inductively coupled plasma-optical emission spectrometry (ICP-OES). The measurements were carried out using a Vista-PRO radial, supplied by Varian Inc.

3.3 Geometric measurements

A dial indicator of type Sylvac S_Dial Nano with a resolution of 0.1 µm was employed to measure the thickness of the individual battery cell components and to monitor the thickness change of battery cells during the electrochemical cycling. During cycling at a constant 25 °C, the tip of the dial indicator was placed centrally on the surface of the battery cell, which was strapped down onto the granite base plate of the dial indicator. The geometric dimensions of the components and the battery cell were estimated with a precision ruler.

3.4 Ultrasonic tests

Ultrasonic measurements in the frequency range of 20 kHz to 0.5 MHz were carried out with a multi-channel sensor bus system for ultrasonic non-destructive testing and structural health monitoring, named US-SBX. The measurement system and the software US-SBX Control used to configure and schedule measurements were developed by Fraunhofer IKTS in Dresden. To ensure electromagnetic compatibility and to reduce the irradiation of electrical noise from the surrounding, the US-SBX was enclosed in a grounded network cabinet and the channels were fed pairwise onto the sockets of a CAT6a Ethernet patch field (Intellinet Network Solutions GmbH). The ground of said patch field was connected to the functional ground of the US-SBX, ensuring a star-wise pathing of the ground until the transducers. Ethernet cables, designed for high-frequency signals and shielded from electromagnetic radiation, were used as measuring leads connecting the transmitting and receiving channels of the US-SBX with the respective piezo elements, mounted to the surface of the battery cells.

A procedure to reproducibly create and mount a sensor stack to battery cells was developed within this work and is described in the following. A sensor stack was constructed from a

piezo element on a brass base and a copper envelope, serving as electromagnetic shielding, made from 20 µm thick copper foil. To attach the piezo element on the copper foil and, in a subsequent step, the hereby-created sensor stack to the battery cell, a two-component epoxy resin UHU Plus Endfest 300 was used. After assembly, this stack was lifted by a vacuum-grabbing device and placed on a pre-applied resin pad on the battery cell. The resin was hardened at room temperature for 24 hours, before further handling. The disc-shaped piezo elements of type PSNK2030 are supplied by EVE GmbH. Their specifications are listed in Table 3.3.

The complete procedure can be split into the following steps:

1) Assembling the sensor stack
   a) Mixing of two-component epoxy resin (UHU Plus Endfest 300) in a 1:1 ratio
   b) Applying a mask, made from 20 µm thick spring steel with a circular hole, to 20 µm copper foil
   c) Creating a pad of epoxy resin film on the copper foil with a defined thickness and shape (negative of the mask) by doctor blading
   d) Grabbing the pristine piezo element disc without contact or wiring with the vacuum grabbing device parallel to a supporting surface
   e) Placing the piezo element in parallel to the surface on the resin pad and applying a defined force by weight
   f) 24 h hardening of the resin at room temperature
2) Attaching the sensor stack to the battery cell
   a) Marking appropriate locations for sensor placement, symmetrically on opposing sides of a battery cell
   b) Cutting the copper foil into a stripe with the piezo element at one side, in preparation for the envelope
   c) Applying a resin pad on the battery surface by masking and doctor blading
   d) Grabbing the sensor stack with the loose stripe of copper foil with the vacuum grabbing device
   e) Placing the piezo element in parallel to the surface on the resin pad and applying a defined force by weight
   f) 24 h hardening of the resin at room temperature
3) Contacting piezo element and shielding
   a) Contacting the piezo element’s top (silver contact layer) and bottom (brass carrier disc) with a wire by soldering
   b) Applying an insulating layer on the piezo element to inhibit short circuit between the piezo element and shielding layer
   c) Folding the copper envelope around the piezo element
   d) Contacting shielding envelope by soldering a wire to the foil
4) Fixing a plug to the three wires (the two red and black measuring leads are twisted to reduce crosstalk)

The cell pictured in Figure 3.2 was equipped with two sensor stacks on opposing sides, following the described procedure. Besides the blue perpendicular lines, marking the center of the stack within the battery cell, placement marks for the vacuum grabbing device (blue rectangles) were drawn onto the pouch foil. The default electrical contacts of the battery cell

have been replaced with a 1.5 mm² lead for applying current and a 0.5 mm² lead for voltage sensing, one for each of the two contacts, as shown in the left of Figure 3.2.

Table 3.3: Selected specification of piezo elements PSNK2030, according to the datasheet [234].

Parameter	Value	Parameter	Value
Resonant frequency	(3.8 ± 0.5) kHz	Diameter of base	(20.0 ± 0.1) mm
Resonant impedance	200 Ohm	Diameter of active disc	(15.0 ± 0.3) mm
Capacitance at 100 Hz	(25.0 ± 7.5) nF	Thickness of active disc	(0.15 ± 0.05) mm
Input voltage	30 V	Thickness of the element	(0.28 ± 0.05) mm
Base material	Brass	Active material	unknown

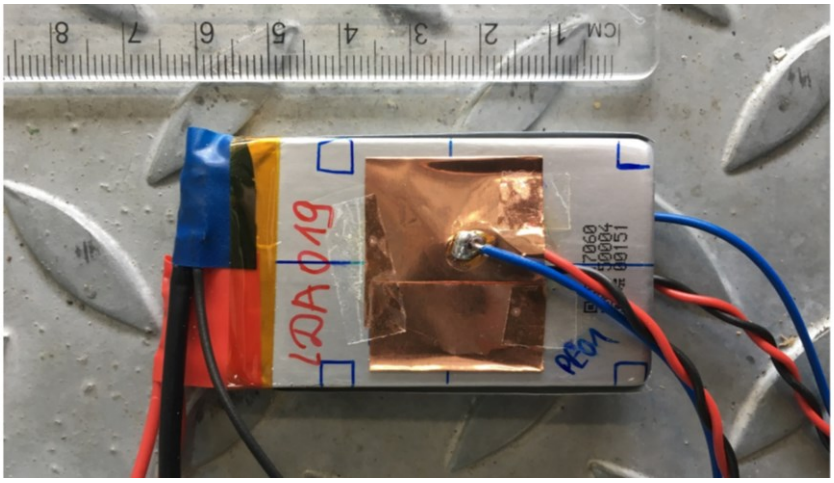

Figure 3.2: A battery cell, LDA019, with an electromagnetically shielded piezo element fitted to its surface. A blue lead contacts the electromagnetic shield, made from copper foil. The twisted red and black leads contact the encapsulated piezo element. The original two-lead electrical connectors were replaced by two individual leads each, for four-point measurement. Blue lines and rectangles were drawn onto the pouch foil to assist the central placement of the sensor stack on opposing sides of the battery cell.

3.5 Analysis of the measurement data

The data presented in this work was analyzed and plotted with the aid of Python 3.8.5 [235], as packaged to a distribution with 300+ packages by Anaconda Inc. [236]. The most important packages, used within this work, and where to find them is listed below:

- NumPy [237] - https://numpy.org/
- pandas [238] - https://pandas.pydata.org/
- SciPy [239] - https://scipy.org/
- Matplotlib [240] - https://matplotlib.org/
- scikit-learn [241] - https://scikit-learn.org
- IPython [242] - https://ipython.org/
- uncertainties [243] - http://pythonhosted.org/uncertainties/
- npTDMS [244] - https://github.com/adamreeve/npTDMS

4 Results & discussion

The results and discussion chapter covers the whole development process of the presented method. Each section/subchapter contains a summary of the respective key messages. In Section 4.1, the lithium-ion battery pouch cells, studied in this work, are interrogated by means of electrochemical and post-mortem methods. This yields an overview of the characteristics and composition of the battery cells. Thereby, a later comparison of variations in mechanical and electrochemical behavior with ultrasonic measurements is enabled. In Section 4.2, the development of the measurement setup, including the manufacturing of sensor stacks from piezo elements and their attachment to the surface of the battery cells is described. Validation of the sensors and their electromagnetic shielding is performed to assure reproducibility of the following experiments. In Section 4.3, the excitation of the piezo elements is displayed and the influence of their resonant behavior on the resulting waveform is discussed. The raw signals, transmitted through the battery cells as a result of this excitation, are displayed as a function of excitation frequency and state of charge. This allows gaining an overview of the dependence on those variables. Section 4.4 describes the processing of transmitted signals, with a focus on the time of flight estimation and a comparison of eligible methods for the extraction of this and other features (signal properties). After three signal properties and methods for their extraction were picked, their suitability for the state of charge estimation is evaluated in Section 4.5. Here, the cycle-to-cycle variation and the influence of C-rate along with the effects of hysteresis are studied. Plotting the chosen signal properties as a function of excitation frequency and evaluating their correlation with the state of charge allows estimating roughly which excitation frequency is preferable for state estimation. Finally, in Section 4.7, a case study, employing a support vector regression in a data-driven machine learning approach to state estimation, is conducted with the selected features on seven different battery cells. Hereby, a proof of concept is provided and an estimate of the potentially achievable accuracy is established.

4.1 Electrochemical and post-mortem analysis of samples

Electrochemical and post-mortem analysis of the sample allows to characterize individual samples and estimate the mean properties of the studied batch. A variety of chemical and physical measurement methods are applied to study the chemical composition, balancing, occurrence of electrochemical processes, and thickness changes of the battery cells. This will, later on, enable relate the effects seen in ultrasonic signals to the electrochemical and mechanical behavior of the battery cells.

Disclosure: Youjin Shin performed some of the measurements, which are analyzed and presented within this section, as a part of her master thesis at Fraunhofer ISC. This master thesis was supervised by the author.

4.1.1 Capacity and impedance test

Before further processing, a check-up was performed. First, an initial CC-CV capacity test at 0.1 C was done. Cells were cycled between 3.0 V and 4.2 V with a constant current. For the constant voltage charging step, a cut-off current of 0.01 C was chosen. The voltage course during such cycles is plotted exemplarily for cell LDA019 in Figure 4.1. Here, charging and discharging half cycles are split and plotted versus (vs.) charging/discharging capacity.

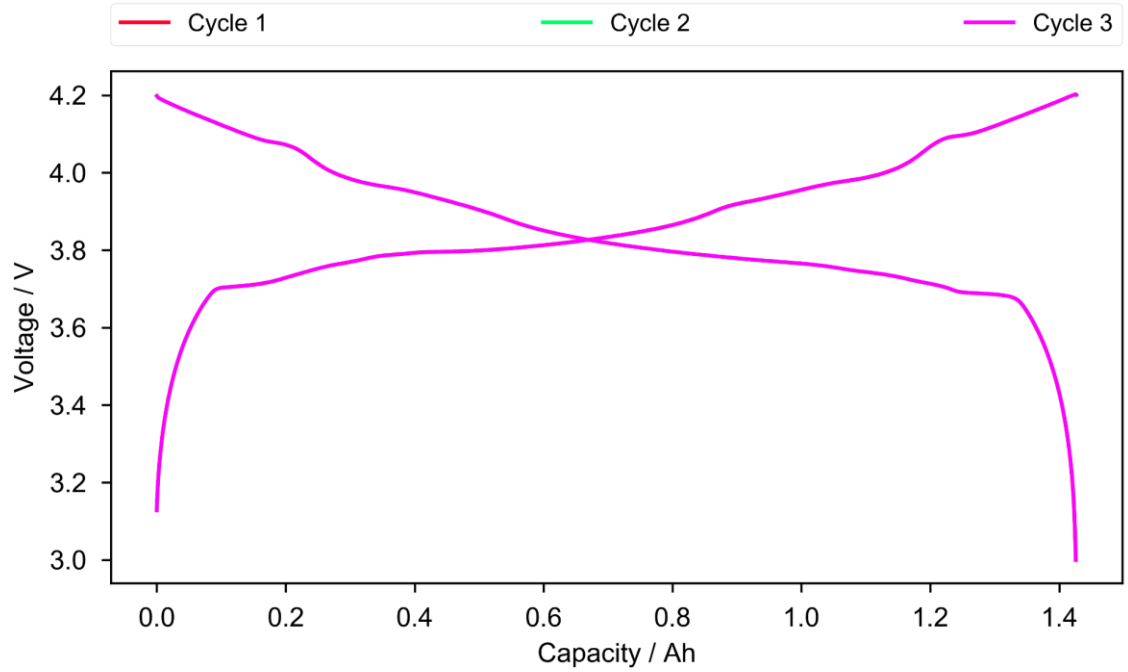

Figure 4.1: Cell voltage of cell LDA019 during the first three cycles of the initial capacity test during a check-up. Charging and discharging half cycles are split. During charging, the voltage rises from about 3.1 V after discharge and rest to 4.2 V. During charging the process is reversed with a cut-off voltage of 3.0 V. Within the plotted accuracy, the three cycles overlap undistinguishably.

The discharge capacity in the third consecutive cycle is taken as a measure of the experimental cell capacity and yields a mean of (1398 ± 22) mAh for 25 cells from the tested batch and a mean of (1411 ± 21) mAh for the seven cells studied in this work. Since the battery cells are designed for high current applications that lead to a reduced discharge capacity, a deviation of about 16.5% from the nominal capacity of 1200 mAh at this comparably small rate is within the expected range.

Additionally, the internal resistance of the battery cells was measured by electrochemical impedance spectroscopy (EIS). A 20 mV single sine frequency sweep from 200 kHz to 100 mHz with 12 points per decade was applied at 50% SoC. Three repetitions were averaged. As depicted in Figure 4.2, the imaginary part was plotted against the real part of the impedance and the intersection with the x-axis was taken as the internal high-frequency resistance (HFR) of the battery cell. The studied cells exhibit an HFR of (3.09 ± 0.22) mOhm. The part of the spectrum below the $-\mathrm{Im}(Z) = 0$ is associated with the inductance of the wires to the battery cell, its metallic components [34] and the tortuous porous, electrolyte filled structure – compare Chapter 2.4. The diameter of the half-circle varies from cell to cell, much more than the HFR does. It is assigned to the migration processes of lithium-ions through the SEI [34,228], the charge transfer resistance (CTR) [34,229], and the double layer capacitance (DLC).

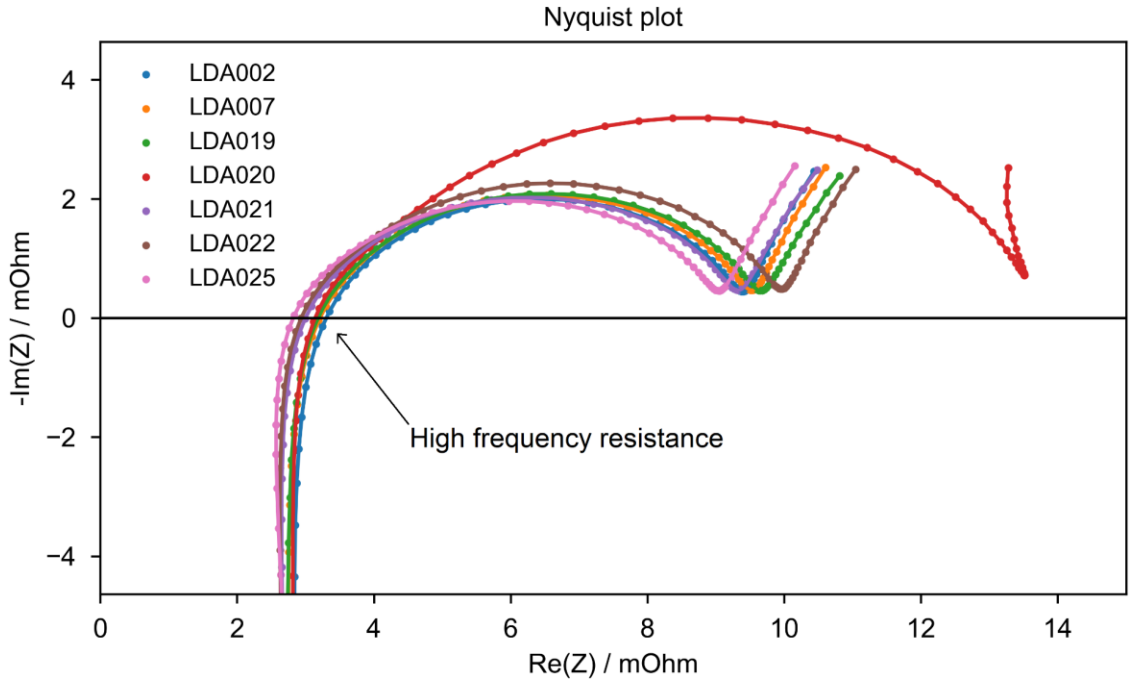

Figure 4.2: Nyquist plot of a selection of battery cells, studied by electrochemical impedance spectroscopy at 50% SoC with an amplitude of 20 mV in the frequency range from 200 kHz to 100 mHz. The solid line is meant as a guide for the eye. The intersection of the plotted lines with the x-axis marks the high-frequency resistance. Deviations in the diameter of the half-circle hint at differences in charge transfer resistance of the battery cells.

Regarding the half-circle, cell LDA020 is an outlier within the group of the seven chosen cells. This part of the frequency spectrum depends highly on SoC, SoH, and temperature [34,222]. Thus, this part of the spectrum might be most affected by a small variation in the battery's state or the experimental conditions.

4.1.2 Results of cell opening

Cells, prepared in charged and discharged state, were opened at 4.17 V and 3.33 V, respectively. Those states were prepared by constant current charging or discharging at 0.1 C until the respective cut-off voltage was reached and then held at constant voltage until the charging current decayed to 0.01 C. The stated cell voltages represent the relaxed open-circuit voltage. Cutting through and removing the pouch foil unveiled that the cell stack was assembled by z-folding. The stack, with the first layer of separator folded to the side, is shown in Figure 4.3 a). The outer electrode sheets are double-sided coated negative electrodes. As the outwards facing active material has no counterpart, it remains inactive during battery operation. A positive electrode at the lithiated state, coated onto aluminum, is shown in Figure 4.3 b). In Figure 4.3 c) and d), negative electrodes at delithiated and lithiated states are shown, respectively. The blueish black and reddish-gold color are typical for lithiated graphite at different lithiation degrees [245]. Looking at the uniformity of the colored area, a homogenous lithiation of the electrodes could be ensured, which is important for a reliable subsequent estimation of the lithium content by ICP-OES. The positive electrodes showed a dark black color, independently of lithiation. The number of layers was counted, the thickness and the geometric area of the individual components were measured. The results are listed in Table 4.1. The anode is designed to overlap the cathode by 0.5 mm in length and width, which is a best practice to account for limited stacking accuracy and to avoid lithium plating.

Table 4.1: Geometric dimensions and derived areal capacity of the cell components

	Anode	Cathode	Separator
Number of layers	34	33	68
Sheet thickness / µm	68.16 ± 0.66	66.99 ± 0.36	11.61 ± 0.26
Current collector thickness / µm	8.73 ± 0.18	16.02 ± 0.46	/
Coating thickness (one side) / µm	29.71 ± 0.34	25.49 ± 0.29	/
Coated area (one side) / cm^2	17.02 ± 0.31	16.61 ± 0.31	/
Total coated area (used) / cm^2	561 ± 10	548 ± 10	/
Nominal areal capacity / $mAh \cdot cm^{-2}$	2.139 ± 0.038	2.190 ± 0.040	/
Experimental areal capacity / $mAh \cdot cm^{-2}$	2.492 ± 0.059	2.551 ± 0.061	/

The experimental areal capacity of about 2.5 mAh/cm^2 can be considered comparably high and puts the battery cells in between the categories of high energy (3 mAh/cm^2 to 4 mAh/cm^2) and high power density (1 mAh/cm^2 to 2 mAh/cm^2) [20,26,246].

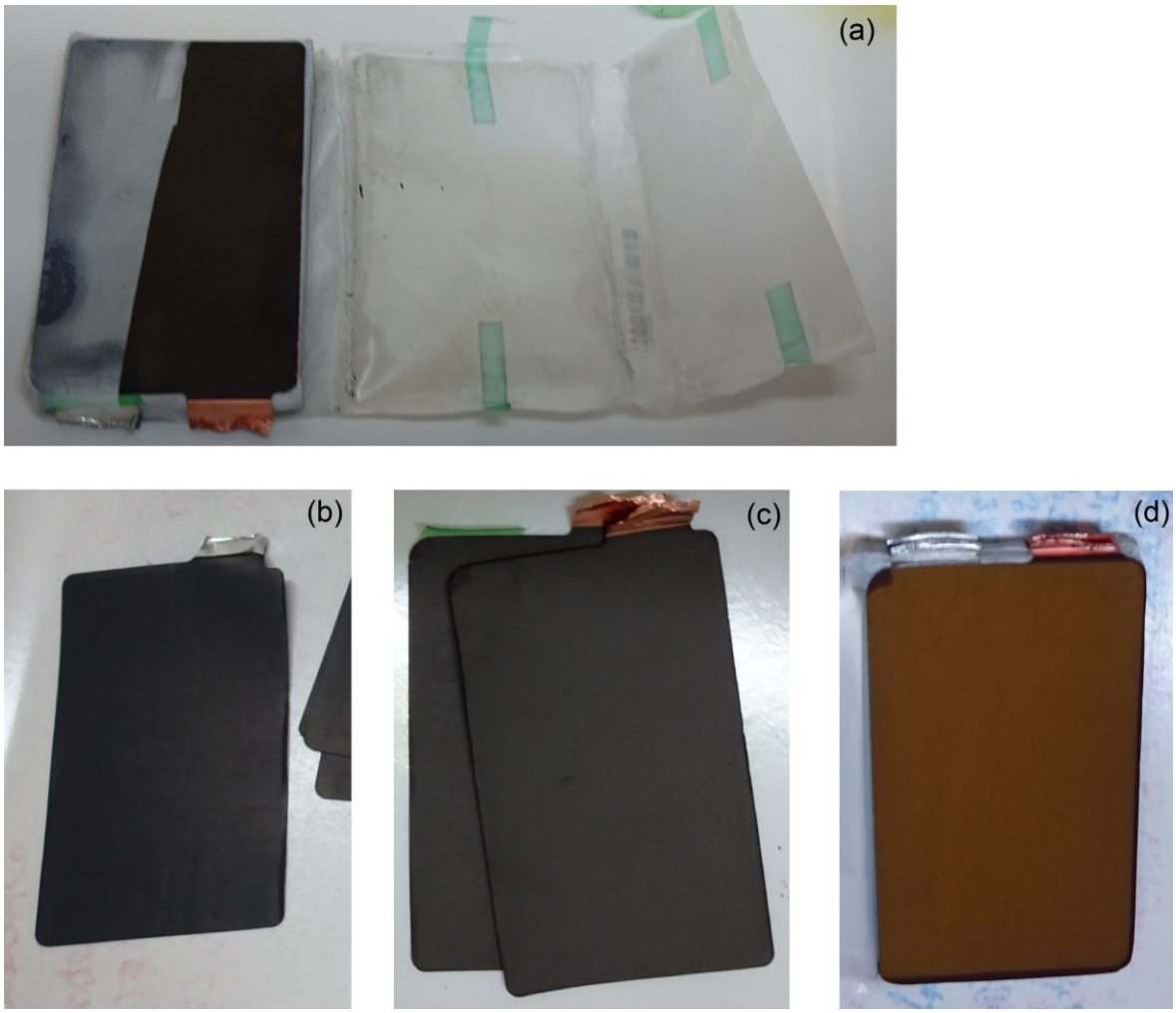

Figure 4.3: Pictures of battery cell components, harvested from cells PM1060-17 and PM1087-17. (a) Z-folded stack, with the first enveloping layer of separator, removed. (b) Positive electrodes at lithiated state. (c) A negative electrode at delithiated state. (d) A negative electrode at lithiated state, exhibiting reddish-golden color, which is typical for the stage 1 to stage 2 transition of lithiated graphite. Images used with kind permission of Youjin Shin.

4.1.3 Results of post-mortem interrogation

ICP-OES allows the analysis of the atomic contents of a solution, prepared from defined pieces of electrode sheets, as described in Chapter 3.2. The element-specific amount of substance is compared at charged and discharged states, as depicted in Table 4.2. Hereby, the range of lithiation degree, at which the electrodes are utilized during operation, can be estimated. Due to washing of the electrodes and thereby removing electrolyte residues, all lithium and all cobalt in the positive electrode solution can be assigned to the active material

$LiCoO_2$. It can be assumed that before formation, the active material was fully lithiated with $x = 1$ in Li_xCoO_2. Subsequently, one can conclude that about 7% of the initial lithium remains in the negative electrode with the battery cell being fully discharged. For the negative electrode, not all lithium and all carbon detected in the solution can be assigned to the active material. During formation, a consumption of up to 10% of the initially in the positive electrode available lithium by the SEI buildup and by other irreversible processes during the first lithiation of graphite is expected [247–250]. Depending on electrode slurry composition, some of the carbon detected in the solution has to be assigned to styrene-butadiene rubber (SBR) binder and a conductive agent. In the safety data sheet, the mass share of each chemical is stated. The SBR is at 1.5% and the graphite at 18% of the total battery mass [232]. Assuming a carbon-based conductive additive content of about a tenth to a third of the binder content, the correction of the lithium content of the negative electrode can be estimated, as stated in the table below. Note that this correction does not account for potentially unconnected active material particles, which are inactive in the electrochemical processes but still contribute to the mass in the chemical analysis [8].

Table 4.2: Amount of substance ratios within electrodes as estimated by ICP-OES

	Battery cell state at cell opening	
Negative electrode	discharged	charged
Amount of substance ratio Li:C	0.1307 ± 0.00023	0.1446 ± 0.0018
x in Li_xC_6	0.0784 ± 0.0014	0.868 ± 0.011
x in Li_xC_6 (corrected by SBR content)	0.0856 ± 0.0011	0.956 ± 0.011
Positive electrode	discharged	charged
Amount of substance ration Li:Co	0.9300 ± 0.0034	0.41258 ± 0.00014
x in Li_xCoO_2	0.9300 ± 0.0034	0.41258 ± 0.00014

Three electrode lab cells were constructed from the harvested battery materials as described in Chapter 3.2. A formation procedure with five cycles at 0.1 C was performed prior to the cycle, depicted in the following three figures. The results from one of three cells are shown exemplarily. To achieve a good resolution in the incremental capacity analysis the depicted cycles were performed at 0.03 C between the voltage bounds, specified by the parenting battery cell's specification. Figure 4.4 depicts the cell voltage and the individual electrode potentials vs. Li/Li^+ reference during a full cycle plotted as a function of SoC. The cell voltage of the lab cell exhibits the same course as the cell voltage of the parenting cells – see Figure 4.1. The features in the cell voltage's course can be traced back to the features in the individual electrode potentials, as it is calculated from the difference of the two.

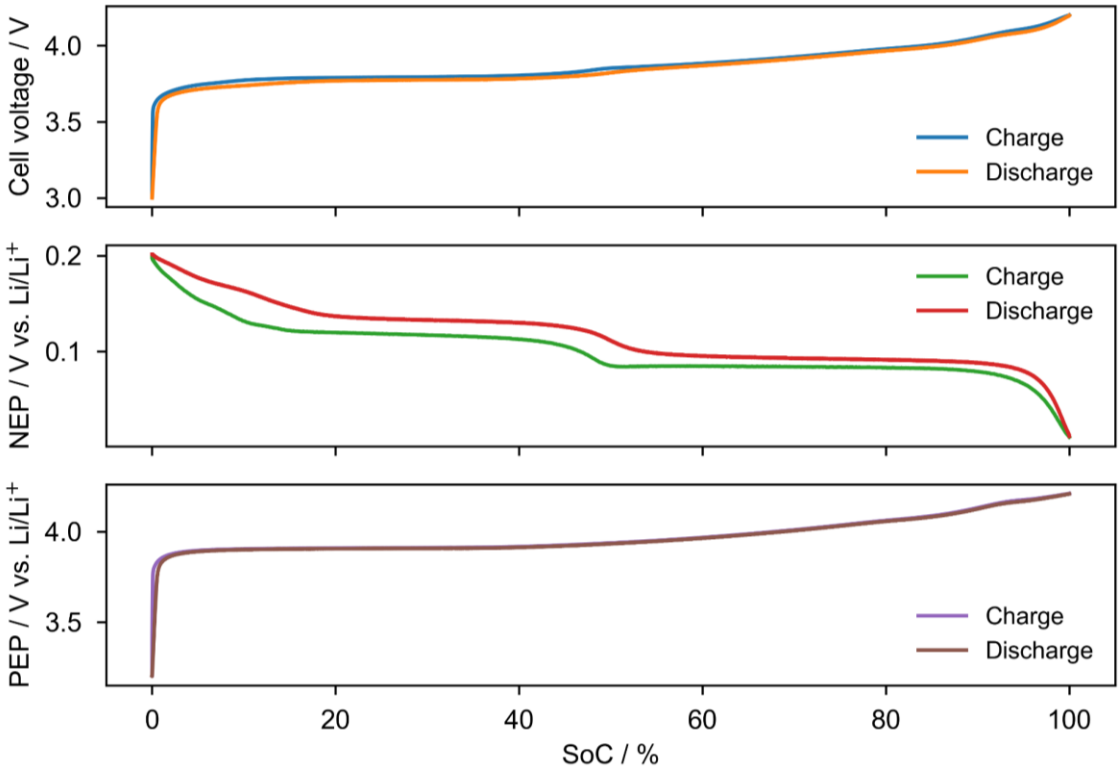

Figure 4.4: (top) Cell voltage, (center) negative electrode potential (NEP), and (bottom) positive electrode potential (PEP) of a three-electrode laboratory cell as a function of the state of charge (SoC). The lab cell was constructed from electrodes that were harvested from a pouch cell (PM1060-17) of the type studied in this work. Charge and Discharge refer to the respective process in the full cell. Subsequently, the positive electrode is depleted during charge and the negative electrode during discharge.

The negative electrode potential (NEP, center plot in Figure 4.4) exhibits two distinct steps that can be assigned to the transition between the three stages of the highest lithiation of graphite. In the 0% to 20% SoC range, one additional shoulder is present. As suggested by the ICP-OES measurements on the charged battery cell, the graphite electrode is utilized almost completely, visible in the NEP approaching the lithium plating potential at 100% SoC. The positive electrode potential (PEP, bottom plot in Figure 4.4) is characterized by a long plateau around 3.7 V with a transition into a steeper slope which incorporates a small shoulder around 90% SoC. Around 0% SoC, the PEP drops down to about 3.2 V, which is expected for a high degree of lithiation as indicated by the ICP-OES measurements on the discharged battery cell. The observations are in good agreement with the potential courses found in the literature for the active materials graphite [10,251–253] and lithium cobalt oxide [8,254], stated as main components in the battery cell's safety data sheet [232].

The derivatives of the cell voltage and individual electrode potentials are shown in Figure 4.5. This incremental capacity analysis exhibits peaks at voltages where the plot of voltage vs. SoC in Figure 4.4 exhibits a plateau. The position of those peaks allows one to identify

the phase transitions occurring in the utilized range of lithiation degree of the active materials. Also, by comparing the individual electrode potential derivatives an assignment of peaks in the cell voltage derivative to one of the electrodes becomes feasible. This was done in Figure 4.5. The peaks in the electrode potentials are named from left to right, with a leading letter indicating positive or negative electrodes. While considering the distance of peaks, the overlap of N2 and P1 peaks in the derivative of the cell voltage can be estimated by the method of elimination.

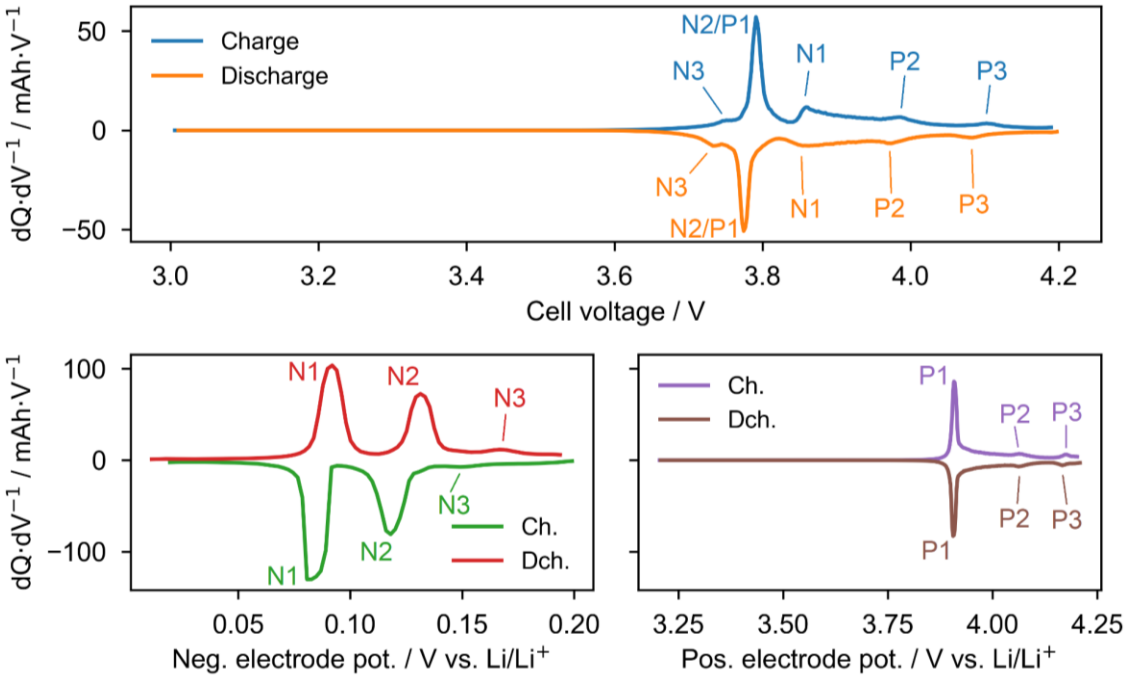

Figure 4.5: Incremental capacity analysis of cell voltage and individual electrode potentials plotted vs. cell voltage or electrode potential, respectively. The peaks in the derivative of the cell voltage are assigned to the peaks in the derivative of the individual electrode potentials. The lab cell was constructed from electrodes that were harvested from a pouch cell (PM1060-17) of the type, studied in this work. Charge and discharge refer to the respective process in the full cell. Subsequently, the positive electrode is depleted during charge and the negative electrode during discharge.

Additional to the plot of the derivatives vs. potential (in Figure 4.5), the plot of the derivative vs. SoC, as shown in Figure 4.6, allows one to identify which phase transitions occur within a certain SoC range in the individual electrodes [8]. Note that due to opposite correlations of the individual electrode potentials with cell SoC, the derivative of the potentials for charging and discharging have opposite signs, e.g., don't appear in the same quadrant of the plot. In the top row, it can be seen that the most dominant peak in the derivative of the cell voltage is a result of a superposition of the N2 and P1 peaks. The bottom row shows the individual electrode potential derivative. Taking the results of ICP-OES measurements into account, the lithium content of the active materials between 0% and 100% SoC can be

estimated. In LCO, *x* in Li_xCoO_2 ranges between 0.93 and 0.41. In graphite, *x* in Li_xC6 ranges between 0.08 and 0.96. For, e.g., 50% SoC, *x* takes values of 0.67 and 0.52 in LCO and in graphite, respectively. The negative electrode shows the utilization of the N1 peak for SoC > 48% ($x \geq 0.50$) and the utilization of the N2 and N3 peak for SoC < 45%. For the positive electrode, the P1 peak is present below 40% SoC ($x = 0.72$) and the P2 and P3 peaks occur around 82% SoC ($x = 0.51$) and 95% SoC ($x = 0.44$), which correspond to the lithium depleted state of $LiCoO_2$.

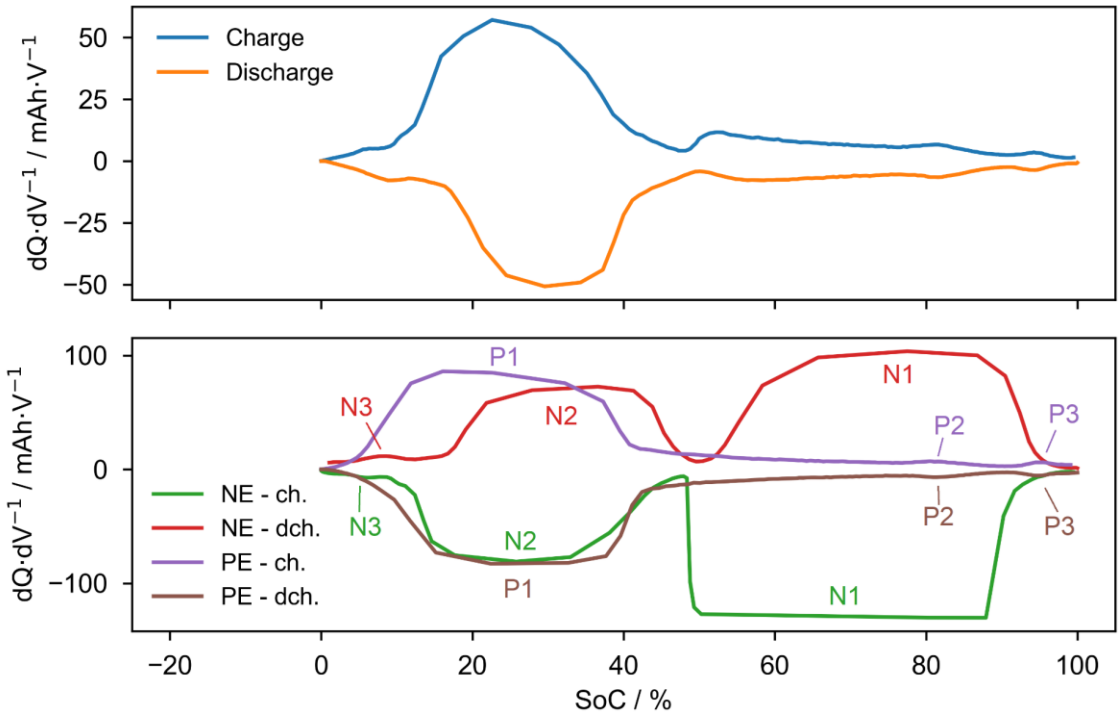

Figure 4.6: Incremental capacity analysis of cell voltage and individual electrode potentials plotted vs. state of charge (SoC). The peaks of the individual electrodes are annotated with the same names as in Figure 4.5 to ease comparison. The lab cell was constructed from electrodes that were harvested from a pouch cell (PM1060-17) of the type studied in this work. Charge and Discharge refer to the respective process in the full cell. Subsequently, the positive electrode is depleted during charge and the negative electrode during discharge.

The procedure, shown in the last three figures, was performed for three individual lab cells. The hereby estimated peak positions were averaged individually for charge and discharge and are displayed with the standard deviation specified as uncertainty in Table 4.3. The phase transitions associated with the peaks in the incremental capacity analysis are assigned to phase transitions, exhibited by the active materials as specified in the cited literature – compare the reference column, and the description in Chapter 2.1.1.

Table 4.3: Peak positions in incremental capacity analysis. Mean values with standard deviation stated as uncertainty are estimated from three individual laboratory three-electrode cells, constructed from an unaged battery cell.

Peak	Charge	Discharge	Transition	Reference
Negative electrode				
N1	(82.10 ± 0.52) mV	(92.17 ± 0.15) mV	Stage 2 → Stage 1	[251,253,255,256]
N2	(118.10 ± 0.50) mV	(131.87 ± 0.45) mV	Stage 2L → Stage 2	[11,251,253,255,256]
N3	(149.60 ± 0.96) mV	(167.03 ± 0.51) mV	Stage 4 → Stage 2L	[251,253,255]
Positive electrode				
P1	(3908.43 ± 0.32) mV	(3906.77 ± 0.47) mV	I → II (hex.)	[8,254,257,258]
P2	(4067.17 ± 0.42) mV	(4064.53 ± 0.21) mV	Hex. → Mono.	[8]
P3	(4175.1 ± 1.1) mV	(4167.07 ± 0.55) mV	Mono. → Hex.	[8]

The negative electrode's potential derivative exhibits three peaks. Those can be associated with the first-order phase transitions between stages of the lithium intercalation in graphite. Dahn *et al.* [256] showed that in a graphite electrode more than two phases coexist if the system is not at equilibrium. Therefore, a strict assignment of lithium content ranges to stages or phase transitions is solely meaningful at ideal conditions. In practical scenarios, the boundaries might thus not be as sharp as suggested by the cited literature. Peak N1 is ascribed to the transition between stage 2 and stage 1 [251], where $0.5 \leq x \leq 0.95$ in Li_xC_6 [251]. Peak N2 is assigned to the transition between the dilute stage 2L and stage 2 [251], where $0.33 \leq x \leq 0.50$ in Li_xC_6 [11]. Instead of the potentially expected stage 3, a liquid-like dilute stage 2L is present in electrochemically intercalated lithium, since stage 3 is an ordered phase, solely occurring at low temperatures [11]. Peak N3 is subsequently associated with the transition between stage 4 and stage 2L [251], where $\sim 0.24 \leq x \leq 0.33$ in Li_xC_6 [251,259,260]. Within the lithium content range $0.085 \leq x \leq 0.956$, estimated by the ICP-OES measurements, two other transitions are expected – from stage 5 to stage 4 for $0.17 \leq x \leq 0.24$ [259] and from stage 8 to stage 4 for $0.08 \leq x \leq 0.17$ and at 210 mV vs. Li/Li^+ [251]. But no matching peak was uncovered in the displayed data. Peaks N1 through N3 match very well with the peak positions estimated during lithiation and delithiation by the

intermittent current technique as studied in [251]. The study by Reynier *et al.* [253], which uses a similar technique and an electrolyte solution comparable to the one used in this work, also confirms the position of the peaks associated with the described phase transitions.

The main peak P1 of the positive electrode is assigned to the first-order phase transition between hexagonal phases I and II occurring at 3.93 V vs. Li/Li^+ for LCO according to [8,254,257,258]. This is the transition between the metallic and the semiconducting phases in hexagonal symmetry [8,257] of Li_xCoO_2 with $0.75 \leq x \leq 0.93$ and is associated with a significant expansion of the c-lattice parameter in the hexagonal unit cell [8,258]. The two distinct peaks P2 and P3 above 4.0 V vs. Li/Li^+ are ascribed to a transition between ordered and disordered lithium-ions within the lattice and a transition between hexagonal and monoclinic symmetry [8]. The lithium content *x* is estimated to be slightly above and below 0.5 at 0.45 and 0.55 for those two peaks [8]. Reimers and Dahn measured the peaks' positions to 4.07 V and 4.19 V, respectively [8]. Deviations in the experimentally determined position of the peaks from the values stated in literature can be associated with differences in the experimental parameters, especially regarding electrolyte – a 1M $LiClO_4$ in PC:EC solution, and the study of the first cycle after cell assembly [8] in contrary to the sixth cycle shown within this work. The voltage drop associated with a finite current along with the internal resistance of the lab cell also contributes to deviations [8].

Combining the results of ICP-OES and incremental capacity analysis allows one to conclude that the LCO positive electrode is utilized in the lithiation range $0.413 \leq x \leq 0.930$ and thus is the capacity limiting electrode. The graphite negative electrode is not fully utilized with *x* being in the range $0.085 \leq x \leq 0.956$, which was probably a design choice to avoid lithium plating during fast charging – the cell is specified up to 2.0 C charging.

4.1.4 Dilatometer experiments to evaluate volume change during cycling

The thickness change of pouch cell was measured by a mechanical dial indicator during several cycles at different C-rates to estimate the relative and absolute volume and thickness change of the studied battery cells due to (de-)intercalation of lithium in the host structure of the active materials. The cell thickness change of one of the studied battery cells during the second cycle at a given C-rate, ranging from 0.1 C to 1.0 C is depicted in Figure 4.7.

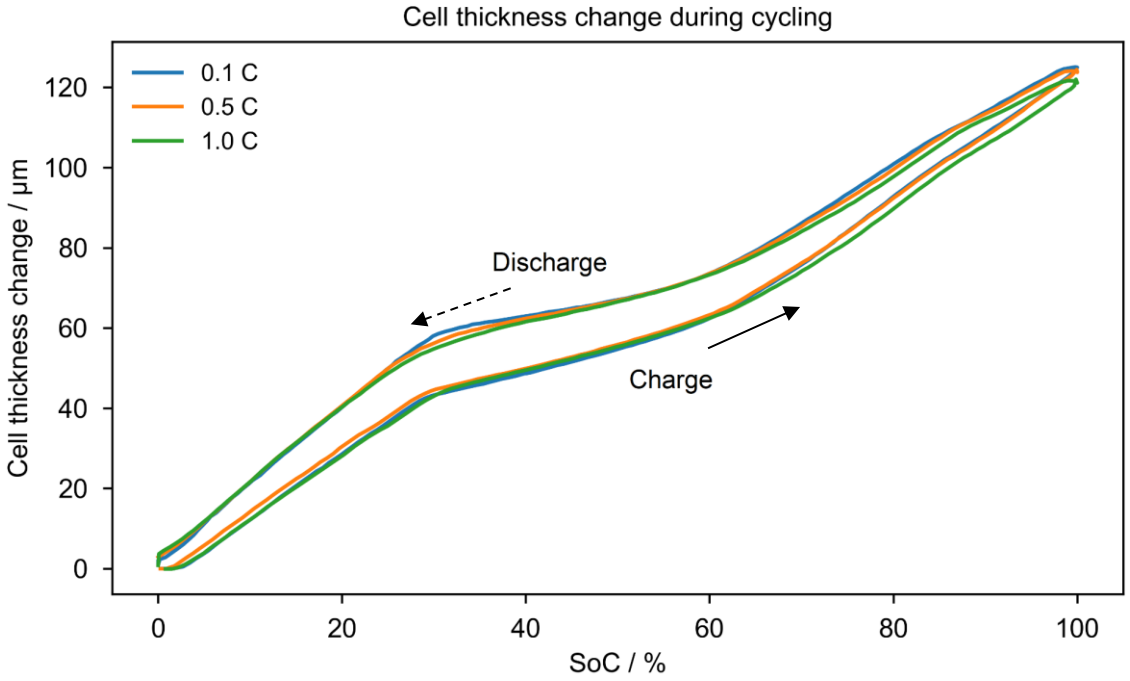

Figure 4.7: Cell thickness change of one of the studied pouch cells (PM1082-17) during cycling at different C-rates. The second cycle at a given C-rate is displayed in the figure. The course of the plot can roughly be divided into three sections of different slopes. Those can be associated with different phase transitions that are shown in Figure 4.6.

In general, the depicted curves can be split into three sections of different slopes with the first section reaching about 30% SoC, the second until about 60% SoC and the third making up for the remaining up to 40% SoC. The absolute thickness increase, as well as the charge capacity (not shown in the plot), varies slightly with C-rate, which is visible at 100% SoC through a decreasing position of the maximum with C-rate. The values of maximum charge capacity and associated thickness increase along with the mean thickness increase per capacity are listed in Table 4.4. The latter yields values from 0.091 µm/mAh to 0.094 µm/mAh. An increase with C-rate is expected due to the diffusion-limited equilibration of lithiation gradients within the active material particles. The outer shell of the particles is lithiated first and thus reaches a higher degree of lithiation than the core of the particles [20,104,261]. The diffusion of lithium-ions into the core of the particle and the thereby created displacement of the border between stages of lithiation is a slow process, particular slower than the lithiation at high C-rates. Since higher stages are associated with a larger volume increase, the mean volume increase is larger if the equilibrium has not yet been reached and thus a larger volume share of the particles is in a higher stage of lithiation, even so, the mean lithium content of the particles would be associated with a lower stage. On the other hand, different studies discussed that the differences in volume expansion might be a result of thermal expansion associated with the substantial heating at high

currents [20,99,100]. One could conclude that during relaxation, after the application of a current both, thermal expansion and expansion due to lithium gradients, undergo relaxation. Oh *et al.* showed that in their case the thermal expansion provides the dominant share [20,98]. In this work, no excess cell thickness increase due to thermal expansion could be witnessed. Table 4.4 even shows that at 1.0 C the total thickness increase of the battery cell was smaller than at lower C-rates. But still, small differences between cycles at different C-rates exist in the shape of the curves. The general trend observed here is that the difference in slope of the described sections reduces with C-rate.

By comparing Figure 4.7 with Figure 4.6, it is possible to roughly assign the sections of different slopes to phase transitions in the active materials. The first section's slope can be attributed to the P1, N3, and N2 peaks. In the associated voltage range, both negative and positive electrodes, exhibit phase transitions causing changes to crystallographic unit cell volume and mechanical properties of the active materials. Differences in charge and discharge half-cycle are visible in both figures – compare the SoC range in which the N2 peak is present in Figure 4.6 with the position of the kink after the first section in Figure 4.7. The second section with the lowest slope seems to be affected by the decaying P1 peak and N1 peak increasing in intensity. The final section with a slope comparable to the first section's slope is expected to be affected from the N1 peak in conjunction with the P2 and P3 peak, associated with the monoclinic/hexagonal symmetry transition in the LCO.

Table 4.4: Maximum values of thickness increase and charge capacity in the second cycle at a given C-rate for an exemplary battery cell (PM1082-17) of the type studied in this work.

C-Rate	0.1 C	0.5 C	1.0 C
Charge capacity / mAh	1371	1336	1302
Thickness increase at 100% SoC / µm	125.1	124.4	122.0
Mean thickness increase per capacity / µm·mAh^{-1}	0.091	0.093	0.094

4.1.5 Summary of this subchapter

This subchapter employed electrochemical techniques and destructive post-mortem methods to interrogate the structure of the battery cells, studied in this work. Initial tests revealed a standard deviation of about 1.5% from the mean capacity of (1411 ± 21) mAh and a spread of 7.1% in high-frequency resistance. Cell opening and measuring the active electrode area yielded an experimental areal capacity of about 2.5 mAh/cm^2, which places the battery cells in between the categories of high energy (3 mAh/cm^2 to 4 mAh/cm^2) and high power density (1 mAh/cm^2 to 2 mAh/cm^2) [20,26,246]. Thus the studied cells can be

considered hybrid and the results from this work should be transferable to other battery cells of either category. A chemical analysis employing ICP-OES confirmed the active materials to be graphite within the negative electrode and lithium cobalt oxide in the positive electrode. The behavior exhibited by this material system can be taken as a representative of up-to-date battery cell chemistries, still involving a dominant share of graphite on the negative electrode and a positive active material such as NCM, with a similar crystal structure as LCO. ICP-OES also unveiled the lithiation range in which the active materials are utilized, which in combination with an incremental capacity analysis allowed assigning electrochemical processes such as phase transitions and staging processes to certain sections of the full SoC range. Finally, dilatometry was performed to quantify the cell thickness change of the battery cells during cycling. A reversible total thickness increase of 1.8% during charging was observed which did not vary significantly with C-rate – only about 2% when cycling with 1.0 C compared to cycles at 0.1 C. Therefore, the relevance and order of magnitude of the thickness change for changes in the time of flight of ultrasonic pulses through the studied battery cells are established.

4.2 Development of the measurement setup

Having a potential mobile or automotive application in mind, disc-shaped piezo elements, acting as the transducer, were mounted to battery cells. For reproducible and reliable measurements, a distinct development of the measurement setup was needed. The shielding of the piezo elements and the wiring plays an important role when it comes to signal quality. In addition, the coupling of the piezoelement to the battery cell will be discussed in the following section. The exact procedure to achieve this setup is described in Chapter 3.4.

4.2.1 Verification of shielded piezo elements mounted on battery cells

To unveil the influence of electromagnetic shielding the piezo elements and the interplay with the multilayer pouch foil, a test with dummy cells - samples of typical battery cell dimensions made from poly-oxy-methylene (POM - chosen due to similarity in mechanical properties – an elastic modulus of about 2.8 GPa - and density of about 1.4 g/cm^3 [262]) was performed. One of the test bodies was packed in a pouch bag, sealed at 50 mbar, which is also the residual pressure in a pouch type lithium-ion battery cell. To both test bodies, one centrally placed shielded piezo element was attached on each side. Another non-shielded piezo element was placed at one-quarter of the length of the test body on both sides. The resulting configuration can be seen in Figure 4.8. Epoxy resin was chosen as an

agent to couple the piezo elements based on its good electrical insulation properties and hardness which ensures a good mechanical coupling between the piezo element and the battery cell [263].

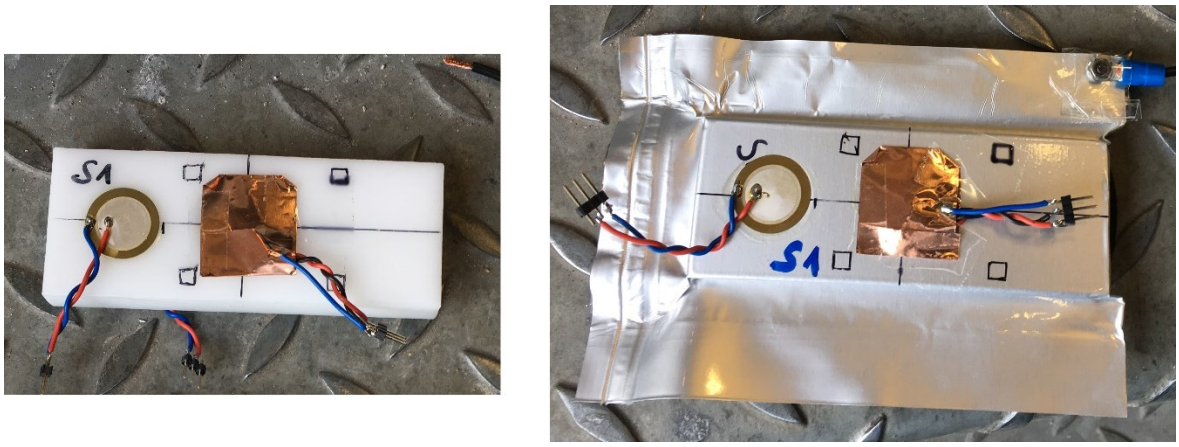

Figure 4.8: Pictures of plastic dummy samples to test the effect of shielding the piezo elements and to test the influence of pouch foil. (Left) unmodified dummy, (right) pouched dummy of the same size. On the back of both samples, piezo elements were placed in the same configuration as in the front. “S1” marks the unmodified piezo elements glued to the surface of the sample, the other piezo elements were shielded by an envelope made from copper foil glued to the piezo elements and the sample.

Raised cosine (RC_n) pulses with *n* oscillations at frequencies between 50 kHz and 250 kHz were used for excitation on each of the piezo elements, the resulting transmitted signals at the other piezo elements attached to the test body were recorded. The exciting waveform and the resulting through transmission (recorded by the directly opposite piezo element) through a battery cell (top right), and the afore-described test bodies (bottom row) are shown in Figure 4.9.

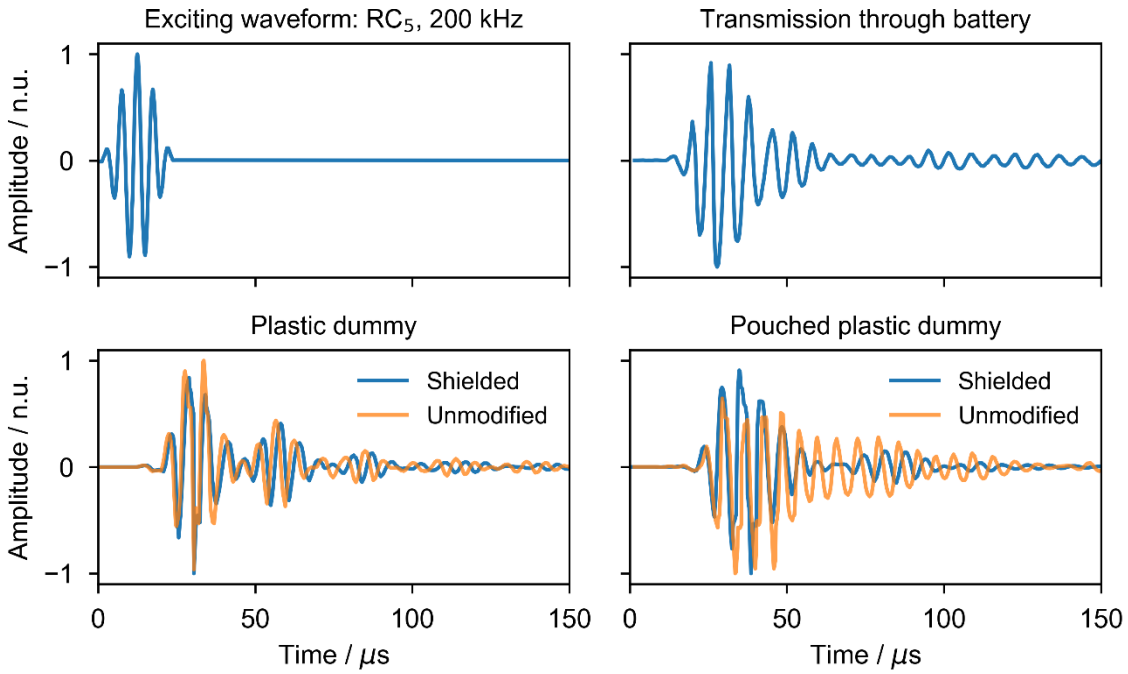

Figure 4.9: Exciting waveform and resulting transmission signals under variation of sample preparation and type. (Top left) Raised cosine waveform at 200 kHz used to excite ultrasonic pulses, and (top right.) transmission signal through a battery following such pulse with shielded piezo elements. (Bottom left) Transmission signals through the bare plastic dummy, and (bottom right) through the pouched plastic dummy as in Figure 4.8.

In Figure 4.9 at 200 kHz, one distinct wave package is observable in the transmission signal through a LIB (compare top right plot) with a shoulder, presumable originating from a second wave package overlying at around 50 µs. The transmission signals through the bare plastic dummy (compare bottom left plot in Figure 4.9) show very similar signals in the case of the unmodified (orange line) and shielded piezo elements (blue line). Three distinct wave packages are observable. Differences in the time of flight/arrival time of those wave packages may originate from differences in positioning of the piezo elements (centered vs. closer to the edge). Several options for the propagation of ultrasound in battery cell materials and geometry were discussed in Chapter 2.2. The transmission signals through the pouched plastic dummy (blue line in the bottom right plot in Figure 4.9) show two distinct wave packages in the case of the shielded piezo elements. The unmodified piezo elements (orange line) show a superposition of some slowly fading oscillation after the arrival of the first wave package and thus make the distinction of wave packages impossible. Therefore, shielding of the piezo elements, at least on the receiving side is necessary. An explanation of how the distortion, leading to the slowly fading overlay in the signal, propagates from the actuator to the sensor is given in Figure 4.10. In the upper row, batteries with mounted piezo elements are depicted. One of the two piezo elements on each battery is connected to the signal generator, the other one is connected to the input of the measurement device, which

is implemented as a differential amplifier feeding an analog to digital converter (ADC). The left column shows the case of an unmodified piezo element glued to the pouch foil of the battery cell, whereas the right column shows the shielded element. A piezo element is basically a capacitor with a piezoelectric material as the dielectric. Thus, by applying a voltage between its two plates, an electrical field is established and charge carriers flow onto the plates. The pouch foil is a multilayer compound with an aluminum layer in the middle. On to this, a mirror charge can be induced by the charge on the plates of the piezo element. Therefore, the pouch foil exhibits an electric potential. By forming a continuously connected enclosure around the pouched body – at least if one side is folded and the others are welded, the pouch foil serves as a medium to transport this electromagnetic interference from one side to the other and thus from the sending to the receiving piezo element.

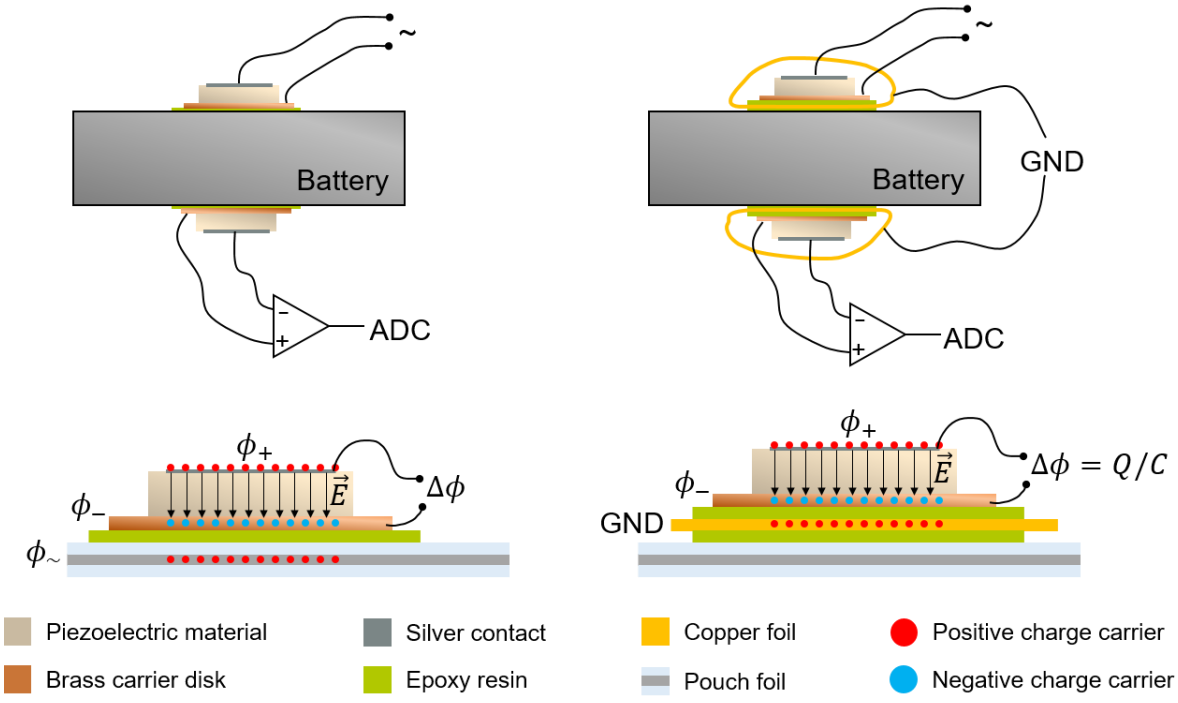

Figure 4.10: Schematic of batteries with piezo elements glued onto the pouch foil to act as ultrasonic transducers and schematic on capacitive crosstalk/coupling and countermeasures. (Left column) Piezo elements unmodified, (right column) piezo elements shielded by a copper envelope. If the piezo element is shielded, the mirror charge induced by the charge on its capacitor-like plates is grounded and therefore does not induce any potential on the pouch foil, which would be sensed by the receiving piezo and would superimpose the acoustic signal.

This problem occurs at high frequencies, densely packed spaces, and high voltages in commonly found applications, mostly communication electronic devices (mobile phones, laptops, etc.), where sensitive electrical components are shielded with thin metal plates from external and internal sources of interference. The disclosed setup, shown in the right column of Figure 4.10, uses the same working principle. In between piezo element and

pouch foil, a copper foil is introduced, insulated by a layer of epoxy resin each against the bottom plate of the piezo element and the pouch foil. By grounding the copper envelope, folded around the piezo element, charge carriers, induced by internal and external sources are led away. Thereby, preventing a superposition of the acoustic signal and electromagnetic interferences.

4.2.2 Impedance spectroscopy of piezo elements

The before described manual procedure introduces an additional source for unwanted variation in the experiment. Therefore, the impedance spectra of all piezo elements are measured and checked for abnormal features after mounting them to the sample. 1000 points in a frequency range of 1 kHz to 1 MHz were scanned at an amplitude of 20 mV. The data presented in Figure 4.11 is collected from the piezo elements of the type specified in Chapter 3.4, mounted on six different battery cells using the previously described procedure. The geometric dimensions of the piezo element are stated in the data sheet – see Table 3.3. From the thickness and diameter of the piezoelectric disc, the resonant frequencies in air can be estimated based on an assumption of the longitudinal (4000 m/s) and transversal (2000 m/s) sound velocities in the unknown, most likely ceramic, piezoelectric material. The radial resonance frequency can be calculated to be (133.3 ± 2.7) kHz and (66.7 ± 1.3) kHz, for longitudinal and transversal propagation, respectively. The resonance frequency for the thickness oscillation can be estimated to be (13.3 ± 4.4) MHz and (6.7 ± 2.2) MHz, for longitudinal and transversal propagation, respectively. These calculations have to be corrected for the mass coupling of the piezo element to its brass base, which inhibits a slower speed of sound and introduces additional uncertainty. By coupling the piezo element to the mass of the sample by attaching it to its surface, the resonant behavior of the piezo element is expected to change [218].

In Figure 4.11 the results of impedance spectroscopy on 15 piezo elements are compared. 14 out of the 15 compared frequency spectra show similar behavior. Shown in the inset, one peak can be identified in the region between 130 kHz and 150 kHz with a variation in height and width. Furthermore, the real part of the impedance asymptotically rises approaching 1 kHz. Besides the main peaks, higher-order harmonics, e.g., at three or five times the main resonance frequency can be seen in a detailed view (not shown here). One of the spectra, plotted as a blue line and annotated by an arrow, differs from this behavior in peak shape, and overall shape, showing distinct discontinuities and steps in its course.

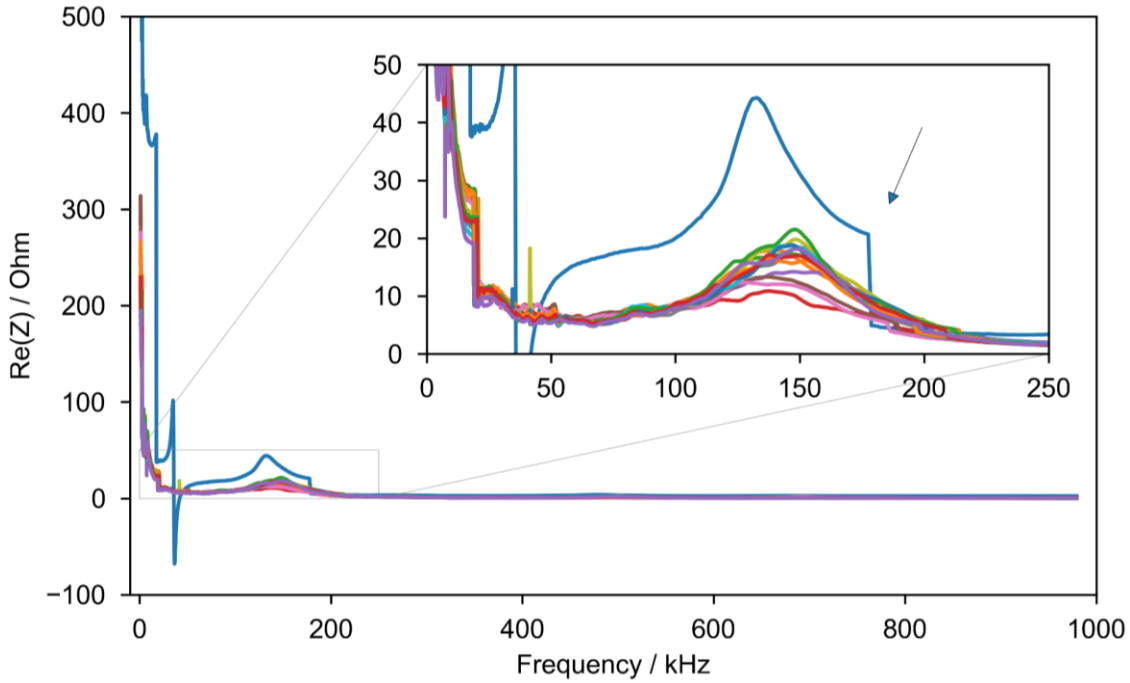

Figure 4.11: Resonant behavior of individual piezo elements attached to LIB pouch cells (LDA002 through LDA025, as listed in Figure 4.2), estimated by impedance spectroscopy. The inset shows the main resonant peak at 143 kHz for the piezo elements firmly attached to the batter cells. The dark blue line, annotated with an arrow, shows the spectrum of a piezo element that had detached during the manufacturing process, which was identified by the impedance spectroscopy through differing resonant peak shapes, a resonance frequency of 135 kHz, and a large jump in the spectrum. This resonance frequency complies with the longitudinal resonance frequency of the piezo element, oscillating radially in air.

Standing out by this abnormal spectrum, the sensor stack in question was visually inspected and was found to have peeled off from the battery cell. This, freely oscillating piezo element, exhibits a resonance frequency of 132.8 kHz, complying well with the radial resonance frequency calculated for the longitudinal propagation in a ceramic piezoelectric disc with the dimensions of the employed type. The same data is presented in the Nyquist plot on the right side of Figure 4.12 along with a descriptive statistic excluding the peeled-off piezo element, on the left.

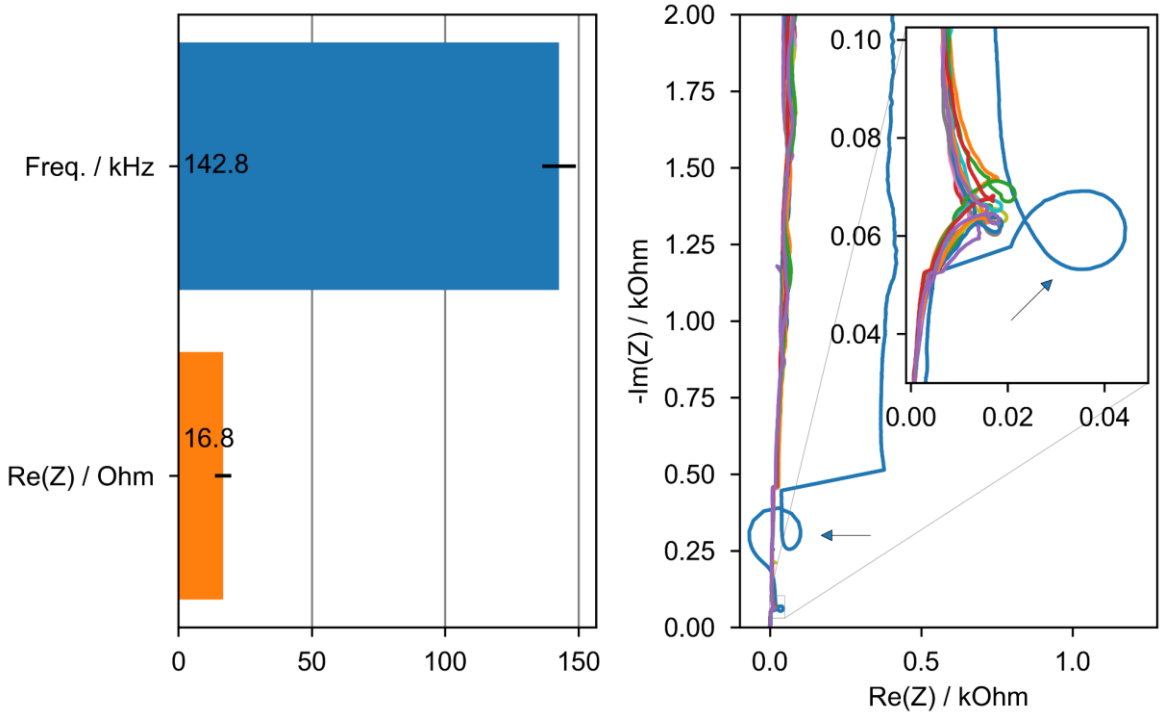

Figure 4.12: Descriptive statistic on resonant behavior of piezo elements and Nyquist plot of the impedance spectra in Figure 4.11. (Left) Peak frequency, and peak amplitude, with the standard deviation of the main resonant peaks in Figure 4.11. (Inset). In the Nyquist plot, the mostly capacitive behavior of the piezo elements becomes visible, except for the characteristic circular course at resonant frequencies. The inset shows the frequency range around the main resonant peak at 143 kHz. From the circular shape, it can be judged how symmetrical the oscillation of a piezo element is. An arrow annotates the spectrum of the detached piezo element, which is excluded from the statistic.

The Nyquist plot allows identifying how symmetrical a piezo element oscillates, as shown in the inset. Since the piezo elements used in this work are not specifically designed for the purpose which they are here used for, inhomogeneity in thickness and diameter can be expected. Furthermore, manually contacting the piezo element with a soldering point on the top introduced an additional mass, potentially off-center, affecting the resonant behavior. This could explain the variations in the shape, position, and height of the peaks depicted in Figure 4.11, as summarized in the descriptive statistic (Figure 4.12, left side). The averaged quantities are estimated to (142.8 ± 6.3) kHz for the resonant frequency and (16.8 ± 3.0) Ohm for the peak height.

4.2.3 Summary of this subchapter

In this subchapter, the process to manufacture sensor stacks from piezo elements and to attach them as ultrasonic transducers to the faces of battery cells was presented. This manual process involves the screen-printing of adhesive layers and the electromagnetically shielding of the piezo elements. The developed process ensures a reproducible mechanical

coupling of the transducers, which are acting as transmitters and receivers on opposing sides of the battery cell. Impedance spectroscopy (IS) was employed to verify the attachment of the piezo elements and to characterize their resonant behavior. The manually crafted and attached sensor stacks showed a spread of about 4.4% in resonance frequency and a spread of about 18% in amplitude at the resonance frequency. IS also proofed useful to discover the detachment of piezo elements from the battery cell's surface. Experiments comparing the signals of shielded and bare piezo elements proofed the necessity of electromagnetic shielding to avoid the superposition of the acoustic signals with capacitive crosstalk. Further, the effect of the shielding on the transmitted waveform and its time of flight could be qualified to be small compared to the effects of crosstalk-induced distortions.

4.3 Excitation of piezo elements and through transmission signals

This section aims to give an overview of the excitation of the piezo elements, acting as transducers for the ultrasonic interrogation of the battery cells, and the therefrom arising transmission signals as a function of excitation frequency and state of charge. Thereby, general trends in the raw data are explored and listed for future reference when testing signal processing and feature extraction. To keep this section reasonably short, the excitation and transmission signals for a single battery cell, LDA019, serving as an example for the interrogated battery cells is chosen. Where not otherwise stated, the signals transmitted through this battery cell in the eleventh full cycle at 0.1 C are shown.

4.3.1 Excitation of the piezo elements

Piezo elements were attached to lithium-ion batteries via epoxy resin, ensuring mechanical coupling. As described above, transmission geometry was chosen. Therefore, two piezo elements, placed along an axis on opposite sides of a battery cell act as sending and receiving transducers. Raised cosine (RC_n) waveforms, with *n* describing the number of oscillations contained in the exciting waveform, are commonly used in non-destructive evaluation [264]. Here $n = 5$ was chosen to achieve sufficiently-short wave package length while maintaining a narrow frequency distribution.

To demonstrate and to examine the excitation of the piezo elements with the RC_n waveform, two examples at 50 kHz and 250 kHz (the lowest and highest frequency in the dataset which is stepped through at 5 kHz intervals) are depicted in Figure 4.13, each in a separate column. The first row shows the output signal under load (blue dots), e.g., with a piezo element connected to the output channel, and the corresponding RC_n function (orange line) which is passed to the digital to analog converter (DAC). Here the dependence of period

and thus wave package length on selected frequency becomes clear with the 50 kHz waveform exhibiting almost five times the length of the 250 kHz waveform. The second row contains power spectral density (PSD) plots of RC_n function and output signal. For 50 kHz, only small deviations from the function's waveform and PSD are present. For 250 kHz, much more prominent deviations are visible in the waveform, especially within the first (2 to 4) µs. In addition, the PSD shows deviations in the frequency distribution. The peak appears slightly thinner than the function's distribution and exhibits a second peak around 8 kHz. The bottom row shows a ten-fold zoom on the PSD in the row above, annotations mark the positions of prominent peaks.

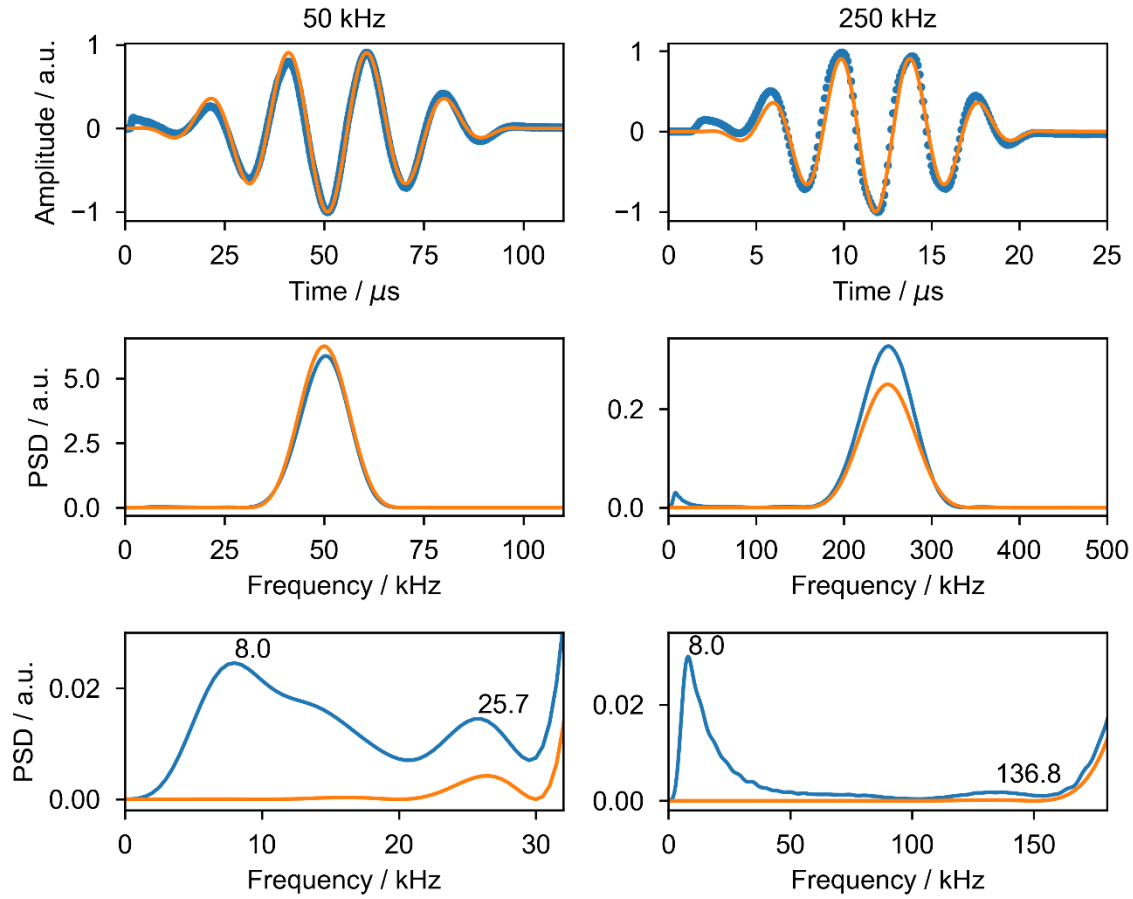

Figure 4.13: Raised cosine (RC_n) pulses with five oscillations at excitation frequencies of 50 kHz and 250 kHz and their calculated power spectral density. The top row shows the mathematical function passed to the DAC (orange) and the output signal under capacitive load (blue dots) is shown. The middle row shows the PSD, calculated by FFT from the shown signals. The bottom row shows a ten-fold zoom on the PSD in the row above, annotations mark the positions of prominent peaks.

For both frequencies, a peak at 8 kHz is visible in the PSD of the output signal under load. For 50 kHz, in the PSD of signal and function, a second peak is visible around 26 kHz. This peak and a shoulder around 14 kHz are most likely caused by spectral leakage in the FFT

used to calculate the PSD. For 250 kHz, a second peak at 136.8 kHz is visible. Since a corresponding peak in the function's PSD is missing, this is most likely a peak caused by the resonance of the piezo element at this frequency. The same assumption seems valid for the peak at 8 kHz. These findings coincide well with the resonant frequencies that are stated in the datasheet of the piezo elements and that are estimated by impedance spectroscopy.

4.3.2 Display of unprocessed transmitted signals

The following figures, depicting transmitted signals through the battery cell LDA019 of the selected type, are chosen as a single reference for through-transmission signals with the experimental setup described in Chapter 3, based on attached piezo discs. Signals at different SoCs were obtained during three cycles of 0.1 C cycling, more precisely from the charging process of the second cycle to avoid bias from relaxation during previous storage. Through transmission signals, resulting from excitation frequencies between 50 kHz and 250 kHz in steps of 5 kHz were recorded approximately every 0.6% SoC. To account for high signal amplitude and thus low dampening in the frequency range of 50 kHz to 75 kHz, an amplitude of 3% of the maximum output amplitude was chosen. For 80 kHz and above, 3.5% of the maximum amplitude was chosen for excitation. To enable a convenient presentation, the signals were normalized to the maximum amplitude and are displayed in normalized units (n.u. or NU). For most frequencies, the second wave package makes up for the portion of the signal with the maximum amplitude. Therefore, the description of the transmitted signals is chosen to always refer to the relative amplitudes.

From the available dataset, frequencies throughout the whole range of 50 kHz to 250 kHz were chosen, to highlight the gradual changes in through-transmitted signals, occurring with a variation of the RC_n excitation frequency. In the following section, transmitted signals in sets of four and with frequency steps of 5 kHz are illustrated. Figure 4.14 shows the transmitted signals for 50 kHz to 65 kHz in steps of 5 kHz, each displayed in a separate subfigure. For each frequency, the signals at three different states of charge (SoC) of the battery cell are plotted.

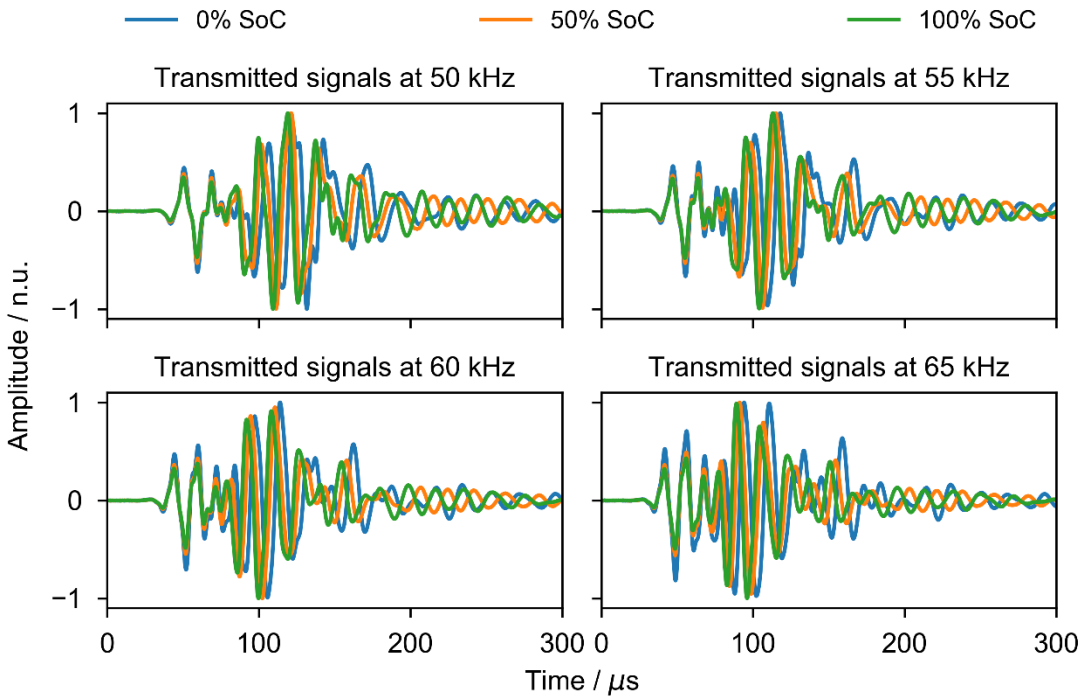

Figure 4.14: Transmission signals through battery LDA019 at SoC 0%, 50%, and 100% with RC_n excitation frequencies of 50 kHz to 65 kHz. Two main wave packages are distinguishable. The first one shows almost no change in position with change in SoC, while the second one is received earlier with rising SoC. Oscillatory patterns following these wave packages are highly distorted and may be a result of the superposition of received wave packages and a fading out oscillation of the receiver.

The signals at these frequencies share that the first wave package shows a declining tendency in amplitude with rising SoC, while the position and shape of this wave package remain mostly unchanged. Further, the second wave package is received earlier with rising SoC. Especially for the signals of frequencies 50 kHz and 55 kHz, the waveform within the packages and in the junction points between those first two are distorted and show discontinuities. Those discontinuities become less prominent with rising RC_n frequency. The oscillatory pattern following the second wave package shows a high number of irregularities and discontinuities and is therefore not easily interpreted. They may result from a superposition of following wave packages and fading out oscillation of the receiver.

Figure 4.15 displays the transmitted signals at 70 kHz, 75 kHz, 80 kHz, and 90 kHz. They share that the first wave package shows a declining tendency in amplitude, while the second wave package arrives earlier with rising SoC.

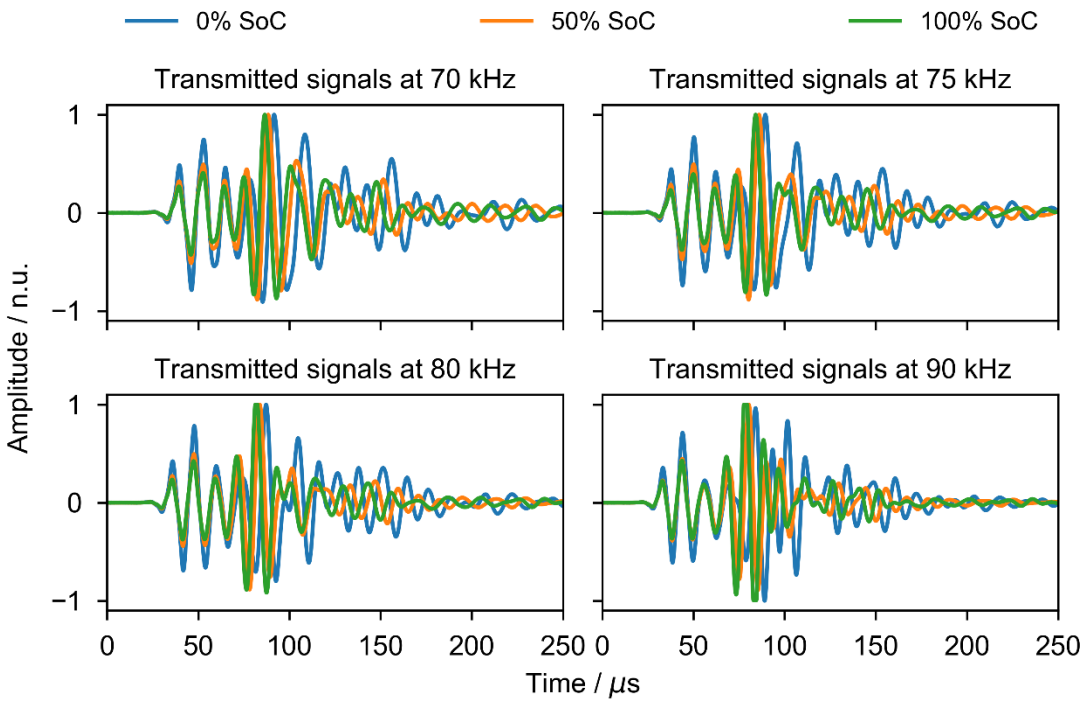

Figure 4.15: Transmission signals through battery LDA019 at SoC 0%, 50%, and 100% with RC_n excitation frequencies between 70 kHz to 90 kHz. The signals have in common that the first wave package shows a declining tendency in amplitude, while the second wave package arrives earlier with rising SoC. The second wave package appears mainly undistorted, but exhibits a discontinuity in the fifth oscillations, increasing with frequency. Gradually, from 70 kHz to 90 kHz, the second wave package at 0% SoC becomes more distant from the wave packages at 50% and 100% SoC, with a distinct discontinuity at about 70 µs.

The second wave package appears mainly undistorted, but exhibits a discontinuity in the fifth oscillations, increasing in intensity with frequency. Gradually from, 70 kHz to 90 kHz, the second wave package at 0% SoC becomes more distant to the wave packages at 50% and 100% SoC, with a distinct discontinuity at about 70 µs.

Figure 4.16 then shows the transmitted signals for 110 kHz to 170 kHz in steps of 20 kHz, each displayed in a separate subfigure. The displayed signals have in common that the first wave package shows a declining tendency in amplitude with rising SoC. Furthermore, through the earlier arrival of the second wave package, the first one is affected by superposition. Hence appearing shorter and exhibiting less than the commonly expected five oscillations. Even though the second wave package appears distorted in shape, the general trend of earlier reception with higher SoC remains visible though out all depicted frequencies.

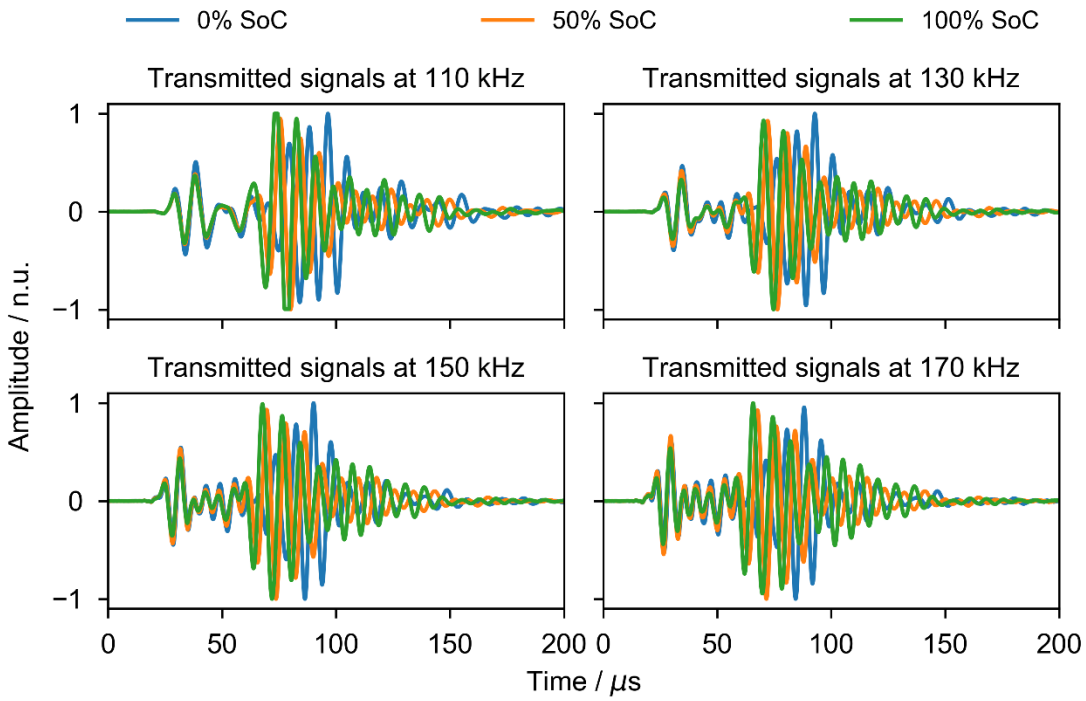

Figure 4.16: Transmission signals through battery LDA019 at SoC 0%, 50%, and 100% with RC_n excitation frequencies between 110 kHz to 170 kHz. The displayed signals have in common that the first wave package shows a declining tendency in amplitude with rising SoC. Even though the second wave package appears distorted in shape, the general trend of earlier reception with higher SoC remains visible though out all depicted frequencies.

Figure 4.17 displays the transmitted signals for frequencies of 190 kHz through 250 kHz in steps of 20 kHz. At these frequencies, the amplitude of the first wave package is maximum at 50% SoC. Furthermore, the first wave package exhibits the overall maximum amplitude within the signal starting at 210 kHz and 50% SoC. The trend of a huge discontinuity at 0% SoC continues at the depicted frequencies. Thus, making the second wave package at this SoC appear a lot later than at 50% and 100% SoC. Additionally, through the superposition of several patterns, the second wave package is not easily distinguishable from fading out oscillations and also shows an increasingly pronounced asymmetry. Therefore, no higher frequencies were investigated with the described measurement setup.

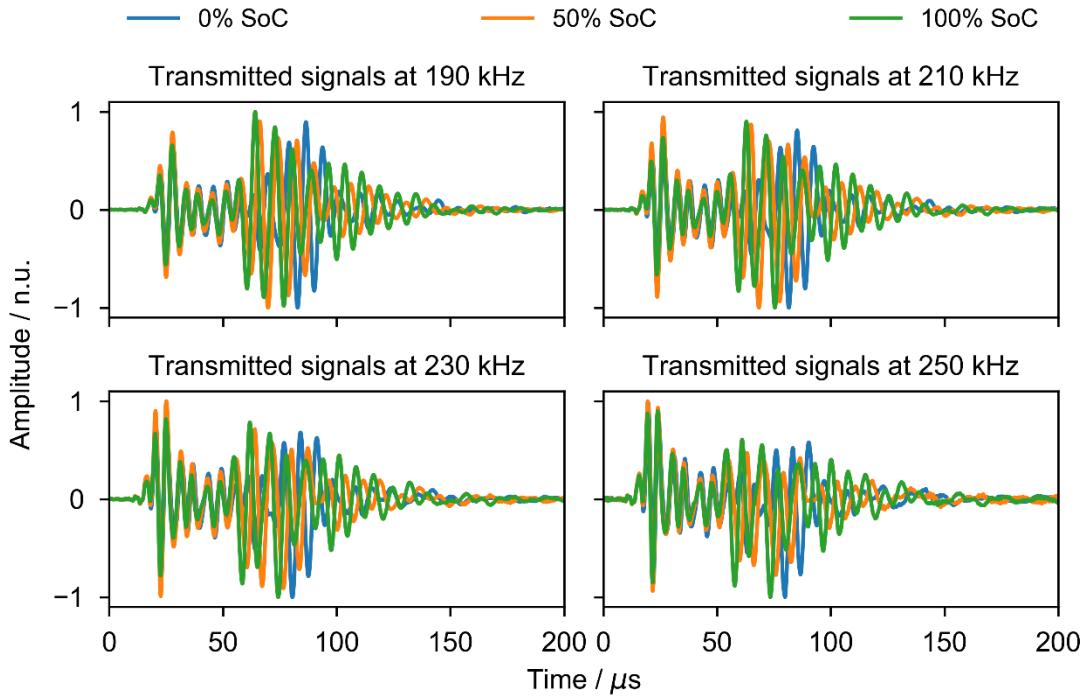

Figure 4.17: Transmission signals through battery LDA019 at SoC 0%, 50%, and 100% with RC_n excitation frequencies between 190 kHz to 250 kHz. At these frequencies, the amplitude of the first wave package is maximum at 50% SoC. Furthermore, the first wave package exhibits the overall maximum amplitude within the signal, starting at 210 kHz and 50% SoC. Through a huge discontinuity, the second wave package appears a lot later at 0% SoC, compared with 50% and 100% SoC. Furthermore, caused by the superposition of several signal constituents, the second wave package appears distorted in shape, especially for the signals at 230 kHz and 250 kHz.

The following two wide-format pages display two figures, Figure 4.18 and Figure 4.19, each consisting of nine heat map plots, converted from the data partially shown in previous graphs. On their vertical axis, the transmission time is plotted which was before plotted on the horizontal axis of Figure 4.14 through Figure 4.17. The color scale displays the absolute signal amplitude in non-normalized units. Therefore, brighter or red-colored pixels correspond to signal portions of high amplitude, darker or blue-colored pixels correspond to signal portions of low amplitude.

In Figure 4.18, the RC_n frequency is plotted on the horizontal axis. The figure is divided into three columns, each displaying another SoC. The first row shows the signals in the range of zero µs to 200 µs, the second row zooms in on the first wave package and the third row zooms in on the second wave package. Overall, an earlier reception of both wave packages with increasing RC_n frequency can be observed. The first arrives around 20 µs to 60 µs, the second around 60 µs to 120 µs, depending on RC_n frequency. For the second wave package, a decrease in arrival time and an increase in amplitude from 0% to 100% SoC can be seen. Furthermore, the second wave package appears to be split in the frequency range 70 kHz to 80 kHz at 50% SoC, as can also be seen in Figure 4.15, where the main peak of the second wave package and a subsequent peak, resulting from superposition, almost exhibit the same amplitude. Both wave packages seem to asymptotically approach a minimum transmission time as RC_n frequency is increased. While this limit appears to be a function of the SoC of the battery cell for the second wave package, it appears to remain unchanged for the first wave package. Therefore, the second wave package’s time of flight is favorable for the estimation of the SoC.

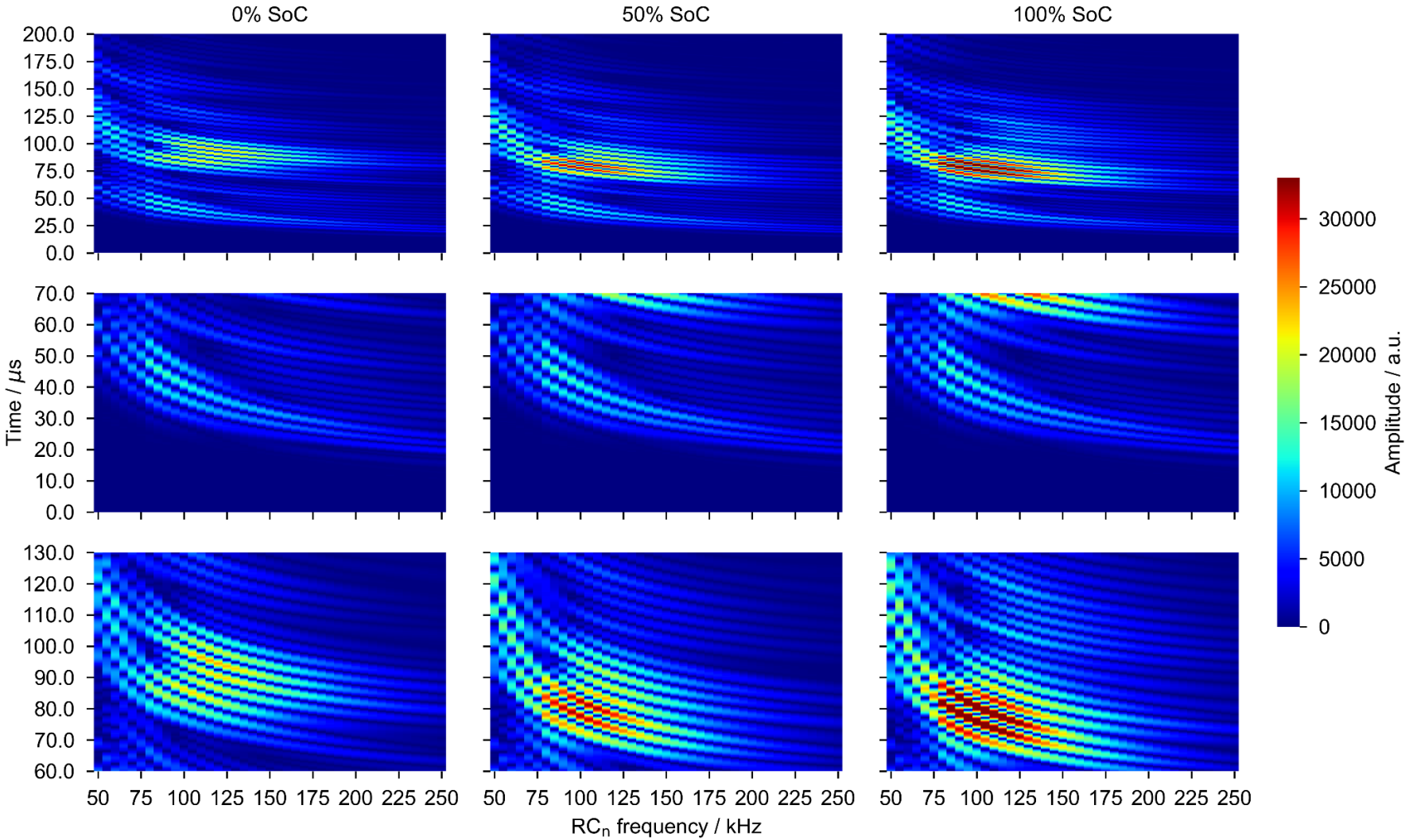

Figure 4.18: Heat map of absolute transmission signals through LDA019 as a function of transmission time (y-axis), plotted vs. RC_n excitation frequency (x-axis) at three selected SoCs (columns). The first row shows a 200 µs long portion of the signals. The second and third-row show regions of the signals, focused on the first and second wave package, respectively. For both wave packages, a declining trend with RC_n frequency is observed.

In Figure 4.19, the transmission time is plotted again on the vertical axis, and the SoC of the battery cell under investigation is plotted on the horizontal axis. As stated by the subplot title, nine RC_n frequencies between 50 kHz and 250 kHz in steps of 25 kHz were selected. The scale of the absolute amplitude remains unchanged with respect to Figure 4.18. In this figure, the SoC dependence of several signal features can be well seen. Among the displayed frequencies, at 100 kHz the amplitude of the first and second wave package appear the highest overall. For the displayed frequencies, the first wave package appears mostly unaltered in amplitude and transmission time in the complete SoC range. For all frequencies, an increase in amplitude with SoC, especially for the second wave package is observed. Furthermore, the decrease in transmission time of the second wave package appears to be almost linear for the lower frequencies 50 kHz to 100 kHz, regarding phase and group velocity. The latter is judged according to the maximum amplitude within the wave package. For higher frequencies, the position of the maximum amplitude seems to shift towards lower transmission times. Therefore, a non-linear course is expected in further detailed signal analysis.

4.3.3 Summary of this subchapter

In this subchapter, the excitation of the piezo elements with a raised cosine (RC_n) pulse, a common waveform in ultrasonic NDE and SHM, was shown. The power spectral density of the waveform under capacitive load was analyzed and peaks other than the center frequency of the exciting waveform were assigned to resonant frequencies of the piezo elements, used as ultrasonic transducers. Then, the raw signals resulting from the transmission of the excited waveform through the battery cells were shown, for an exemplary battery cell. The selection of several RC_n frequencies and three states, namely 0%, 50%, and 100% SoC allowed identifying rough trends. The plot of the raw signals over the whole frequency and SoC range as heat maps enabled the identification of trends – a decrease in time of flight of the wave packages with SoC and RC_n frequency – within the signals, which are rather easily spotted with the human eye but are difficult to quantify and extract automatically by means of algorithms. The here-listed trends will serve as a reference for the feature extraction showcased in a later chapter.

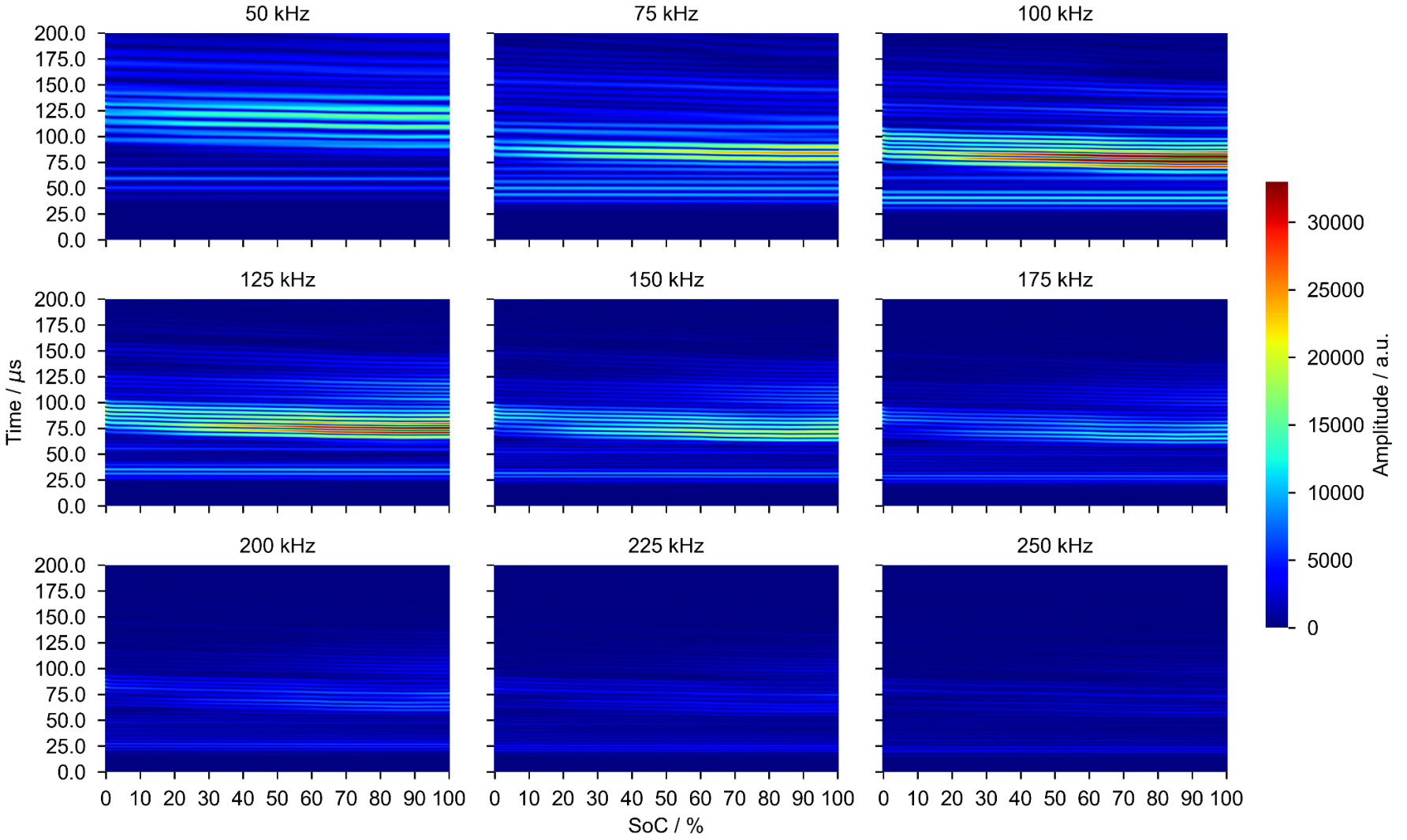

Figure 4.19: Heat map of the absolute amplitude of transmission signals through battery LDA019as a function of transmission time (y-axis), plotted vs. SoC (x-axis) at nine selected RC_n excitation frequencies (subplot titles). For all depicted frequencies, an almost steady course for the first wave package and a declining trend with SoC for the second wave package is observable.

4.4 Automated estimation of signal properties through algorithms

To feed SoC estimation algorithms with ultrasonic signal data and thereby increase estimation accuracy is the distinct aim of this work. To enable such a signal analysis, it is necessary to design it fully implementable on microprocessors, independent of human input, and robust against parameter variation. The first portion of this section treats signal properties such as maximum amplitude (position) and transmitted energy content. The second and larger portion of this section is dedicated to the time of flight estimation and the here for necessary signal processing in the time and frequency domain.

4.4.1 Properties other than the time of flight

Especially in Figure 4.19, a good correlation between maximum amplitude and SoC became apparent. As the signal data is available as a one-dimensional array, picking the entry with the maximum amplitude and estimating its position is an easy task. The results are displayed in the following figures. In Figure 4.20, the maximum amplitude is plotted against RC_n frequency for three different SoCs. For 0% and 100% SoC, the curves show a bell shape-like course with a maximum of around 120 kHz and 95 kHz, respectively. Due to the measurement tool's input being partially in saturation, the maximum amplitude of the signal remains constant for the frequency range of 80 kHz to 120 kHz.

In this range, a compromise between a well-resolved waveform (reasonable amplitude) and resolving all peaks in the transmitted signal had to be made. Thus, the highest peak of the second wave package in this frequency range is cut. Therefore, the frequency at which the amplitude is maximum at 100% SoC cannot be estimated from this dataset. One prominent point can be found at 140 kHz, where the maximum amplitude at 0% and 50% SoC is almost identical. Going towards higher frequencies, the maximum amplitude at 50% SoC becomes the smallest out of the selected three SoCs, until about 220 kHz after which the order is entirely reversed and the maximum signal amplitude is the highest at 0% SoC.

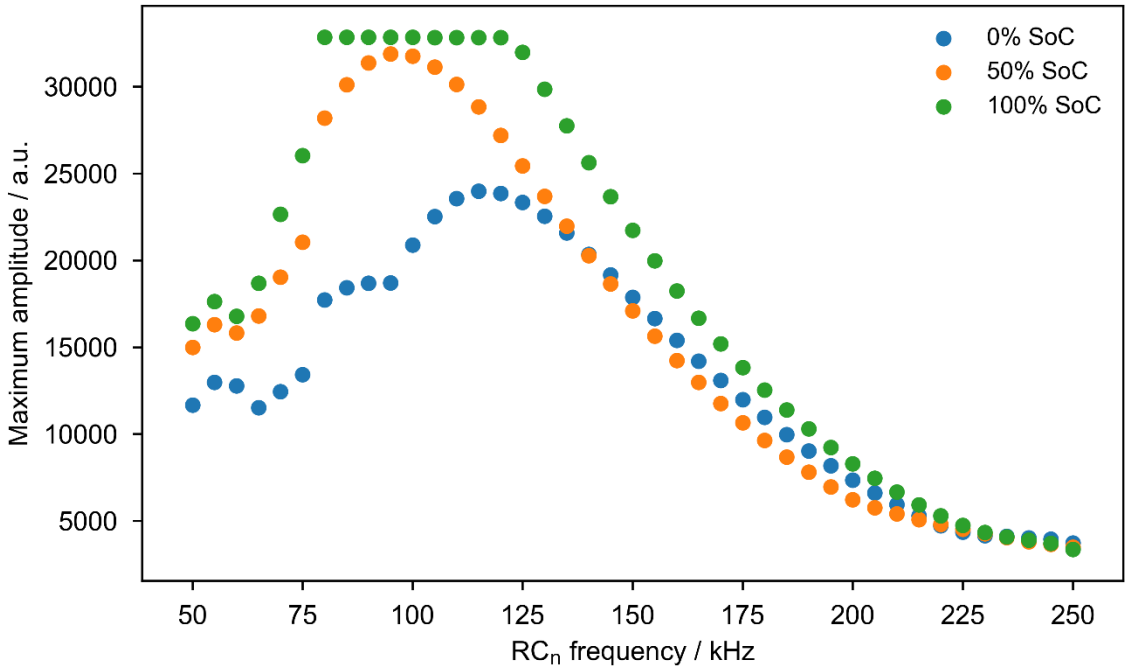

Figure 4.20: Maximum amplitude of signals, transmitted through battery cell LDA019, for different SoCs and RC_n excitation frequencies. Remark: In the frequency range between 80 kHz and 120 kHz and at an SoC of 100%, the ADC of the measurement device is in saturation due to too high signal amplitude. Therefore, a 17% lower excitation amplitude was chosen for 75 kHz and below, which causes the step seen in this frequency range.

In Figure 4.21, the position of the maximum amplitude is plotted against RCn frequency for three different SoCs. For the displayed SoCs, the course of the plots is non-monotonously but are broken at different frequencies. In a large portion of the frequency range, e.g., from 95 kHz to 200 kHz, the maximum amplitude at 0% SoC is recorded at noticeable later transmission times, compared to 100% and 50% SoC. With respect to the change in transmission time from 100% to 50% SoC, this huge jump does not represent the physical change in transmission time or velocity of the ultrasonic wave packages involved. Therefore, it is suspected to be a result of the superposition of several wave packages in a way that leads to a low amplitude in the junction between two subsequent wave packages, which can be seen while comparing the signals at 90 kHz and 110 kHz in Figure 4.15 and Figure 4.16 with attention on discontinuities. The section between 50 kHz and 90 kHz, and the section between 230 kHz and 250 kHz, with data points aligned closely together, are much more likely to well represent physical changes to the system battery cell. On the other hand, abrupt changes in the frequency-dependent behavior (at all three SoCs), such as the jumps occurring at 60 kHz and between 200 kHz and 230 kHz are most likely an artifact

resulting from the limitations of this simple analytical procedure, since these observations are not corresponding to the continuous behavior visible to the bare eye in Figure 4.19.

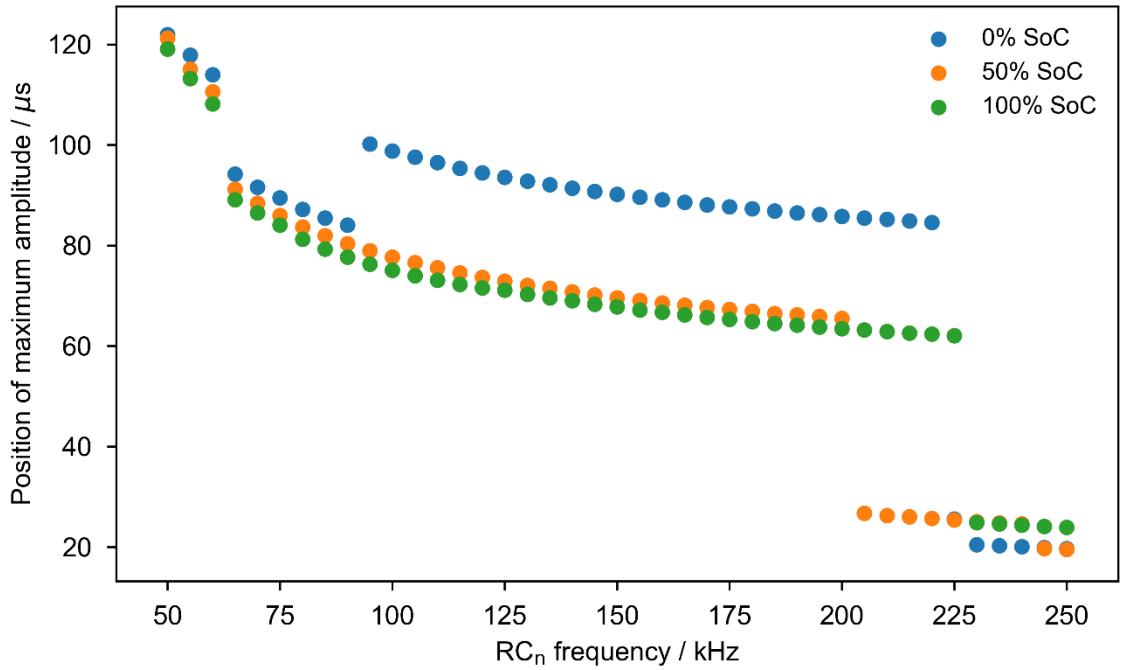

Figure 4.21: Position of the maximum amplitude within the acquired signal, transmitted through LDA019, for different SoCs and RC_n excitation frequencies. For most frequencies, the position of the maximum amplitude is the highest for 0% SoC and the lowest for 100% SoC. Starting at 205 kHz, this order is changed. Until 225 kHz, the position of the maximum amplitude is the lowest at 50% SoC. Followed by a frequency range where the order is completely inverted. The origin of the described behavior can be traced back to the signal amplitudes at different SoCs in section 4.3.2.

Figure 4.22 depicts the maximum amplitude as a continuous plot vs. SoC. The color of the lines indicates the RC_n frequency, spaced by 5 kHz, as referred to by the color bar on the right. Three main trends are observable. First, for the larger portion of the SoC range, the maximum amplitude increases with SoC. Second, the minimum and maximum within the maximum amplitude of the signal rise with RC_n frequency until 100 kHz and then fall off until 250 kHz. For all frequencies, a local maximum exists at 0% SoC. Depending on the frequency, the local minimum is reached within a few % SoC or up to 20% SoC. Another noticeable feature is the capping of the amplitude at 33000 a.u. at frequencies between 80 kHz and 120 kHz, which can be traced back to the saturation of the input channel of the measurement tool that was described before.

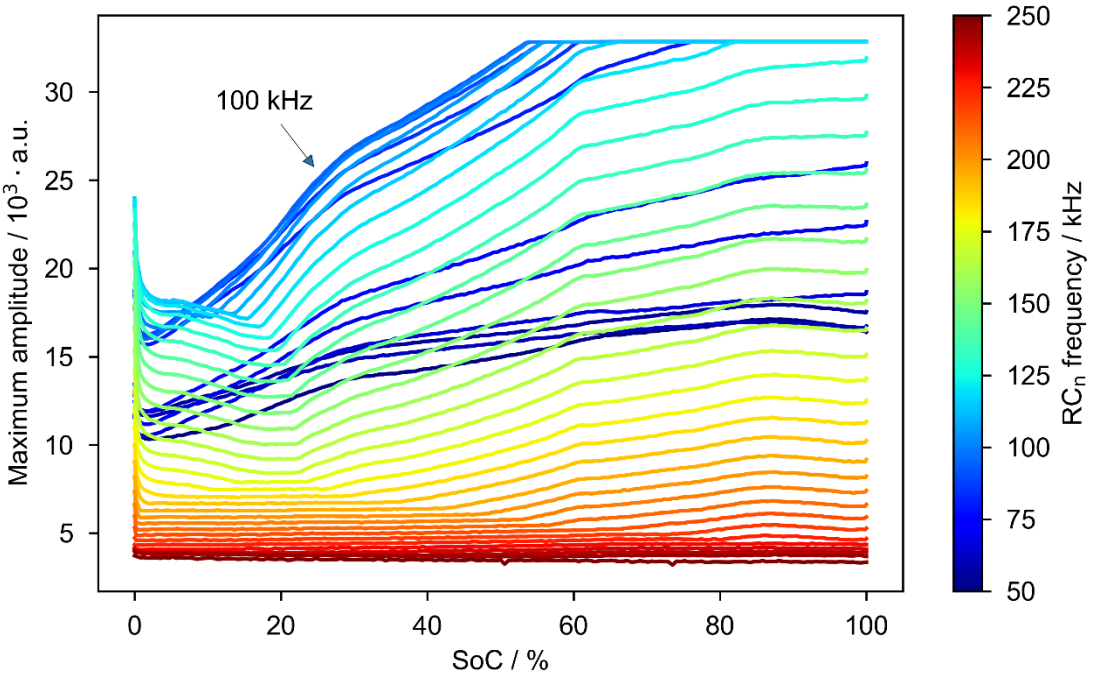

Figure 4.22: Maximum amplitude of signals, transmitted through LDA019, for various RC_n excitation frequencies plotted vs. SoC. Continuous plot over the full SoC range, showcasing the trends with SoC and RC_n frequency. The plots of the depicted frequencies have in common that they show a sign-change in slope at low SoC. Remark: In the frequency range between 80 kHz and 120 kHz and at an SoC of 100%, the ADC of the measurement device is in saturation due to too high signal amplitude. Therefore, a 17% lower excitation amplitude was chosen for 75 kHz and below.

Between the lines of 75 kHz and 80 kHz (the sixth and seventh blue lines from the bottom), a gap is visible. This gap may partially result from differing excitation amplitudes – 3% and 3.5% of the maximum output amplitude, respectively. Even though the displayed amplitudes were corrected by the resulting factor, this effect remains visible and thus suggests a high sensitivity of the setup towards amplitude variations. Overall, an amplitude decrease with frequency can be observed beyond 100 kHz. As a consequence of this and the fact that the variation of the amplitude depends on several other factors, the analysis of the amplitude variation with SoC is deprioritized in this work.

The following figure, Figure 4.23, displays the position of the maximum amplitude within the transmitted signals as a function of SoC for different RC_n frequencies. As before, the color bar on the right assigns a color to a frequency. For frequencies up to 90 kHz (ninth blue line, counted from the top), a continuously decreasing slope is observed for all lines but the 50 kHz line. In general, the spacing between the lines decreases with increasing frequency, until the sudden drop towards the last five frequencies in the displayed spectrum. These findings align well with the results plotted in Figure 4.21. The sudden jumps in the position of maximum amplitude, which can be identified by vertical lines in the plot, were already anticipated in Figure 4.21. Once again, these are a result of the superposition, occurring in

the transmitted signals at some frequencies and SoCs, which lead to a wave package pattern being inadequately interpreted by the here employed simple algorithm. Nevertheless, these findings reveal which frequencies result in easily interpretable signals, e.g., frequencies up to 90 kHz. Discontinuities, present at some frequencies caused by a switch in the wave package carrying the maximum amplitude – e.g., at a certain SoC the maximum amplitude of the signal is placed within the first wave package, then with increasing SoC the amplitude of the second wave package increases and becomes the overall maximum amplitude within the signal.

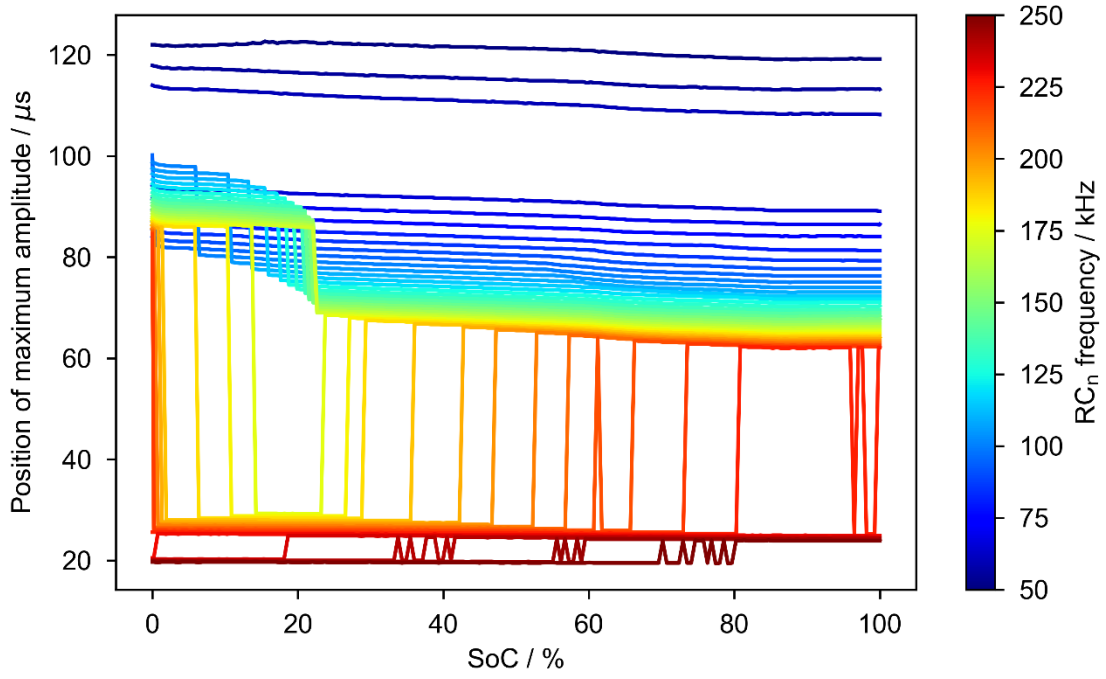

Figure 4.23: Position of the maximum amplitude within signals, transmitted through LDA019, plotted vs SoC for various RC_n frequencies. Plot over the full SoC range shows discontinuities that are associated with either the first or the second wave package being the one with the maximum amplitude and the switch between them.

Another, easy to obtain signal quantity is the transmitted energy content E_{tt}. To estimate it, the squared signal amplitude x is integrated over its duration $(t_1 - t_0)$. For a sampled and therefore discrete signal the integral is substituted with a sum over N data points [265]:

$$\boldsymbol{E_{tt} = \int_{t_0}^{t_1} |x(t)|^2 dt \approx \sum_{n=0}^{N-1} |x(n)|^2 \, , n = 0, 1, \ldots, N-1.} \quad \textbf{(74)}$$

Figure 4.24 shows the transmitted energy content (EC, E_{tt}) as a function of SoC for several RC_n excitation frequencies. In general, the features present in this plot are similar to those in Figure 4.22 with the difference that the saturation of the input does not affect the energy content in such a dramatic way. Since the energy transferred within the maximum amplitude, which is cut for some frequencies in the range of 80 kHz to 120 kHz above 50% SoC, has

a small contribution to the overall transferred energy, no asymptotic behavior is shown. Again, a gap between the lines of 75 kHz and 80 kHz (sixth and seventh blue line, counted from the bottom) is present due to a change in excitation amplitude, described earlier. Nevertheless, the spacing between lines is increasing from 50 kHz to 80 kHz, subsequently decreases until 100 kHz, and then increases again until about 150 kHz to afterwards decrease until 250 kHz. With 100 kHz being the line with the overall highest amplitude or energy content in Figure 4.22 and Figure 4.24, it can be assumed that the 100% SoC scatter plot in Figure 4.20 would also exhibit a maximum at this frequency.

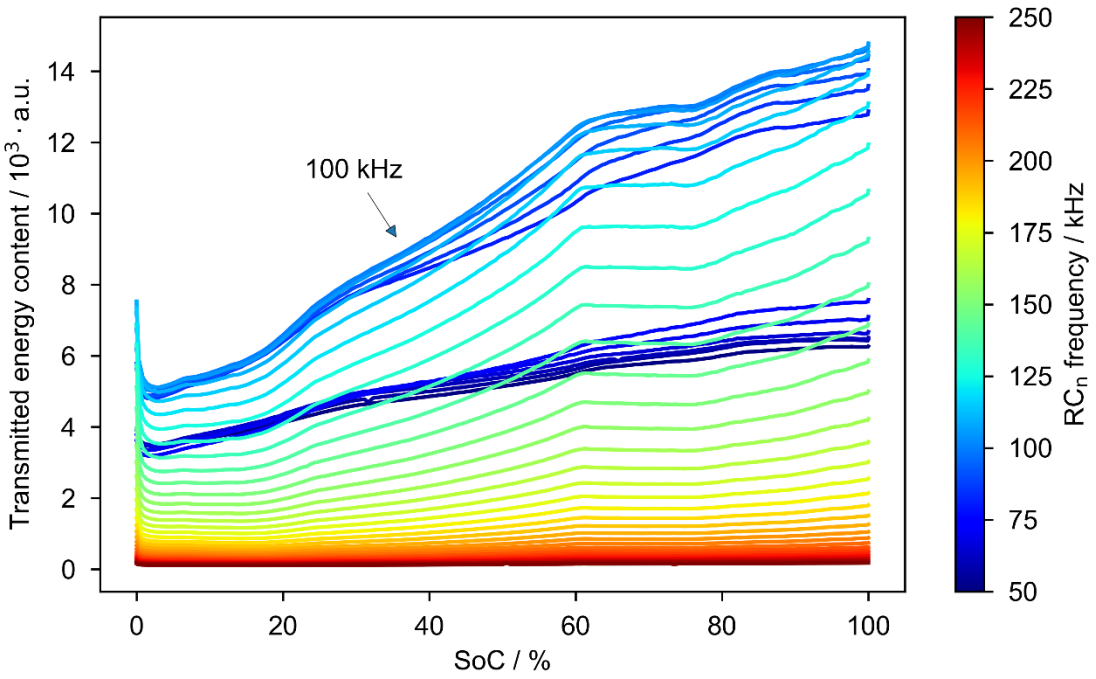

Figure 4.24: Transmitted energy content, estimated by integration of the squared signal amplitude, for several RC_n excitation frequencies plotted vs. SoC. The data shown here represents the signals transmitted through battery cell LDA019. In principle, similar trends as in Figure 4.22 are observed. With rising SoC, a higher amount of energy is transmitted within the signal. At 100 kHz the overall maximum energy is transmitted in the ultrasonic signal. And all frequencies show a sign-change in the slope of the plot at low SoC. Remark: Here the saturation of the ADC, for some frequencies and SoCs, is expected to alter the course of affected frequencies.

For frequencies below 100 kHz, a monotonously increasing slope is observed except for the local minimum around 0% SoC. Above 100 kHz, the local minimum around 0% and up to 15% SoC is more and more pronounced. In addition, the decreasing slope is accompanied by a plateau between 60% and 80% SoC.

4.4.2 Adaptation of time of flight estimation methods in the literature

The before described signals are analyzed by algorithms to find a stable and accurate estimate for the time of flight of the contained wave packages. The small spacing and partial overlap of the wave packages make some of the estimation methods, described in Chapter 2.3.6, suitable for the first wave package alone. Therefore, the results from several methods will be compared here.

4.4.2.1 Comparison of frequency spectra of sent pulse and received signal

As described in Chapter 2.3.6, the bandwidth and the shape of the sent ultrasonic pulse play a key role in the accuracy of ToF estimation methods. Therefore, the sent pulses (at different RC_n frequencies) are analyzed regarding their bandwidth, according to the procedure described in Chapter 2.2.6.3. By comparing the frequency spectrum of the transducers with the frequency spectrum of the received wave packages, the suitability of ToF estimation methods that rely on the validity of the assumption of unchanged pulse shape can be assessed.

Figure 4.25 compares the power spectral densities of the sent pulse under load (blue) and of the received signal at three different SoC and four different RC_n frequencies. The plots show two main trends that can also be seen for all frequencies in Figure 4.27. Firstly, at lower RCn frequencies, up to about 125 kHz (not shown here, see the Appendix), the maxima/peaks of the PSD of the received signal lie within the bell of the frequency distribution of the sent pulse. Beyond the RC_n frequency of 125 kHz, these peaks shift to lower frequencies, implying that the spectrum of the sent pulse is representing the spectrum of the received signal badly. Secondly, the peaks within the PSD of the received signal shift towards higher frequencies with rising SoC.

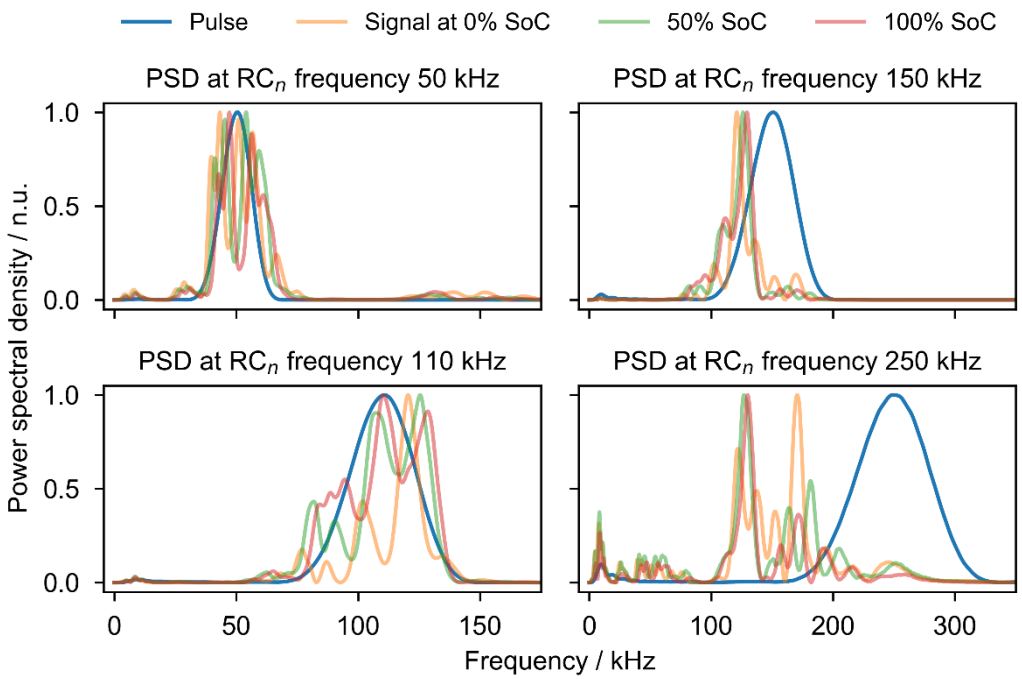

Figure 4.25: Power spectral density (PSD) of the sent pulse and the received signal at three selected SoCs for four selected RC$_n$ frequencies. Signals transmitted through LDA019 are exemplarily shown here. With rising frequency, the received signal's PSD differs increasingly from the sent pulse's PSD. The distribution contains an increasing number of peaks and shifts towards lower frequencies compared to the single bell-shaped peak in the pulse's PSD. Further, the peaks in the distribution shift towards higher frequencies with rising SoC. For an extended selection PSD of transmitted signals at other RC$_n$ frequencies refer to the appendix.

Figure 4.26 describes the bandwidth of the original waveform as handed to the DAC, and of the resulting pulse under load, with three distinct points in the frequency spectrum. For reference to sample signals and spectra, refer to Figure 4.13. The peak frequency f_p, and the two frequencies that meet the -3 dB criteria f_a and f_b are taken from the frequency spectra. The relative bandwidth is calculated according to Equation (48). Figure 4.26 depicts the absolute bandwidth of pulse and waveform as the transparent blue and green spurs, respectively. The center line marks the peak frequency f_p, while the borders of that spur mark the frequencies f_a and f_b. For the RC$_n$ waveform, the relative bandwidth remains constant at 28.82%, while for the pulse, the relative bandwidth lies lower and decreases with RC$_n$ frequency, as depicted on the right-hand axis.

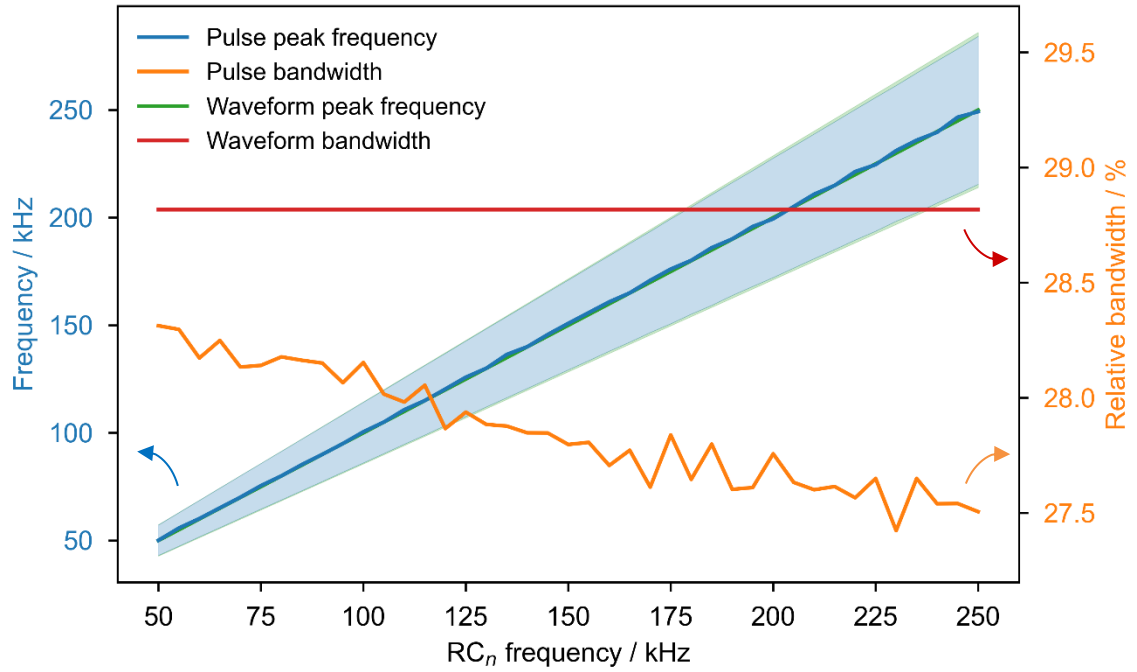

Figure 4.26: Analysis result of frequency spectra (PSD) of the RCn waveform handed to the DAC and the resulting pulse under load. The peak frequency f_p is plotted along with the frequencies f_a and f_b at -3 dB in the form of a partially transparent spur (representing the absolute bandwidth). On the secondary axis, the relative bandwidth is plotted.

In Figure 4.27, nine heat maps at SoCs from 0% to 100% in steps of approximately 12.5% (compare subplot titles) are shown. These heatmaps plot the power spectral density (color value) vs. frequency component (y-axis) for all measured RC_n frequencies (x-axis). Each heatmap is overlaid with plots of the frequencies f_a, f_b and f_c as introduced in Figure 4.26. This allows comparing the sent pulse's PSD with the PSD of the received signal and to estimate where deviations of the peak frequency (dark red color in the heatmap vs. the center white line) and the frequencies at -3 dB (bright green color in the heatmap vs. outer white lines) occur. Several general trends can be observed. For RCn frequencies up to about 100 kHz, most of the PSD lies within the boundaries of f_a and f_b (outer white lines). From about 100 kHz on, increasingly more content of the PSD lies without these boundaries. Horizontal lines of red color indicate peaks in the PSD at certain frequencies that are populated as soon as the spectrum of the sent pulse contains those frequencies. Or put in other words, some of the sent frequencies are hugely attenuated and therefore not contained in the received frequency spectrum while other frequency bands are favored. These bands exist around 50 kHz, 75 kHz, 105 kHz, 125 kHz and 175 kHz. Going towards higher SoC, these bands seem to shift to higher frequencies. The band around 175 kHz is fading out towards 100% SoC as less of the spectrum lies above 125 kHz and the band around 125 kHz becomes wider with increasing SoC.

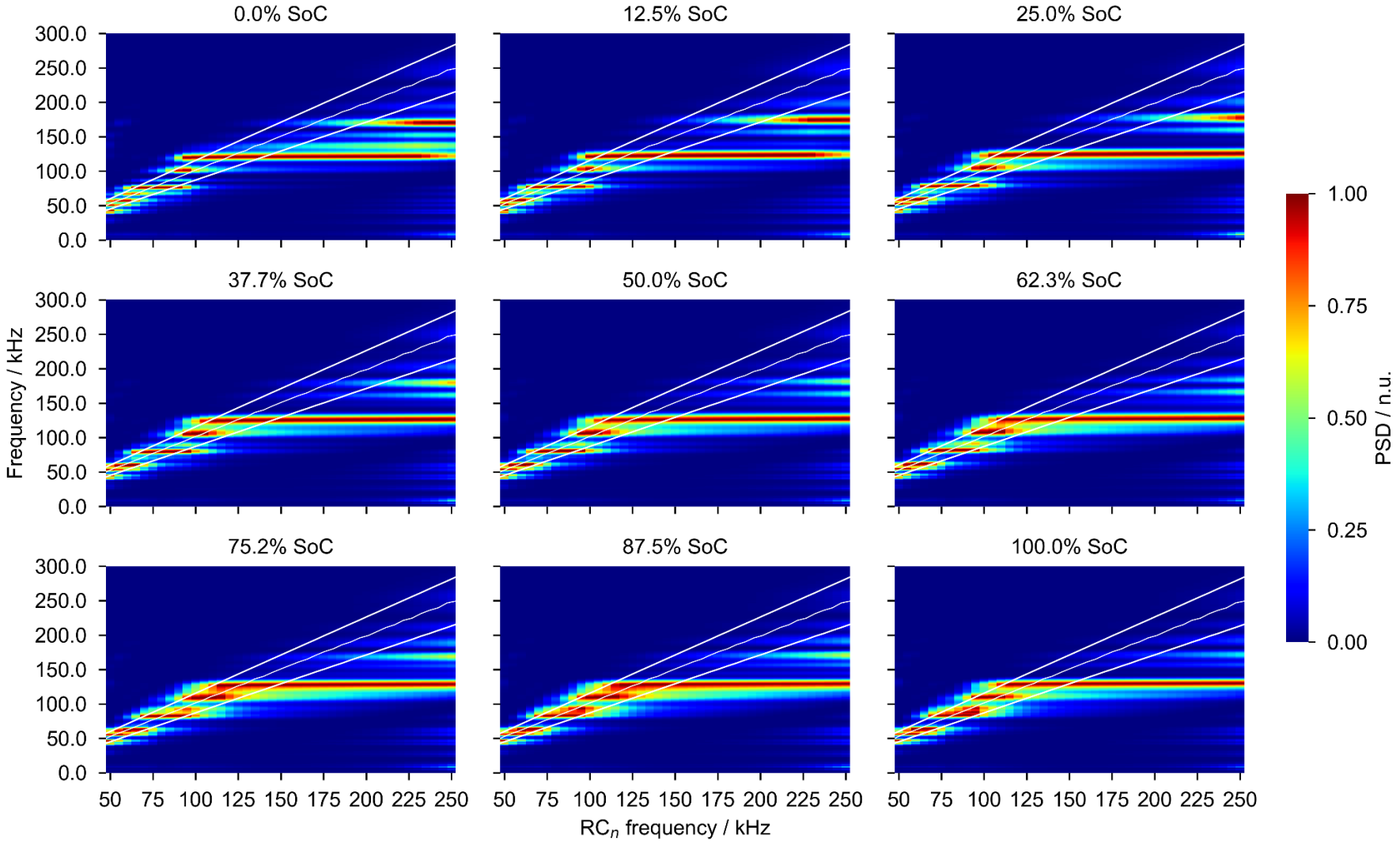

Figure 4.27: Heat map of power spectral density (PSD) of signals, transmitted through LDA019, as a function of frequency (y-axis), plotted vs. RC_n excitation frequency (x-axis) at nine selected SoCs (subplot titles). The absolute bandwidth and peak frequency of the sent pulse, as displayed in Figure 4.26 are overlaid as white lines. This shows that the position of the signal's peak frequency shifts out of the bandwidth of the sent pulse with rising RC_n frequency.

Since the appearance of the PSD of the received signals is not single bell-like (see Figure 4.25), the quantitative description by a center frequency and bandwidth are not as meaningful as for the sent pulse's PSD. For a symmetrically shaped distribution, the center frequency and the center of mass (CoM), also called centroid, coincide. Borrowing the concept of the expected value of a normalized distribution of a random variable, the center of mass μ of the power spectral density ρ_{PS} can be calculated according to Equation (75).

$$\boldsymbol{\mu = \sum_{k=0}^{N-1} f_k p_k} \quad \textbf{(75)}$$

$$\boldsymbol{p_k = \rho_{PS}(f_k) / \sum_{k=0}^{N-1} \rho_{PS}(f_k)} \quad \textbf{(76)}$$

Here, f_k is the frequency at index k, corresponding to *N* computed DFT coefficients. The weighting factor p_k for each frequency, the component is normalized as in Equation (76). The direct result of processing each received signal's PSD according to these equations is displayed in the appendix, see Figure 8.5. Figure 4.28 shows the deviation of the expected value of the PSD from the excitation frequency. This relative deviation is plotted as a color value in percentage for different SoCs (y-axis) and RCn frequencies (x-axis). This presentation shows that the CoM deviates significantly from the exciting RC_n frequency with increasing RC_n frequency. Above 100 kHz, the deviation lies well above 5% for all SoC. Further, for high RC_n frequencies, the CoM shifts towards lower frequencies with increasing SoC, being well in accordance with the trends observed in Figure 2.19.

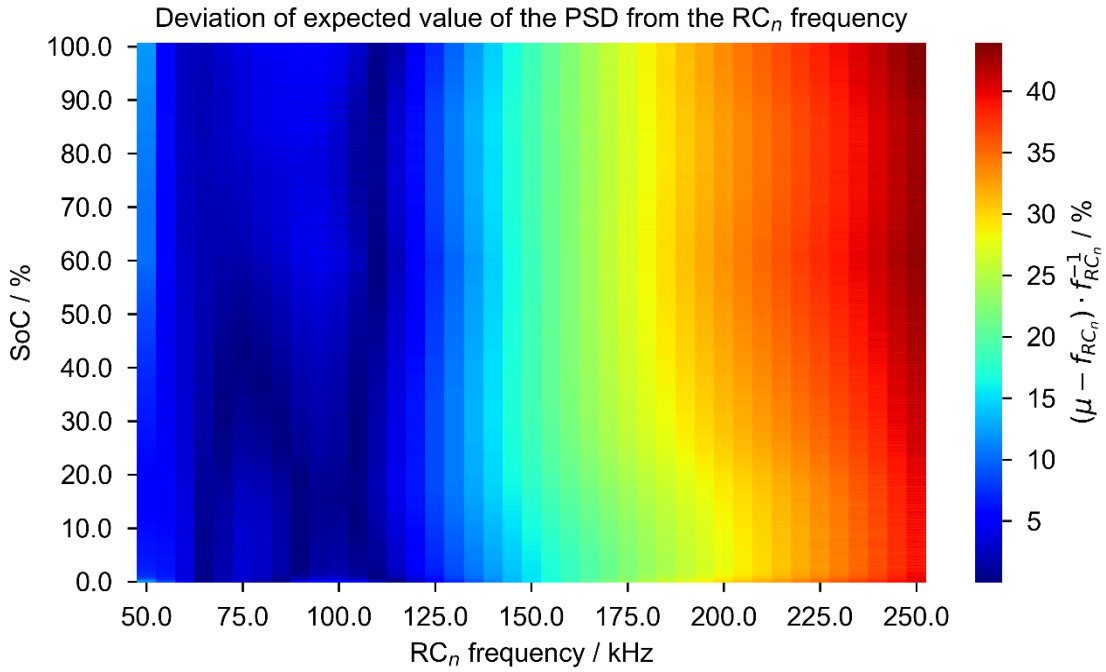

Figure 4.28: Relative deviation of the expected value of the power spectral density of the signals, transmitted through battery cell LDA019 as described in Figure 4.27, from the exciting RC_n frequency. The expected value describes the center of mass of the PSD and is calculated according to Equations (75) and (76).

This subchapter established, that ToF estimation methods, which rely on the matching of the PSDs of sent pulse and received signal, would not be suitable for the displayed data above a certain frequency. This frequency lies between 100 kHz and 125 kHz. Furthermore, the PSD of the received signals showed bands of high amplitude, shifting with SoC.

This changing frequency filtering behavior of the battery cell could be related to the changing structure and mechanical properties within/of the battery cells. As stated in Chapter 2.1.1, the changes in the geometry of the battery cell mainly originate from the anode, where the volume of graphite particles and following the thickness of the anode layers is changing with lithiation. Thus, a change in periodicity of the layered structure can be deducted. Along with lithiation comes an increase in elastic modulus and decrease in density, therefore an increase in the speed of sound, resulting in a larger wavelength at the same frequency. Altogether, the battery's structure may act as some sort of bandpass filter to the ultrasonic waves that dampens predominantly frequencies at which the wavelength is in the order of magnitude of the layered structure or the particle size. Subsequently, the shift of the cut-off frequency towards higher frequencies with rising SoC becomes reasonable.

4.4.2.2 Threshold and sliding-window (double threshold) method

As established in Chapter 2.3.6.1, ToF estimation based on a threshold is suitable for the first wave package in the received signal. Following the example in [205], the threshold is chosen based on the standard deviation σ of the noise of the signal. Therefore, a portion of the signal that only contains noise is chosen and analyzed. As can be seen in Figure 4.18, no wave package is contained in the portion of the signal before 25 µs or 9 µs for RC_n frequencies of 50 kHz and 250 kHz, respectively. For simplicity, the slope between those RC_n frequencies is fitted with an empirical estimated exponential decay function, and thereby a section to estimate the noise's standard deviation (STD) is selected. The estimated STD σ lies between 0.1% and 0.6% of the maximum amplitude and can be taken as a measure for the uncertainty of the amplitude. In accordance with [205], choosing the threshold $\tau_{th} = 5\sigma$, leads to a threshold level in the described range at about 0.5% to 3.1% of the peak of the signal, depending on SoC and RCn frequency.

For the sliding-window ToF estimation method, two thresholds (τ_{th} and m_{th}) are set. As for the regular threshold method, the threshold level τ_{th} is set to five times the STD of the noise. The second threshold m_{th} is set similar as in [205], to a number of samples equal to 25% of the length of the sliding-window, while the window length N_{th} is set to be about 1% of the approximated length of a wave package – see Figure 4.18.

Figure 4.29 compares the result of basic thresholding (TH) and the sliding-window (SW) method. For the sliding-window, several points within the window can be chosen to mark the ToF. Here, the first point (FP), the window's center point (WC), and the $(N_{th} - m_{th})^{\text{th}}$ point are selected. ToF(TH) and ToF(SW, N-m) are very similar, and also often coincide, if the following m_{th} points after the first point also exceed the threshold τ_{th}. ToF(SW, WC) and ToF(SW, FP) represent earlier points within the same window and might therefore be able to reduce the offset towards the "real ToF" or even set the arrival too early, depending largely on the set window length.

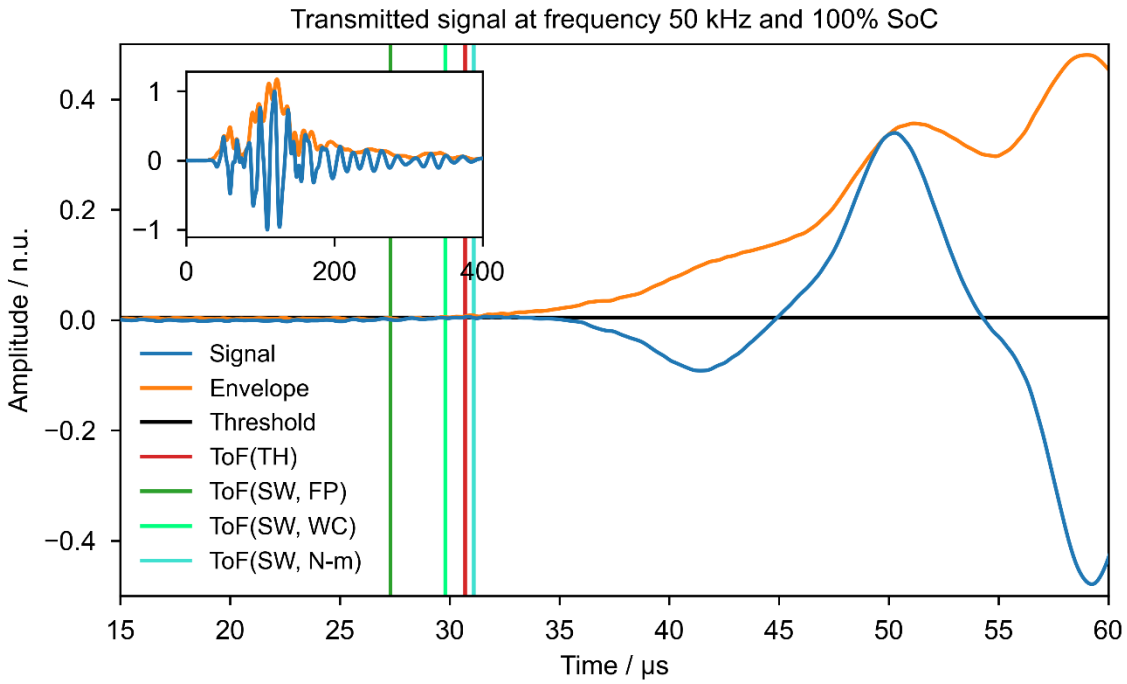

Figure 4.29: Comparison of the threshold and the sliding-window method, applied to a signal, transmitted through LDA019, at an RC_n frequency of 50 kHz and 100% SoC. In this signal, the noise was estimated from the first 25 µs. Along with a zoom-in on the signal and the envelope, the threshold, a multiple of the standard deviation of the noise of the signal, $\tau_{th} = 5\sigma$ is plotted as horizontal line and the ToF estimated by variants of the two methods is plotted as vertical lines. These include basic thresholding (TH), the sliding-window method at the first point of the window (SW, FP), at the window's center (SW, WC), and at the $(N_{th} - m_{th})^{\text{th}}$ point of the window (SW, N-m). The inset shows the signal and the envelope at full length, for comparison.

As pointed out in [205], the variants (SW, FP) and (SW, CW) yield the smallest offset. Since this work aims to utilize the differences in ToF between different battery states, the robustness of the estimation method is the primary priority and the accuracy is secondary. Therefore, the parameters were adapted from [205] and are not further optimized.

The ToF, estimated by the threshold-based methods, is plotted vs. SoC for a charging half cycle in Figure 4.30. As the three variants of the sliding-window methods differ only in the position of the reference point within the window, they share the same standard deviation, which is hence only depicted for the (SW, FP) variant. In general, a slight decrease in ToF with SoC can be observed for the first arrival, as estimated by the threshold-based methods.

The simple threshold method shows a comparable standard deviation but with larger outliers than the sliding-window variants.

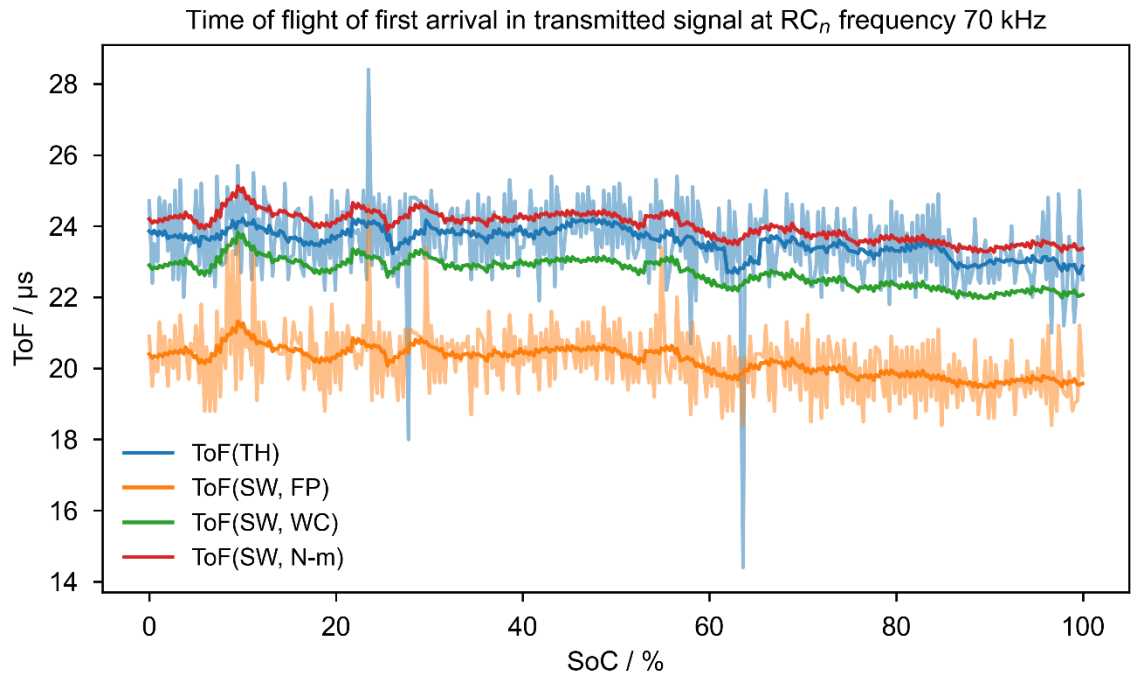

Figure 4.30: ToF estimates by thresholding (TH) and sliding-window (SW) method variants. The opaque lines represent a 13-point rolling mean of the unfiltered estimates (partially transparent lines), corresponding to a smoothing window of about 5% SoC. The results of all three SW variants show the same standard deviation but exhibit smaller spikes than the TH method's result. A slight declining trend in the ToF with rising SoC is observed. The plot shows the data derived from the signals transmitted through battery cell LDA019.

4.4.2.3 Envelope method

The envelope method relies on the Hilbert transform which is implemented with the fast Fourier transform (FFT) algorithm, as described in Chapter 2.3.6.2. The FFT is based on the assumption of the signal being cyclic. To ensure this, the signals are tapered with a window function, such as the Tukey window. The tapered section of the signal is chosen to include the noise alone and an equally long section at the end of the signal, which only hosts a decaying oscillation of the excited receiving piezo element. In that way, the information contained in the signal remains virtually unaltered.

Figure 4.31 depicts the resulting sent pulse and transmitted signal, after performing such a tapering with a Tukey window. Along with the amplitude, the envelope is displayed and the most prominent peaks of the envelope are marked. In part visible in the envelope of the pulse, but more distinctly in the envelope of the transmitted signal, the envelope does not

show the smooth bell shape, as expected from an RC_n pulse, but follows the enveloped oscillations too closely. The resulting shape of the envelope makes the automated identification of the wave packages by peak-picking unpractical. Parameters to select certain peaks have to be hand-tuned regarding minimum height, prominence, and distance to neighboring peaks to achieve the peak picking as seen in Figure 4.31 on the right. Hand tuning those parameters makes the process deceptive to instability and brings an arbitrary component to the analysis. The following pages demonstrate which properties of the signal cause the distorted shape of the envelope and how the signal can be processed to avoid these and therefore make the envelope-based method a stable one.

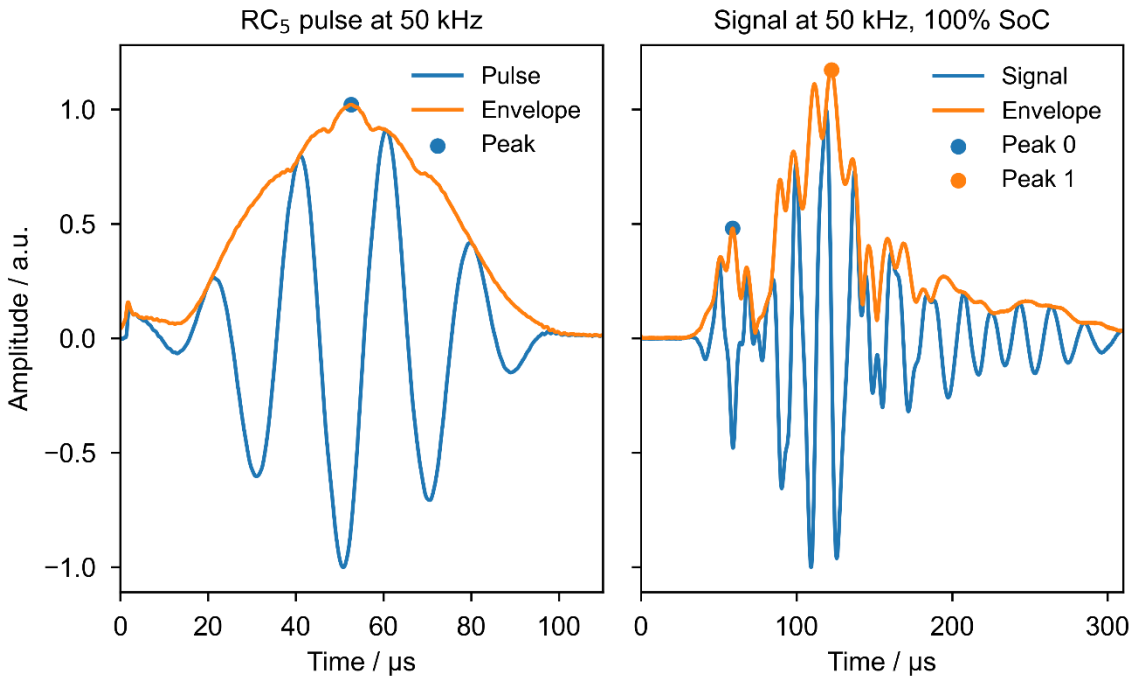

Figure 4.31: Example of envelope-based ToF estimation. (Left) envelope of the sent waveform – RC_5 pulse under capacitive load. (Right) envelope of the received signal with the most prominent peak in the first and second wave package marked by colored dots. Both subplots show an envelope with a distorted shape that makes reliable peak picking difficult to achieve. The depicted data originates from the excitation of the piezo elements mounted on battery cell LDA019 and the resulting signal transmitted through the latter.

A non-zero offset, as in Figure 4.32 (middle), lead to a change of the envelope. This can be deducted from the calculation of the envelope via the Hilbert transform. As described in Equations (65) to (68), the envelope is calculated from the absolute of the analytical signal. If the signal contains an offset, e.g., $y'(t) = y(t) + c$, the analytical signal becomes $\psi'(t) = y(t) + c + i\hat{y}(t)$, since the Hilbert transform of a constant is zero. The envelope calculated as in $E'(t) = \sqrt{\psi'^2(t)} = \sqrt{(y(t) + c)^2 + \hat{y}^2(t)}$ then contains the mixed term $2cy(t)$ and is

weighted more towards the real component of the analytical signal, thus enhancing the peak shape as in Figure 4.32 (middle). This effect increased with the magnitude of the constant – compare the shape of the envelope with increasing offset (trend) from left to right in Figure 4.32 (right). Adding a trend to the signal leads to a non-zero difference between the beginning and end of the sampled signal. Therefore, the cyclic Fourier transform, as performed during the Hilbert transform, leads to frequency leakage and unwanted components at the site of this discontinuity (beginning and end of the signal), as can be seen in Figure 4.32 (right). Both described effects are also visible in the envelope of the transmitted signal – see Figure 4.31 – even though the signal was preprocessed with a linear “detrending” method, which applies a linear fit to the data and subtracts the hereby-estimated trend from the signal. It can be concluded that the underlying offset in the signal is not solely of a linear nature. “Detrending” with other fit functions such as an exponential function to simulate a capacitance-charging effect of the piezo elements could not improve the result further. Therefore, the offset is probably of another origin. A guess on the cause could be a parasitic harmonic oscillator-like disturbance that propagates along the signal path, excited by the RC_n pulse. Such a process is highly complex, may change with frequency and from measurement to measurement, and is difficult to model in such a way that the “detrending” operation can remove the resulting trend completely.

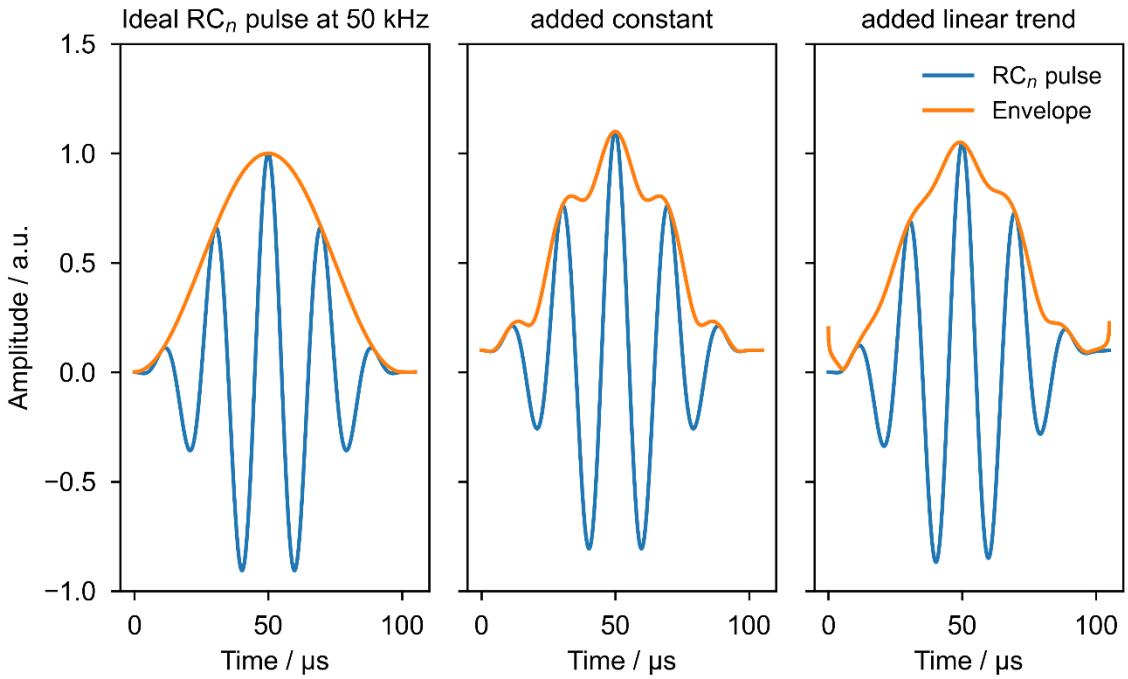

Figure 4.32: Demonstration of the effect of and additive offset on the shape of the envelope. (Left) ideal RC$_n$ pulse at 50 kHz, (middle) pulse with an added constant of 0.1, and (right) added linear trend that increases during the duration of signal from 0 to 0.1. The FFT-based Hilbert transform used to construct the envelope makes the signal cyclic and therefore the difference between start and endpoint becomes a discontinuity that affects the shape of the envelope.

Even after detrending, the envelope may still be following the individual peaks of the signal too closely, as can be seen in Figure 4.33. The peak picking of the maximum envelope amplitude may therefore be unstable. As seen from the comparison of two signals, acquired just 0.2% SoC apart from each other, small amplitude fluctuations of the signal can lead to a change in the position of the envelope's maximum, which results in the peak picking algorithm choosing a neighboring peak over another. Therefore, the estimated ToF shows a large step of about eight µs, not correlating well with the rather small SoC change of 0.2%.

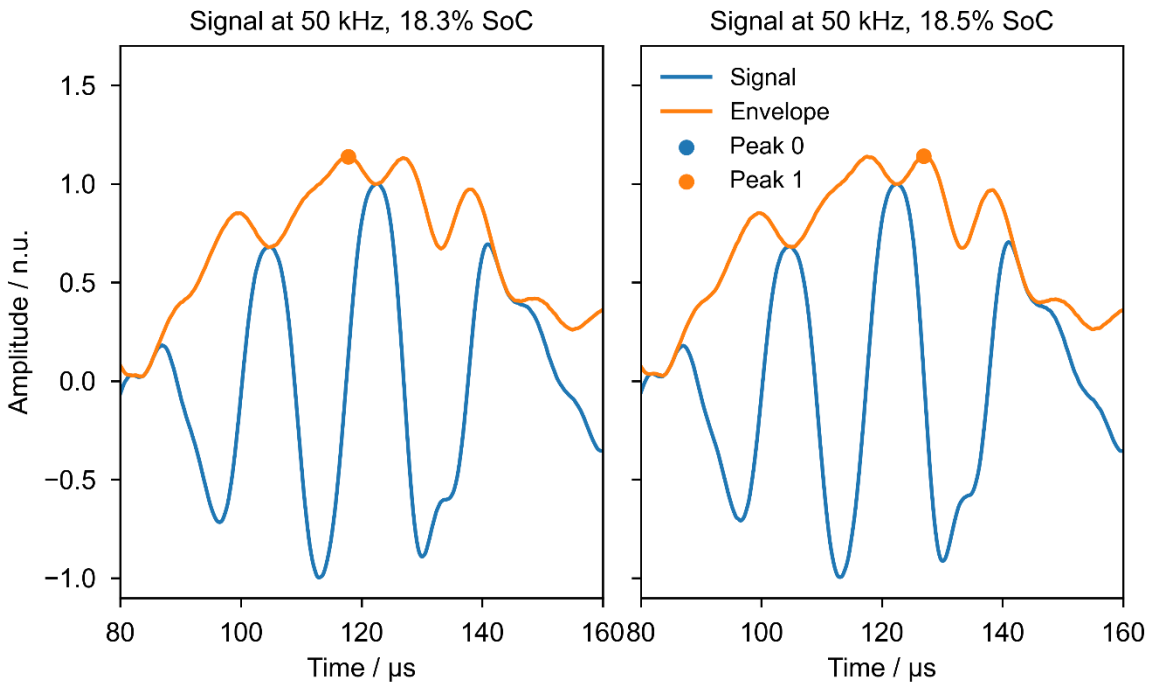

Figure 4.33: Comparison of the envelope of the signals, transmitted through battery cell LDA019, (cut to the second wave package) at an RCn frequency of 50 kHz during the charging, 0.2% SoC apart from each other. Here it can be seen that even a small change in SoC can cause a significant difference in the position of the picked peak, which is not representative of the change in the physical properties of the battery in this SoC range.

To improve the reliability of the envelope method further, a finite impulse response (FIR) filter was designed in such a way that frequency components, which most likely do not represent an acoustic process, are removed without significantly altering the frequency spectrum around the exciting RC_n frequency. Designing an appropriate FIR filter, as depicted in Figure 4.34, is a complex task and involves tuning several parameters to fit the desired behavior while maintaining an acceptable computational effort. By studying the frequency spectra in Figure 4.27, one can estimate the passband of the filter for each RC_n frequency. Empirically tested, the lower cut-off frequency of the passband was estimated to be 20 kHz, linearly increasing to 45 kHz with RC_n frequency (from 50 kHz to 250 kHz). The upper cut-off frequency of the passband was found to yield the best result at 175% of the RC_n frequency. The stopband attenuation was selected to 40 dB, corresponding to an amplitude reduction of 99%, resulting in acceptable ripple boundaries in the passband. Rather small ripples are important to reduce the alteration of the frequency spectrum in the passband, introduced by the filter. Since the number of filter coefficients, also called taps, scales, among others, with the steepness of the transition region between stopband and passband, the width of the transition region, also called the roll-off region, is set to 10 kHz. Due to the cut-off frequencies being much smaller than the Nyquist frequency at 5 MHz, a

large number of taps (2235) is required to meet the filter demands. To reduce the computational cost of the filtering process the input signal can be cut in length to the region of interest, which has been estimated to be about 250 µs long for all RC_n frequencies, containing the first three wave packages.

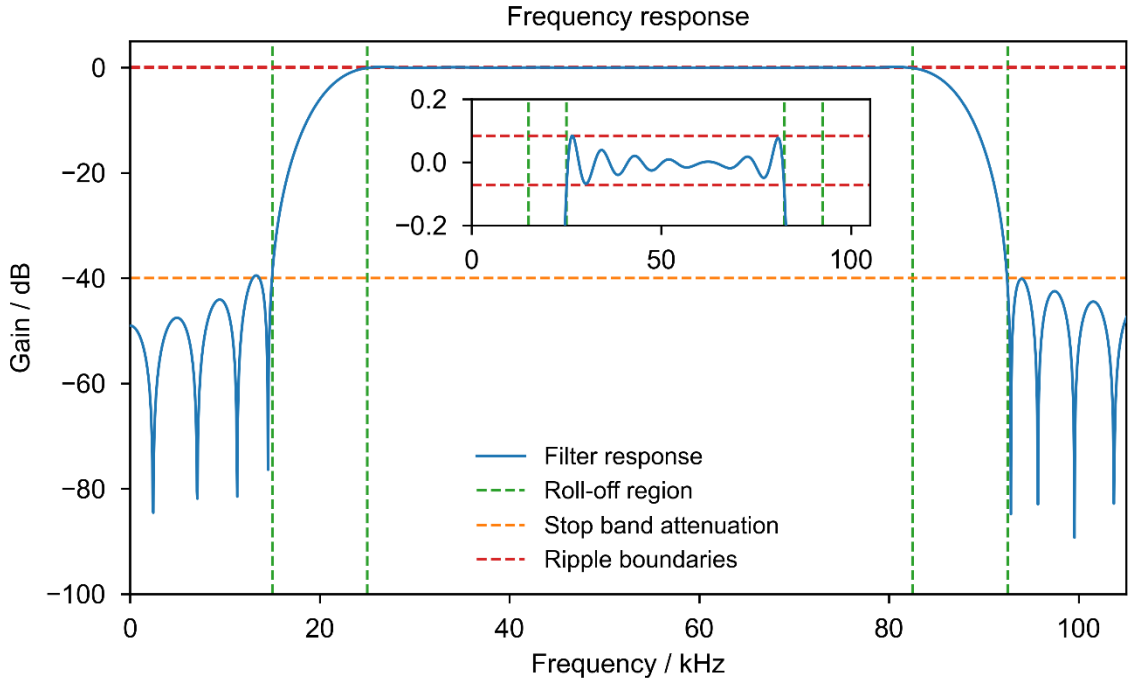

Figure 4.34: Frequency response of the designed FIR filter. Cut-off frequencies: 20 kHz and 87.5 kHz (175% of the RC_n frequency), roll-off width: 10 kHz, stopband attenuation: 40 dB, ripple delta < 0.2 dB. The window used in the FIR filter: Kaiser. The inset of the figure shows the central frequency range in which the amplitude of the processed signal is not to be altered significantly. In the zoomed-out view, the typical side lobes beyond the cut-off frequencies and the roll-off region can be identified by the colored dashed lines.

The filtering process involves the convolution of the input signal with the filter (coefficients). Depending on the length of the two and therefore which method is faster, either the point-by-point multiplication and shifting of the input signal and filter is performed or the convolution is performed in the Fourier space by point-by-point multiplication. The input and output of the filter operation are displayed for a sample signal at 50 kHz and 100% SoC in Figure 4.35. The top row shows the signal and its envelope. The signal, displayed on the left, was preprocessed by detrending as described before. On the right, a Tukey window was applied and the filtering operation was performed. As seen here, filtering removes most of the discontinuities in the signal and yields a smooth envelope that does not follow the single oscillations too closely. The bottom left plot highlights the filter coefficients of the filter, designed in Figure 4.34 and applied here. The bottom right depicts the power spectral density of the filter and allows comparing the PSD of the signal pre and post-filtering. As

seen here, the filter reduces the amplitude of frequencies outside the center of gravity without altering the distribution around the excitation frequency significantly. As established in Chapter 4.4.2.1, the CoM of the transmitted frequency spectrum deviates significantly from the exciting RCn frequency, especially above about 100 kHz. Therefore, the described filter is the best fit for the frequency range in which sent pulse and received signal PSD match well.

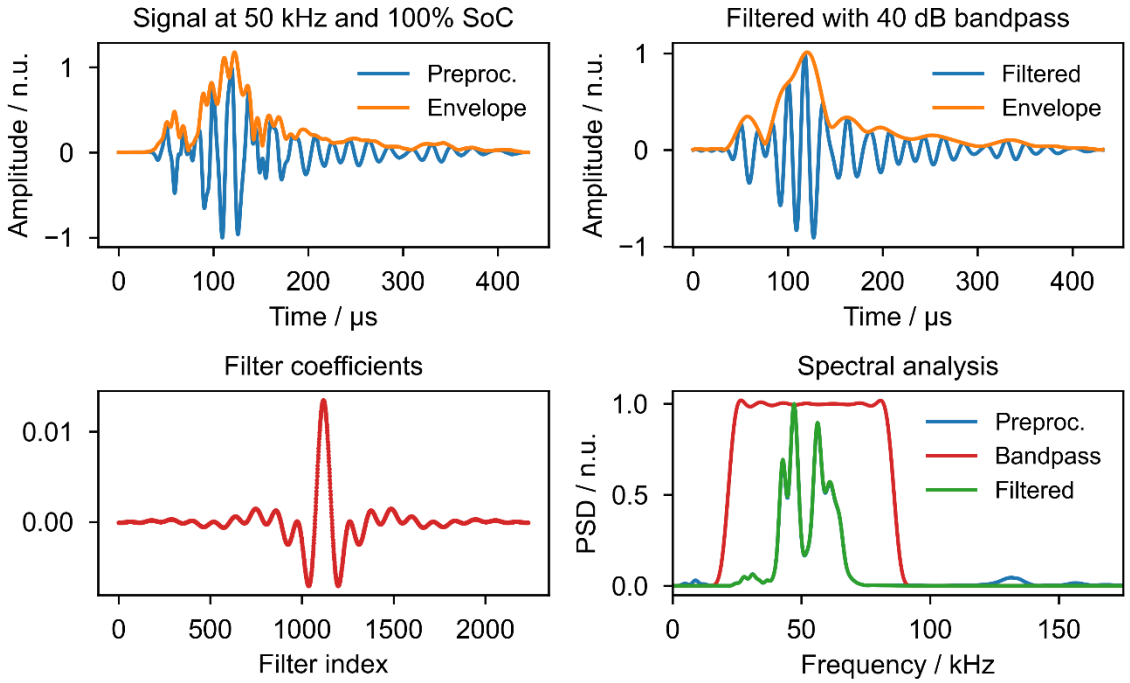

Figure 4.35: Pre-processing (Detrending + Tukey window tapering) and FIR filtering of the signal, transmitted through LDA019, to enhance the envelope-based ToF estimation method. (Top left) preprocessed signal and resulting envelope at 50 kHz and 100% SoC, (top right) filtered signal and resulting envelope, (bottom left) FIR filter coefficients, and (bottom right) PSD of the preprocessed signal, FIR filter, and filtered signal. Here, the influence of the filtering process on the frequency content of the signal can be estimated – the attenuation is very little within the band pass and as desired beyond the cut-off frequencies.

The envelope of the filtered signal is then passed to a peak picking algorithm that tracks the peak with the maximum amplitude and the first peak, exceeding 20% of the maximum amplitude. These refer to the first two, by eye well distinguishable, wave packages. To calculate the resulting time of flight (ToF), the position of the maximum peak within the envelope of the sent pulse is subtracted from the peak position. Figure 4.36 shows the tracking of the two peaks during a charging half-cycle and an RC_n frequency of 50 kHz. As seen here, the first peak shows an almost linearly falling trend with SoC, while the maximum peak shows a monotonously decrease with SoC, incorporating sections of different slopes. An advantage of the ToF estimation methods presented before is the high stability of the algorithm, leading to a low standard deviation. Further, by peak picking the envelope, the

ToF of two or more wave packages can be extracted. As seen already in the study of the raw transmitted signals, the shape of the wave packages is distorted above 100 kHz, making the envelope-based method applicable in the range from 50 kHz to 100 kHz. In the appendix, additional frequencies are covered.

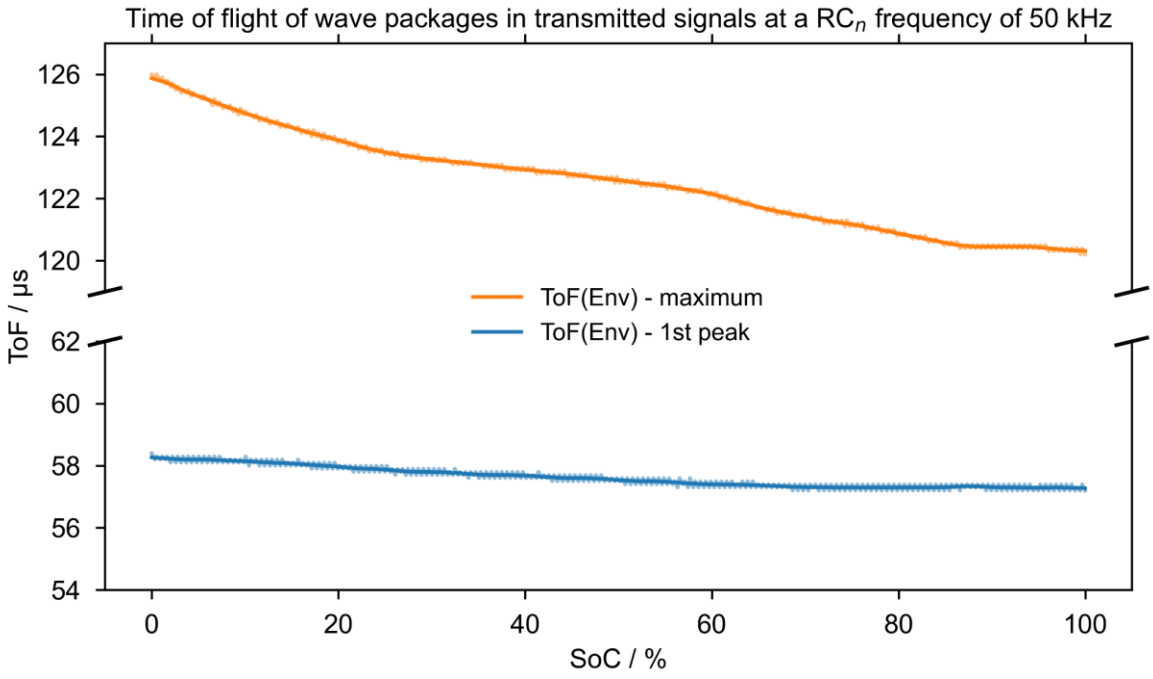

Figure 4.36: Time of flight (ToF), estimated by peak picking the envelope of the filtered signals at 50 kHz, transmitted through LDA019. The opaque lines represent a 13-point rolling mean of the unfiltered estimates (partially transparent lines). Here, it can be seen that the first and second wave packages show a declining trend with SoC. Since the slope of the two lines, representing the ToF of the wave packages, have a different slope, the ToF difference between the two is reduced with SoC.

Each ToF estimation method inherits a different reference point. The methods, described in this chapter above, take the trigger point, at which the pulse is sent, as “0 µs”. While this introduces a negligible offset for narrow pulses or waveforms, the offset has to be accounted for in this case. The frequency-dependent offset (position of the reference point within the signal vs. trigger point) for each method is depicted in Figure 4.37. Since the standard deviation of the noise cannot be estimated in the sent pulse, lacking a “silent” signal section, the threshold is set to 3% of the absolute amplitude’s maximum. The length of the raised cosine pulse depends on the RC_n frequency – the period length of the envelope and the contained oscillations decrease with frequency. Therefore, the position of the reference points shifts with frequency, approximately proportional to $1/f = T$, but with different scaling factors. The position of the maximum of the envelope, containing five oscillations, is at the center of the RC_n pulse and thus is affected the most. The reference points of the threshold methods shift with the period length of the first oscillations. To be able to

accurately compare up to now presented ToF estimation methods with the cross-correlation technique, the estimated ToF has to be corrected by the position of the reference point within the sent signal, depicted in Figure 4.37.

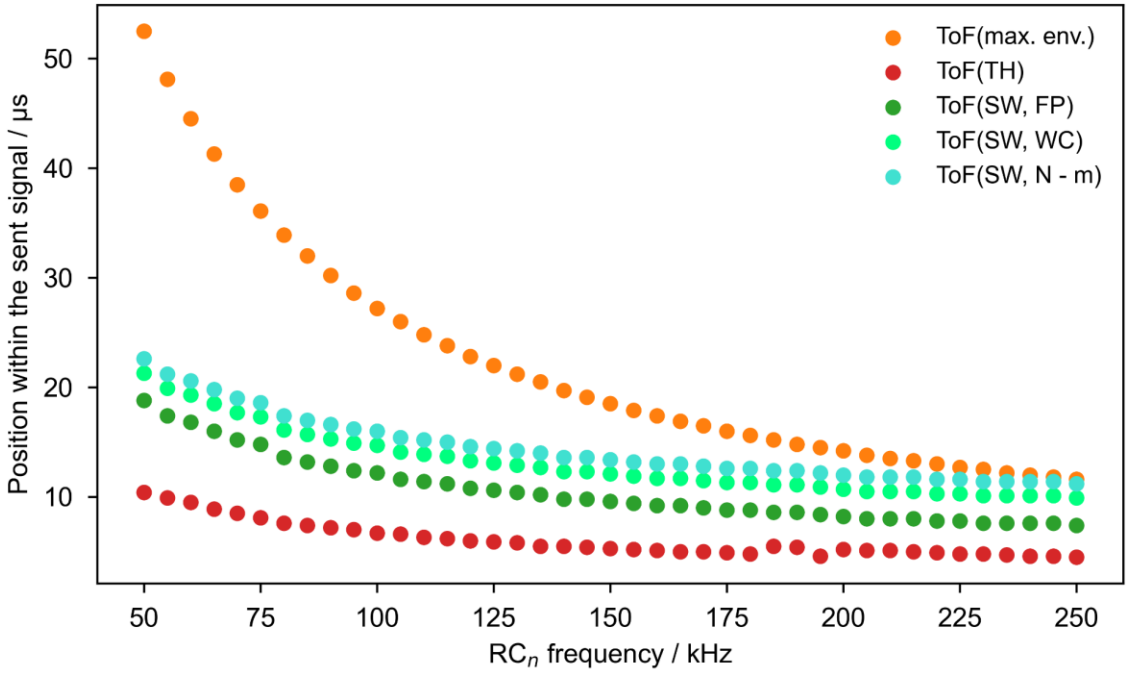

Figure 4.37: Position of the reference point within the signal that fulfills the respective ToF criterion. A decrease proportionally to $1/f = T$ is expected, since the position depends on the period length of the RCn pulse and the contained oscillations.

4.4.2.4 Cross-correlation method

As described in Chapter 2.3.6.3, cross-correlation is used to estimate the delay between two signals. If applied to a sent pulse and a transmitted signal, the wave packages in the signal should resemble the sent pulse. The cross-correlation peaks at the delay at which the resemblance is the largest. This delay can be taken as the time of flight of the respective wave package. By default, the correlation is influenced by the similarity of pulse and signal and the amplitude. Therefore, the wave package yielding the highest correlation is not necessarily the wave package with the best resemblance or the highest amplitude. If in doubt, a comparison with the ToF, yielded from the envelope method (in the chosen 50 kHz, 100% SoC example about 120 µs) and corrected by the position of the reference point within the sent pulse (53 µs), will allow to assign delays (67 µs) to wave packages. Figure 4.38 depicts the preprocessed (detrended and Tukey windowed) and filtered sent pulse and transmitted signal, as well as the cross-correlation for both inputs. Even though the preprocessed and filtered signals differ significantly, the cross-correlation is almost identical.

Here, the underlying process of multiplication of the frequency spectra of the inputs in the Fourier domain becomes apparent. Similar to applying a filter by multiplying the input with the filter coefficients, the cross-correlation is performed by point-by-point multiplication and shifting of the inputs with an additional integrating step. In this process, the input with the narrower frequency spectrum dominates the frequency spectrum of the cross-correlation output. Since the applied filter is specifically tuned to not alter the sent pulse's frequency spectrum significantly, the result is almost identical. The cross-correlation can be interpreted as a measure of the similarity of the two input signals.

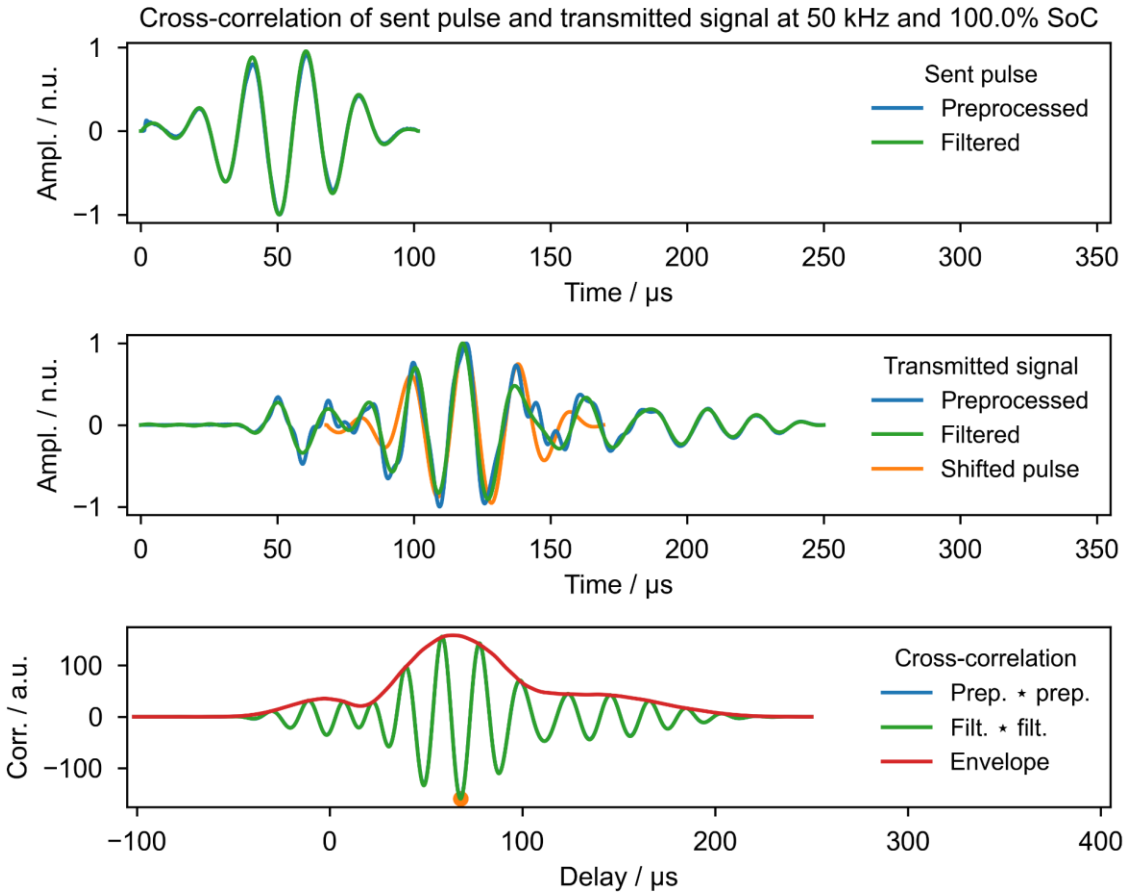

Figure 4.38: Cross-correlation (bottom) of the sent pulse (top) and transmitted signal (middle) at 50 kHz and 100% SoC. The sent pulse under load and the transmitted signal are recorded from battery cell LDA019. The pulse and signal were preprocessed and filtered prior to cross-correlation. In the bottom plot, an orange dot marks the absolute maximum of the cross-correlation. The corresponding delay is used to shift the pulse and overlay it with the signal in the plot in the middle, demonstrating that cross-correlation can be used to estimate the time of flight.

The cross-correlation in Figure 4.38 exhibits positive and negative correlation values. In this example, the negative peak at around 67 µs, marked by an orange dot, can be understood by shifting the sent pulse by about 67 µs and multiplying it with -1, leading to a maximum

overlap of the two. Without the multiplication, the two would be opposite, hence the negative correlation.

The envelope provided a good basis for the estimation of wave packages by peak picking if applied to the filtered signals. For the cross-correlation method, it would be desirable to use the envelope to pick the section of the cross-correlation in which to look for the local maximum and thereby estimate the time of flight of respective wave packages. Due to the proximity of the wave packages, the envelope of the cross-correlation does not provide distinct peaks for the first two wave packages at all frequencies over the whole SoC range, as shown in Figure 4.39. As exemplarily shown for 50 kHz and 100 kHz, the height of the peak changes with the strength of the correlation, as the distance and amplitude of neighboring wave packages change with SoC. Therefore, the position of the first peak shows huge jumps, e.g., from about 0 µs to about 70 µs for 50 kHz, as indicated by the colored dots. Without the local minimum between two peaks, the cross-correlation cannot be split up into sections, to search. Therefore, only the absolute maximum of the cross-correlation and its envelope can be utilized.

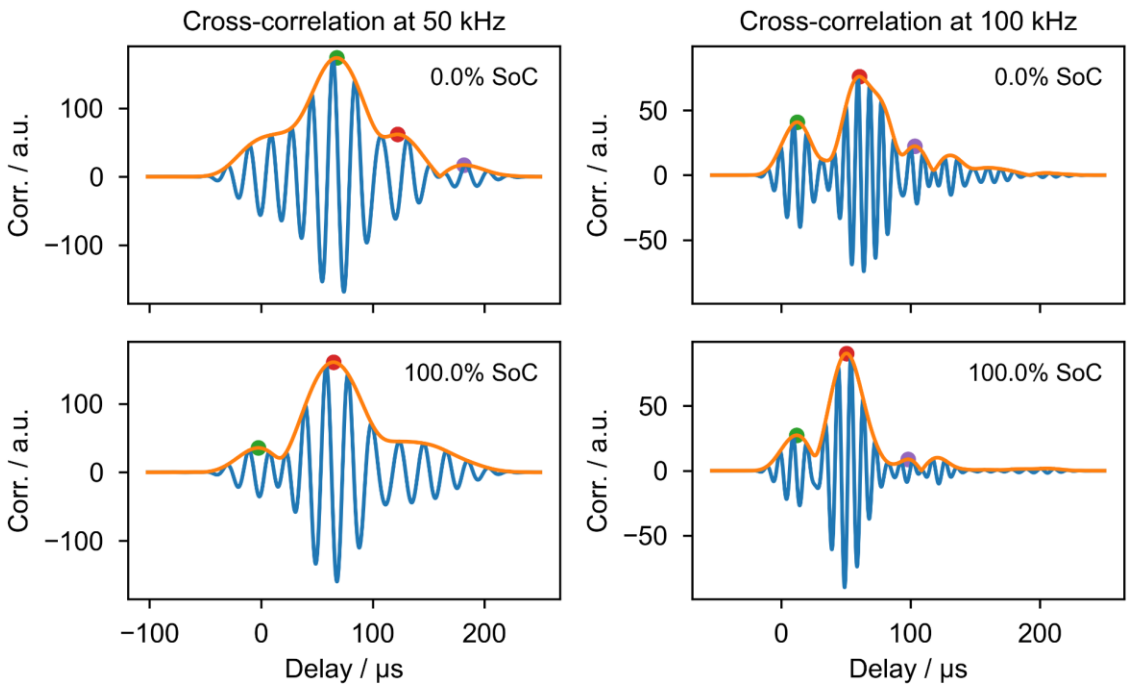

Figure 4.39: Cross-correlation of sent pulse and transmitted signal, analog to Figure 4.38, for 50 kHz and 100 kHz at 0% SoC and 100% SoC. The blue and orange curves represent the cross-correlation and its envelope, respectively. Colored dots mark the first three peaks in the envelope selected by peak picking. The distance and height of the peaks in cross-correlation change with SoC, leading to a change in the shape of the envelope. The disappearing of a distinct peak into a shoulder renders the envelope unfit for the estimation of a section, representing a wave package. Thus, only the absolute maximum of the cross-correlation and its envelope are used for ToF estimation.

4.4.2.5 Comparison of time of flight estimation techniques

As explained beforehand, the ToF estimation methods introduce an offset to the ToF, but the cross-correlation technique. Therefore, the ToF is corrected by the offset introduced by different reference points which are depicted in Figure 4.37. The resulting corrected ToF is compared with the delay, estimated by cross-correlation, in Figure 4.40 and Figure 4.41, for 50 kHz and 55 kHz, respectively. Analogous plots for more RC_n frequency can be found in Appendix, see Figure 8.8 and Figure 8.9.

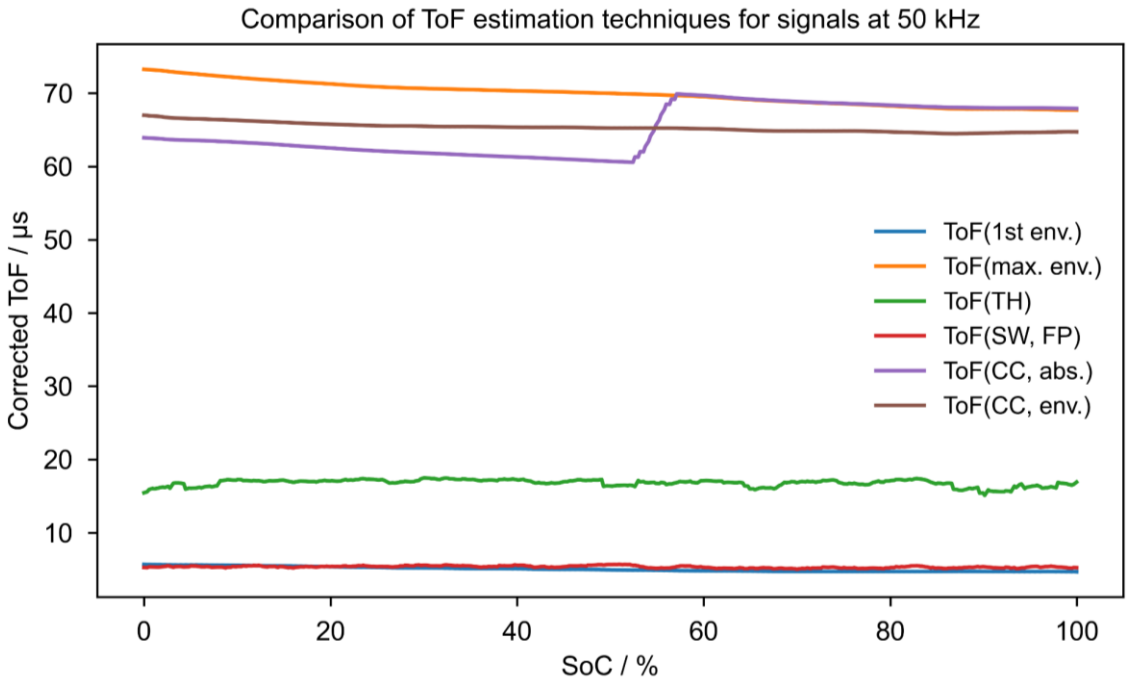

Figure 4.40: Comparison of ToF estimation techniques for signals, transmitted through LDA019, at 50 kHz in an SoC range of 0% to 100%. The opaque lines represent a 13-point rolling mean of the unfiltered estimates (not shown). After the correction of the ToF, estimated by different techniques, the offset introduced by those methods can be compared. For 50 kHz, ToF(SW, FP) and ToF(1st env) yield very similar results. The basic threshold method shows a comparably large offset and appears unstable. ToF(max. env.) and ToF(CC, abs.) coincide for a portion of the SoC range, while ToF(CC, env.) lies between the two. The discontinuity of ToF(CC, abs.) is not representative of the gradually changing mechanical properties of the battery cell with SoC and hence renders the ToF estimation method at least for some RC_n frequencies unsuited.

At 50 kHz, the ToF estimated by the first peak of the envelope – ToF(1st env.) – and the ToF estimated by the sliding-window method – ToF(SW, FP) – coincide, but show a small discrepancy in slope. As discussed before, the offset of the sliding-window depends on the choice of reference point within the sliding-window. Therefore, the displacement between the two is not necessarily a piece of evidence for a reliable ToF estimation result. As can be seen exemplary in Figure 4.41, depending on RC_n frequency, the displacement between

the two may vary. Judging from Figure 4.40, the course of the threshold-based ToF estimate is similar and almost parallel to the sliding-window estimate, but shows more unevenness and abrupt changes in slope. Based on the stability, the envelope is selected as the preferred method for the first wave package.

For the wave package with the maximum envelope at frequencies between 50 kHz and 100 kHz in the SoC range from 0% to 100%, three methods are evaluated. Besides the position of the maximum of the envelope – ToF(max. env.), the position of the absolute maximum cross-correlation – ToF(CC, abs.) – and of the maximum of the envelope of the latter – ToF(CC, env.) – are presented. While at 55 kHz (see Figure 4.41) the three methods yield very similar results, the offset and the monotony of the plots differ significantly for the three methods at 50 kHz (see Figure 4.40). The absolute maximum of the cross-correlation even shows a transition region with a big step around 50% SoC, coinciding with the maximum of the envelope afterward.

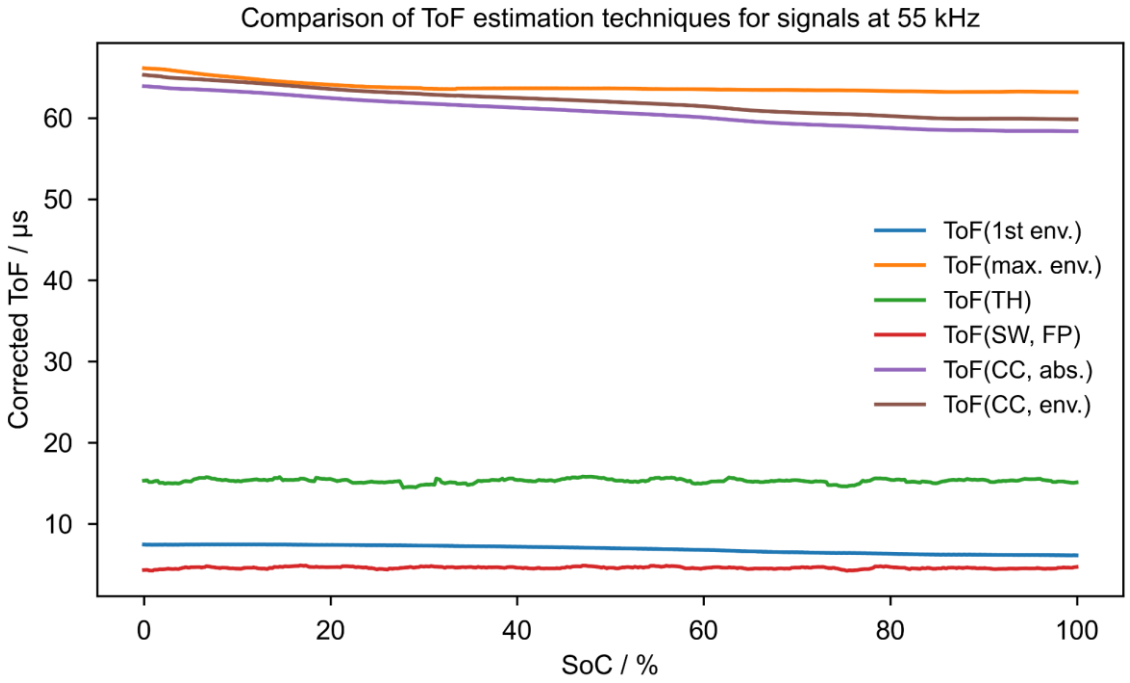

Figure 4.41: Comparison of ToF estimation techniques for signals, transmitted through LDA019, at 55 kHz in an SoC range of 0% to 100%. The opaque lines represent a 13-point rolling mean of the unfiltered estimates (not shown). At 55 kHz the results differ qualitatively from what is shown in Figure 4.40 – ToF(1st env.) and ToF(SW, FP) don't coincide. The cross-correlation-based techniques and ToF(max. env.) yield different results over the whole SoC range and therefore differ in slope and offset.

As seen in Figure 4.25, the frequency content of the transmitted signal changes with varying SoC, which is also present in the shape of the signal. The herein also present pulse-

broadening effect is visualized in the middle of Figure 4.38 by a comparison of sent pulse and received wave package. Le stated that the cross-correlation technique should not be used if the effect of pulse-broadening is significant [204] since it will yield inaccurate ToF estimates, which is supported by the findings of this study.

4.4.3 Summary of this subchapter

The first section of this subchapter treated the signal properties other than the ToF, namely the maximum signal amplitude, its position within the signal, and the transmitted energy content. This easy to extract properties already allowed estimating some basic trends with the SoC. In the frequency range of 50 kHz to 125 kHz, the maximum amplitude increases with SoC, and its position decreases with SoC. The RC_n frequency at which the absolute maximum within a dataset is reached shifts with SoC along the frequency axis and lies in the range of 70 kHz to 120 kHz. These trends were confirmed by the calculation of the transmitted energy content. Here, the overall amplitude maximum is achieved at 100 kHz while the energy content increases from 50 kHz to 100 kHz to subsequently fall off. From these three properties - amplitude maximum, its position within the signal, and the transmitted energy content – the RC_n frequency range in which the correlation of the latter and the SoC is best suited for state estimation could already be narrowed down to about 50 kHz to 125 kHz.

The second section of this subchapter opened with an analysis of the frequency spectra of sent pulses and received signals which were compared to lay the base for the subsequent signal processing and time of flight estimation. The frequency analysis, as a function of RC_n frequency and SoC, unveiled that the transmission through the battery cells dampens frequencies above a certain cutoff frequency – about 125 kHz significantly. Depending on SoC, bands at higher frequencies around 175 kHz are populated if the exciting RC_n waveform contains these frequencies. Then simple ToF estimation methods, based on thresholding, were tested for the detection of the first arrival in the transmission signals. To preprocess the signals for more complex ToF estimation methods, an FIR filter was designed to attenuate frequencies not contained in the exciting waveform. Subsequently, the envelope and cross-correlation techniques were tested to estimate the time of flight of the first and second wave packages in the transmission signals. All employed methods were finally compared regarding their robustness, reliability, and the offset they introduce to the ToF. As discussed by Le in 1998 [204], the different ToF estimation methods are expected to yield different results due to the pulse broadening effect in absorptive media. Judging from the presented data, the envelope-based ToF estimation method is best suited for

dispersive, absorptive media, as was stated by Le [204]. As showcased for the battery, being such a medium with SoC-dependent properties, the envelope method yields a consistent and stable ToF estimation and was therefore selected as the ToF estimation method of choice. In section 4.4.2.3, it was shown that due to the nature of the transmitted signals, a preprocessing is necessary to achieve this stable ToF estimate.

4.5 Assessing the suitability of different signal properties for SoC estimation

Best suited for SoC estimation would be signal properties whose course, plotted vs. SoC, is strictly monotone and unambiguous for charging and discharging. In the following, the signal properties will be assed regarding this requirement. In the beginning, the impact of cycle-to-cycle and C-rate variations on the signal properties' behavior is studied. Then the so-called dispersion – the frequency dependency of the signal properties – and the correlation of those signal properties with SoC are explored to study relevant trends in the data in a condensed fashion. As the display of the signal and the test of the estimation methods were performed exemplary on signals with an RCn frequency of 50 kHz, the following section will also treat the datasets at this frequency.

4.5.1 Cycle-to-cycle variation and hysteresis of signal properties

As battery cells consist of several layers with a particle coating, they are considered many-particle systems, exhibit inertia through limited transport and exchange processes in the electrolyte and active materials, and are therefore known to exhibit hysteresis in their mechanical and electrochemical properties. In a system, which is modeled by a dependent state variable and an independent variable, hysteresis describes the effect that the state variable's values depend not only on the independent variable but also on the prior value of the state variable thus its history. Within battery cells, prominent examples are cell volume and cell voltage. Within this chapter, the hysteresis of the signal properties, as estimated by the algorithms introduced in Chapter 4.4, will be described.

Figure 4.42 shows the corrected ToF of the first and second wave package, estimated by the first peak and the maximum of the envelope, during the first two cycles after the rest of a battery cell, cycled at 0.1 C. The start of the first cycle at 0% SoC is marked by a hollow dot, and the end of the second cycle at 0% SoC is marked by a filled dot. Both, the ToF of the first and the second wave package show a declining trend with SoC. The discharging half-cycle lies above the charging half cycle. While exhibiting a high coherence at high SoCs, the drift between cycles is especially visible at low SoCs. When comparing these two

cycles, the effect of relaxation on the signal properties becomes apparent. The first cycle is affected by the prior rest, as its start lies much lower than the start of the second cycle (turning point between the two dots at 0% SoC). This effect is much more pronounced for the second wave package, as will be shown for subsequent cycles later in this section. Another distinguishing feature is the presence/absence of a crossing point of charging and discharging half cycle. Even though the second wave package's plot doesn't show a crossing point, both wave packages exhibit a change of slope around 80% SoC that can be linked to the P2 peak, visible in the incremental capacity analysis of the studies battery cells, as shown in section 4.1.3, and might be a result of drastically changing mechanical properties of the positive active material at the respective SoC.

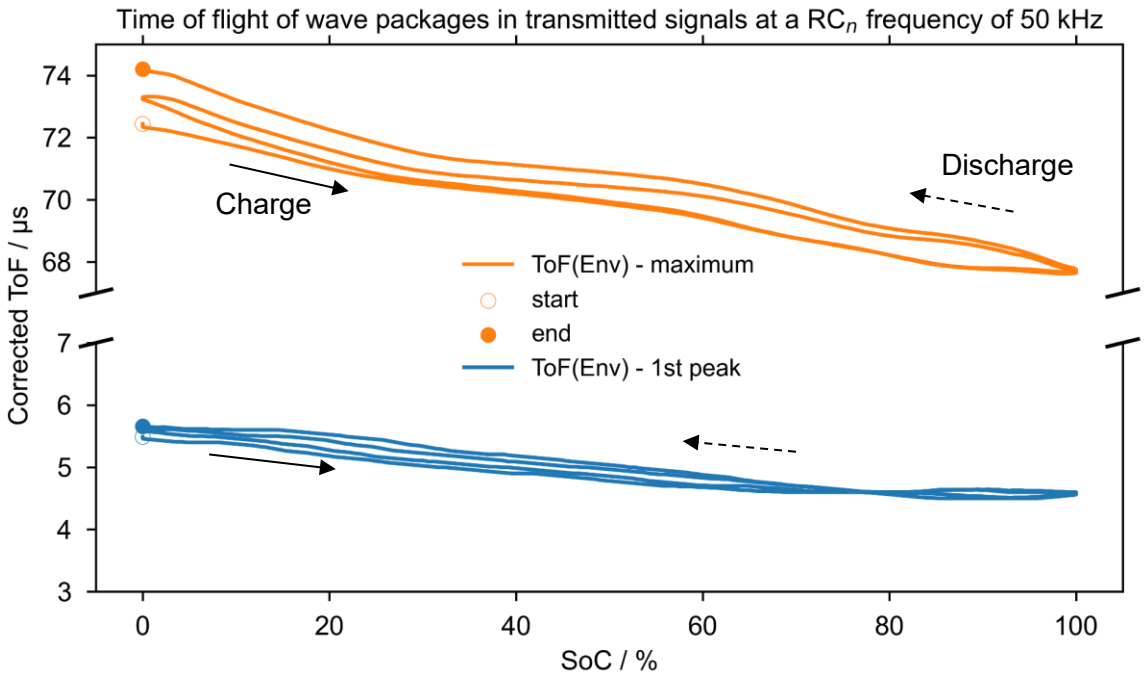

Figure 4.42: Corrected time of flight, estimated by the envelope method, for battery cell LDA019 cycled at 0.1 C during the first two cycles after rest. The beginning of the first cycle is marked by a hollow circle and the end of the second cycle is marked by a filled circle. In both, the ToF of the first and second wave package, the effect of the relaxation during a rest period prior to the first cycle is visible. The course of both ToF shows a change of slope around 80% SoC that leads to a crossing of charge and discharges half cycle for the first wave package. This behavior can be correlated with the position of the P2 peak in the incremental capacity analysis of the studied battery cells.

The area between the curves of charging and discharging half cycle can be taken as a measure for the hysteresis of this signal property while comparing the slope and the delta of the curve with the resolution can give a hint on the potential accuracy of an SoC estimate. Another influence on the SoC estimation accuracy is the reproducibility from cycle to cycle. The course of the ToF, estimated by the first peak and the maximum of the envelope, during

the first four cycles after rest are plotted in Figure 4.43 and Figure 4.44, respectively. For the ToF estimated by the first peak, the course shows a mild hysteresis between charging and discharging half-cycles and the overall trend remains the same overall depicted cycles. While cycle four lies in between the other cycles for the linear section until about 75% SoC, the plateau from about 75% to 100% SoC is shifted to higher ToF. This plateau might be linked to the mechanical property changes of the active materials in this SoC range, as estimated by the peaks P2 and N1 in the incremental capacity analysis, see Figure 4.6. Due to the sampling of the transmitted signal into discrete steps of 0.1 µs, the resolution of the ToF estimate is limited to the same step size. Due to the small delta between 0% and 100% SoC, minor fluctuations in the estimated ToF, by only a single bin, become very visible. While the mostly linear course of the ToF of the first arrival is very well suited for SoC estimation, the relatively large fluctuations compared to the total delta and the shallow section above 80% SoC are unfavorable for a precise SoC estimation. Especially, the ambiguity of the shallow section might lead to an increased inaccuracy in this SoC range if this signal property is used alone. A combination with another signal property such as the ToF of the second wave package or the transmitted energy content might be able to compensate for this.

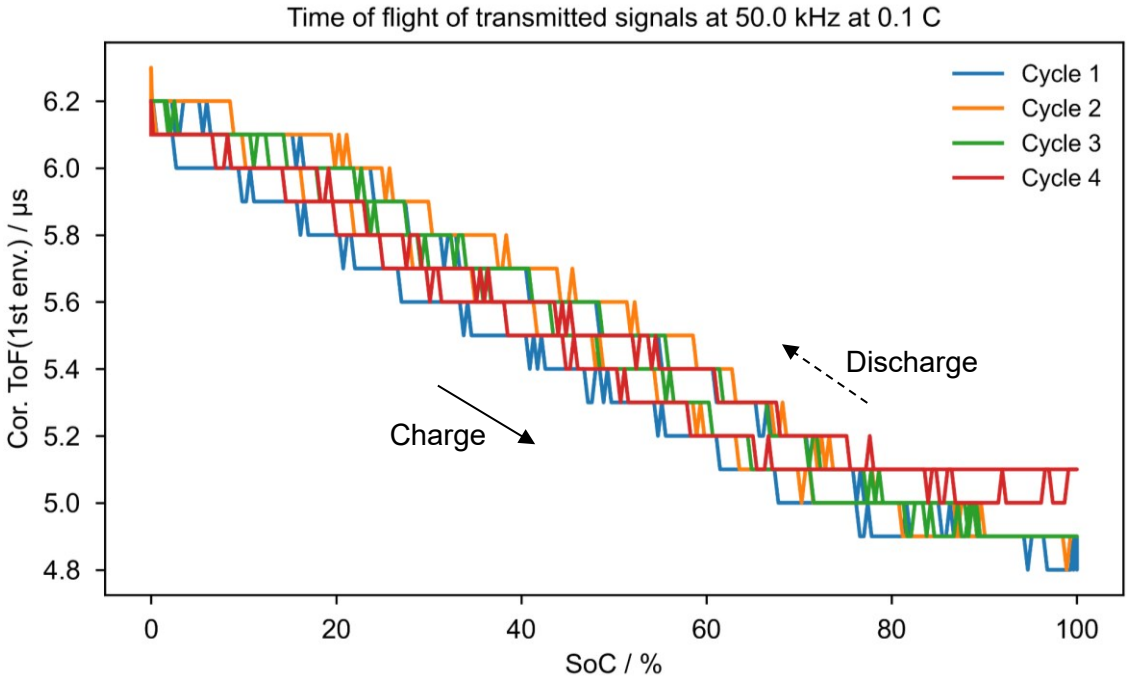

Figure 4.43: Corrected time of flight of the first arrival in the signals, transmitted through LDA019 at an RC_n frequency of 50 kHz during four cycles at 0.1 C after rest, estimated by peak picking of the envelope of the filtered signal. Until about 80% SoC, the slope of the course is monotonously decreasing, merging into a plateau that extends up to 100% SoC. The incremental capacity analysis in section 4.1.3 suggests that this plateau might result from opposing mechanical property changes of the positive and negative active material in this SoC range.

Due to the higher delta in ToF, estimated by the maximum envelope, the course is more fine-grained, and more detailed features are distinguishable. The cycles in the data are cut to start after the rest of the prior with the first charging and to include the rest after the discharge. The discharge half cycle can be identified by the vertical line at 0% SoC, representing the relaxation during rest. In all four cycles, a common trend is observed - the course of ToF vs. SoC can be divided into three sections of about 33% SoC with differing slopes, which is reminiscent of the plot of cell thickness increase plotted vs. SoC in Figure 4.7. The middle section is the shallowest. The section between 0% and 30% SoC is the steepest and shows a homogenous slope. The Section from 65% to 100% SoC is declining for the most part but shows a plateau from about 85% SoC during charging and an inverted parabolic shape during discharging. Within the data an underlying drift is present - in cycles one to three, the discharging half-cycle lies above the charging half cycle and the spacing between charging and discharging reduces step by step, until the discharging curve intersects with the charging curve at around 55% SoC in cycle four. This described shift might be associated with a break-in period in the first up to 12 cycles of a battery cell after formation. This break-in period was described by Knehr *et al.* in 2018 [25] as a few cycles post-formation needed to reach a steady-state. In these few initial cycles, the mechanical behavior of battery cells is expected to differ from steady-state, as the repeated breathing of the electrodes and the cracking of active material particles allows to access until then electrochemically inactive surfaces through the wetting with electrolyte [109].

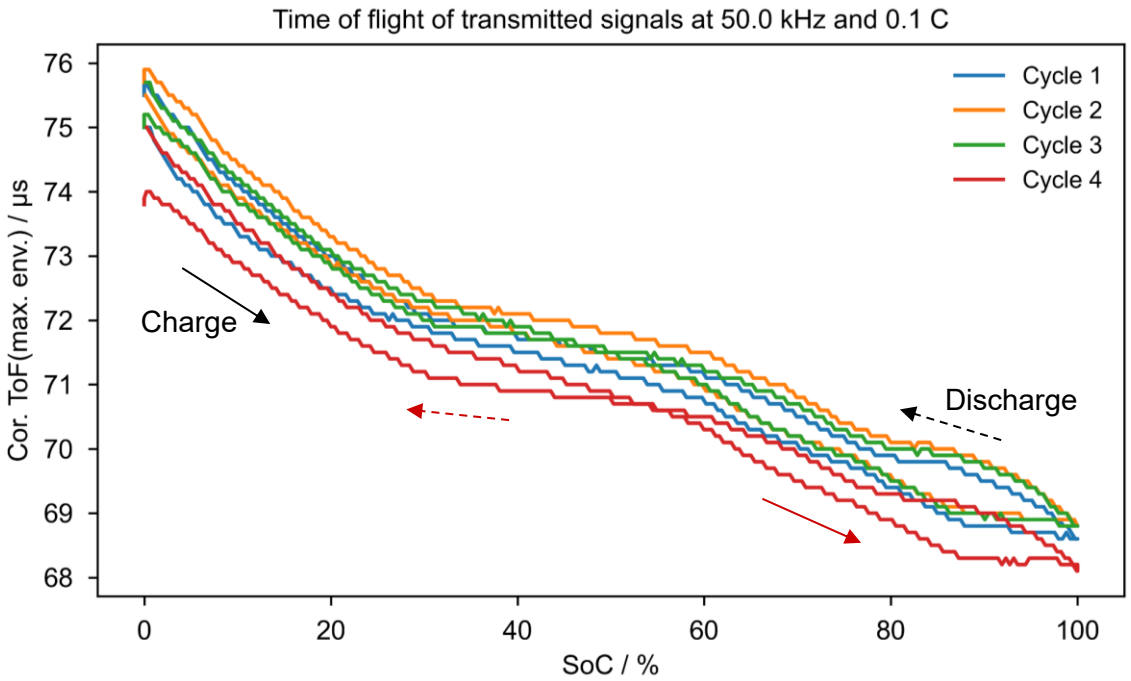

Figure 4.44: Corrected time of flight at the maximum envelope of the filtered signals, transmitted through LDA019 at an RC_n frequency of 50 kHz during four cycles at 0.1 C after rest. The course of ToF vs. SoC can be divided into three approximately equally sized sections of a differing slope. The last of the three, close to 100% SoC exhibits a plateau during charging and an inverted square-root-like shaped section during discharge, leading to a significantly larger area between charging and discharging half cycle, compared to other sections of the curve. Overall, an underlying drift in the data leads to a reduced area between the charging and discharging curves from cycle one to three and leads to an intersection of the curves in cycle four.

The described break-in period can also be seen in the datasets of this study. Since the end of charge point – the turning point of the plots in Figure 4.44 – is a well-defined state in each cycle. As the state is prepared through CC-CV charging, with the CV step being the same at each C-rate, it serves as a reference point for the vertical shift in the cycle. As depicted in Figure 4.45, the development of the minimum of the corrected time of flight in each cycle illustrates the break-in process. During the first four experiments, 0.1 C and higher C-rate (0.5 C and 0.25 C) cycles were alternated. During those 16 cycles, the value of the minimum appears to reach a steady-state after about 13 cycles. This state seems to not be altered by the subsequent high C-rate cycles (0.75 C and 1.0 C). The alongside depicted maximum of each full cycle shows a much higher and also non-unidirectional variation during the different experiments. Nevertheless, the maximum at a certain C-rate is shifted relative to the minimum by a fixed amount, specific to a certain C-rate. The effect of C-rate variation on charging and discharging half cycle will be discussed in the next subchapter.

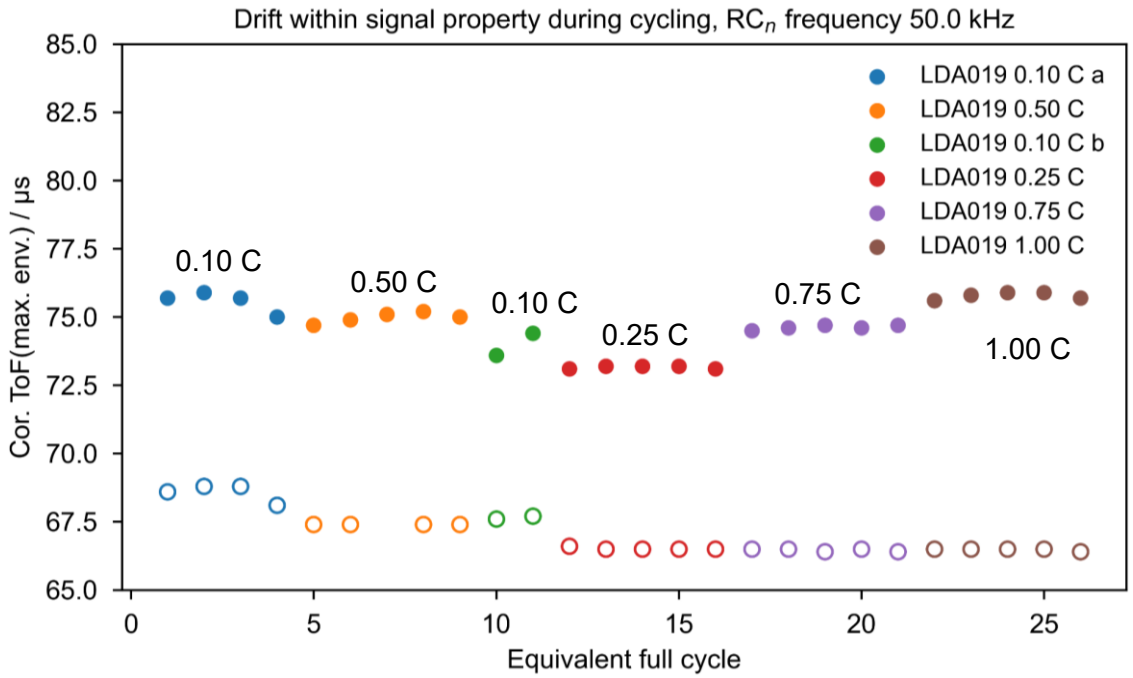

Figure 4.45: Plot of the minimum (hollow circles) and maximum (filled circles) in each cycle of the corrected ToF, estimated by the maximum envelope. The data points represent a cycle each, and are plotted in the order the experiments were performed on a single cell, LDA019. During the first 11 cycles, the minimum still varies significantly, while reaching a steady state in the following cycles. Cycle seven, at 0.50 C, has been masked as an outlier caused by a faulty signal at 41% SoC.

In other signal properties, such as the transmitted energy content – the integrated squared amplitude of the signal, the first cycle after rest does also differ significantly from the subsequent cycles at the same C-rate, as depicted in Figure 4.46. As energy content (EC) and SoC are positively correlated, the upper half cycle represents the charging branch. Relaxation, taking place during the rest periods at 0% and 100% SoC is visible as a rising vertical line. In the range of 0% to 5% SoC, the slope of the curve changes from negative to positive. This change of slope might originate from mechanical property changes in the active material associated with the N3 peak and the decline of the P1 peak in the incremental capacity analysis within this SoC range. Therefore, the energy content to SoC relation is ambiguous for the range of 0% to 20% SoC. Taking only instantaneous values into account, this would render transmitted energy content unsuitable as an input for SoC estimation. When including historical data (e.g., values of transmitted energy content and electrical current) the feature of slope sign change could act as an alarm that the last 5% SoC is reached during discharge. The influence of the break-in period is not present in the same distinct way for this signal property, as can be seen in Figure 4.47. The delta between minimum and maximum in a full cycle seemingly depends on C-rate, which will in detail be studied in the following subchapter.

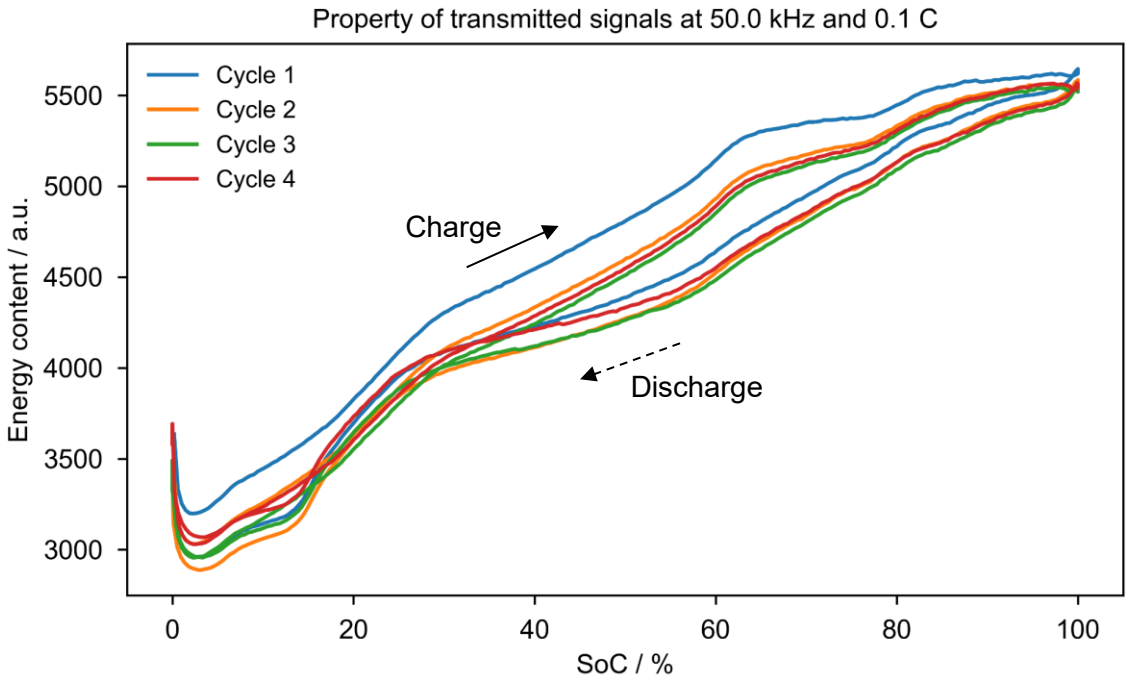

Figure 4.46: Transmitted energy content vs. SoC during four 0.1 C cycles, measured at an RC_n frequency of 50 kHz. Here the data of cell LDA019 is displayed. As energy content and SoC show a positive correlation, the charging half cycle's curve is the upper one. For a purely instantaneous value-based SoC estimation, the change of slope between 5% and 0% SoC is difficult to coop with but could act as an alarm during discharge to mark low SoC if historical data is taken into account. The change of slope in this range might originate from the N3 peak in the incremental capacity analysis associated with this SoC range.

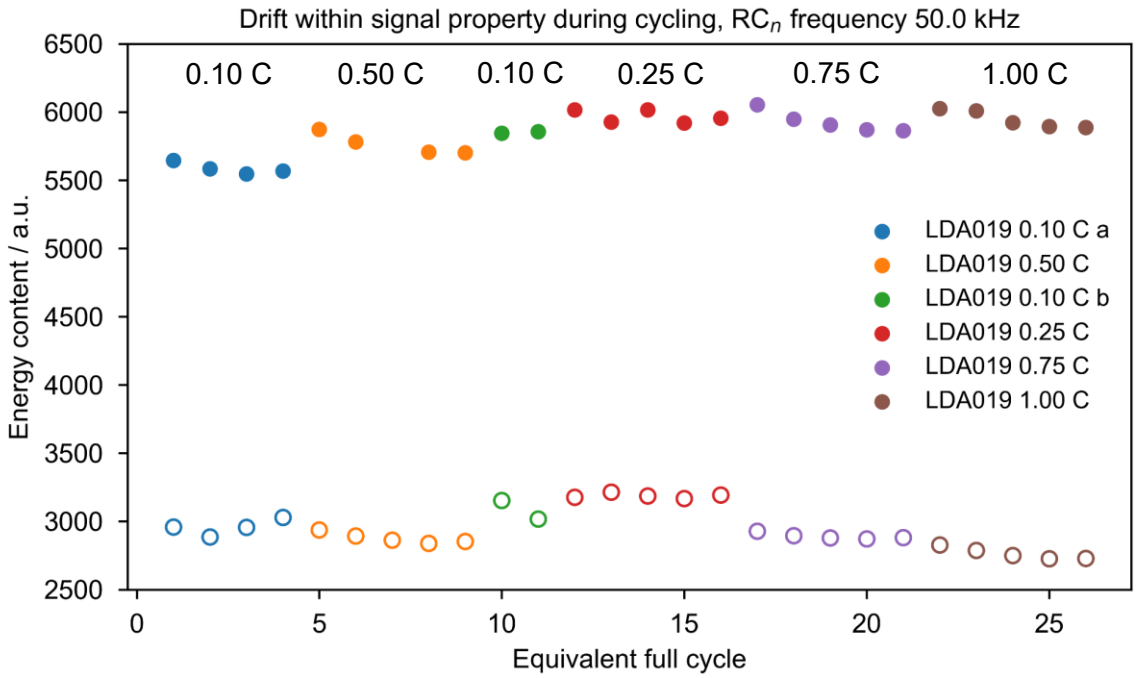

Figure 4.47: Plot of the minimum (hollow circles) and maximum (filled circles) in each cycle of the transmitted energy content. The data points represent a cycle each, and are plotted in the order the experiments were performed on a single cell, LDA019. Minimum and maximum of the transmitted energy content don't exhibit the same break-in characteristic as their counterparts in ToF but show a similar C-rate dependency.

4.5.2 C-rate dependency of signal properties

Here, the effect of the C-rate on the extent of the hysteresis is studied exemplarily on cells at an RC_n frequency of 50 kHz. The dataset contains five different C-rates. The cell was cycled four to five times at each C-rate. Due to the effect of the prior rest period, as demonstrated in Figure 4.42, the first cycle at each C-rate is disregarded and the second cycle is displayed here.

Figure 4.48 depicts the corrected time of flight, estimated by picking the first peak of the envelope of the filtered, transmitted signal. The datasets at different C-rates were shifted to align at their minimum around 85% SoC. The most prominent trend here is an increase of the area between charge and discharge curve with C-rate, in the linearly decreasing section below 85% SoC as well as in the section above 85% SoC with an opposite slope. In the delta of the ToF, no trend with C-rate is visible.

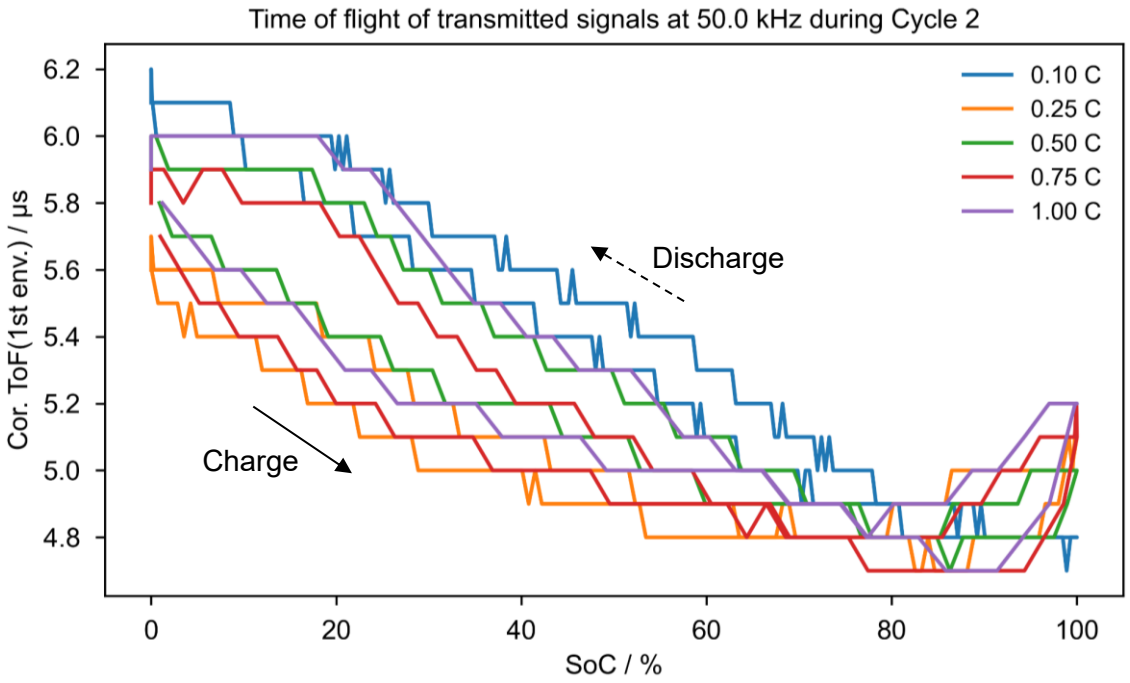

Figure 4.48: Plot of corrected ToF, estimated by the first peak of the envelope of the filtered signal, transmitted through LDA019. The second cycle of an experiment at each C-rate is plotted. Cycles from different C-rates have been shifted vertically to align at their minimum. With increasing C-rate, the area between charging (lower curve of each color) and discharging (upper) half cycle, which is a measure for the hysteresis, increases.

In Figure 4.49 the corrected time of flight (ToF), estimated by the maximum of the envelope of the filtered, transmitted signal at 50 kHz is plotted vs. SoC. The second out of four to five cycles at a given C-rate is displayed. The datasets at different C-rates were vertically shifted to align at 100% SoC, which corresponds to the minimum ToF. During charging (the lower curve of a color), the curve exhibits an increasing number of plateaus with an increasing C-rate. While for the 0.1 C curve a single plateau in the mid-SoC range is visible, two additional inflections at about 70% and 80% SoC are incorporated at higher C-rates, forming a second plateau. Alongside this effect, the shallow section between 40% and 60% SoC decreases in slope with increasing C-rate, and the prior section from 0% to 30% SoC increases in steepness. During the rest period following the CC-CV charging step, the relaxation is equally small for all C-rates. As described before, the CV step, equal for all C-rates, seems to be the dominant element at this point. For the discharging half cycle, the effect of C-rate variation is even more pronounced. Starting from 100% SoC, the initial climb increases in steepness with C-rate, stacking the curves in order of C-rate on top of each other. Subsequently, the area between the charging/discharging curves increases with C-rate. The extent of the relaxation at the end of each cycle is similarly affected and increases with C-rate.

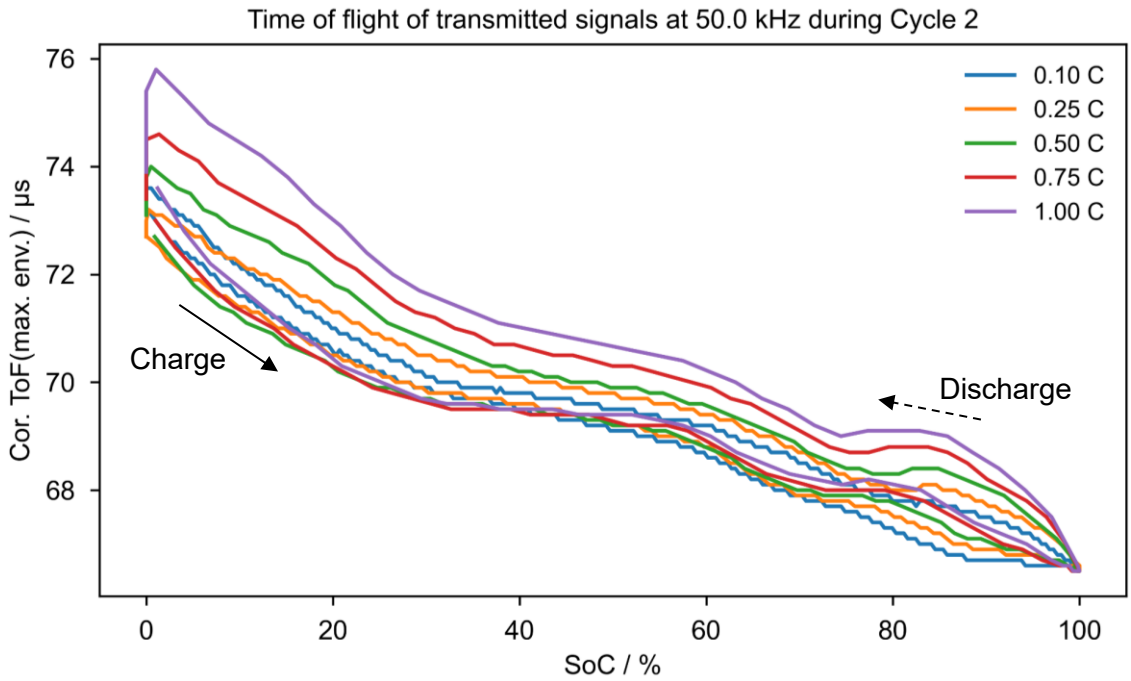

Figure 4.49: The second cycle after rest, cycles from different C-rates have been vertically shifted to align at 100% SoC to make a comparison of charging/discharging specific features easier. Here, the data of cell LDA019 is displayed. During charging (lower curve of a color/C-rate), the steepness of the first third increased with C-rate and the middle part flattened, while the last third exhibits a pronounced “S”-shape. During discharging similar trends continue as the steepness of the climbing curve increases with C-rate, leading to a more pronounced relaxation after discharge.

To explain this, the model of macroscopic and microscopic lithiation can be employed. The instantaneous cell voltage during charging/discharging reflects the microscopic lithiation at the interface between active material particles and the electrolyte. It includes several overpotentials and the voltage drop on the internal resistance of the battery cell. But even for a substantial amount of time in a subsequent rest period, the cell voltage does not represent the electromotive force of the system at that macroscopic lithiation or the state of charge. Due to diffusion limitation, the surface and shell of an active material particle are higher (charging) or lower (discharging) lithiated than the core of the said particle, compare to the two-phase core-shell model for single-crystal graphite proposed in [11]. This gradient is reduced during rest periods by relaxation, finally leading to an equilibrium state at which the cell voltage corresponds to the electromotive force at the macroscopic lithiation of the battery cell. With high C-rates, the (de-)lithiation process at the surface of an active material particle is much faster than the diffusion process. Therefore, the gradient increases with C-rate. As described in Chapter 2.1.1, the mechanical properties of the active materials change with lithiation and are not a linear function of the degree of lithiation. The overall change is dominated by the change within the negative active material. In the case of graphite, this process happens in stages [11,266], with the stage of highest lithiation degree

exhibiting the highest volume increase compared to the unlithiated stage – up to 10% – and the highest gain in elastic modulus – up to 280%. As a consequence, a battery cycled at higher C-rates contains a higher volume fraction of active material at the state introduced by the charging/discharging process than a battery cycled at a lower C-rate. Applying this to the discharging process means that at a higher C-rate the battery cell contains a higher volume fraction at a smaller elastic modulus and volume, leading to a reduced speed of sound and an increased ToF. For the charging half-cycle, the described process is not as pronounced, as the state at the end of the charging process is prepared by constant voltage charging at the end of charge voltage, independently of the applied C-rate.

For the transmitted energy content (EC), shown in Figure 4.50, a similar C-rate dependency can be observed. The second out of four to five cycles at a given C-rate is displayed. The datasets at different C-rates were vertically shifted to align at 100% SoC, which corresponds to the maximum transmitted energy content. A positive correlation between SoC and transmitted energy content is observed. Therefore, the upper half cycle of a C-rate, respective color, is the charging half cycle. Starting at 0% SoC, an initial decay in parabolic shape is observed, which depth is proportional to C-rate, stacking the curves on top of each other, with 0.1 C being at the top and 1.0 C at the bottom. This order remains intact up to 100% SoC with 0.25 C and 0.5 C overlapping for the most part. During discharge, the splitting of the set of curves is analogical. Again, the curve at 1.0 C is the outermost and the relaxation at 0% SoC is the largest within the set of curves. The transmitted energy provides information on the dampening of the signal. This dampening has several components, e.g., the scattering of the sound waves within the sample, the transformation efficiency from an electrical signal to ultrasound and vice versa, and the coupling efficiency of ultrasonic transducers to the battery cells, and thus might be affected by several parameters. It is known, that the speed of sound and the rate of dampening is positively affected by the stiffness of the interrogated sample. For now, the increase in E-modulus and stiffness thereby can serve as an explanation for an increase in signal amplitude and transmitted energy content with increasing SoC, as speed of sound c is proportional to $\sqrt{E/\rho}$, with density ρ and E-modulus E. Since the nature of the sound propagation within the battery cells at the frequencies, used in this study, is not entirely elucidated, the effect of C-rate on the transmitted energy content cannot be settled, yet.

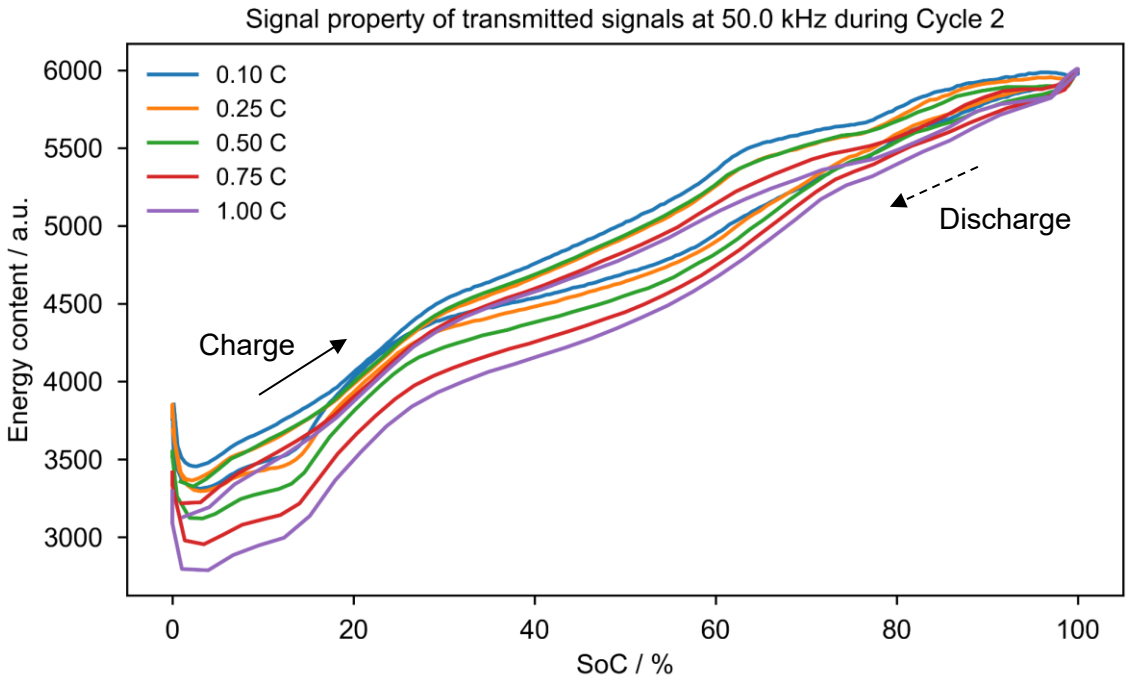

Figure 4.50: The second cycle after rest, cycles from different C-rates have been vertically shifted to align at 100% SoC to make a comparison of charging/discharging specific features easier. The steepness of the curves, during charging and discharging, increases with C-rate, leading to a splitting of the set of curves in order of decreasing the C-rate. Here, the data of cell LDA019 is displayed.

Overall, the influence of C-rate on the relation of signal properties and SoC might result in an increased estimation inaccuracy. This might apply to a machine learning model that was trained with datasets of uniform C-rate and is tested with datasets of non-uniform C-rate throughout the cycle(s), as is the case in this study. To research this, the correlation between single signal properties and SoC will be assessed in a separate subchapter.

4.5.3 Dispersion of signal properties

In the prior subchapters, the datasets were analyzed at 50 kHz, serving as an example for the analysis at all RC_n frequencies, contained in the datasets. In this subchapter, the analysis of the datasets will be displayed in a summarized fashion. The values of the chosen signal properties are picked at three distinct points and averaged over all completed full cycles at a certain C-rate. The hereby obtained standard deviation is represented by a vertical error bar in the plots. The mean values are connected by lines whose style corresponds to an SoC – 0% (dotted line), 50% (dashed line), and 100% SoC (solid line).

In Figure 4.51, the ToF as estimated by the first peak of the envelope of the filtered, transmitted signal is plotted versus RC_n frequency for three SoC. As can be followed from

the dotted lines (0% SoC) lying in between the dashed (50% SoC) and the solid lines (100% SoC), the slope of the ToF vs. SoC curve changes sign at least once between 0% and 100% SoC, forming a parabola-like curve. Otherwise, the line corresponding to different SoCs would appear in ascending (positive slope) or descending order (negative slope). An example of this behavior can be found in Figure 4.48.

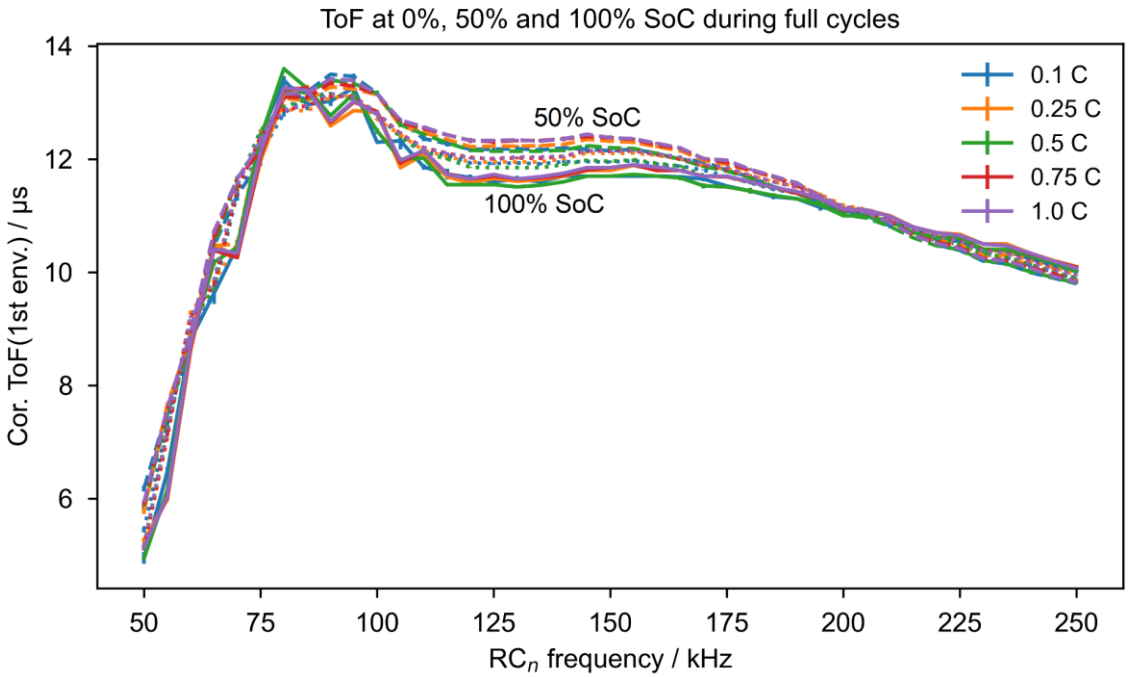

Figure 4.51: Plot of corrected ToF, estimated by the first peak of the envelope of the filtered, transmitted signal vs. RC_n frequency. The solid line represents the value at 100%, the dashed line at 50%, and the dotted line at 0% SoC. Available full cycles from the dataset of cell LDA019 were averaged, and the standard deviation is displayed as an error bar, as indicated by the colored legend. Due to their small magnitude, the error bars in the plot are barely visible.

Analogically, the ToF estimated by the maximum of the envelope of the filtered, transmitted signal is depicted in Figure 4.52. Above 205 kHz the second wave package could not be identified at all C-rates in all cycles. Here, the first peak of the envelope and the envelope maximum coincided, leading to a ToF result that is discarded due to laying outside the bounds defined by the regular continuous evolution of the ToF. Subsequently, the plotted data points in this frequency range are made up of single points, thus not having an error bar, or are cut from the plot for being outliers. Judging from the descending order (0% to 100% SoC) in which the lines, corresponding to different SoCs, are drawn in the plot, the ToF decreases with increasing SoC for most RC_n frequencies in the range of 50 kHz to 200 kHz. Above 205 kHz the lines of 0% and 100% SoC partially overlap, making a low correlation or positive correlation between ToF and SoC at these RC_n frequencies likely. The trends, observed in the dispersion of the first and second wave package's ToF, are for

parts of the frequency range opposite to each other, suggesting that the two wave packages originate from different modes of sound propagation. Several propagation modes are potential candidates - plate waves, where the symmetrical and asymmetrical modes could each make up one of the wave packages; bulk pressure and shear waves, as described by Biot; surface waves traveling along the hull of the battery cells. At the moment none of those can be ruled out completely and future research should focus on understanding which propagation mode or combination of propagation modes is most dominant at which frequency.

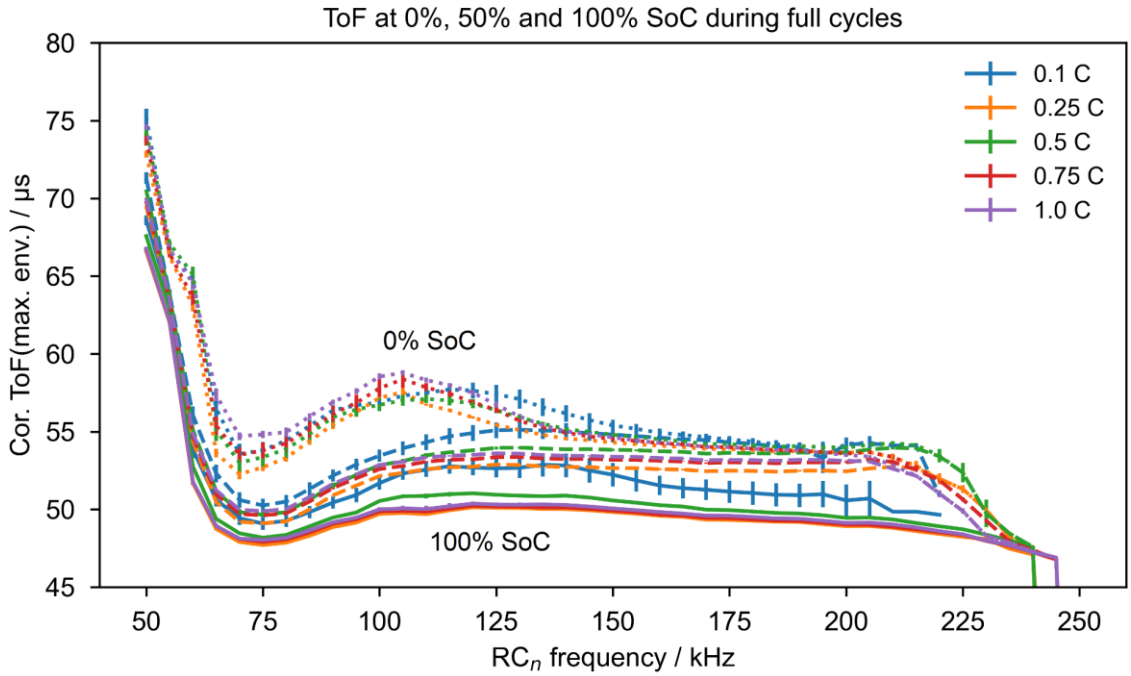

Figure 4.52: Plot of corrected ToF, estimated by the maximum envelope of the filtered, transmitted signal vs. RC_n frequency. The solid line represents the value at 100%, the dashed line at 50%, and the dotted line at 0% SoC. Available full cycles from the dataset of cell LDA019 were averaged, and the standard deviation is displayed as an error bar, as indicated by the colored legend. The y-scale was adjusted to cut where no second wave package could be identified (above 240 kHz) and envelope maximum and first peak fall together.

Finally, the transmitted energy content of the transmitted (unfiltered) signal is depicted in Figure 4.53. The prominent step in the data between 75 kHz and 80 kHz was previously explained in Chapter 4.4.1 – it is a consequence of adjusted excitation amplitude in the frequency range below 80 kHz, which is chosen to avoid saturation of the ADC at the receiver side. When considering the lines of a selected C-rate, almost equidistant spacing of the lines corresponding to 0%, 50%, and 100% SoC is visible, which is in good agreement with the almost linear course of energy content vs. SoC, seen in Figure 4.50. Especially at 100% SoC, which serves as a reference point independent of the C-rate in all cycles, the

line of 0.25 C, 0.75 C, and 1.0 C overlap at almost all frequencies, once again reinforcing that the break-in period of that particular cell had been completed during the cycles at 0.1 C and 0.5 C. Overall, the transmitted energy content peaks at different RC_n frequencies. Depending on C-rate, the completion of the break-in period, and the SoC, the maximum lies between 100 kHz and 110 kHz, which was also identified as the turning point in Figure 4.24.

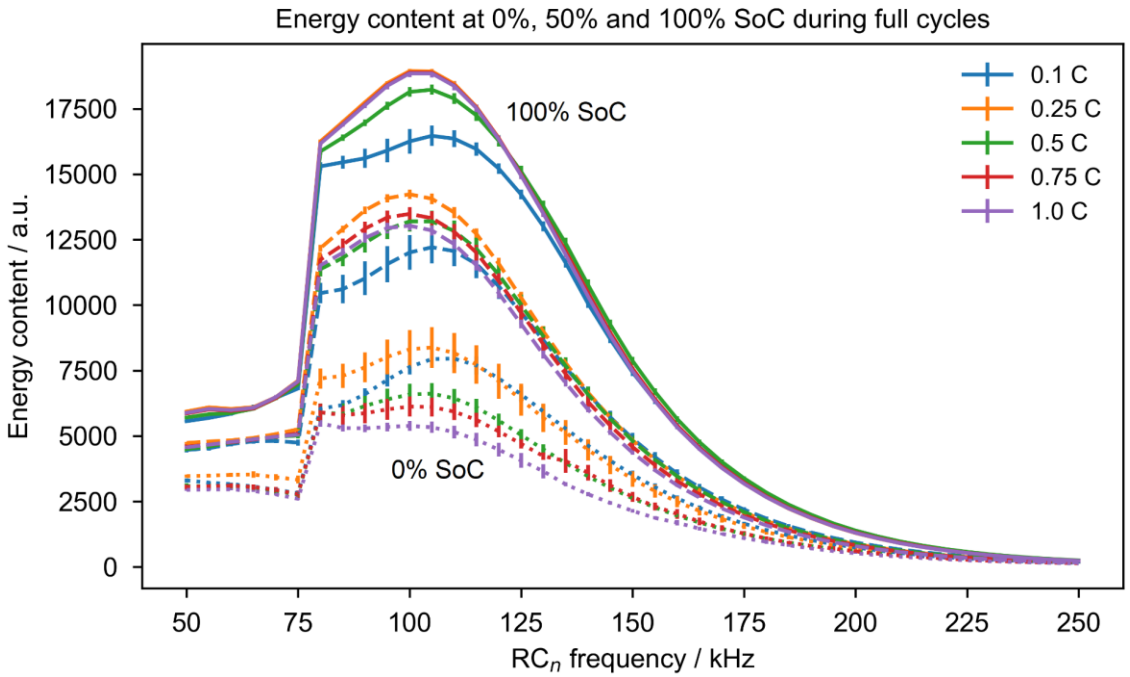

Figure 4.53: Plot of transmitted energy content, estimated by the integration of the squared amplitude of the unfiltered, transmitted signal vs. RC_n frequency. The solid line represents the value at 100%, the dashed line at 50%, and the dotted line at 0% SoC. Available full cycles from the dataset of cell LDA019 were averaged, and the standard deviation is displayed as an error bar, as indicated by the colored legend. The step in the data between 75 kHz and 80 kHz is caused by an adjusted excitation amplitude below 80 kHz, which was chosen to avoid oversaturation of the receiver ADC.

4.5.4 Correlation of signal properties and SoC

With the aid of the Pearson correlation coefficient, the linear correlation between two sets of data can be measured. Since estimating the SoC from our data is the goal, a good correlation between signal properties of interest and SoC is favorable. The correlation coefficient can take values between -1 and 1 with negative values describing an opposite trend in the correlated data and positive values describing a trend in both datasets with a common direction. Low absolute values, close to 0, state that there is little (linear) correlation between the datasets. High absolute values, close to -1 or +1, indicate a good correlation between the compared datasets [267,268]. The three signal properties, assessed in this chapter were tested against SoC. The correlation of SoC and the time of

flight, estimated by the first peak in the envelope of the filtered, transmitted signal – ToF(1st env.), is displayed in Figure 4.54. Here, the ToF during all cycles, available in the dataset at a certain C-rate, usually four to five, were averaged. The error bar states the standard deviation. In the frequency range of 50 kHz to 110 kHz, SoC and ToF(1st env.) exhibit a changing correlation with negative and positive values. As seen exemplary in Figure 4.48, the ToF vs. SoC plot shows a section with the opposite slope. This means that the value of ToF at 50% SoC potentially lies below the values at 0% and 100% SoC, as seen in Figure 4.51. Since the correlation takes all points into account sections of opposite slope partially compensate for each other as negative and positive correlation, leading to an overall reduced correlation. In cases where the slope of a linear fit to the ToF vs. SoC plot would be almost horizontal, e.g., the ToF is scattered around a constant value, the correlation coefficient is also zero or close to zero. Therefore, the frequencies at which the correlation in Figure 4.54 takes values around zero, can be correlated with the frequencies at which the ToF at 0%, 50%, and 100% SoC coincide in Figure 4.51. When now comparing the frequency range from about 120 kHz to 250 kHz in the two graphs, the transition from a negative correlation (ToF at 100% below ToF at 50% and 0% SoC), as low as -0.97, to a positive correlation (ToF at 100% above ToF at 50% and 0% SoC), as high as 0.94, becomes plausible. The behavior in the frequency range of 50 kHz to 120 kHz can be explained analogically. Here, the order in which the ToF values at 0%, 50%, and 100% SoC appear, changes several times, as can be seen in Figure 4.51.

The variation between the datasets of different C-rates – especially for the 0.1 C dataset – was described already in Chapter 4.5.1, see Figure 4.45 and Figure 4.47, and attributed to the break-in period. Therefore, it is unclear if the variation in the correlation between the different C-rates is similarly related to this effect. In any case, this shows that an SoC estimation based on the ToF, estimated by the first peak of the envelope, will lead to largely different estimation accuracy if applied to cycles with non-uniform C-rate.

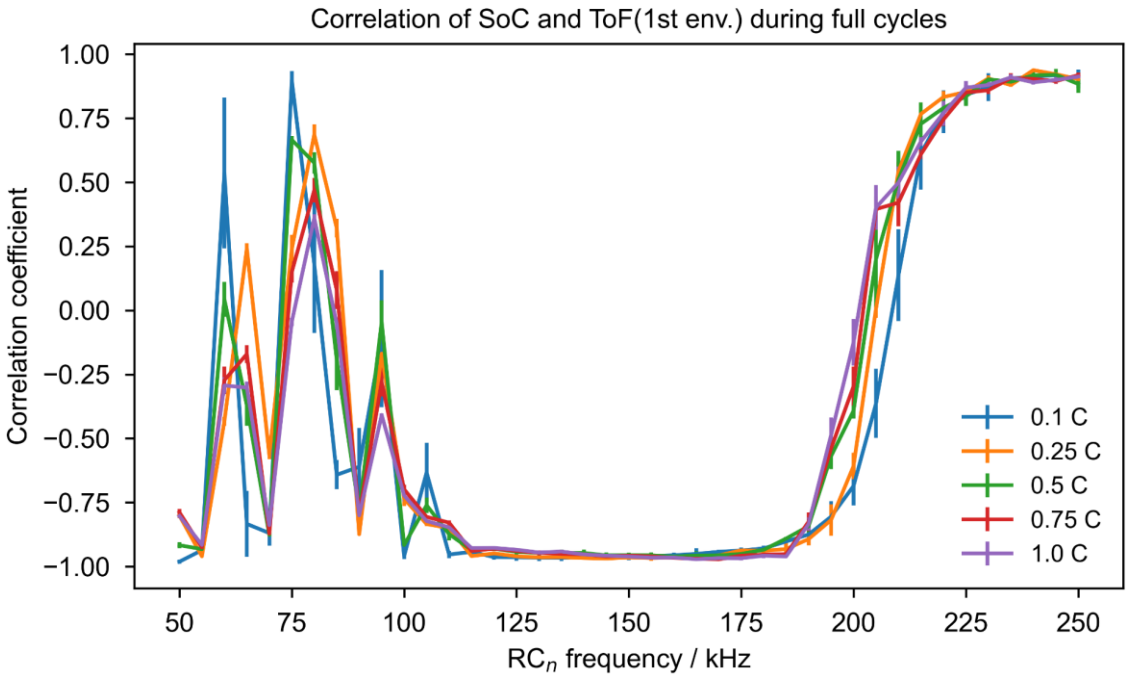

Figure 4.54: Correlation of SoC and corrected ToF, estimated by the first peak of the envelope of the filtered, transmitted signal. The error bars in this graph depict the standard deviation of the mean of four to five cycles. The full cycles in the available datasets of battery cell LDA019 - see Figure 4.45 - were averaged at each C-rate. Sections of different behavior, e.g., the stable negative correlation between 120 kHz and 180 kHz and the transition to a positive correlation up to 250 kHz, can be derived from the course of ToF vs. SoC, summarized in Figure 4.51 and exemplarily shown in Figure 4.44 and Figure 4.48.

Figure 4.55 depicts the correlation of SoC and the ToF, estimated by the maximum envelope of the filtered, transmitted signal. Following the same procedure as before, the course of the correlation coefficient vs. RC_n frequency can be explained by looking at the values of ToF at 0%, 50%, and 100% SoC in Figure 4.52. Due to the impact of the relaxation period at the end of discharge – a fixed amount of data points in each cycle that shows no linear correlation of SoC and ToF, but form a vertical line – an overall lower correlation coefficient (absolute value) is expected for the higher C-rate datasets. Since the deviation from a linear correlation is more pronounced at high C-rates due to a larger vertical line, this expectation is met well for a large portion of the plotted RC_n frequency. For the frequency range of 50 kHz to 205 kHz, the correlation coefficient evaluates to -0.83 to -0.97 with the exception of 55 kHz, where the course of ToF vs. SoC is largely different from the rest. Here, lines of the value at 0% and 100% SoC also show a kink in Figure 4.52. Furthermore, the correlation at 0.1 C is behaving differently than at other C-rates throughout this frequency range, which might be again attributed to the break-in period, taking place mostly during the cycles of the 0.1 C and 0.5 C cycles. Above 210 kHz, the transition from a negative to a positive correlation is observed as the ToF at 0% and 50% SoC starts to overlay in Figure 4.52.

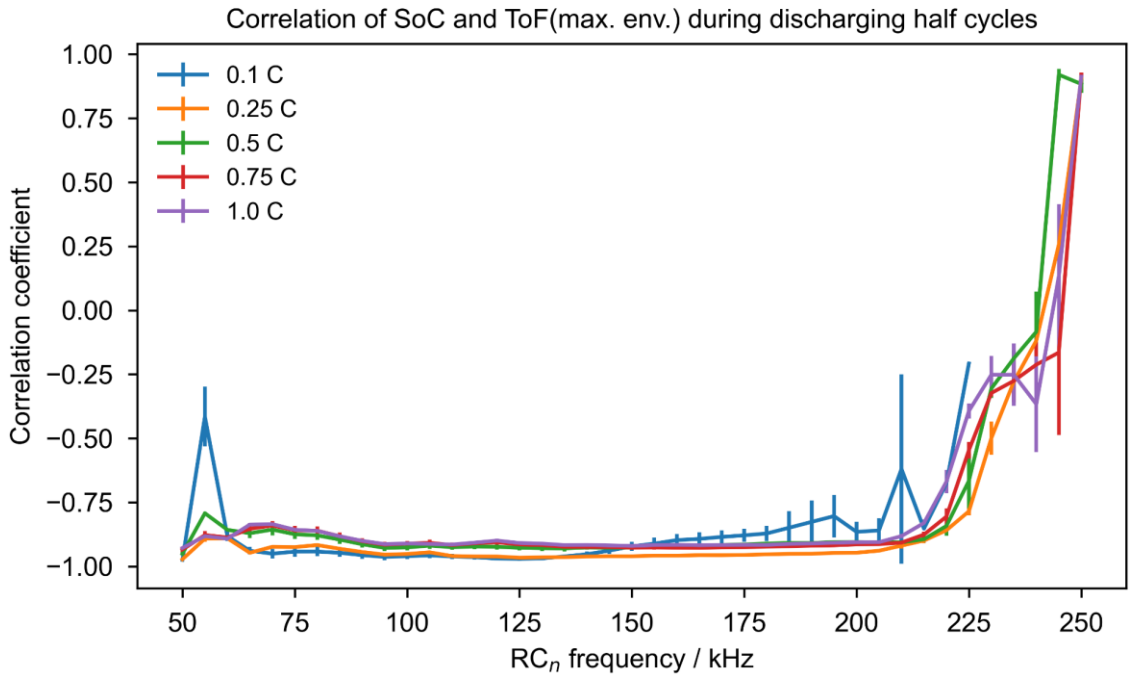

Figure 4.55: Correlation of SoC and corrected ToF, estimated by the maximum envelope of the filtered, transmitted signal. The error bars in this graph depict the standard deviation of the mean of four to five cycles. The full cycles in the available datasets of battery cell LDA019, see the legend of Figure 4.45, were averaged at each C-rate. The trends in correlation can be linked to the trends in ToF vs. SoC, as summarized in Figure 4.52.

Combining the information summarized in the plots of ToF vs. RC_n frequency and correlation coefficient vs. RC_n frequency, it seems that during frequency sweeping a transition, regarding which wave propagation mode is the dominant one, occurs. For a wave propagation mode, the relation between ToF or velocity and mechanical properties, which are linked to the SoC, is assumed to not change. At all frequencies and SoCs, an overlay of wave packages was observed, making the tracking of the ToF of particular wave packages while sweeping RC_n frequency and changing SoC difficult. The finding above suggests, that the wave packages tracked by the first peak and the maximum of the envelope consisted of several overlying components whose ratios changed depending on SoC and RC_n frequency. These components could originate from different resonant frequencies, which are excited along with the selected RC_n frequency, as was observed in the frequency spectrum of the excitation signal under load, compare Chapter 4.3.1, Figure 4.13, and Chapter 4.4.2.1.

Finally, the correlation between SoC and energy content of the unfiltered signal is studied in Figure 4.56. Due to the relation between SoC and energy content, the correlation coefficient evaluates to positive values at all frequencies – see the ascending order in which the lines, corresponding to 0%, 50%, and 100% SoC, appear in Figure 4.53. The effect of

relaxation during rest periods plays an important role in the correlation of SoC and energy content. As seen for an RC_n frequency of 50 kHz in Figure 4.50, the regain of energy content around 0% SoC and the relaxation at 0% SoC increases with C-rate, creating a large section of SoC in which the energy content to SoC relation is ambiguous. This trend increases further with an increase in RCn frequency, which can be validated on the plot at 250 kHz, shown in Figure 8.12 in the appendix. Along with the deviation from a linear relation, this effect influences the overall correlation of a cycle at a certain C-rate and RC_n frequency. Especially in the range of 50 kHz to 125 kHz, the relatively high correlation of up to 0.993 between 75 kHz and 85 kHz make the utilization for SoC estimation favorable.

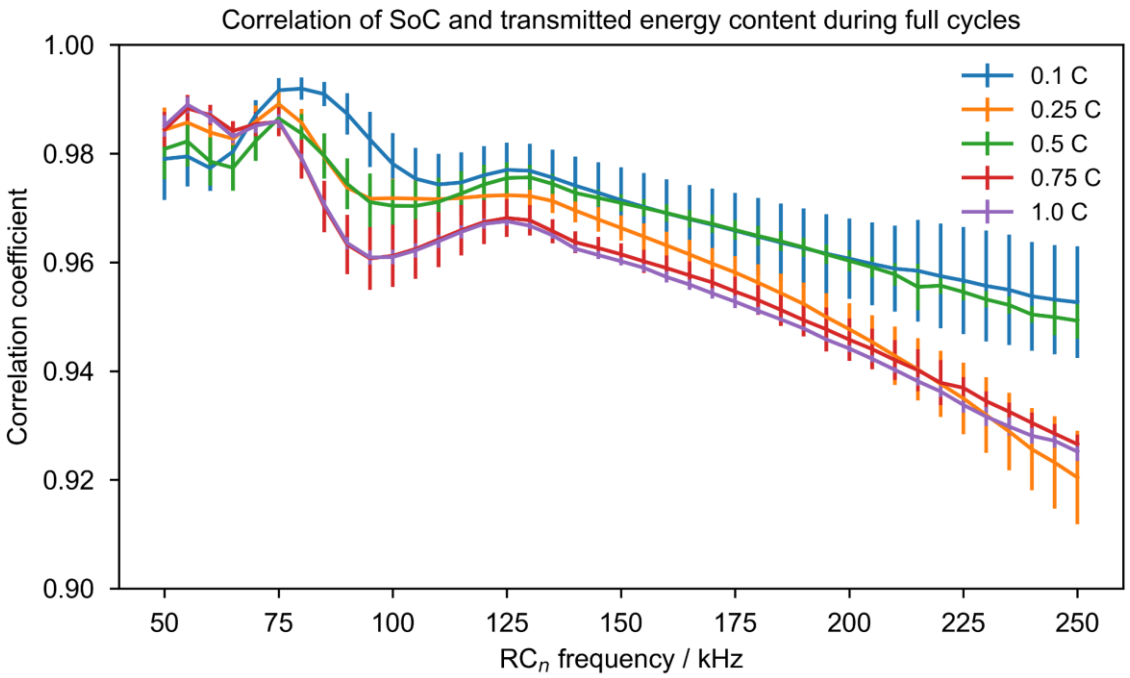

Figure 4.56: Correlation of SoC and energy content of the transmitted (unfiltered) signal. The error bars in this graph depict the standard deviation of the mean of four to five cycles. The full cycles in the available datasets of battery cell LDA019, see the legend of Figure 4.45, were averaged at each C-rate. The trends in correlation can be linked to the trends in ToF vs. SoC, as summarized in Figure 4.53.

4.5.5 Summary of this subchapter

In this subchapter, the evolution of several ultrasonic signal properties with state of charge was characterized regarding the cycle-to-cycle variation, the hysteresis, the effect of varied C-rate, and the dependence on RC_n frequency. From the available dataset, the time of flight of the first and second transmitted wave package and the transmitted energy content of the signal was chosen for further investigation. From the relation of those signal properties with frequency alone, the dominant mode of ultrasound propagation could not be concluded

unequivocally. To do so, further experiments with additional battery cells, posing a variation in dimension and available sensor geometry, would be required. Those signal properties generally exhibit a trend with SoC – a decrease in ToF and a reduced attenuation. The relation between the signal properties and SoC is not a strictly linear one. Sections of different slopes can be linked to the transitions between phases in the positive active material or the staging in the negative active material, as unveiled by the incremental capacity analysis in chapter 4.1. The study of cycle-to-cycle variation revealed a significant effect of relaxation during rest steps. Therefore, the first and subsequent cycles after rest differ, which may reduce achievable SoC estimation accuracy. Besides relaxation, a second effect was found to cause a difference between cycles – a kind of break-in period, following the formation process, that leads to a change in mechanical parameters of lithium-ion battery cells until a steady state is reached [25]. The charging and discharging half-cycles showed differences in their course that are an exhibit of the hysteresis that is common to multi-particle systems such as LIBs. The hysteresis of the system can be quantified by the area between the charging and the discharging half-cycle's curve of a certain signal property vs. SoC. A variation of C-rate pronounced the difference between charging and discharging half-cycle, increasing the hysteresis with C-rate. This can be attributed to a cell operation that is far from equilibrium, as is the case at higher C-rates, followed by a relaxation to equilibrium.

The studied datasets contain transmission signals, resulting from the excitation of piezo elements with RC_n pulses in the frequency range of 50 kHz to 250 kHz. Therefore, a description of the signal properties in dependence on the RC_n frequency is possible. This dispersion relation allowed viewing the dataset as a whole, estimating trends with SoC and RC_n frequency, thereby providing a forecast of which frequency subsets from the dataset might be best suited for SoC estimation. The correlation of signal properties with SoC was then tested to extend the generalized description of the datasets. The implications of correlation on the SoC estimation accuracy are to be validated in the following chapter with the aid of machine learning such as support vector regression.

4.6 Case study: application of a support vector regression to test SoC estimation via ultrasonic sensing

In this last chapter, the ultrasonic signal properties are used alongside cell voltage and current as feature vectors in training and test datasets, fed to a support vector machine. With this machine learning approach, a case study is performed, providing a proof of concept of ultrasound-based state estimation for lithium-ion batteries, and an estimate for the achievable accuracy is established.

4.6.1 Overview of features, SVR parameters, and scaling techniques

In the following, a support vector regression (SVR) with a radial basis function (RBF) kernel is used to explore the benefit of using an ultrasonic signal or their analytical excerpt along with electrical data on a cell to estimate its state of charge. The parameters of the SVR are held constant at epsilon $\varepsilon = 0.1$, gamma $\gamma = 0.1$ and regularization parameter $C = 100$ throughout this case study. Epsilon describes the radius of the epsilon tube. Points lying within this tube are not associated with a penalty. Gamma is a parameter that controls how much the distance between points or to the epsilon tube is penalized. At high values of gamma, the shape of the epsilon tube relies strongly on individual data points. Finally, the regularization parameter C controls the weighing between loss function and complexity of the model – at high C, overfitting of the data is more likely, but an overall smaller value of the loss function is achieved. The values chosen here, present an overall moderate choice and are common start parameters for testing an SVR. Generally, a parameter variation is performed on a representative dataset to evaluate the score (accuracy, mean square error, or else) of a trained model and to fix these parameters to test different datasets against each other. Since this is a complex task and beyond the scope of this work, the parameters will remain fixed for the following analysis, as described before. To achieve reasonable results within the computing accuracy available to modern computers, and to ensure an equal weighing of the input features, it is necessary to scale training and testing data to a certain range. There are two common ways to do so: the standard scaler, shifting the data by its mean value and scaling it by division by its standard deviation; and the min-max-scaler, scaling the data to values between 0 and 1, normalized to the difference between minimum and maximum of the data. As outliers have been removed from the datasets by hand already, the min-max-scaler is applicable here, even though it is very sensitive to outliers. The scaler is applied to each feature of the training and testing data separately. To avoid information leakage between training and test data, the scaler is fit to the training data, resulting in a scale, which is then applied to the test data. Feature, in this context,

means a measured quantity, e.g., SoC, cell voltage, current, ToF, or transmitted energy content (EC). In an industrial application of SoC estimation, a similar procedure would be applied to scale measured quantities to a certain range, allowing to use of a smaller bit count to store and process associated values. In this case, the scaling factor would have to be estimated based on a norm cycle or a priori tests of comparable cell-actor-sensor configurations.

The features of the datasets tested in this study are

- SoC
- Voltage
- Current
- ToF(1st env.)
- ToF(max. env.)
- Transmitted energy content (EC)

The features can be assigned to two groups – electrical features and ultrasonic features, as indicated by color. These features make up the components of a multidimensional feature vector, with each feature being represented by one dimension. The SoC is the state variable that the SVR is trained to predict.

The test datasets include several samples and different C-rates. Abbreviations prepended in brackets are chosen to shorten the legend entries in the following graphs. The grey font color indicates the exclusion of the respective datasets in the averaging in subsequent subchapters.

- (1.10) LDA002 – 0.10 C
- (2.10) LDA007 – 0.10 C
- (3.10a) LDA019 – 0.10 C, run a
- (3.10ba) LDA019 – 0.10 C, run b, sensor and actor switched
- (3.10bb) LDA019 – 0.10 C, run b
- (3.25) LDA019 – 0.25 C
- (3.50) LDA019 – 0.50 C
- (3.75) LDA019 – 0.75 C
- (3.00) LDA019 – 1.00 C
- (4.10) LDA020 – 0.10 C
- (5.10) LDA021 – 0.10 C
- (6.10a) LDA022 – 0.10 C, run a
- (6.10b) LDA022 – 0.10 C, run b
- (7.10) LDA025 – 0.10 C

4.6.2 Test procedure

To test the accuracy of the SoC estimation with the support vector regression, the datasets above are tested in two ways. To estimate the accuracy of a trained model, the R^2 score is used. During the first test, the model is trained with a portion (90%) and tested with a second non-overlapping portion (10%) of the feature vectors in a dataset. This portion is randomly

selected and the process of training and accuracy estimation is repeated ten times. The average of these ten iterations was taken as the accuracy. During the second test, the data feature vectors of one dataset are used as training data and the feature vectors of another dataset are used as test data. In both test cases, the datasets are filtered to contain feature vectors of only a single RC_n frequency, which is the implementation that is the most feasible. The best accuracy of an individual test is displayed in the following heat maps, in which the row entries mark the training datasets and the column entries mark the test datasets. Therefore, the diagonal line in the heat map represents the first test case where a dataset is tested against itself (self-test). The tests where training and test data don't originate from the same dataset will be referred to as cross-test.

Out of the tested feature selections, the test matrix for electrical and ultrasonic features combined is depicted in Figure 4.57. Here, the best R^2 score is plotted as the color value. The RC_n frequency at which the corresponding R^2 score was achieved along with the corresponding root mean square error (RMSE) can be found in the appendix, see Figure 8.13 and Figure 8.14. As seen in the diagonal entries, self-tests consistently evaluate to comparably high values around 0.96 to 0.98. For the cross-tests in the upper left-hand corner (5 times 5 tiles), similar results are achieved. This allows the conclusion, that the features in the corresponding datasets of cells LDA002, LDA007, and LDA019 achieve similarity regarding the correlation of SoC and the tested features. Especially the rows and columns belonging to LDA020 (4.10) and LDA021 (5.10) show much lower R^2 scores, hinting that the correlation of SoC and the tested features doesn't match the behavior of other tested cells.

For an application to SoC estimation, e.g., in a vehicle, this would imply that cells would either have to be categorized into groups of matching behavior or the sensor actor configuration and parameters affecting the ultrasonic propagation through the battery cells and along their surface would have to be revisited. Another sensor actor configuration, e.g., placement of both on the same side of a battery cell, which was not possible due to space limitation within this study, could result in a smaller cell-to-cell variation in ultrasonic propagation and should be considered in the future research.

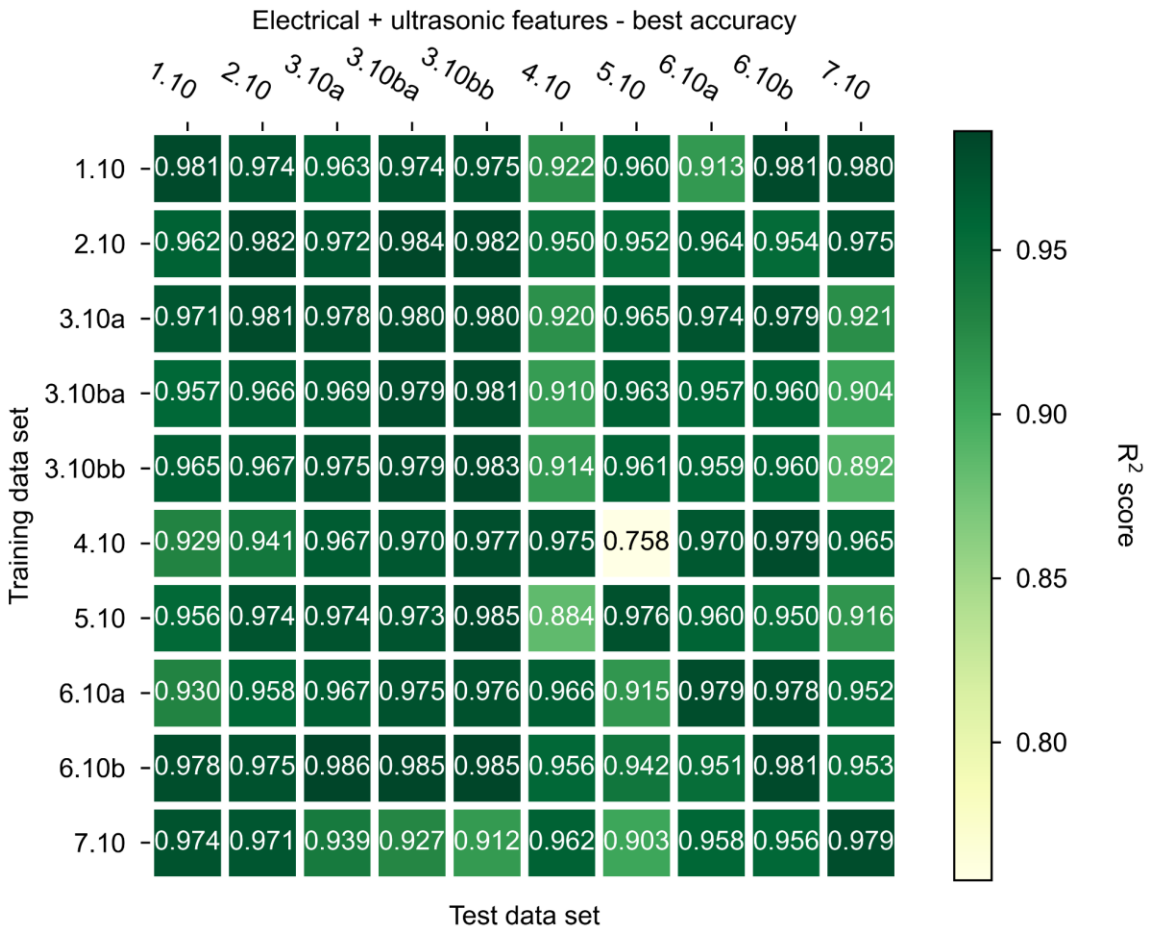

Figure 4.57: Model accuracy of a support vector regression, estimated by the R² score. The datasets used for training and testing are listed as row labels and column labels, respectively. The diagonal entries represent the average of 10 self-tests of a dataset, where 10% of the data acts as test data and 90% as training data. These tests evaluate to an accuracy of up to 0.98. The overall accuracy is consistently higher compared to the model trained with electrical or ultrasonic features alone, as shown in the appendix, Figure 8.14.

4.6.3 Assessing the effect of additional features on the estimation accuracy of an SVR

As described before, the RC_n frequency at which the best accuracy is achieved varies depending on the datasets evaluated, but also on the features selected. Here, the benefit of taking additional features or varying the combination of features is evaluated. Especially the potential benefit of combining the electrical features, cell voltage, and current, with ultrasonic features is of interest to test whether the sensing of physical properties can improve state estimation. In Figure 4.58, the R² score, the RMSE, and the RC_n frequency at which the best accuracy is achieved are plotted as a function of features included in the training and test datasets.

As described before, ten runs of the self-test are performed. Again, the 0.1 C cycling of LDA019 is chosen to be presented here to be able to retrace trends to before described phenomena. When taking the correlation of the displayed features with SoC into account, as shown in Figure 4.54, Figure 4.55, and Figure 4.56, the observed trends can be explained. The RC_n frequencies at which the best R^2 scores and at which frequencies are achieved, match the RCn frequencies at which the correlation of the respective features with SoC is particularly high (close to +1 or -1). For energy content, this is the case around 85 kHz for ToF(1st env.) at 50 kHz and for ToF(max. env.) at 105 kHz. For other combinations of these features, the best R^2 score is achieved at RC_n frequencies at which the correlation of the selected features with SoC is rather high for both features, e.g., at 50 kHz for both ToF features or at 125 kHz for all ultrasonic and electrical features combined. Therefore, the Pearson correlation coefficient can act as guidance for the selection of features to achieve a high estimation accuracy and low RMSE. It can also be concluded that the addition of a measured variable to the set of features aids the estimation accuracy of an SVR if the measured variable exhibits a strong correlation to the state variable. Nevertheless, additional features can negatively contribute to the best achievable estimation accuracy, as seen in the R^2 scores of “Electrical + Ultrasonic” compared with “Electrical + both ToF”.

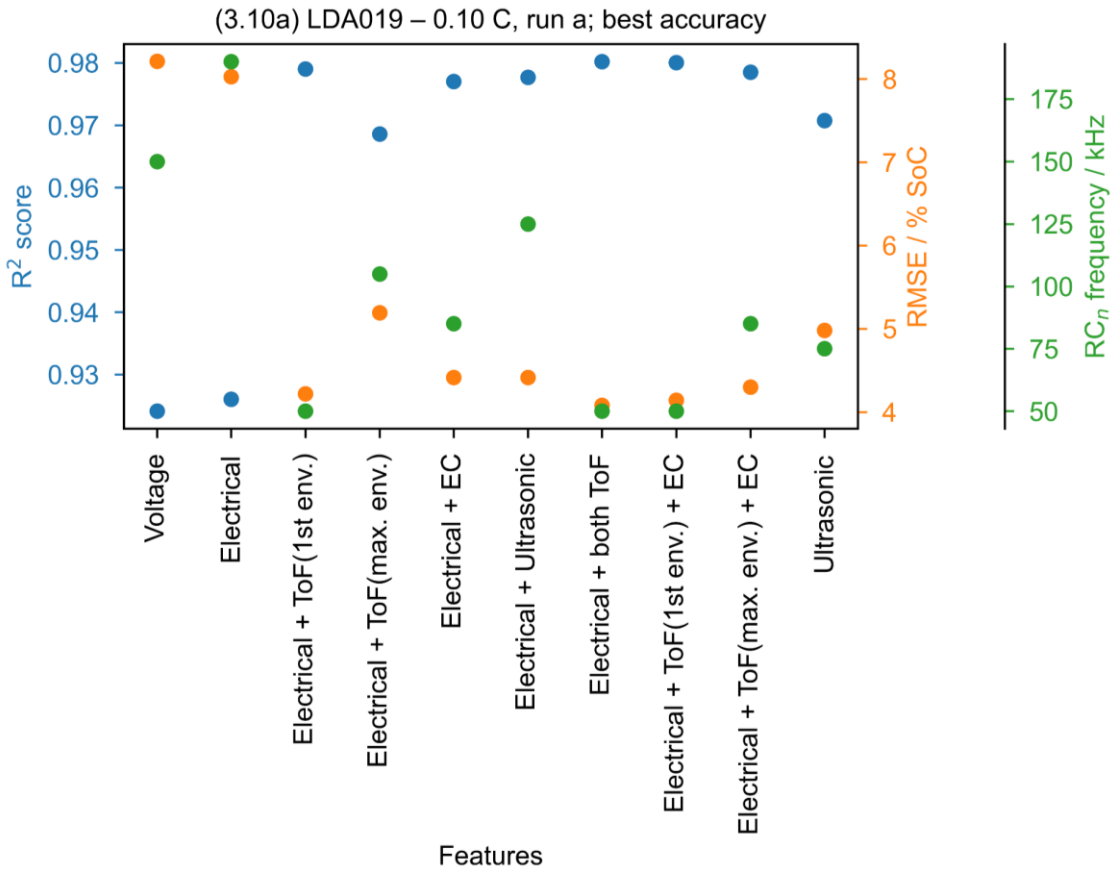

Figure 4.58: Model accuracy (R^2 score), RMSE, and RC_n frequency at which the best accuracy is achieved plotted versus utilized features for the self-test of the dataset (3.10a) LDA019 – 0.1 C, run a. As seen from the first two entries, the accuracy of a model trained and tested with electrical features alone is rather poor, yielding an RMSE of about 8% SoC and an R^2 score of about 0.92. With the addition of ultrasonic features, the RMSE can be reduced to about 4% SoC and the R^2 score increased to about 0.98. Trends of the R^2 score and RMSE with features and RC_n frequency can be predicted based on the Pearson correlation of selected features with SoC, which is depicted in Figure 4.54, Figure 4.55, and Figure 4.56. At RC_n frequencies where a feature achieves a high correlation, a high R^2 score and a low RMSE can be expected for an SVR utilizing this feature.

The above-described test was repeated for all seven available battery cells on one selected dataset per sell, at 0.1 C each. The averaged results with standard deviation as error bars are depicted in Figure 4.59. The general trends are similar to what can be observed for dataset 3.10a, as depicted in Figure 4.60. The model fit to the electrical features alone has again the worst performance with an R^2 score of about 0.92 and an RMSE of about 8% SoC. Adding a single ultrasonic feature improves the R^2 score to about 0.97 and the RMSE to about 5% SoC. Judging from the mean values and specified standard deviation, adding additional features does not improve the result further. The RC_n frequency, at which the best result is achieved, varies within a large range. Most of the tested features result in a mean RC_n frequency around 100 kHz to 150 kHz, which is the center of the studied frequency range. For the test of ultrasonic features alone, the RC_n frequency of the best result lies

within 50 kHz to 100 kHz, which is the range in which, at least for most frequencies, a well-defined correlation between SoC and the ultrasonic features exists. In this range, the ToF estimation algorithms yield reasonable results, as the frequency distribution of the PSD of the transmitted signal is centered on the excited RC_n frequency of the sent waveform – see Figure 4.28.

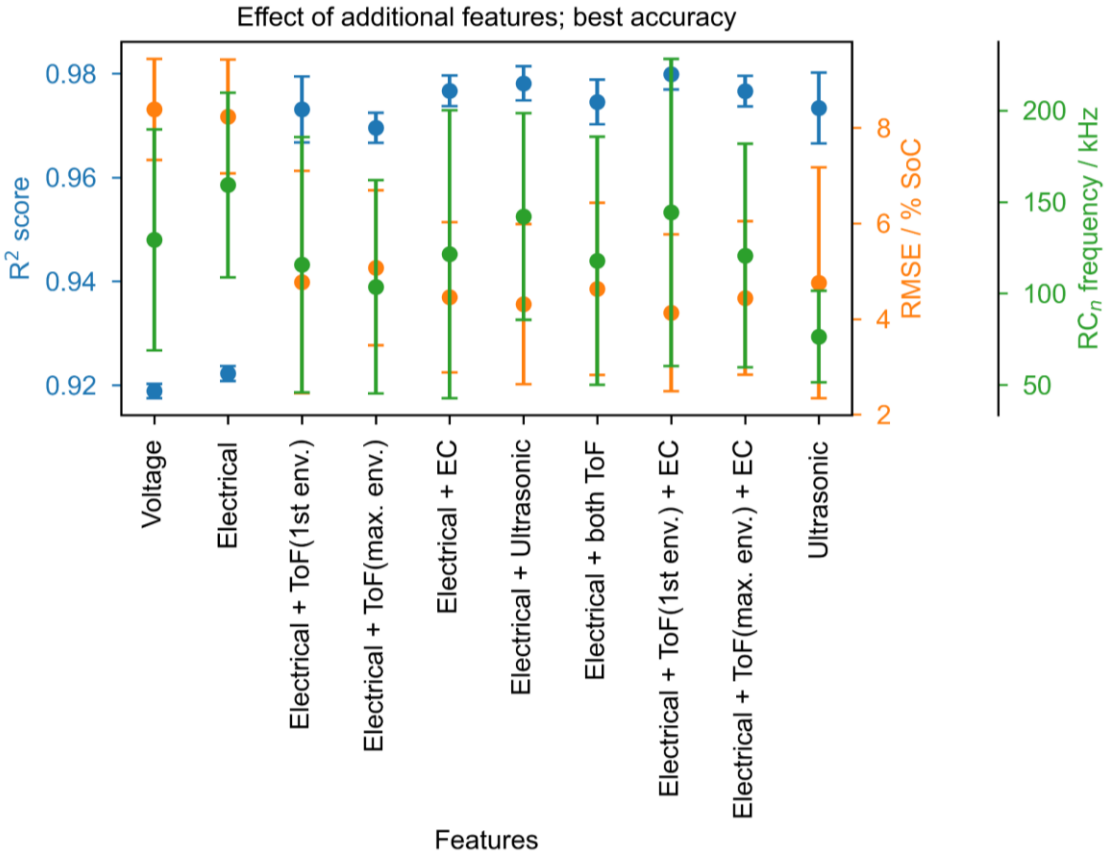

Figure 4.59: Model accuracy (R^2 score), RMSE, and RC_n frequency at which the best accuracy is achieved plotted versus utilized features for the self-test of seven selected datasets – compare the list at the beginning of this chapter.

4.6.4 Assessing deviation of prediction from test data

When assessing the suitability of an SoC estimation method, the maximum estimation error and the SoC the which the deviation of prediction from the true value occurs are important quality criteria, besides, mean estimation error. The latter is correlated with the R^2 score but is explicitly depicted in the appendix, Figure 8.14. Here, an overall RMSE of about 4% SoC is achievable for almost all self-tests on electrical and ultrasonic features combined, depicted in the tiles along the diagonal line, as confirmed for the dataset (3.10a) – see Figure 4.58. A comparison of prediction and true SoC is displayed in Figure 4.60 for the RC_n frequency of 50 kHz, which corresponds to the dataset discussed in the previous

subchapters 4.5.1 and 4.5.2. Here a prediction for every vector in the training data is shown, while the model generating this output was trained with a portion of the training data as in the before described self-tests. To comply with the previous presentation where cell voltage and signal properties were plotted as a function of SoC, the same presentation was chosen in the following graphs. Mind that the prediction is a function of the feature displayed on the y-axes. Therefore, the deviation of prediction from true SoC is visible through a horizontal shift of prediction against training data. The most prominent is the under-estimation (shift to the left) at low and high SoC values, especially well visible for the plot of voltage vs. SoC. Over-estimation is pronounced between 20% and 40% SoC, which is especially well observable in the plot of energy content vs. SoC.

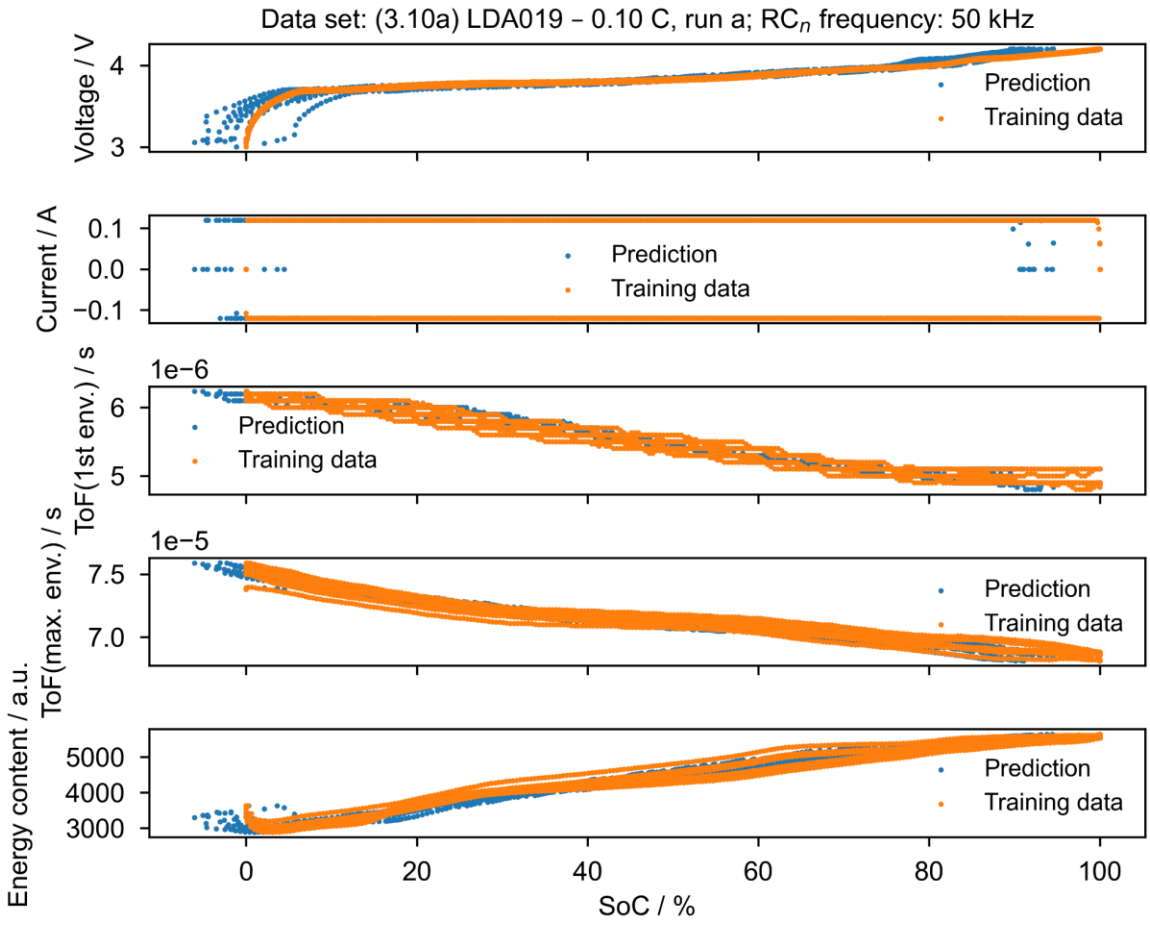

Figure 4.60: Comparison of training data and model prediction. The predicted value SoC is plotted on the x-axis and the features are plotted on the y-axis. Therefore, the deviation of the prediction from the training data can be estimated as the horizontal shift of the blue points against the orange points. As the behavior at an RC_n frequency of 50 kHz has been described extensively in the previous chapters, the same frequency is chosen here, which yields an R^2 score of 0.918 and an RMSE of 8.7% SoC.

The deviation of the prediction from the training data, involving all available features, is plotted as a function of SoC in Figure 4.61. By comparing the number of points above or below the 0% line, the over or under-estimation in a certain SoC range can be judged. Here, two cases are tested to evaluate the effect of the deviating behavior of the first cycle following a long rest period. In the first case, all five cycles are included in the training and test dataset. In the second case, all cycles but the first cycle after rest are included. It can be observed, that in the low SoC range up to about 15% the deviation of prediction from training data is more negative for the data containing all cycles. This can be traced to the features' differing behavior in that range for the first cycle – compare Chapter 4.5.1. In both cases, an overall trend is seen, which aligns well with the observations in Figure 4.60. In the section up to 40% SoC, the deviation is mostly positive. Between 40% and 70% SoC, the deviation is almost equally spread around zero. Above 70% SoC, the deviation is mostly negative, which can be confirmed by the absence of prediction points (blue dots) in the section above 90% SoC in Figure 4.60. For comparison, the result for the RC_n frequency achieving the best R^2 score is shown in the appendix, see Figure 8.10 and Figure 8.11.

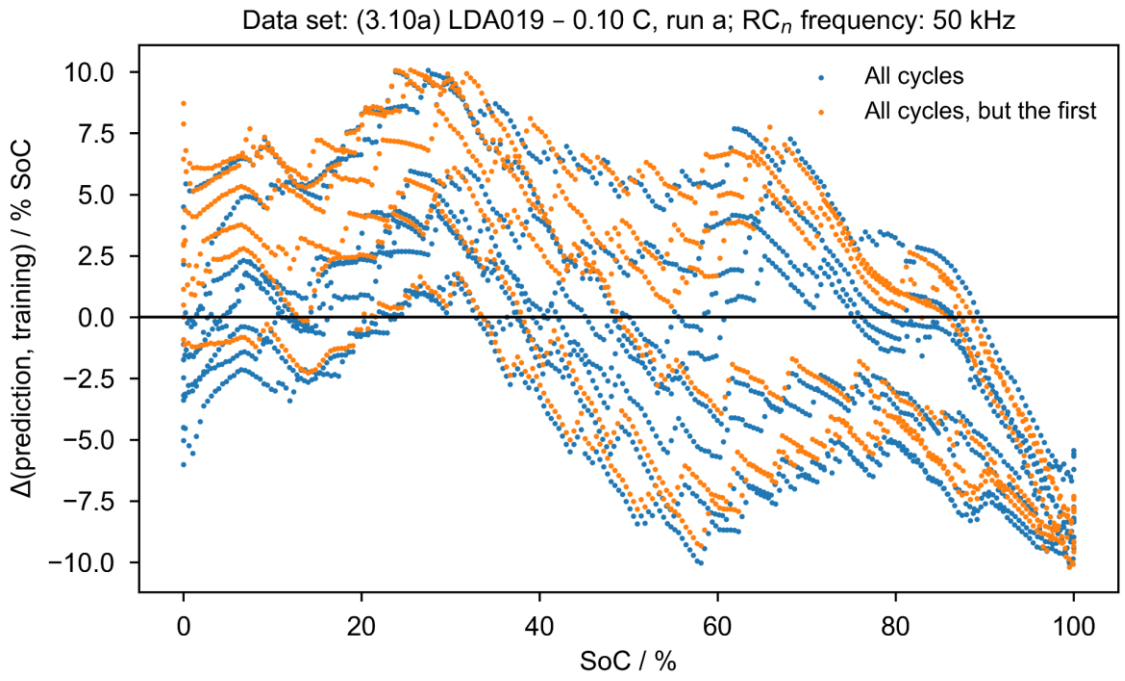

Figure 4.61: Deviation of the predicted value from the training data, plotted vs. the (true) SoC of the training data. Regions of over and under-estimation can be attributed to a misfit of the trained model, as seen in Figure 4.60.

The separation into two branches around 60% to 100% SoC suggests that the deviation differs in magnitude and sign depending on whether the feature vector, being used for prediction, is assigned to charging or discharging half cycle. This would imply that the SVR

does not differentiate between the two and fits the model to both, charging and discharging half-cycles at once. In that case, implementing a mechanism that discriminates between charging and discharging could improve the estimation accuracy significantly. A possible solution could be the first derivative of the electric current.

4.6.5 Assessing the transferability of the training results in unknown cycling conditions

For any real-world application, the state estimation model's ability to predict the state at a condition that was not included in the training data is essential. To assess the transferability of the training results to unknown cycling conditions, the datasets of battery cell LDA019 at different C-rates are studied. In the following, out of the five available C-rate datasets (at 0.10 C, 0.25 C, 0.50 C, 0.75 C, and 1.00 C), one serves as the test dataset and the other four combined serve as the training dataset. To exclude the influence of the first cycle after rest, the datasets are set to begin with the second complete cycle. As before, the training data and the test data are scaled separately to avoid information leakage between the two. The training data is scaled to its minimum and maximum. The hereby estimated parameters for scaling are then applied to the test data. This procedure emulates the scaling of instantaneous measured values according to the boundaries of a known dataset, which would be the case in a real-world application, where the knowledge about the minimum and maximum of the test dataset is unavailable or can only be estimated.

Since the acquisition rate for ultrasonic signals is limited to a rate of about once per RC_n frequency every 50 seconds, the number of ultrasonic data points per cycle is limited. For higher C-rates, e.g., 1.0 C, at which a cycle takes about 70 minutes to complete, the number of data points is substantially lower than at low C-rates, e.g., 0.1 C, at which a cycle takes about 1450 minutes to complete. The number of cycles and the number of data points per cycle is listed C-rate specifically in Table 4.5.

Table 4.5: Number of data points in each subset of the combined dataset, depending on C-rate

C-rate / C	Number of full cycles	Avg. data points per cycle	Total number of data points
0.10	3	483	1449
0.25	4	296	1184
0.50	4	156	624
0.75	4	109	436
1.00	4	86	344

Even though the number of points in a cycle differs from dataset to dataset, depending on the C-rate, only those feature vectors that are selected as support vectors influence the shape of the epsilon tube. Therefore, a higher number of feature vectors in a subset does not necessarily lead to a higher weighing of that particular subset in the combined dataset.

In Figure 4.62, the result of the described assessment is shown. A general trend can be observed here. If the C-rate of a test dataset lies outside of the C-rates, included in the training data, the R^2 score is lower and the RMSE is higher compared to cases where the C-rate of the test dataset lies within the range of C-rates included in the training data. In that case, some of the feature vectors of the test data are not contained in the range of the model, fitted by the SVR. Especially in the lower SoC range, where the value of the signal quantity (e.g., ToF) strongly depends on the C-rate, this contributes to a higher estimation error. The difference in ToF(max. env.) at 0% SoC at 1.0 C and smaller C-rates, as seen in Figure 4.49, may illustrate this. An epsilon tube fitted to the data of 0.1 C to 0.75 C would select the support vectors in a way that minimizes the distance to the feature vectors and thus contain some of the “outer” values of the training data. Therefore, a deviation from the trained value range and slope, as is very likely for some of the data points at 1.0 C would lead to an under-estimation or over-estimation and thus to a higher estimation error. Due to the smaller deviation of the 0.1 C data compared to the C-rates above the described effect is smaller than at 1.0 C. Since almost all feature vectors of the 0.5 C data are expected to lie within the range of the training data, the 0.5 C test case is expected to yield the best result, as is confirmed in Figure 4.62. With the additional data points and a potentially larger range of the epsilon tube, the 0.5 C test case can even achieve better accuracy than the 0.1 C self-test – see Figure 4.58.

From the results presented here, one can conclude that in an application utilizing a data-driven approach for SoC estimation, the best result can be obtained by a) including as diversified training data as possible and b) training the model with a range of conditions that include all the conditions to be tested or faced during application.

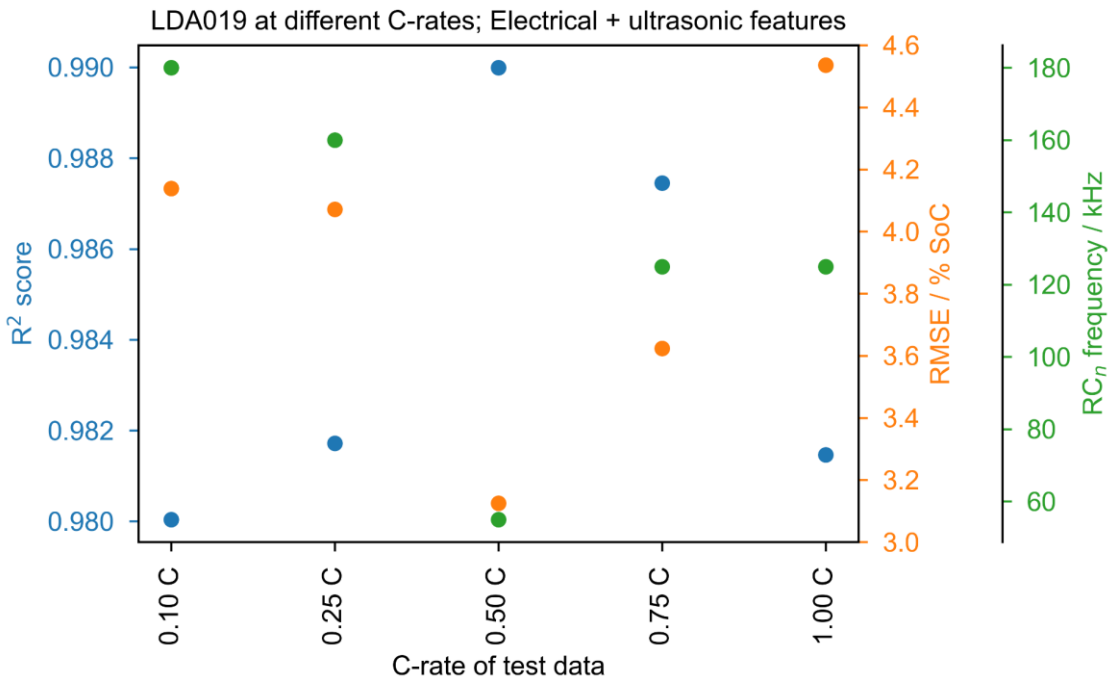

Figure 4.62: Assessment of the SoC estimation accuracy according to R² score and RMSE for unknown cycling conditions. In this test case, four subsets at different C-rates are combined to form a training dataset, while the remaining fifth out of the available five subsets acts as test data. Thereby the estimation accuracy of a model applied to a dataset recorded at a C-rate unknown to that model can be assessed. The C-rate of the test data is listed on the x-axis.

4.6.6 Assessing the transferability of training results to a battery cell, unknown to the trained model

A last important test case is to assess how well a model, trained with a selection of battery cells, can estimate the SoC of battery cells not included in this selection. For any application, the training of a model with every single cell produced before deployment is not desirable. Therefore, the following procedure is chosen to assess the transferability of training results to a battery cell, which is not known to the trained model. As depicted in Figure 4.63, the data of seven battery cells, cycled at 0.1 C were chosen, while the dataset named in the x-axis label acts as test data and the remaining datasets act as training data. Prior to scaling, the training data is appended together from the individual subsets. As before, the training and test data are scaled separately to avoid information leakage between the two. Analogously to Chapter 4.6.5, the minimum, the maximum, and the standard deviation of the training data are used to scale the data. This procedure also emulates the case where the instantaneous measured values (feature vectors) are recorded independently and scaled without prior knowledge of the minimum and maximum within that dataset. To comply with the before demonstrated test cases, the electrical and ultrasonic features were used

for testing. The test cases, depicted in Figure 4.63, achieve R^2 between 0.915 and 0.960 except for the test case 5.10 at 0.541. RMSE varies between 5.85% SoC and 8.52% SoC except for the test case 5.10 at 19.85% SoC. The RC_n frequency, at which the best R^2 score is reached, varies from 50 kHz to 195 kHz. At almost 20% SoC RSME, the model trained for the 5.10 test case is not suitable for SoC estimation and has to be treated as an outlier. This bad performance with dataset 5.1 being the test case seems reasonable when looking at Figure 4.57, where dataset 5.1 yields the overall lowest mean R^2 score of 9.30. Further research would be required to link the differing behavior of this cell to the low SoC estimation accuracy, achieved by the SVR. Disregarding this outlier, the overall result averages to an R^2 score of (0.941 ± 0.015) and an RSME of (7.03 ± 0.89)% SoC, which is comparable to the range which is achieved during the feature selection test (compare Chapter 4.6.3), but still poses an improvement compared to the test case with solely electrical features for single-cell self-test.

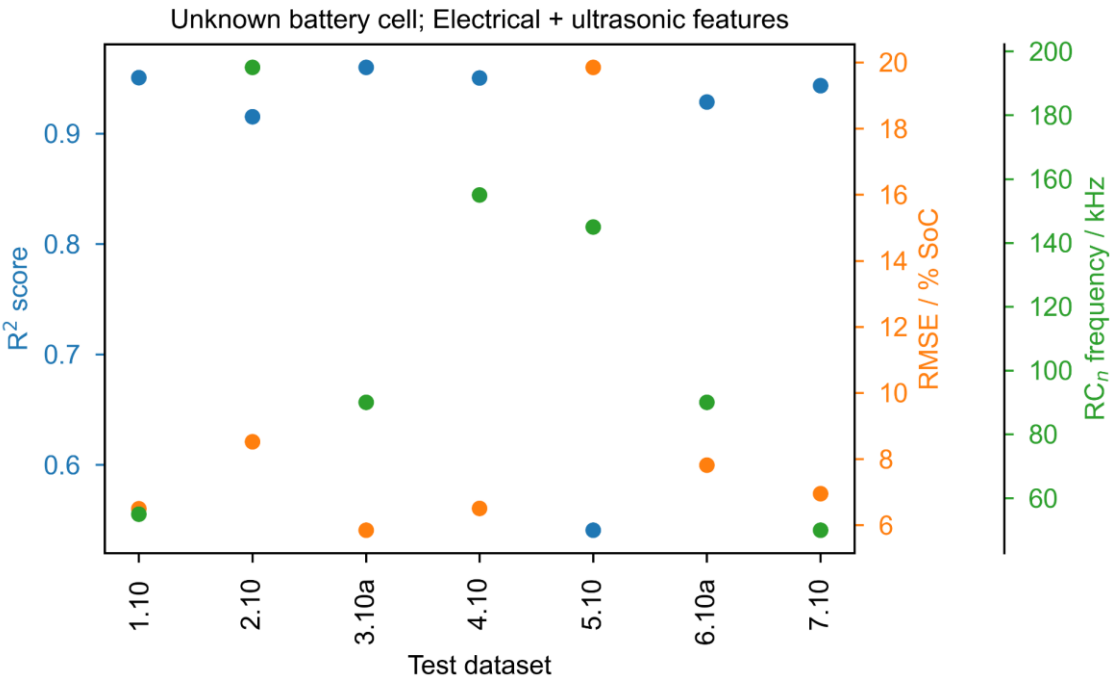

Figure 4.63: Assessment of the SoC estimation accuracy according to R^2 score and RMSE for an unknown battery cell. In this test case, six subsets of different battery cells, cycled at 0.1 C, are combined to form a training dataset, while the remaining subset, out of seven selected sets, acts as the test data. Thereby the estimation accuracy of a model trained with a variety of battery cells of the same type and applied to an unknown cell can be assessed. The label of the test data is listed on the x-axis.

4.6.7 Summary of this subchapter

In this subchapter, datasets from seven individual battery cells of the same type and a dataset with five different C-rates were used as training data for an SVR. The parameters of this SVR were held constant, while the number and selection of features and tested datasets were varied to assess different use cases. The features used to train and subsequently predict the state variable SoC were electrical features such as cell voltage and current, and ultrasonic features such as ToF of the first and second wave package and the energy content transmitted within the signal.

First, a self-test and cross-test of the 0.1 C datasets were performed. Self-tests, where different portions of a dataset are used for training and testing, yielded R^2 scores of 0.975 to 0.983 and MSRE of 3.9% to 4.8% SoC. Cross-tests, involving the training with one dataset and a test with another, yielded R^2 scores of 0.884 to 0.981 and MRSE of 3.6% to 10.0% SoC, with the exception of one outlier. This gives a rough estimate of the achievable accuracy but also states that the studied cells differ in SoC-dependent mechanical behavior, as far as ultrasonic signal properties allow to draw a conclusion.

Then the effect of additional features was studied on a number of datasets. While rather large standard deviations of the resulting mean accuracy and R^2 scores don't allow a final assessment, trends can be stated. A combination of electrical features and ultrasonic features consistently yields better accuracy than those features alone, but a maximum number of features does not necessarily provide the best result. Here, mean accuracies of 4% to 5% SoC were achieved.

The datasets of the seven cells were also used to test which accuracy is achievable if six datasets are used for training and the seventh for testing. The resulting accuracy was between 6% to 9% SoC. One outlier, dataset 5.10, suggests that the behavior of cell LDA020 significantly differs from those of the other battery cells.

Then the battery cell and associated datasets, used in the exemplary in-depth study throughout the results chapter, were employed for further tests. It could be shown that the deviations of the prediction from the training data vary with SoC. At low SoC, overestimation is especially present and at high SoC, an underestimation is pronounced. As the study of the signal properties at the showcased RC_n frequency showed, these are the regions where the effect of hysteresis is especially present and where the relaxation during rest periods plays a significant role.

Finally, the transferability of the training results to a dataset, recorded at a C-rate, not included in the training dataset, was assessed. Here, accuracies between 3.1% and 4.6% SoC were achieved, with the best result at a C-rate between the C-rates included in the training dataset. This suggests that a model can be trained with C-rates representing the limits of the use-cases and still achieve good accuracy for test cases that were not explicitly trained, which is well achievable in a laboratory environment before deployment of the SoC estimation in the field.

5 Summary & Conclusion

5.1 Retrospect on the content of this work

This work introduced the reader to all relevant fields to tap into an ultrasound-based state of charge estimation and provides a blueprint for the procedure to achieve and test the fundamentals of such an approach. It spanned from an in-depth electrochemical characterization of the studied battery cells over establishing the measurement technique, digital processing of ultrasonic transmission signals, and characterization of the SoC dependent property changes of those signals to a proof of concept of an ultrasound-based state of charge estimation.

The State of the art & theoretical background chapter focused on the battery section on the mechanical property changes of lithium-ion batteries during operation. The components and the processes involved to manufacture a battery cell were described to establish the fundamentals for later interrogation. A comprehensive summary of methods for state estimation was given and an emphasis was laid on mechanical methods, including a critical review of the most recent research on ultrasound-based state estimation. Afterward, the fundamentals of ultrasonic non-destructive evaluation were introduced, starting with the sound propagation modes in isotropic boundary-free media, followed by the introduction of boundaries and non-isotropic structure to finally approach the class of fluid-saturated porous media, which batteries can be counted to. As the processing of the ultrasonic signals transmitted through lithium-ion battery cells with the aim of feature extraction was one of the main goals of this work, the fundamentals of digital signal processing and methods for the time of flight estimation were reviewed and compared in a separate section.

All available information on the interrogated battery cell and the instrumentation was collected in the Experimental methods & instrumentation chapter, including a detailed step-by-step manual of the process developed in this work to create and attach a sensor stack for ultrasonic interrogation based on low-cost off-the-shelf piezo elements.

The Results & discussion chapter opened with an in-depth electrochemical and post-mortem interrogation to reverse engineer the battery cell design and its internal structure. The combination of inductively coupled plasma-optical emission spectrometry and incremental capacity analysis applied to three-electrode lab cells, constructed from the studied battery cell's materials, allowed to identify the SoC ranges in which phase transitions and staging occur and thereby directly links changes in the ultrasonic signal properties with

the state of the active materials, which makes this work stand out among other studies on ultrasound-based state estimation. Additional dilatometer experiments were able to prove that the measured effect in ultrasonic time of flight cannot originate from the thickness increase of the battery cells alone, as this thickness increase is smaller and in opposite direction to the change in time of flight. Therefore, changes in elastic modulus and density have to be responsible for the observed effect.

The construction of the sensor stack from off-the-shelf piezo elements, its electromagnetic shielding, and attachment to both sides of the battery cells was treated in a subsequent section. Experiments verified the necessity of shielding and its negligible influence on the ultrasonic signals. A hypothesis describing the metal layer in the pouch foil to be the transport medium of an electrical coupling/distortion between sending and receiving sensor was formulated and tested. Impedance spectroscopy was shown to be a useful tool to characterize the resonant behavior of piezo elements and ensure the mechanical coupling of such to the surface of the battery cells. The excitation of the piezo elements by a raised cosine (RC_n) waveform with varied center frequency in the range of 50 kHz to 250 kHz was studied in the frequency domain and the influence of the resonant behavior, as identified prior by impedance spectroscopy, on waveform and frequency content was evaluated to be uncritical. Therefore, the forced oscillation produced by this excitation was assumed to be mechanically coupled as ultrasonic waves into the battery cells.

The ultrasonic waves transmitted through the battery cell were recorded by piezo elements on the opposing side. A first inspection of the raw, unprocessed signals identified the transmission of two main wave packages and allowed the identification of two major trends: the time of flight of ultrasonic wave packages decreases with the center frequency of the RC_n waveform, and with state of charge. These trends were to be assessed further in the subsequent sections. Therefore, methods for the extraction of features (properties) from the ultrasonic signals were established, compared, and tested in a dedicated section. Several simple and advanced thresholding methods were compared with envelope-based and cross-correlation methods to estimate the time of flight (ToF). It was demonstrated that the envelope-based method yields the most robust estimate for the first and second wave package. This finding is in accordance with the literature stating that an envelope-based method is best suited for dispersive, absorptive media [204], to which lithium-ion batteries are counted. Respective trends were already suggested by the heatmap plots of the raw signals vs. RC_n frequency and SoC. To enable such a robust estimate, an FIR filter had to be designed to preprocess the transmitted signals and thereby attenuate frequency components that verifiably lead to a distorted shape of the envelope.

With a robust ToF estimation method selected, the characterization of the signal properties ToF and transmitted energy content (EC) was performed in-depth. A study of cycle-to-cycle variations unveiled that the signal properties are affected by a long rest period and the associated relaxation of the multi-particle system “battery cell” to equilibrium. In detail, during cycling, the signal properties don’t reach the same value at a given SoC in two subsequent cycles if the first of the two cycles follows a long rest period. In accordance with the literature, a break-in period, making up for more than ten cycles post-formation, was observed. During this break-in period, the mechanical properties of the system are said to change until a steady state is reached [25]. Experiments at different C-rate showed that ultrasonic signal properties can sense the non-equilibrium state of a battery cell, characterized by an increasing area between charge and discharge curve of the respective signal property vs. SoC plot. This non-equilibrium state relaxes in the rest period following the discharge after the cut-off voltage is reached. The relaxation in the rest period following the charge is much smaller and shows little C-rate dependency as the state is prepared by constant voltage charging at the end of charge voltage. For a purely statistical SoC estimation approach, as employed in this work, where only instantaneous measurements are taken into account and the historic course of the measurement is not utilized as a source of information, the presence of hysteresis and relaxation leads to a reduced estimation accuracy. Future research should address this issue or even utilize the relaxation to improve the estimation accuracy, by incorporating historic information, e.g., by using the derivative of a signal property as an additional feature. The signal properties were then tested for their correlation with SoC as a function of RC_n frequency. This allowed identifying trends in the behavior of the signal properties as a function of RC_n frequency and C-rate in a condensed fashion and thereby enabled to predict the frequency range, about 50 kHz to 125 kHz, in which the course of the signal properties is best suited for SoC estimation.

The final section provided a proof of concept of the ultrasound-based SoC estimation, by applying a support vector regression (SVR) to before thoroughly studied ultrasonic signal properties, as well as current and battery cell voltage. The included case study was split into different parts that assessed the ability of an SVR to estimate the SoC in a variety of scenarios. Seven battery cells, prepared with sensor stacks attached to both faces, were used to generate 14 datasets. First, a comparison of self-tests, where a portion of a dataset is used for training and another for testing, and cross-tests, which use the dataset of one cell for training and the dataset of another for testing, was performed. A root mean square error (RMSE) of 3.9% to 4.8% SoC and 3.6% to 10.0% SoC was achieved, respectively. In general, it was observed that the SVR is prone to overestimation at low SoCs and

underestimation at high SoCs, which was attributed to the pronounced hysteresis and relaxation of the ultrasonic signal properties in this SoC ranges. The fact that higher accuracy is achieved, if the exact cell is known to the model, indicates that a variation between cells exists. This variation between cells can originate from differences in mechanical properties as a result of production variations or from differences in manual sensor placement, mechanical coupling, or resonant behavior of the ultrasonic sensors. To mitigate the effect of the cell-to-cell variations, a test was performed, where the datasets of six out of the seven cells were combined as training data, and the dataset of the seventh cell was used for testing. This reduced the spread of the RMSE from (3.6 - 10.0)% SoC to (5.9 – 8.5)% SoC, respectively, once again stating that a databased approach for state estimation becomes more reliable with a large data basis. Utilizing self-tests on seven datasets, the effect of additional features on the state estimation result was tested. The involvement of an additional feature did not necessarily improve the estimation accuracy, but it was shown that a combination of ultrasonic and electrical features is superior to the training with these features alone. To test the ability of the model to estimate the SoC in unknown cycling conditions, a test was performed where the C-rate of the test dataset was not included in the training data. The result suggests that for practical applications it might be sufficient to perform training with the boundary of the use cases in a controlled laboratory environment to handle the estimation in a broad spectrum of use cases.

In comparison with literature, this study stands out by utilizing and modifying off-the-shelf piezo elements to equip state-of-the-art lithium-ion battery cells with ultrasonic sensors, employing a range of center frequencies for the waveform, transmitted through the battery cell, instead of a fixed frequency and by allowing the SVR to choose the frequency that yields the best result. The characterization of the ultrasonic signal properties as a function of RC_n frequency and SoC and the assignment of characteristic changes in the signal properties to electrochemical processes, such as phase transitions and staging, makes this work unique. By studying a range of use cases, it was demonstrated that an improved SoC estimation accuracy can be achieved with the aid of ultrasonic measurements – thanks to the correlation of the mechanical properties of the battery cells with the SoC.

5.2 Outlook on future applications of ultrasound to lithium-ion batteries

The application of ultrasound to probe the state of lithium-ion batteries is still a considerably young field of research. Therefore, many more potential research questions are to be answered. Of particular interest is which of the presented propagation modes is the most dominant in the chosen setup. Here, laser vibrometer studies on the oscillation of the battery

cell's surface and finite element models of the wave propagation could enable further insight. With more datasets available in the future, the parameters of the SVR should be optimized to find a generalized model. Additional features, such as properties of the frequency spectrum of the ultrasonic signals, or even whole sections of ultrasonic signals might be used to further increase estimation accuracy in the future, but might require the use of neural networks for feature recognition. Thus many options for the improvement of the state estimation exist.

The reach of this work is already extended by several freshly started projects at Fraunhofer ISC, involving the study of degradation and aging phenomena (MADAM4Life), and the integration of ultrasonic transducers with other mechanical and temperature sensors (SPARTACUS) on the surface of large-capacity high-energy battery cells in automotive conditions, e.g., mechanical clamping of the battery cells.

This work also sparked the idea to use ultrasound to monitor the wetting process of lithium-ion batteries during production, which is developed within the project Cell-Fill. The aim is to shorten the time attributed to wetting and thereby reduce cost, by being able to precisely measure the point in time at which the wetting is sufficient to begin the next production step, formation.

6 Zusammenfassung & Ausblick

6.1 Rückblick auf den Inhalt dieser Arbeit

Diese Arbeit bot dem Leser eine Einführung in alle Bereiche an, die relevant sind um eine ultraschallbasierte Ladungszustandsbestimmung (Ladezustand – engl.: state of charge, SoC) umzusetzen, und zeigt einen Weg auf, wie ein solcher Ansatz in seinen Grundlagen geprüft und umgesetzt werden kann. Hierzu wurde ein Bogen gespannt von einer eingehenden elektrochemischen Charakterisierung der untersuchten Batteriezellen über die Etablierung der Messtechnik, die digitale Verarbeitung von Ultraschalltransmissionssignalen und die Charakterisierung der Ladezustands-abhängigen Eigenschaftsänderungen dieser Signale bis hin zu einem Proof-of-Concept für eine ultraschallbasierte Ladezustandsbestimmung.

Das Kapitel „State of the art & theoretical background“ konzentrierte sich in einem Abschnitt über Batterien auf die Veränderungen der physikalischen Eigenschaften von Lithium-Ionen-Batterien während des Betriebs und der Alterung. Um die Grundlage für die spätere Untersuchung zu schaffen, wurden die Komponenten und die Prozesse zur Herstellung einer Batteriezelle beschrieben. Anschließend wurde ein umfassender Überblick über die Methoden zur Zustandsschätzung gegeben, wobei der Schwerpunkt auf den mechanischen Methoden lag, einschließlich einer kritischen Zusammenstellung der neuesten Forschungsergebnisse zur ultraschallbasierten Zustandsbestimmung. Danach wurden die Grundlagen der zerstörungsfreien Bewertung mit Ultraschall vorgestellt, beginnend mit den Schallausbreitungsmoden in isotropen, unbegrenzten Medien, gefolgt von der Einführung von Grenzen und nicht-isotropen Strukturen, um sich schließlich der Klasse der flüssigkeitsgesättigten porösen Medien zu nähern, zu denen Batterien gezählt werden können. Da die Verarbeitung der durch die Lithium-Ionen-Batteriezellen übertragenen Ultraschallsignale mit dem Ziel der Merkmalsextraktion eines der Hauptziele dieser Arbeit war, wurden die Grundlagen der digitalen Signalverarbeitung und Methoden zur Laufzeitschätzung in einem eigenen Abschnitt behandelt und verglichen.

Alle verfügbaren Informationen über die abgefragte Batteriezelle und die verwendeten Messgeräte wurden im Kapitel „Experimental methods & instrumentation“ zusammengestellt, einschließlich einer detaillierten Schritt-für-Schritt-Anleitung des in dieser Arbeit entwickelten Verfahrens zur Erstellung und Anbringung einer Sensoranordnung für die Ultraschallprüfung auf der Grundlage kostengünstiger, handelsüblicher Piezoelemente.

Das Kapitel „Results & discussion“ begann mit einer eingehenden elektrochemischen und Post-Mortem-Untersuchung, um das Design der Batteriezelle und ihre interne Struktur zu untersuchen. Durch die Kombination von induktiv gekoppelter Plasma-optischer Emissionsspektrometrie und inkrementeller Kapazitätsanalyse an Drei-Elektroden-Laborzellen, die aus den Materialien der untersuchten Batteriezelle konstruiert wurden, konnten die SoC-Bereiche identifiziert werden, in denen Phasenübergänge auftreten, wodurch Änderungen der Ultraschallsignaleigenschaften direkt mit dem Zustand der Aktivmaterialien verknüpft werden, was diese Arbeit unter anderen Studien zur ultraschallbasierten Zustandsschätzung hervorhebt. Durch zusätzliche Dilatometer-experimente konnte nachgewiesen werden, dass der gemessene Effekt in der Ultraschalllaufzeit nicht allein von der Volumenänderung der Batteriezellen herrühren kann, da diese Volumenänderung kleiner ist und in die Gegenrichtung zur Änderung der Laufzeit verläuft. Entsprechend müssen Änderungen in E-Modul und Dichte der Aktivmaterialien für den beobachteten Effekt verantwortlich sein.

Der Aufbau der Sensoranordnung aus handelsüblichen Piezoelementen, seine elektromagnetische Abschirmung und die Befestigung an beiden Seiten der Batteriezellen wurden in einem späteren Abschnitt behandelt. Experimente bestätigten die Notwendigkeit dieser Abschirmung und ihren vernachlässigbaren Einfluss auf die Ultraschallsignale. Es wurde eine Hypothese formuliert, die die Metallschicht in der Pouch-Folie als Transportmedium einer elektrischen Kopplung/Übersprechens zwischen Sende- und Empfangssensor beschreibt. Die Impedanzspektroskopie erwies sich als nützliches Werkzeug zur Charakterisierung des Resonanzverhaltens der Piezoelemente und zur Sicherstellung der mechanischen Kopplung dieser Elemente mit der Oberfläche der Batteriezellen. Die Anregung der Piezoelemente durch eine Raised-Cosine-Wellenform (RC_n) mit variierter Mittenfrequenz im Bereich von 50 kHz bis 250 kHz wurde mittels Fourier-Transformation im Frequenzraum untersucht. Der Einfluss des Resonanzverhaltens, welches zuvor durch die Impedanzspektroskopie ermittelt wurde, auf die Wellenform und den Frequenzinhalt wurde als unkritisch bewertet. Daher wurde angenommen, dass die durch die RC_n Anregung erzeugte erzwungene Schwingung mechanisch als Ultraschallwellen in die Batteriezellen eingekoppelt wird.

Die durch die Batteriezelle transmittierten Ultraschallwellen wurden von Piezoelementen auf der gegenüberliegenden Seite aufgezeichnet. Eine erste Prüfung der rohen, unverarbeiteten Signale ergab die Übertragung von zwei Hauptwellenpaketen und ermöglichte die Identifizierung von zwei Haupttrends: Die Laufzeit der Ultraschallwellenpakete nimmt mit der Mittenfrequenz, der RC_n-Wellenform und mit dem

Ladezustand ab. Diese Trends sollten in den folgenden Abschnitten weiter bewertet werden. Daher wurden in einem eigenen Abschnitt Methoden zur Extraktion von Merkmalen (Eigenschaften) aus den Ultraschallsignalen implementiert, verglichen und getestet. Mehrere einfache und fortgeschrittene Schwellenwertverfahren wurden mit hüllkurvenbasierten und Kreuzkorrelationsverfahren zur Schätzung der Laufzeit (engl.: „time of flight“, ToF) verglichen. Es wurde gezeigt, dass die hüllkurvenbasierte Methode die stabilste Schätzung für das erste und zweite Wellenpaket liefert. Dieses Ergebnis steht im Einklang mit der Literatur, die beschreibt, dass eine hüllkurvenbasierte Methode am besten für dispersive, absorbierende Medien [234], wie z. B. Lithium-Ionen-Batterien, geeignet ist, was bereits durch die Heatmap-Diagramme der Rohsignale aufgetragen gegen RCn-Frequenz und SoC suggeriert wurde. Um eine solche robuste Laufzeit-Schätzung zu ermöglichen, musste ein FIR-Filter implementiert werden, der die übertragenen Signale vorverarbeitet und dabei Frequenzkomponenten abschwächt, die nachweislich zu einer verzerrten Form der Hüllkurve führen.

Nach der Auswahl einer robusten Methode zur ToF-Schätzung die Signaleigenschaften ToF und übertragener Energiegehalt (engl.: energy content, EC) eingehend charakterisiert. Eine Untersuchung der Zyklus-zu-Zyklus-Schwankungen ergab, dass die Signaleigenschaften durch eine lange Ruhephase und die damit verbundene Relaxation des Vielteilchensystems "Batteriezelle" bis zur Erreichung des Gleichgewichtzustands beeinflusst werden. Die Signaleigenschaften erreichten während des Zyklus nicht den gleichen Wert bei einem bestimmten SoC in zwei aufeinanderfolgenden Zyklen, wenn der erste der beiden Zyklen auf eine lange Ruhephase folgte. In Übereinstimmung mit der Literatur wurde eine Einlaufphase (engl.: „break-in period“) beobachtet, die mehr als zehn Zyklen nach der Formierung umfasst. Während dieser Einlaufphase ändern sich die mechanischen Eigenschaften des Systems, bis ein stabiler Zustand erreicht ist [25]. Experimente bei unterschiedlichen C-Raten zeigten, dass die Ultraschallsignaleigenschaften sensitiv für den Nicht-Gleichgewichtszustand einer Batteriezelle sind, der durch eine zunehmende Fläche zwischen der Lade- und Entladekurve der jeweiligen Signaleigenschaft in der Auftragung über SoC gekennzeichnet ist. Dieser Nicht-Gleichgewichtszustand entspannt sich in der Ruhephase nach der Entladung, nachdem die Abschaltspannung erreicht ist. Die Relaxation in der Ruhephase nach dem Laden ist wesentlich geringer und zeigt kaum eine Abhängigkeit von der C-Rate, da der Zustand durch Laden mit konstanter Spannung nach Erreichen der Ladeschlussspannung präpariert wird. Bei einem rein statistischen SoC-Bestimmungsansatz, wie er in dieser Arbeit verwendet wird, bei dem nur instantane Messwerte berücksichtigt werden und die historischen Messwerte nicht als

Informationsquelle genutzt wird, führt das Vorhandensein von Hysterese und Relaxation zu einer geringeren Schätzgenauigkeit. Zukünftige Forschungsarbeiten sollten sich mit diesem Problem befassen oder sogar die Relaxation zur Verbesserung der Bestimmungsgenauigkeit nutzen, indem historische Informationen einbezogen werden, z. B. durch Verwendung der Ableitung einer Signaleigenschaft als zusätzliches Merkmal. Die Signaleigenschaften wurden dann auf ihre Korrelation mit SoC als Funktion der RC_n-Frequenz getestet. Dies ermöglichte es, Trends innerhalb der Daten in verdichteter Form zu identifizieren und dadurch den Frequenzbereich (etwa 50 kHz bis 125 kHz) vorherzusagen, in dem der Verlauf der Signaleigenschaften am besten für die SoC-Bestimmung geeignet ist.

Im letzten Abschnitt wurde ein Proof-of-Concept für die ultraschallbasierte SoC-Schätzung erbracht, indem eine Support-Vektor-Regression (SVR) auf die zuvor eingehend untersuchten Ultraschallsignaleigenschaften sowie auf Strom und Zellspannung der Batterie angewendet wurde. Die enthaltene Fallstudie war in verschiedene Teile aufgeteilt, die die Fähigkeit einer SVR zur Bestimmung des SoC in einer Vielzahl von Szenarien bewerteten. Sieben Batteriezellen, die mit jeweils zwei Sensoranordnungen auf gegenüberliebenden Seiten präpariert wurden, dienten zur Erzeugung von 14 Datensätzen. Zunächst wurde ein Vergleich zwischen Selbsttests, bei denen ein Teil eines Datensatzes zum Training und ein anderer zum Testen verwendet wird, und Kreuztests, bei denen der Datensatz einer Zelle zum Training und der einer anderen zum Testen verwendet wird, durchgeführt. Dabei wurde ein mittlerer Fehler von 3,9% bis 4,8% SoC bzw. 3,6% bis 10,0% SoC erreicht. Im Allgemeinen wurde festgestellt, dass die SVR bei niedrigen SoCs zu einer Überschätzung und bei hohen SoCs zu einer Unterschätzung neigt, was auf die ausgeprägte Hysterese und Relaxation der Ultraschallsignaleigenschaften in diesen SoC-Bereichen zurückgeführt wurde. Die Tatsache, dass eine höhere Genauigkeit erreicht wird, wenn die genaue Zelle dem Regressionsmodell bekannt ist, deutet darauf hin, dass eine Variation zwischen den Zellen besteht. Diese Variation zwischen den Zellen kann auf Unterschiede in den mechanischen Eigenschaften infolge von Produktionsschwankungen oder auf Unterschiede in der manuellen Sensorplatzierung, der mechanischen Kopplung oder dem Resonanzverhalten der Ultraschallsensoren zurückzuführen sein. Um die Auswirkungen der Schwankungen zwischen den Zellen auf die Schätzgenauigkeit abzuschwächen, wurde ein Test durchgeführt, bei dem die Datensätze von sechs der sieben Zellen als Trainingsdaten kombiniert wurden und der Datensatz der siebten Zelle für den Test verwendet wurde. Dadurch verringerte sich die Streuung des mittleren Fehlers von (3,6 - 10,0)% SoC auf (5,9 - 8,5)% SoC, was einmal mehr zeigt, dass ein datenbasierter

Ansatz zur Zustandsbestimmung durch eine großen Datenbasis zuverlässiger wird. Anhand von Selbsttests mit sieben Datensätzen wurde die Auswirkung zusätzlicher Merkmale auf das Ergebnis der Zustandsbestimmung getestet. Die Einbeziehung eines zusätzlichen Merkmals verbesserte nicht unbedingt die Schätzgenauigkeit, aber es wurde gezeigt, dass eine Kombination von Ultraschall- und elektrischen Merkmalen dem Training mit diesen Merkmalen allein überlegen ist. Um die Fähigkeit des Modells zur Bestimmung des Ladezustands unter unbekannten Zyklusbedingungen zu testen, wurde ein Test durchgeführt, bei dem die C-Rate des Testdatensatzes nicht in den Trainingsdaten enthalten war. Das Ergebnis deutet darauf hin, dass es für praktische Anwendungen ausreichend sein könnte, das Training mit Datensätzen unter den Grenzbedingungen der Anwendungsfälle in einer kontrollierten Laborumgebung durchzuführen, um die Schätzung in einem breiten Spektrum von Anwendungsfällen zu bewältigen.

Im Vergleich zur Literatur hebt sich diese Studie dadurch ab, dass handelsübliche Piezoelemente verwendet und modifiziert wurden, um moderne Lithium-Ionen-Batteriezellen mit Ultraschallsensoren auszustatten, wobei eine Reihe von Mittenfrequenzen für die durch die Batteriezelle übertragene Wellenform anstelle einer festen Frequenz verwendet wird und der SVR die Frequenz wählen kann, die das beste Ergebnis liefert. Die Charakterisierung der Ultraschallsignaleigenschaften als Funktion der RC_n-Frequenz und des SoC sowie die Zuordnung charakteristischer Veränderungen der Signaleigenschaften zu elektrochemischen Prozessen wie den Phasenübergängen in den Aktivmaterialien machen diese Arbeit einzigartig. Durch die Untersuchung einer Reihe von Anwendungsfällen konnte gezeigt werden, dass mit Hilfe von Ultraschallmessungen eine verbesserte SoC-Abschätzungsgenauigkeit erreicht werden kann - dank der Korrelation der mechanischen Eigenschaften der Batteriezellen mit dem SoC.

6.2 Ausblick auf zukünftige Anwendungen von Ultraschall auf Lithium-Ionen-Batterien

Die Anwendung von Ultraschall zur Untersuchung und Bestimmung des Zustands von Lithium-Ionen-Batterien ist noch ein recht junges Forschungsgebiet. Daher sind noch viele Fragen in diesem Feld zu beantworten und neue Ideen umzusetzen. Von besonderem Interesse ist, welche der vorgestellten Ausbreitungsmoden in dem gewählten Aufbau am dominantesten ist. Hier könnten Laservibrometer-Untersuchungen der Schwingung der Oberfläche der Batteriezelle und Finite-Elemente-Modelle der Wellenausbreitung weitere Erkenntnisse liefern. In der Zukunft werden durch verschiedene Projekte deutlich mehr Datensätze mit mechanischen Messgrößen während der Zyklisierung von Batterien zur

Verfügung stehen, sodass es dann möglich sein wird die Parameter der SVR für den hier beschriebenen Anwendungsfall zu optimieren, um ein verallgemeinertes Modell zu erzeugen. Zusätzliche Merkmale, wie z. B. die Eigenschaften des Frequenzspektrums der Ultraschallsignale oder sogar ganze Abschnitte von Ultraschallsignalen, könnten in Zukunft verwendet werden, um die Bestimmungsgenauigkeit weiter zu erhöhen, erfordern aber möglicherweise den Einsatz von neuronalen Netzen zur Merkmalserkennung. Es gibt also viele Optionen für die Verbesserung der Zustandsbestimmung.

Die Reichweite dieser Arbeit wird bereits durch mehrere vor kurzem gestartete Projekte am Fraunhofer ISC erweitert, welche die Untersuchung von Degradations- und Alterungsphänomenen (MADAM4Life) und die Integration von Ultraschallwandlern mit anderen mechanischen Sensoren und Temperatursensoren (SPARTACUS) auf der Oberfläche von Hochenergie-Batteriezellen mit großer Kapazität unter automobilen Bedingungen, insbesondere unter mechanischer Verspannung der Batteriezellen beinhalten.

Aus dieser Arbeit entstand auch die Idee, Ultraschall zur Überwachung des Benetzungsprozesses von Lithium-Ionen-Batterien während der Produktion einzusetzen, die im Rahmen des Projekts Cell-Fill entwickelt wird. Ziel ist es, die Benetzungszeit zu verkürzen und damit die Kosten zu senken, indem der Zeitpunkt, an dem die Benetzung ausreichend fortgeschritten ist, um mit dem nächsten Produktionsschritt, der Formation, zu beginnen, genau bestimmt werden kann.

7 References

1. Diesendorf, M.; Elliston, B. The feasibility of 100% renewable electricity systems: A response to critics. *Renewable Sustainable Energy Rev.* **2018**, *93*, 318–330, doi:10.1016/j.rser.2018.05.042.
2. Waag, W.; Fleischer, C.; Sauer, D.U. Critical review of the methods for monitoring of lithium-ion batteries in electric and hybrid vehicles. *J. Power Sources* **2014**, *258*, 321–339, doi:10.1016/j.jpowsour.2014.02.064.
3. Loveridge, M.; Remy, G.; Kourra, N.; Genieser, R.; Barai, A.; Lain, M.; Guo, Y.; Amor-Segan, M.; Williams, M.; Amietszajew, T.; et al. Looking Deeper into the Galaxy (Note 7). *Batteries* **2018**, *4*, 3, doi:10.3390/batteries4010003.
4. Tan, C.C.; Loveridge, M.J.; Dixon, S.; Remy, G.; Kourra, N.; Genieser, R.; Barai, A.; Lain, M.J.; Guo, Y.; Amor-Segan, M.; et al. Pushing to the Limit: Samsung Galaxy Note 7 and Fitbit Flex 2. *Meet. Abstr.* **2018**, doi:10.1149/MA2018-02/7/482.
5. Garche, J.; Dyer, C.K. *Encyclopedia of electrochemical power sources;* Academic Press; Imprint of Elsevier: Amsterdam, Boston, 2009, ISBN 9780444527455.
6. Rodriguez, M.A.; Ingersoll, D.; Doughty, D.H. *In-situ x-ray characterization of $LiMn_2O_4$: A comparison of structural and electrochemical behavior*, Washington, D.C, Oak Ridge, Tenn, 1998. Available online: http://www.osti.gov/bridge/servlets/purl/634074-Rofgp5/webviewable/634074.pdf.
7. Märkle, W.; Colin, J.-F.; Goers, D.; Spahr, M.E.; Novák, P. In situ X-ray diffraction study of different graphites in a propylene carbonate based electrolyte at very positive potentials. *Electrochim. Acta* **2010**, *55*, 4964–4969, doi:10.1016/j.electacta.2010.03.103.
8. Reimers, J.N. Electrochemical and In Situ X-Ray Diffraction Studies of Lithium Intercalation in Li[sub x]CoO[sub 2]. *J. Electrochem. Soc.* **1992**, *139*, 2091, doi:10.1149/1.2221184.
9. Yin, S.-C.; Rho, Y.-H.; Swainson, I.; Nazar, L.F. X-ray/Neutron Diffraction and Electrochemical Studies of Lithium De/Re-Intercalation in Li 1-x Co 1/3 Ni 1/3 Mn 1/3 O 2 (x = 0 → 1). *Chem. Mater.* **2006**, *18*, 1901–1910, doi:10.1021/cm0511769.
10. Aurbach, D. The Study of Li-Graphite Intercalation Processes in Several Electrolyte Systems Using In Situ X-Ray Diffraction. *J. Electrochem. Soc.* **1995**, *142*, 1746, doi:10.1149/1.2044188.
11. Qi, Y.; Guo, H.; Hector, L.G.; Timmons, A. Threefold Increase in the Young's Modulus of Graphite Negative Electrode during Lithium Intercalation. *J. Electrochem. Soc.* **2010**, *157*, 558–566, doi:10.1149/1.3327913.
12. Qi, Y.; Hector, L.G.; James, C.; Kim, K.J. Lithium Concentration Dependent Elastic Properties of Battery Electrode Materials from First Principles Calculations. *J. Electrochem. Soc.* **2014**, *161*, 3010–3018, doi:10.1149/2.0031411jes.
13. Shenoy, V.B.; Johari, P.; Qi, Y. Elastic softening of amorphous and crystalline Li–Si Phases with increasing Li concentration: A first-principles study. *Journal of Power Sources* **2010**, *195*, 6825–6830, doi:10.1016/j.jpowsour.2010.04.044.

14. Figgemeier, E.; Teuber, M. Bedeutsame Batterien. *Physik-Journal* **2019**, *12/2019*, 28–33.
15. Swallow, J.G.; Woodford, W.H.; McGrogan, F.P.; Ferralis, N.; Chiang, Y.-M.; van Vliet, K.J. Effect of Electrochemical Charging on Elastoplastic Properties and Fracture Toughness of LiXCoO2. *Journal of the Electrochemical Society* **2014**, *161*, F3084-F3090, doi:10.1149/2.0141411jes.
16. Robinson, J.B.; Maier, M.; Alster, G.; Compton, T.; Brett, Dan J. L.; Shearing, P.R. Spatially resolved ultrasound diagnostics of Li-ion battery electrodes. *Phys. Chem. Chem. Phys.* **2019**, *21*, 6354–6361, doi:10.1039/c8cp07098a.
17. Davies, G.; Knehr, K.W.; van Tassell, B.; Hodson, T.; Biswas, S.; Hsieh, A.G.; Steingart, D.A. State of Charge and State of Health Estimation Using Electrochemical Acoustic Time of Flight Analysis. *J. Electrochem. Soc.* **2017**, *164*, A2746-A2755, doi:10.1149/2.1411712jes.
18. Maxisch, T.; Ceder, G. Elastic properties of olivine LixFePO4 from first principles. *Phys. Rev. B* **2006**, *73*, 1101, doi:10.1103/PhysRevB.73.174112.
19. Samba, A.; Omar, N.; Gualous, H.; Firouz, Y.; van den Bossche, P.; Van Mierlo, J.; Boubekeur, T.I. Development of an Advanced Two-Dimensional Thermal Model for Large size Lithium-ion Pouch Cells. *Electrochim. Acta* **2014**, *117*, 246–254, doi:10.1016/j.electacta.2013.11.113.
20. Popp, H.; Koller, M.; Jahn, M.; Bergmann, A. Mechanical methods for state determination of Lithium-Ion secondary batteries: A review. *J. Energy Storage* **2020**, *32*, 101859, doi:10.1016/j.est.2020.101859.
21. Sauerteig, D.; Ivanov, S.; Reinshagen, H.; Bund, A. Reversible and irreversible dilation of lithium-ion battery electrodes investigated by in-situ dilatometry. *J. Power Sources* **2017**, *342*, 939–946, doi:10.1016/j.jpowsour.2016.12.121.
22. Yi, T.-F.; Xie, Y.; Zhu, Y.-R.; Shu, J.; Zhou, A.-N.; Qiao, H.-B. Stabilities and electronic properties of lithium titanium oxide anode material for lithium ion battery. *J. Power Sources* **2012**, *198*, 318–321, doi:10.1016/j.jpowsour.2011.10.014.
23. Shu, J. Electrochemical behavior and stability of Li4Ti5O12 in a broad voltage window. *J. Solid State Electrochem.* **2009**, *13*, 1535–1539, doi:10.1007/s10008-008-0723-z.
24. Sauerteig, D. *Implementierung und Parametrierung eines physikalischen Simulationsmodells einer Lithium-Ionen Zelle zur Analyse elektrochemisch-mechanischer Wechselwirkungen;* Universitätsbibliothek: Ilmenau, 2018.
25. Knehr, K.W.; Hodson, T.; Bommier, C.; Davies, G.; Kim, A.; Steingart, D.A. Understanding Full-Cell Evolution and Nonchemical Electrode Crosstalk of Li-Ion Batteries. *Joule* **2018**, *2*, 1146–1159, doi:10.1016/j.joule.2018.03.016.
26. Andre, D.; Kim, S.-J.; Lamp, P.; Lux, S.F.; Maglia, F.; Paschos, O.; Stiaszny, B. Future generations of cathode materials: an automotive industry perspective. *J. Mater. Chem. A* **2015**, *3*, 6709–6732, doi:10.1039/C5TA00361J.
27. Nitta, N.; Wu, F.; Lee, J.T.; Yushin, G. Li-ion battery materials: present and future. *Materials Today* **2015**, *18*, 252–264, doi:10.1016/j.mattod.2014.10.040.
28. Beaulieu, L.Y.; Eberman, K.W.; Turner, R.L.; Krause, L.J.; Dahn, J.R. Colossal Reversible Volume Changes in Lithium Alloys. *Electrochem. Solid-State Lett.* **2001**, *4*, A137, doi:10.1149/1.1388178.

29. Li, P.; Hwang, J.-Y.; Sun, Y.-K. Nano/Microstructured Silicon-Graphite Composite Anode for High-Energy-Density Li-Ion Battery. *ACS Nano* **2019**, *13*, 2624–2633, doi:10.1021/acsnano.9b00169.
30. Shi, C.; Zhang, P.; Chen, L.; Yang, P.; Zhao, J. Effect of a thin ceramic-coating layer on thermal and electrochemical properties of polyethylene separator for lithium-ion batteries. *J. Power Sources* **2014**, *270*, 547–553, doi:10.1016/j.jpowsour.2014.07.142.
31. Reddy, T.B. *Linden's handbook of batteries*: *Set 2*, 4th ed.; McGraw-Hill Professional; McGraw-Hill [distributor]: New York, London, 2010, ISBN 978-0071624213.
32. Budde-Meiwes, H.; Drillkens, J.; Lunz, B.; Muennix, J.; Rothgang, S.; Kowal, J.; Sauer, D.U. A review of current automotive battery technology and future prospects. *Proc. Inst. Mech. Eng., Part D* **2013**, *227*, 761–776, doi:10.1177/0954407013485567.
33. Heimes, H.H. *Lithium-ion battery cell production process;* PEM der RWTH Aachen University; DVMA: Aachen, Frankfurt am Main, 2018, ISBN 9783947920037.
34. Günter, F.J.; Habedank, J.B.; Schreiner, D.; Neuwirth, T.; Gilles, R.; Reinhart, G. Introduction to Electrochemical Impedance Spectroscopy as a Measurement Method for the Wetting Degree of Lithium-Ion Cells. *J. Electrochem. Soc.* **2018**, *165*, A3249-A3256, doi:10.1149/2.0081814jes.
35. Danzer, M.A.; Liebau, V.; Maglia, F. Aging of lithium-ion batteries for electric vehicles. In *Advances in battery technologies for electric vehicles,* First edition; Scrosati, B., Garche, J., Tillmetz, W., Eds.; Woodhead Publishing: Cambridge, UK, 2015; pp 359–387, ISBN 9781782423775.
36. Huang, S.-C.; Tseng, K.-H.; Liang, J.-W.; Chang, C.-L.; Pecht, M. An Online SOC and SOH Estimation Model for Lithium-Ion Batteries. *Energies* **2017**, *10*, 512, doi:10.3390/en10040512.
37. Farmann, A.; Sauer, D.U. A comprehensive review of on-board State-of-Available-Power prediction techniques for lithium-ion batteries in electric vehicles. *J. Power Sources* **2016**, *329*, 123–137, doi:10.1016/j.jpowsour.2016.08.031.
38. Farmann, A.; Waag, W.; Marongiu, A.; Sauer, D.U. Critical review of on-board capacity estimation techniques for lithium-ion batteries in electric and hybrid electric vehicles. *Journal of Power Sources* **2015**, *281*, 114–130, doi:10.1016/j.jpowsour.2015.01.129.
39. Hu, X.; Feng, F.; Liu, K.; Zhang, L.; Xie, J.; Liu, B. State estimation for advanced battery management: Key challenges and future trends. *Renewable and Sustainable Energy Reviews* **2019**, *114*, 109334, doi:10.1016/j.rser.2019.109334.
40. Vetter, J.; Novák, P.; Wagner, M.; Veit, C.; Möller, K.-C.; Besenhard, J.; Winter, M.; Wohlfahrt-Mehrens, M.; Vogler, C.; Hammouche, A. Ageing mechanisms in lithium-ion batteries. *J. Power Sources* **2005**, *147*, 269–281, doi:10.1016/j.jpowsour.2005.01.006.
41. Birkl, C.R.; Roberts, M.R.; McTurk, E.; Bruce, P.G.; Howey, D.A. Degradation diagnostics for lithium ion cells. *J. Power Sources* **2017**, *341*, 373–386, doi:10.1016/j.jpowsour.2016.12.011.

42. Schlasza, C.; Ostertag, P.; Chrenko, D.; Kriesten, R.; Bouquain, D. Review on the aging mechanisms in Li-ion batteries for electric vehicles based on the FMEA method. In *IEEE Transportation Electrification Conference and Expo (ITEC), 2014*, 15 - 18 June 2014, Adoba Hotel Dearborn/Detroit, Dearborn, Michigan, USA. 2014 IEEE Transportation Electrification Conference and Expo (ITEC), Dearborn, MI, 6/15/2014 - 6/18/2014; IEEE: Piscataway, NJ, 2014; pp 1–6, ISBN 978-1-4799-2262-8.
43. Barré, A.; Deguilhem, B.; Grolleau, S.; Gérard, M.; Suard, F.; Riu, D. A review on lithium-ion battery ageing mechanisms and estimations for automotive applications. *J. Power Sources* **2013**, *241*, 680–689, doi:10.1016/j.jpowsour.2013.05.040.
44. Keil, P. *Aging of Lithium-Ion Batteries in Electric Vehicles;* Technischen Universität München: München, 2017.
45. Liu, K.; Li, K.; Peng, Q.; Zhang, C. A brief review on key technologies in the battery management system of electric vehicles. *Front. Mech. Eng.* **2019**, *14*, 47–64, doi:10.1007/s11465-018-0516-8.
46. Ali, M.U.; Zafar, A.; Nengroo, S.H.; Hussain, S.; Alvi, M.J.; Kim, H.-J. Towards a Smarter Battery Management System for Electric Vehicle Applications: A Critical Review of Lithium-Ion Battery State of Charge Estimation. *Energies* **2019**, *12*, 446, doi:10.3390/en12030446.
47. Chang, W.-Y. The State of Charge Estimating Methods for Battery: A Review. *ISRN Applied Mathematics* **2013**, *2013*, 1–7, doi:10.1155/2013/953792.
48. Rivera-Barrera, J.; Muñoz-Galeano, N.; Sarmiento-Maldonado, H. SoC Estimation for Lithium-ion Batteries: Review and Future Challenges. *Electronics* **2017**, *6*, 102, doi:10.3390/electronics6040102.
49. How, D.N.T.; Hannan, M.A.; Hossain Lipu, M.S.; Ker, P.J. State of Charge Estimation for Lithium-Ion Batteries Using Model-Based and Data-Driven Methods: A Review. *IEEE Access* **2019**, *7*, 136116–136136, doi:10.1109/ACCESS.2019.2942213.
50. Hannan, M.A.; Lipu, M.; Hussain, A.; Mohamed, A. A review of lithium-ion battery state of charge estimation and management system in electric vehicle applications: Challenges and recommendations. *Renewable Sustainable Energy Rev.* **2017**, *78*, 834–854, doi:10.1016/j.rser.2017.05.001.
51. Fleischer, C.; Waag, W.; Heyn, H.-M.; Sauer, D.U. On-line adaptive battery impedance parameter and state estimation considering physical principles in reduced order equivalent circuit battery models. *J. Power Sources* **2014**, *260*, 276–291, doi:10.1016/j.jpowsour.2014.01.129.
52. Zheng, Y.; Ouyang, M.; Han, X.; Lu, L.; Li, J. Investigating the error sources of the online state of charge estimation methods for lithium-ion batteries in electric vehicles. *Journal of Power Sources* **2018**, *377*, 161–188, doi:10.1016/j.jpowsour.2017.11.094.
53. Murnane, M.; Ghazel, A. *A Closer Look at State of Charge (SOC) and State of Health (SOH) Estimation Techniques for Batteries*, 2017. Available online: https://www.analog.com/media/en/technical-documentation/technical-articles/A-Closer-Look-at-State-Of-Charge-and-State-Health-Estimation-Techniques-…pdf.
54. Coleman, M.; Lee, C.K.; Zhu, C.; Hurley, W.G. State-of-Charge Determination From EMF Voltage Estimation: Using Impedance, Terminal Voltage, and Current

for Lead-Acid and Lithium-Ion Batteries. *IEEE Trans. Ind. Electron.* **2007**, *54*, 2550–2557, doi:10.1109/TIE.2007.899926.
55. Waag, W.; Sauer, D.U. Adaptive estimation of the electromotive force of the lithium-ion battery after current interruption for an accurate state-of-charge and capacity determination. *Appl. Energy* **2013**, *111*, 416–427, doi:10.1016/j.apenergy.2013.05.001.
56. Lu, L.; Han, X.; Li, J.; Hua, J.; Ouyang, M. A review on the key issues for lithium-ion battery management in electric vehicles. *J. Power Sources* **2013**, *226*, 272–288, doi:10.1016/j.jpowsour.2012.10.060.
57. Zhang, R.; Xia, B.; Li, B.; Cao, L.; Lai, Y.; Zheng, W.; Wang, H.; Wang, W. State of the Art of Lithium-Ion Battery SOC Estimation for Electrical Vehicles. *Energies* **2018**, *11*, 1820, doi:10.3390/en11071820.
58. Mehne, J.; Nowak, W. Improving temperature predictions for Li-ion batteries: data assimilation with a stochastic extension of a physically-based, thermo-electrochemical model. *J. Energy Storage* **2017**, *12*, 288–296, doi:10.1016/j.est.2017.05.013.
59. Lee, K.-T.; Dai, M.-J.; Chuang, C.-C. Temperature-Compensated Model for Lithium-Ion Polymer Batteries With Extended Kalman Filter State-of-Charge Estimation for an Implantable Charger. *IEEE Trans. Ind. Electron.* **2018**, *65*, 589–596, doi:10.1109/TIE.2017.2721880.
60. Raijmakers, L.H.J.; Danilov, D.L.; van Lammeren, J.P.M.; Lammers, T.J.G.; Bergveld, H.J.; Notten, P.H.L. Non-Zero Intercept Frequency: An Accurate Method to Determine the Integral Temperature of Li-Ion Batteries. *IEEE Trans. Ind. Electron.* **2016**, *63*, 3168–3178, doi:10.1109/TIE.2016.2516961.
61. Dai, H.; Zhu, L.; Zhu, J.; Wei, X.; Sun, Z. Adaptive Kalman filtering based internal temperature estimation with an equivalent electrical network thermal model for hard-cased batteries. *J. Power Sources* **2015**, *293*, 351–365, doi:10.1016/j.jpowsour.2015.05.087.
62. Angeles Cabañero, M.; Altmann, J.; Gold, L.; Boaretto, N.; Müller, J.; Hein, S.; Zausch, J.; Kallo, J.; Latz, A. Investigation of the temperature dependence of lithium plating onset conditions in commercial Li-ion batteries. *Energy* **2019**, *171*, 1217–1228, doi:10.1016/j.energy.2019.01.017.
63. Edwards, C.; Spurgeon, S.K.; Tan, C.P. On the Development and Application of Sliding Mode Observers. In *Variable Structure Systems: Towards the 21st Century*; Yu, X., Xu, J.-X., Eds.; Springer Berlin Heidelberg: Berlin, Heidelberg, 2002; pp 253–282, ISBN 978-3-540-42965-4.
64. Grewal, M.S.; Andrews, A.P. Applications of Kalman Filtering in Aerospace 1960 to the Present [Historical Perspectives]. *IEEE Control Syst.* **2010**, *30*, 69–78, doi:10.1109/MCS.2010.936465.
65. Xiong, R.; He, H.; Sun, F.; Zhao, K. Evaluation on State of Charge Estimation of Batteries With Adaptive Extended Kalman Filter by Experiment Approach. *IEEE Trans. Veh. Technol.* **2013**, *62*, 108–117, doi:10.1109/TVT.2012.2222684.
66. He, H.; Xiong, R.; Guo, H. Online estimation of model parameters and state-of-charge of LiFePO4 batteries in electric vehicles. *Appl. Energy* **2012**, *89*, 413–420, doi:10.1016/j.apenergy.2011.08.005.
67. Jiang, C.; Taylor, A.; Duan, C.; Bai, K. Extended Kalman Filter based battery state of charge(SOC) estimation for electric vehicles. In *IEEE Transportation*

Electrification Conference and Expo (ITEC), 2013, 16 - 19 June 2013, Adoba Hotel Dearborn/Detroit (former Hyatt Regency), Dearborn, Michigan, USA. 2013 IEEE Transportation Electrification Conference and Expo (ITEC), Metro Detroit, MI, USA, 6/16/2013 - 6/19/2013; IEEE: Piscataway, NJ, 2013; pp 1–5, ISBN 978-1-4799-0148-7.

68. He, W.; Williard, N.; Chen, C.; Pecht, M. State of charge estimation for electric vehicle batteries using unscented kalman filtering. *Microelectronics Reliability* **2013**, *53*, 840–847, doi:10.1016/j.microrel.2012.11.010.
69. Yatsui, M.W.; Bai, H. Kalman filter based state-of-charge estimation for lithium-ion batteries in hybrid electric vehicles using pulse charging. In *IEEE Vehicle Power and Propulsion Conference (VPPC), 2011*, 6 - 9 Sept. 2011, Chicago, IL, USA. 2011 IEEE Vehicle Power and Propulsion Conference (VPPC), Chicago, IL, USA, 9/6/2011 - 9/9/2011; IEEE: Piscataway, NJ, 2011; pp 1–5, ISBN 978-1-61284-248-6.
70. Lee, S.J.; Kim, J.H.; Lee, J.M.; Cho, B.H. The State and Parameter Estimation of an Li-Ion Battery Using a New OCV-SOC Concept. In *IEEE Power Electronics Specialists Conference, 2007*, PESC 2007 ; 17 - 21 June 2007, Orlando, Florida, USA. 2007 IEEE Power Electronics Specialists Conference, Orlando, FL, USA, 6/17/2007 - 6/21/2007; IEEE Service Center: Piscataway, NJ, 2007; pp 2799–2803, ISBN 978-1-4244-0654-8.
71. Utkin, V.I. *Sliding Modes in Control and Optimization;* Springer: Berlin, Heidelberg, 1992, ISBN 9783642843815.
72. Hu, X.; Li, S.E.; Yang, Y. Advanced Machine Learning Approach for Lithium-Ion Battery State Estimation in Electric Vehicles. *IEEE Trans. Transp. Electrific.* **2016**, *2*, 140–149, doi:10.1109/TTE.2015.2512237.
73. Sanger, T.D. Optimal unsupervised learning in a single-layer linear feedforward neural network. *Neural Networks* **1989**, *2*, 459–473, doi:10.1016/0893-6080(89)90044-0.
74. Hannan, M.A.; Lipu, M.S.H.; Hussain, A.; Saad, M.H.; Ayob, A. Neural Network Approach for Estimating State of Charge of Lithium-Ion Battery Using Backtracking Search Algorithm. *IEEE Access* **2018**, *6*, 10069–10079, doi:10.1109/ACCESS.2018.2797976.
75. Kang, L.; Zhao, X.; Ma, J. A new neural network model for the state-of-charge estimation in the battery degradation process. *Appl. Energy* **2014**, *121*, 20–27, doi:10.1016/j.apenergy.2014.01.066.
76. Cui, D.; Xia, B.; Zhang, R.; Sun, Z.; Lao, Z.; Wang, W.; Sun, W.; Lai, Y.; Wang, M. A Novel Intelligent Method for the State of Charge Estimation of Lithium-Ion Batteries Using a Discrete Wavelet Transform-Based Wavelet Neural Network. *Energies* **2018**, *11*, 995, doi:10.3390/en11040995.
77. Chaoui, H.; Ibe-Ekeocha, C.C. State of Charge and State of Health Estimation for Lithium Batteries Using Recurrent Neural Networks. *IEEE Trans. Veh. Technol.* **2017**, *66*, 8773–8783, doi:10.1109/TVT.2017.2715333.
78. Vapnik, V.N. *The Nature of Statistical Learning Theory;* Springer: New York, NY, 1995, ISBN 9781475724424.
79. Vanderplas, J.T. *Python data science handbook*: *Tools and techniques for developers;* O'Reilly: Beijing, 2016, ISBN 1491912057.

80. Vanderplas, J. In-Depth: Support Vector Machines. Available online: https://jakevdp.github.io/PythonDataScienceHandbook/05.07-support-vector-machines.html (accessed on 5 September 2020).
81. *Efficient Learning Machines*: *Theories, Concepts, and Applications for Engineers and System Designers;* Awad, M.; Khanna, R., Eds.; Apress; Imprint: Berkeley, CA, 2015, ISBN 978-1-4302-5989-3.
82. Sharp; Tom. An Introduction to Support Vector Regression (SVR): Using Support Vector Machines (SVMs) for Regression. Available online: https://towardsdatascience.com/an-introduction-to-support-vector-regression-svr-a3ebc1672c2 (accessed on 5 September 2020).
83. Álvarez Antón, J.C.; García Nieto, P.J.; Cos Juez, F.J. de; Sánchez Lasheras, F.; González Vega, M.; Roqueñí Gutiérrez, M.N. Battery state-of-charge estimator using the SVM technique. *Applied Mathematical Modelling* **2013**, *37*, 6244–6253, doi:10.1016/j.apm.2013.01.024.
84. Alvarez Anton, J.C.; Garcia Nieto, P.J.; Blanco Viejo, C.; Vilan Vilan, J.A. Support Vector Machines Used to Estimate the Battery State of Charge. *IEEE Trans. Power Electron.* **2013**, *28*, 5919–5926, doi:10.1109/TPEL.2013.2243918.
85. Hsieh, A.G.; Bhadra, S.; Hertzberg, B.J.; Gjeltema, P.J.; Goy, A.; Fleischer, J.W.; Steingart, D.A. Electrochemical-acoustic time of flight: in operando correlation of physical dynamics with battery charge and health. *Energy Environ. Sci.* **2015**, *8*, 1569–1577, doi:10.1039/C5EE00111K.
86. Bhadra, S. Methods for Characterization of Batteries Using Acoustic Interrogation. Dissertation; Princeton University, Princeton, NJ, 2015.
87. Ladpli, P.; Kopsaftopoulos, F.; Nardari, R.; Chang, F.-K. Battery charge and health state monitoring via ultrasonic guided-wave-based methods using built-in piezoelectric transducers. In . SPIE Smart Structures and Materials + Nondestructive Evaluation and Health Monitoring, Portland, Oregon, United States, Saturday 25 March 2017; Meyendorf, N.G., Ed.; SPIE, 2017; p 1017108.
88. Ladpli, P.; Kopsaftopoulos, F.; Chang, F.K. Battery state of charge estimation using guided waves - Numerical validation and statistical analysis. *Structural Health Monitoring 2017: Real-Time Material State Awareness and Data-Driven Safety Assurance - Proceedings of the 11th International Workshop on Structural Health Monitoring, IWSHM 2017*, 2017; pp 1839–1849, ISBN 9781605953304.
89. Gold, L.; Bach, T.; Virsik, W.; Schmitt, A.; Müller, J.; Staab, T.E.; Sextl, G. Probing lithium-ion batteries' state-of-charge using ultrasonic transmission – Concept and laboratory testing. *J. Power Sources* **2017**, *343*, 536–544, doi:10.1016/j.jpowsour.2017.01.090.
90. Wu, Y.; Wang, Y.; Yung, W.K.C.; Pecht, M. Ultrasonic Health Monitoring of Lithium-Ion Batteries. *Electronics* **2019**, *8*, 751, doi:10.3390/electronics8070751.
91. Hsieh, A.G.; van TASSELL, B.J.; MOHR, R.C.; Wilkinson, A.; Ajo-Franklin, J.; Biswas, S. Nonlinear acoustic resonance spectroscopy (nars) for determining physical conditions of batteries. App. No.: US15/836,531, December 8, 2017, Pat. No.: US2018/0164383A1.
92. Sauer, D.U.; Fuchs, G.; Gitis, A.; Jöst, D.; Knips, M.; Kuipers, M.; Ringbeck, F.; Willenberg, L.K.; Zappen, H. *Future Battery Management - Next generation diagonstic algorithms and advanced measurement technologie*, 2019.

93. Steingart, D.A.; Bhadra, S.; Hsieh, A.G.; Hertzberg, B.; GJELTEMA, P.J.; ROWLEY, C.W.[.; Goy, A.S.; Fleischer, J.W. Apparatus and method for determining state of change (soc) and state of health (soh) of electrical cells. App. No.: US16/150,655, October 3, 2018, Pat. No.: US2019/0064123A1.
94. Ladpli, P.; Liu, C.; Kopsaftopoulos, F.; Chang, F.-K. Estimating Lithium-ion Battery State of Charge and Health with Ultrasonic Guided Waves Using an Efficient Matching Pursuit Technique. In *E-mobility: a journey from now and beyond*, 2018 IEEE Transportation Electrification Conference and Expo Asia-Pacific (ITEC Asia-Pacific) : 6-9 June 2018 at BITEC, Bangkok, Thailand. 2018 IEEE Transportation Electrification Conference and Expo, Asia-Pacific (ITEC Asia-Pacific), Bangkok, Thailand, 6/6/2018 - 9/6/2018; IEEE: [Piscataway, NJ], 2018; pp 1–5, ISBN 978-1-5386-5782-9.
95. Lee, J.H.; Lee, H.M.; Ahn, S. Battery dimensional changes occurring during charge/discharge cycles—thin rectangular lithium ion and polymer cells. *J. Power Sources* **2003**, *119-121*, 833–837, doi:10.1016/S0378-7753(03)00281-7.
96. Bauer, M.; Wachtler, M.; Stöwe, H.; Persson, J.V.; Danzer, M.A. Understanding the dilation and dilation relaxation behavior of graphite-based lithium-ion cells. *J. Power Sources* **2016**, *317*, 93–102, doi:10.1016/j.jpowsour.2016.03.078.
97. Louli, A.J.; Li, J.; Trussler, S.; Fell, C.R.; Dahn, J.R. Volume, Pressure and Thickness Evolution of Li-Ion Pouch Cells with Silicon-Composite Negative Electrodes. *J. Electrochem. Soc.* **2017**, *164*, A2689-A2696, doi:10.1149/2.1691712jes.
98. Oh, K.-Y.; Epureanu, B.I. A novel thermal swelling model for a rechargeable lithium-ion battery cell. *J. Power Sources* **2016**, *303*, 86–96, doi:10.1016/j.jpowsour.2015.10.085.
99. Grimsmann, F.; Brauchle, F.; Gerbert, T.; Gruhle, A.; Knipper, M.; Parisi, J. Hysteresis and current dependence of the thickness change of lithium-ion cells with graphite anode. *J. Energy Storage* **2017**, *12*, 132–137, doi:10.1016/j.est.2017.04.006.
100. Oh, K.-Y.; Siegel, J.B.; Secondo, L.; Kim, S.U.; Samad, N.A.; Qin, J.; Anderson, D.; Garikipati, K.; Knobloch, A.; Epureanu, B.I.; et al. Rate dependence of swelling in lithium-ion cells. *J. Power Sources* **2014**, *267*, 197–202, doi:10.1016/j.jpowsour.2014.05.039.
101. Rieger, B.; Schlueter, S.; Erhard, S.V.; Schmalz, J.; Reinhart, G.; Jossen, A. Multi-scale investigation of thickness changes in a commercial pouch type lithium-ion battery. *J. Energy Storage* **2016**, *6*, 213–221, doi:10.1016/j.est.2016.01.006.
102. Spingler, F.B.; Wittmann, W.; Sturm, J.; Rieger, B.; Jossen, A. Optimum fast charging of lithium-ion pouch cells based on local volume expansion criteria. *J. Power Sources* **2018**, *393*, 152–160, doi:10.1016/j.jpowsour.2018.04.095.
103. Bitzer, B.; Gruhle, A. A new method for detecting lithium plating by measuring the cell thickness. *J. Power Sources* **2014**, *262*, 297–302, doi:10.1016/j.jpowsour.2014.03.142.
104. Grimsmann, F.; Gerbert, T.; Brauchle, F.; Gruhle, A.; Parisi, J.; Knipper, M. Determining the maximum charging currents of lithium-ion cells for small charge quantities. *J. Power Sources* **2017**, *365*, 12–16, doi:10.1016/j.jpowsour.2017.08.044.

105. Cannarella, J.; Arnold, C.B. State of health and charge measurements in lithium-ion batteries using mechanical stress. *J. Power Sources* **2014**, *269*, 7–14, doi:10.1016/j.jpowsour.2014.07.003.
106. Cannarella, J.; Leng, C.Z.; Arnold, C.B. On the coupling between stress and voltage in lithium-ion pouch cells. In *Energy Harvesting and Storage: Materials, Devices, and Applications V.* SPIE Sensing Technology + Applications, Baltimore, Maryland, USA, Monday 5 May 2014; Dhar, N.K., Balaya, P., Dutta, A.K., Eds.; SPIE, 2014; 91150K.
107. Mohan, S.; Kim, Y.; Stefanopoulou, A.G. On Improving Battery State of Charge Estimation Using Bulk Force Measurements. In *Volume 1: Adaptive and Intelligent Systems Control; Advances in Control Design Methods; Advances in Non-Linear and Optimal Control; Advances in Robotics; Advances in Wind Energy Systems; Aerospace Applications; Aerospace Power Optimization; Assistive Robotics; Automotive 2: Hybrid Electric Vehicles; Automotive 3: Internal Combustion Engines; Automotive Engine Control; Battery Management; Bio Engineering Applications; Biomed and Neural Systems; Connected Vehicles; Control of Robotic Systems.* ASME 2015 Dynamic Systems and Control Conference, Columbus, Ohio, USA, 28–30 Oct. 2015; American Society of Mechanical Engineers, 10282015, ISBN 978-0-7918-5724-3.
108. Figueroa-Santos, M.A.; Siegel, J.B.; Stefanopoulou, A.G. Leveraging Cell Expansion Sensing in State of Charge Estimation: Practical Considerations. *Energies* **2020**, *13*, 2653, doi:10.3390/en13102653.
109. Cannarella, J.; Arnold, C.B. Stress evolution and capacity fade in constrained lithium-ion pouch cells. *J. Power Sources* **2014**, *245*, 745–751, doi:10.1016/j.jpowsour.2013.06.165.
110. Meyer, J.; Nedjalkov, A.; Doering, A.; Angelmahr, M.; Schade, W. Fiber optical sensors for enhanced battery safety. In *Fiber Optic Sensors and Applications XII.* SPIE Sensing Technology + Applications, Baltimore, Maryland, United States, Monday 20 April 2015; Pickrell, G., Udd, E., Du, H.H., Eds.; SPIE, 2015; 94800Z.
111. Willenberg, L.K.; Dechent, P.; Fuchs, G.; Sauer, D.U.; Figgemeier, E. High-Precision Monitoring of Volume Change of Commercial Lithium-Ion Batteries by Using Strain Gauges. *Sustainability* **2020**, *12*, 557, doi:10.3390/su12020557.
112. Willenberg, L.; Dechent, P.; Fuchs, G.; Teuber, M.; Eckert, M.; Graff, M.; Kürten, N.; Sauer, D.U.; Figgemeier, E. The Development of Jelly Roll Deformation in 18650 Lithium-Ion Batteries at Low State of Charge. *J. Electrochem. Soc.* **2020**, *167*, 120502, doi:10.1149/1945-7111/aba96d.
113. Bae, C.-J.; Manandhar, A.; Kiesel, P.; Raghavan, A. Monitoring the Strain Evolution of Lithium-Ion Battery Electrodes using an Optical Fiber Bragg Grating Sensor. *Energy Technol.* **2016**, *4*, 851–855, doi:10.1002/ente.201500514.
114. Gong, Z.; Xiang, Z.; OuYang, X.; Zhang, J.; Lau, N.; Zhou, J.; Chan, C.C. Wearable Fiber Optic Technology Based on Smart Textile: A Review. *Materials* **2019**, *12*, doi:10.3390/ma12203311.
115. Raghavan, A.; Kiesel, P.; Sommer, L.W.; Schwartz, J.; Lochbaum, A.; Hegyi, A.; Schuh, A.; Arakaki, K.; Saha, B.; Ganguli, A.; et al. Embedded fiber-optic sensing for accurate internal monitoring of cell state in advanced battery management systems part 1: Cell embedding method and performance. *J. Power Sources* **2017**, *341*, 466–473, doi:10.1016/j.jpowsour.2016.11.104.

116. Ganguli, A.; Saha, B.; Raghavan, A.; Kiesel, P.; Arakaki, K.; Schuh, A.; Schwartz, J.; Hegyi, A.; Sommer, L.W.; Lochbaum, A.; et al. Embedded fiber-optic sensing for accurate internal monitoring of cell state in advanced battery management systems part 2: Internal cell signals and utility for state estimation. *J. Power Sources* **2017**, *341*, 474–482, doi:10.1016/j.jpowsour.2016.11.103.
117. Popp, H.; Glanz, G.; Alten, K.; Gocheva, I.; Berghold, W.; Bergmann, A. Mechanical Frequency Response Analysis of Lithium-Ion Batteries to Disclose Operational Parameters. *Energies* **2018**, *11*, 541, doi:10.3390/en11030541.
118. Pham, H.L.; Dietz, J.E.; Adams, D.E.; Sharp, N.D. Lithium-Ion Battery Cell Health Monitoring Using Vibration Diagnostic Test. In *Volume 4B: Dynamics, Vibration and Control.* ASME 2013 International Mechanical Engineering Congress and Exposition, San Diego, California, USA, 15–21 Nov. 2013; American Society of Mechanical Engineers, 11152013, ISBN 978-0-7918-5625-3.
119. Berg, P.; Soellner, J.; Herrmann, M.; Jossen, A. Structural dynamics of lithium-ion cells—part II: Investigation of large-format prismatic cells and method evaluation. *J. Energy Storage* **2020**, *28*, 101246, doi:10.1016/j.est.2020.101246.
120. Berg, P.; Soellner, J.; Jossen, A. Structural dynamics of lithium-ion cells – Part I: Method, test bench validation and investigation of lithium-ion pouch cells. *J. Energy Storage* **2019**, *26*, 100916, doi:10.1016/j.est.2019.100916.
121. Hooper, J.M.; Marco, J. Experimental modal analysis of lithium-ion pouch cells. *J. Power Sources* **2015**, *285*, 247–259, doi:10.1016/j.jpowsour.2015.03.098.
122. Raj, B.; Jayakumar, T.; Thavasimuthu, M. *Practical non-destructive testing;* Woodhead Publishing, 2002.
123. Kircheva, N.; Genies, S.; Brun-Buisson, D.; Thivel, P.-X. Study of Solid Electrolyte Interface Formation and Lithium Intercalation in Li-Ion Batteries by Acoustic Emission. *J. Electrochem. Soc.* **2011**, *159*, A18-A25, doi:10.1149/2.045201jes.
124. Kircheva, N.; Genies, S.; Chabrol, C.; Thivel, P.-X. Evaluation of acoustic emission as a suitable tool for aging characterization of LiAl/LiMnO2 cell. *Electrochim. Acta* **2013**, *88*, 488–494, doi:10.1016/j.electacta.2012.10.121.
125. Komagata, S.; Kuwata, N.; Baskaran, R.; Kawamura, J.; Sato, K.; Mizusaki, J. Detection of Degradation of Lithium-Ion Batteries with Acoustic Emission Technique. *ECS Trans.* **2009**, *25*, 163–167, doi:10.1149/1.3334804.
126. Beganovic, N.; Söffker, D. Estimation of Remaining Useful Lifetime of Lithium-Ion Battery Based on Acoustic Emission Measurements. *Journal of Energy Resources Technology* **2019**, *141*, 679, doi:10.1115/1.4042234.
127. Sood, B.; Osterman, M.; Pecht, M. *Health monitoring of lithium-ion batteries*. Available online: http://www.asminternational.org/documents/10192/18102672/edfa1602p04.pdf/0a0779c8-bebd-4686-878c-bc5b1f6e086e.
128. Hsieh, A.G.; Bhadra, S.; Gjeltema, P.J.; Steingart, D.A. Investigating Failure of Li-Ion Batteries Using in Operando Electrochemical-Acoustic Time-of-Flight Analysis. *Meet. Abstr.* **2015**, doi:10.1149/MA2015-02/1/85.
129. Ladpli, P.; Kopsaftopoulos, F.; Chang, F.-K. Estimating state of charge and health of lithium-ion batteries with guided waves using built-in piezoelectric sensors/actuators. *J. Power Sources* **2018**, *384*, 342–354, doi:10.1016/j.jpowsour.2018.02.056.

130. Ladpli, P.; Liu, C.; Kopsaftopoulos, F.; Chang, F.-K. Health Prognostics of Lithium-ion Batteries and Battery-Integrated Structures. In *Structural Health Monitoring 2019.* Structural Health Monitoring 2019, 10/24/2018 - 10/26/2018; DEStech Publications, Inc: Lancaster, PA, 2018 - 2018, ISBN 978-1-60595-601-5.
131. Popp, H.; Koller, M.; Keller, S.; Glanz, G.; Klambauer, R.; Bergmann, A. State Estimation Approach of Lithium-Ion Batteries by Simplified Ultrasonic Time-of-Flight Measurement. *IEEE Access* **2019**, *7*, 170992–171000, doi:10.1109/ACCESS.2019.2955556.
132. Sharapov, V.M. *Piezoceramic sensors;* Springer: Heidelberg, New York, 2011, ISBN 3642153119.
133. Eichler, H.J.; Kronfeldt, H.-D.; Sahm, J. *Das Neue Physikalische Grundpraktikum*, 2., erw. und aktualisierte Aufl.; Springer: Berlin, 2006.
134. Zhang, Y.M. Real-Time Weld Process Monitoring. *Real-Time Weld Process Monitoring*, 2008; pp 1–299, ISBN 9781845692681.
135. National Science Foundation. History of Ultrasonics. Available online: https://www.nde-ed.org/EducationResources/CommunityCollege/Ultrasonics/Introduction/history.htm (accessed on 29 May 2018).
136. Rose, J.L. *Ultrasonic waves in solid media*, 1st paperback ed.; Cambridge University Press: Cambridge, 2014, ISBN 0521548896.
137. Leighton, T.G. What is ultrasound? *Prog. Biophys. Mol. Biol.* **2007**, *93*, 3–83, doi:10.1016/j.pbiomolbio.2006.07.026.
138. Bergmann, L. *Der Ultraschall und seine Anwendung in Wissenschaft und Technik*, 6., völlig überarb. und erw. Aufl.; Hirzel: Stuttgart, 1954.
139. Krautkrämer, J.; Krautkrämer, H. *Werkstoffprüfung mit Ultraschall, von Josef Krautkrämer und Herbert Krautkrämer. Unter Mitarbeit von Werner Grabendörfer und Ludwig Niklas;* Springer: Berlin, 1961.
140. Schubert, L. *Zustandsüberwachung an Faserverbundwerkstoffen mit geführten Wellen;* TUDpress: Dresden, 2012, ISBN 978-3-942710-72-5.
141. Demtröder, W. *Experimentalphysik 1*: *Mechanik und Wärme*, 4., neu bearb. und aktualisierte Aufl.; Springer: Berlin [u.a.], 2006, ISBN 3-540-26034-x.
142. Demtröder, W. *Experimentalphysik 2*: *Elektrizität und Optik*, 5., überarb. und erw. Aufl.; Springer: Berlin, Heidelberg, New York, ISBN 978-3-540-68210-3.
143. Bronštejn, I.N. *Taschenbuch der Mathematik*, 8., vollst. überarb. Aufl.; Harri Deutsch: Frankfurt am Main, 2012, ISBN 978-3-8171-2007-9.
144. Haken, H.; Wolf, H.C. *Atom- und Quantenphysik*: *Einführung in die experimentellen und theoretischen Grundlagen;* Springer: Berlin, Heidelberg, 2004, ISBN 978-3-642-18519-9.
145. Strutt, John William, Lord Rayleigh. On Waves Propagated along the Plane Surface of an Elastic Solid. *Proceedings of the London Mathematical Society* **1885**, *s1-17*, 4–11, doi:10.1112/plms/s1-17.1.4.
146. Šutilov, V.A. *Physik des Ultraschalls*: *Grundlagen;* Springer: Wien, New York, 1984, ISBN 9780387817989.
147. Achenbach, J.D. *Wave propagation in elastic solids*, Transfered to digital print, 2005, ISBN 0720403251.

148. The reflection of X-rays by crystals. *Proc. R. Soc. Lond. A* **1913**, *88*, 428–438, doi:10.1098/rspa.1913.0040.
149. Schoch, A. Schallreflexion, Schallbrechung und Schallbeugung. In *Ergebnisse der Exakten Naturwissenschaften*; Flügge, S., Trendelenburg, F., Eds.; Springer: Berlin, Heidelberg, 1950; pp 127–234, ISBN 9783540014553.
150. *Ultrasonic testing;* Workman, G.L.; Kishoni, D.; Moore, P.O., Eds., 3. ed.; American Society for Nondestructive Testing: Columbus, Ohio, 2007, ISBN 978-1-57117-105-4.
151. Nayfeh, A.H. *Wave propagation in layered anisotropic media*: *With applications to composites;* Elsevier: Amsterdam, 1995, ISBN 0-444-89018-1.
152. Rose, J.L. Ultrasonic guided waves in structural health monitoring. *Key Engineering Materials* **2004**, *270-273*, 14–21.
153. Carcione, J.M.; Kosloff, D.; Behle, A. Long-wave anisotropy in stratified media: A numerical test. *Geophysics* **1991**, *56*, 245–254, doi:10.1190/1.1443037.
154. Melia, P.J.; Carlson, R.L. An experimental test of P -wave anisotropy in stratified media. *Geophysics* **1984**, *49*, 374–378, doi:10.1190/1.1441673.
155. Biot, M.A. Theory of Propagation of Elastic Waves in a Fluid-Saturated Porous Solid. I. Low-Frequency Range. *J. Acoust. Soc. Am.* **1956**, *28*, 168–178, doi:10.1121/1.1908239.
156. Biot, M.A. Theory of Propagation of Elastic Waves in a Fluid-Saturated Porous Solid. II. Higher Frequency Range. *J. Acoust. Soc. Am.* **1956**, *28*, 179–191, doi:10.1121/1.1908241.
157. Pakula, M.; Padilla, F.; Laugier, P.; Kaczmarek, M. Application of Biot's theory to ultrasonic characterization of human cancellous bones: determination of structural, material, and mechanical properties. *J. Acoust. Soc. Am.* **2008**, *123*, 2415–2423, doi:10.1121/1.2839016.
158. Langton, C.M.; Njeh, C.F. The measurement of broadband ultrasonic attenuation in cancellous bone--a review of the science and technology. *IEEE Trans. Ultrason. Ferroelectr. Freq. Control* **2008**, *55*, 1546–1554, doi:10.1109/TUFFC.2008.831.
159. Plona, T.J. Observation of a second bulk compressional wave in a porous medium at ultrasonic frequencies. *Appl. Phys. Lett.* **1980**, *36*, 259, doi:10.1063/1.91445.
160. Fellah, Z.A.; Sebaa, N.; Fellah, M.; Mitri, F.G.; Ogam, E.; Lauriks, W.; Depollier, C. Application of the biot model to ultrasound in bone: direct problem. *IEEE Trans. Ultrason. Ferroelectr. Freq. Control* **2008**, *55*, 1508–1515, doi:10.1109/TUFFC.2008.826.
161. Gómez Alvarez-Arenas, T.E.; Riera-Franco de Sarabia, E.; Montero de Espinosa-Feijo, F.R. Observation of a very slow ultrasonic bulk compressional wave in an inhomogeneous porous material. *Ultrasonics* **1994**, *32*, 131–140, doi:10.1016/0041-624X(94)90021-3.
162. Gómez-Alvarez Arenas, T.E.; Riera Franco De Sarabia, E. The generation of the Biot's slow wave at a fluid-porous solid interface. The influence of impedance mismatch. *J. Phys. IV France* **1994**, *04*, 187, doi:10.1051/jp4:1994535.
163. Lee, K.I.; Yoon, S.W. Comparison of acoustic characteristics predicted by Biot's theory and the modified Biot-Attenborough model in cancellous bone. *J. Biomech.* **2006**, *39*, 364–368, doi:10.1016/j.jbiomech.2004.12.004.

164. Berryman, J.G. Seismic wave attenuation in fluid-saturated porous media. *PAGEOPH* **1988**, *128*, 423–432, doi:10.1007/BF01772607.
165. Jocker, J.; Smeulders, D. Ultrasonic measurements on poroelastic slabs: determination of reflection and transmission coefficients and processing for Biot input parameters. *Ultrasonics* **2009**, *49*, 319–330, doi:10.1016/j.ultras.2008.10.006.
166. Kurzeja, P.S.; Steeb, H. About the transition frequency in Biot's theory. *J. Acoust. Soc. Am.* **2012**, *131*, EL454-60, doi:10.1121/1.4710834.
167. Hofmann, A.; Schulz, M.; Indris, S.; Hanemann, T. Electrolytes for Li-Ion Batteries with Highly Improved Safety Issues. Available online: https://www.google.com/url?sa=t&rct=j&q=&esrc=s&source=web&cd=7&ved=2ahUKEwi17729sezmAhWJRMAKHYtVCScQFjAGegQIBhAC&url=https%3A%2F%2Fpublikationen.bibliothek.kit.edu%2F220097329%2F3816639&usg=AOvVaw360MQRE_GKwnqgX7M_Fb46 (accessed on 5 January 2019).
168. Shearing, P.R.; Howard, L.E.; Jørgensen, P.S.; Brandon, N.P.; Harris, S.J. Characterization of the 3-dimensional microstructure of a graphite negative electrode from a Li-ion battery. *Electrochemistry Communications* **2010**, *12*, 374–377, doi:10.1016/j.elecom.2009.12.038.
169. Weller, M.; Overton, T.; Rourke, J.; Armstrong, F.A. *Inorganic chemistry*, Sixth edition, ISBN 019964182X.
170. Biot, M.A.; Willis, D.G. The Elastic Coefficients of the Theory of Consolidation. *Journal of Applied Mechanics* **1957**, 594–601.
171. Diallo, M.S.; Appel, E. Acoustic wave propagation in saturated porous media: Reformulation of the Biot/Squirt flow theory. *Journal of Applied Geophysics* **2000**, *44*, 313–325, doi:10.1016/S0926-9851(00)00009-4.
172. Dvorkin, J.; Nur, A. Dynamic poroelasticity: A unified model with the squirt and the Biot mechanisms. *Geophysics* **1993**, *58*, 524–533, doi:10.1190/1.1443435.
173. Kudryavtsev, B.B. *Anwendung von Ultraschallverfahren bei physikalisch-chemischen Untersuchungen;* Deutscher Verlag der Wissenschaften: Berlin, 1955.
174. Rueter, D.; Morgenstern, T. Ultrasound generation with high power and coil only EMAT concepts. *Ultrasonics* **2014**, *54*, 2141–2150, doi:10.1016/j.ultras.2014.06.012.
175. Monchalin, J.-P. LASER-ULTRASONICS: PRINCIPLES AND INDUSTRIAL APPLICATIONS. In *Ultrasonic and advanced methods for nondestructive testing and material characterization*; Chen, C., Ed.; WORLD SCIENTIFIC: Singapore, Hackensack, NJ, 2007; pp 79–115, ISBN 978-981-270-409-2.
176. Kuttruff, H. *Physik und Technik des Ultraschalls*: *Mit … 14 Tabellen;* Hirzel: Stuttgart, 1988, ISBN 9783777604275.
177. olympus. Übersicht über die Schallbündeleigenschaften bei konventionellem Ultraschall. Available online: https://www.olympus-ims.com/de/ndt-tutorials/transducers/characteristics/ (accessed on 16 February 2020).
178. Tucker, B.J.; Diaz, A.A.; Eckenrode, B.A. Advanced ultrasonic measurement methodology for non-invasive interrogation and identification of fluids in sealed containers. In . Nondestructive Evaulation for Health Monitoring and Diagnostics, San Diego, CA, Sunday 26 February 2006; Diaz, A.A., Wu, H.F., Doctor, S.R., Bar-Cohen, Y., Eds.; SPIE, 2006; 61780K.

179. American Institute of Ultrasound in Medicine. Transducer Characterisation Subcommittee. *Standard methods for testing single-element pulse-echo ultrasonic transducers;* Saunders, W. B.: Philadelphia, Pa., 1982.
180. Lyons, R.G. *Understanding Digital Signal Processing, Third Edition;* Prentice Hall, 2010.
181. Smith, S.W. *Digital signal processing*: *A practical guide for engineers and scientists*, Druk na żądanie; Newnes: Amsterdam [etc], 2012, ISBN 075067444X.
182. Tan, L. *Digital signal processing*: *Fundamentals and applications;* Academic Press: Amsterdam, op. 2008, ISBN 0123740908.
183. Proakis, J.G.; Manolakis, D.G. *Digital signal processing*: *Principles, algorithms, and applications*, 3. ed., internat. ed.; Prentice-Hall: Upper Saddle River, NJ, 1996, ISBN 0133942899.
184. dspillustrations.com. Spectral Leakage and Zero-Padding of the Discrete Fourier Transform. Available online: https://dspillustrations.com/pages/posts/misc/spectral-leakage-zero-padding-and-frequency-resolution.html (accessed on 22 December 2019).
185. Tom O'Haver. A Pragmatic Introduction to Signal Processing: with applications in scientific measurement. An illustrated essay with free software to download. Available online: https://terpconnect.umd.edu/~toh/spectrum/index.html (accessed on 6 December 2020).
186. Werner, M. *Digitale Signalverarbeitung mit MATLAB®*: *Grundkurs mit 16 ausführlichen Versuchen ; mit 76 Tabellen*, 5., durchges. und aktualisierte Aufl.; Vieweg + Teubner: Wiesbaden, 2012, ISBN 3834814733.
187. J. Sallard and L. Paradis. Use of a Priori Information for the Deconvolution of Ultrasonic Signals. *Review a/Progress in Quantitative Nondestructive Evaluation* **1998**, *17*, 735-742.
188. Herrera, R.H.; Orozco, R.; Rodriguez, M. Wavelet-based deconvolution of ultrasonic signals in nondestructive evaluation. *J. Zhejiang Univ. - Sci. A* **2006**, *7*, 1748–1756, doi:10.1631/jzus.2006.A1748.
189. Neelamani, R. Deconvolution and Optimal Filtering in Seismology. In *Handbook of Signal Processing in Acoustics*; Havelock, D., Kuwano, S., Vorländer, M., Eds.; Springer New York: New York, NY, 2008; pp 1571–1584, ISBN 978-0-387-77698-9.
190. Neelamani, R.N.; Deffenbaugh, M.; Baraniuk, R.G. Texas Two-Step: A Framework for Optimal Multi-Input Single-Output Deconvolution. *IEEE Trans. on Image Process.* **2007**, *16*, 2752–2765, doi:10.1109/TIP.2007.906251.
191. Benammar, A.; Drai, R.; Guessoum, A. Detection of delamination defects in CFRP materials using ultrasonic signal processing. *Ultrasonics* **2008**, *48*, 731–738, doi:10.1016/j.ultras.2008.04.005.
192. Herrera, R.H.; Moreno, E.; Calas, H.; Orozco, R. Blind Deconvolution of Ultrasonic Signals Using High-Order Spectral Analysis and Wavelets. In *Progress in Pattern Recognition, Image Analysis and Applications*; Hutchison, D., Kanade, T., Kittler, J., Kleinberg, J.M., Mattern, F., Mitchell, J.C., Naor, M., Nierstrasz, O., Pandu Rangan, C., Steffen, B., Sudan, M., Terzopoulos, D., Tygar, D., Vardi, M.Y., Weikum, G., Sanfeliu, A., Cortés, M.L., Eds.; Springer Berlin Heidelberg: Berlin, Heidelberg, 2005; pp 663–670, ISBN 978-3-540-29850-2.

193. Olugboji, O.A.; Hale, J.M. Development of Damage Reconstruction Techniques From Impulsive Events Based on Measurements Made Remotely. In *Volume 12: Vibration, Acoustics and Wave Propagation.* ASME 2012 International Mechanical Engineering Congress and Exposition, Houston, Texas, USA, 09–15 Nov. 2012; American Society of Mechanical Engineers, 2012; pp 409–415, ISBN 978-0-7918-4528-8.
194. Adam, D.; Michailovich, O. Blind deconvolution of ultrasound sequences using nonparametric local polynomial estimates of the pulse. *IEEE Trans. Biomed. Eng.* **2002**, *49*, 118–131, doi:10.1109/10.979351.
195. Honarvar, F.; Sheikhzadeh, H.; Moles, M.; Sinclair, A.N. Improving the time-resolution and signal-to-noise ratio of ultrasonic NDE signals. *Ultrasonics* **2004**, *41*, 755–763, doi:10.1016/j.ultras.2003.09.004.
196. Kormylo, J.J.; Mendel, J.M. Maximum-Likelihood Seismic Deconvolution. *IEEE Trans. Geosci. Remote Sensing* **1983**, *GE-21*, 72–82, doi:10.1109/TGRS.1983.350532.
197. Goussard, Y.; Demoment, G. Recursive deconvolution of Bernoulli-Gaussian processes using a MA representation. *IEEE Trans. Geosci. Remote Sensing* **1989**, *27*, 384–394, doi:10.1109/36.29558.
198. Benammar, A.; Drai, R.; Kechida, A.; Guessoum, A. Deconvolution of ultrasonic echoes using Bernoulli-Gaussian processes for composite materials inspection. *Int. J. Simul. Multidisci. Des. Optim.* **2008**, *2*, 107–111, doi:10.1051/smdo:2008014.
199. Yildirim, S.; Cemgil, A.T.; Ertuzun, A.B. A hybrid method for deconvolution of Bernoulli-Gaussian processes. In *2009 IEEE International Conference on Acoustics, Speech, and Signal Processing*, Proceedings : April 19-24, 2009, Taipei International Convention Center, Taipei, Taiwan. ICASSP 2009 - 2009 IEEE International Conference on Acoustics, Speech and Signal Processing, Taipei, Taiwan; IEEE: Piscataway, NJ, 2009; pp 3417–3420, ISBN 978-1-4244-2353-8.
200. Roberto H Herrera; Zhaorui Liu; Natasha Raffa; Paul Christensen; Adrianus Elvers. *Improving Time Estimation by Blind Deconvolution*: *With Applications to TOFD and Backscatter Sizing*, 2015.
201. Carcreff, E.; Bourguignon, S.; Idier, J.; Simon, L.; Duclos, A. Including frequency-dependent attenuation for the deconvolution of ultrasonic signals. In . ICA 2013 Montreal, Montreal, Canada, 2 - 7 June 2013; ASA, 2013; p 55029.
202. Peters, F.; Petit, L. A broad band spectroscopy method for ultrasound wave velocity and attenuation measurement in dispersive media. *Ultrasonics* **2003**, *41*, 357–363, doi:10.1016/S0041-624X(03)00109-4.
203. Svilainis, L. Review of high resolution time of flight estimation techniques for ultrasonic signals. *52nd Annual Conference of the British Institute of Non-Destructive Testing 2013 (NDT 2013)*: *Held 10-12 September 2013, Telford, United Kingdom*; Telford, United Kingdom, 2013.
204. Le, L.H. An investigation of pulse-timing techniques for broadband ultrasonic velocity determination in cancellous bone: A simulation study. *Physics in Medicine and Biology* **1998**, *43*, 2295–2308, doi:10.1088/0031-9155/43/8/021.

205. Barshan, B. Fast processing techniques for accurate ultrasonic range measurements. *Meas. Sci. Technol.* **2000**, *11*, 45–50, doi:10.1088/0957-0233/11/1/307.
206. Jackson, J.C.; Summan, R.; Dobie, G.I.; Whiteley, S.M.; Pierce, S.G.; Hayward, G. Time-of-flight measurement techniques for airborne ultrasonic ranging. *IEEE Trans. Ultrason. Ferroelectr. Freq. Control* **2013**, *60*, 343–355, doi:10.1109/TUFFC.2013.2570.
207. Espinosa, L.; Bacca, J.; Prieto, F.; Lasaygues, P.; Brancheriau, L. Accuracy on the Time-of-Flight Estimation for Ultrasonic Waves Applied to Non-Destructive Evaluation of Standing Trees: A Comparative Experimental Study. *Acta Acustica united with Acustica* **2018**, *104*, 429–439, doi:10.3813/AAA.919186.
208. El Guerjouma, R.; Mouchtachi, A.; Jayet, Y.; Baboux, J.C. Nondestructive evaluation of graphite by ultrasonic velocity measurement using cross-correlation and Hilbert transform methods. In *IEEE 1992 Ultrasonics Symposium Proceedings.* IEEE 1992 Ultrasonics Symposium Proceedings, Tucson, AZ, USA, 20-23 Oct. 1992; IEEE, 1992; pp 829–832, ISBN 0-7803-0562-0.
209. McMullan, W.G.; Delaghe, B.A.; Bird, J.S. A simple rising-edge detector for time-of-arrival estimation. *IEEE Trans. Instrum. Meas.* **1996**, *45*, 823–827, doi:10.1109/19.517003.
210. Barshan, B.; Kuc, R. A bat-like sonar system for obstacle localization. *IEEE Trans. Syst., Man, Cybern.* **1992**, *22*, 636–646, doi:10.1109/21.156577.
211. Gan, T.H.; Hutchins, D.A.; Billson, D.R.; Schindel, D.W. The use of broadband acoustic transducers and pulse-compression techniques for air-coupled ultrasonic imaging. *Ultrasonics* **2001**, *39*, 181–194, doi:10.1016/S0041-624X(00)00059-7.
212. Buchberger, I.; Seidlmayer, S.; Pokharel, A.; Piana, M.; Hattendorff, J.; Kudejova, P.; Gilles, R.; Gasteiger, H.A. Aging Analysis of Graphite/LiNi 1/3 Mn 1/3 Co 1/3 O 2 Cells Using XRD, PGAA, and AC Impedance. *J. Electrochem. Soc.* **2015**, *162*, A2737-A2746, doi:10.1149/2.0721514jes.
213. Schuster, S.F.; Brand, M.J.; Campestrini, C.; Gleissenberger, M.; Jossen, A. Correlation between capacity and impedance of lithium-ion cells during calendar and cycle life. *J. Power Sources* **2016**, *305*, 191–199, doi:10.1016/j.jpowsour.2015.11.096.
214. Cui, Y.; Zuo, P.; Du, C.; Gao, Y.; Yang, J.; Cheng, X.; Ma, Y.; Yin, G. State of health diagnosis model for lithium ion batteries based on real-time impedance and open circuit voltage parameters identification method. *Energy* **2018**, *144*, 647–656, doi:10.1016/j.energy.2017.12.033.
215. Zhu, X.; Fernández Macía, L.; Jaguemont, J.; Hoog, J. de; Nikolian, A.; Omar, N.; Hubin, A. Electrochemical impedance study of commercial LiNi0.80Co0.15Al0.05O2 electrodes as a function of state of charge and aging. *Electrochim. Acta* **2018**, *287*, 10–20, doi:10.1016/j.electacta.2018.08.054.
216. Waag, W.; Käbitz, S.; Sauer, D.U. Experimental investigation of the lithium-ion battery impedance characteristic at various conditions and aging states and its influence on the application. *Appl. Energy* **2013**, *102*, 885–897, doi:10.1016/j.apenergy.2012.09.030.
217. Rao, K.S.; Murali Krishna, P.; Swarna Latha, T.; Madhava Prasad, D. Impedance-spectroscopy analysis and piezoelectric properties of Pb2KNb5O15

ceramics. *Materials Science and Engineering: B* **2006**, *131*, 127–134, doi:10.1016/j.mseb.2006.04.005.
218. Perrissin-Fabert, I.; Jayet, Y. Simulated and experimental study of the electric impedance of a piezoelectric element in a viscoelastic medium. *Ultrasonics* **1994**, *32*, 107–112, doi:10.1016/0041-624X(94)90018-3.
219. Darestani, M.T.; Chilcott, T.C.; Coster, H.G.L. Electrical impedance spectroscopy study of piezoelectric PVDF membranes. *J. Solid State Electrochem.* **2014**, *18*, 595–605, doi:10.1007/s10008-013-2286-x.
220. González, A.M.; García, Á.; Benavente-Peces, C.; Pardo, L. Revisiting the Characterization of the Losses in Piezoelectric Materials from Impedance Spectroscopy at Resonance. *Materials (Basel)* **2016**, *9*, doi:10.3390/ma9020072.
221. Bowen, C.; Lopez-Prieto, M.; Mahon, S.; Lowrie, F. Impedance spectroscopy of piezoelectric actuators. *Scripta Materialia* **2000**, *42*, 813–818, doi:10.1016/S1359-6462(00)00300-6.
222. Andre, D.; Meiler, M.; Steiner, K.; Wimmer, C.; Soczka-Guth, T.; Sauer, D.U. Characterization of high-power lithium-ion batteries by electrochemical impedance spectroscopy. I. Experimental investigation. *J. Power Sources* **2011**, *196*, 5334–5341, doi:10.1016/j.jpowsour.2010.12.102.
223. Lvovich, V.F. *Impedance spectroscopy*: *Applications to electrochemical and dielectric phenomena;* Wiley: Hoboken, N.J, 2012, ISBN 1280880341.
224. Barai, A.; Uddin, K.; Widanage, W.D.; McGordon, A.; Jennings, P. A study of the influence of measurement timescale on internal resistance characterisation methodologies for lithium-ion cells. *Sci. Rep.* **2018**, *8*, 21, doi:10.1038/s41598-017-18424-5.
225. Omar, N.; Daowd, M.; van den Bossche, P.; Hegazy, O.; Smekens, J.; Coosemans, T.; Van Mierlo, J. Rechargeable Energy Storage Systems for Plug-in Hybrid Electric Vehicles—Assessment of Electrical Characteristics. *Energies* **2012**, *5*, 2952–2988, doi:10.3390/en5082952.
226. Ratnakumar, B.; Smart, M.; Surampudi, S. Electrochemical Impedance Spectroscopy and Its Applications to Lithium Ion Cells. *ChemInform* **2002**, *33*, 229.
227. Landesfeind, J.; Pritzl, D.; Gasteiger, H.A. An Analysis Protocol for Three-Electrode Li-Ion Battery Impedance Spectra: Part I. Analysis of a High-Voltage Positive Electrode. *J. Electrochem. Soc.* **2017**, *164*, A1773-A1783, doi:10.1149/2.0131709jes.
228. Levi, M.; Gamolsky, K.; Aurbach, D.; Heider, U.; Oesten, R. On electrochemical impedance measurements of LixCo0.2Ni0.8O2 and LixNiO2 intercalation electrodes. *Electrochim. Acta* **2000**, *45*, 1781–1789, doi:10.1016/S0013-4686(99)00402-8.
229. Landesfeind, J.; Hattendorff, J.; Ehrl, A.; Wall, W.A.; Gasteiger, H.A. Tortuosity Determination of Battery Electrodes and Separators by Impedance Spectroscopy. *J. Electrochem. Soc.* **2016**, *163*, A1373-A1387, doi:10.1149/2.1141607jes.
230. Vyroubal, P.; Kazda, T. Equivalent circuit model parameters extraction for lithium ion batteries using electrochemical impedance spectroscopy. *J. Energy Storage* **2018**, *15*, 23–31, doi:10.1016/j.est.2017.10.019.

231. Barsoukov, E.; Macdonald, J.R. *Impedance Spectroscopy*: *Theory, Experiment, and Applications*, 3rd ed.; John Wiley & Sons Incorporated: Newark, 2018, ISBN 9781119074083.
232. Conrad Electronic SE. Material Safety Data Sheet: Item no.: 517990. Rechargeable Polymer Li-Ion Battery. Available online: https://asset.conrad.com/media10/add/160267/c1/-/en/000517990SD01/sicherheitsdatenblatt-517990-conrad-energy-modellbau-akkupack-lipo-37-v-1200-mah-zellen-zahl-1-20-c-softcase-offene-kabelenden.pdf (accessed on 31 August 2021).
233. Conrad Electronic SE. Conrad energy Modellbau-Akkupack (LiPo) 3.7 V 1200 mAh Zellen-Zahl: 1 20 C Softcase Offene Kabelenden: Technical Data. Available online: https://www.conrad.de/de/p/conrad-energy-modellbau-akkupack-lipo-3-7-v-1200-mah-zellen-zahl-1-20-c-softcase-offene-kabelenden-517990.html (accessed on 31 August 2021).
234. EVE GmbH. PSNK2030: Technical data. Available online: https://www.conrad.de/de/p/psnk2030-piezokeramisches-element-spannung-30-v-dauerton-1-st-1461364.html (accessed on 8 September 2021).
235. van Rossum, G.; Boer, J. de. Interactively testing remote servers using the Python programming language. *CWI Quarterly* **1991**, *4*, 283–304.
236. Anaconda. *Anaconda Distribution*: The world's most popular open-source Python distribution platform, 2020.11, 2020. Available online: https://anaconda.com.
237. Harris, C.R.; Millman, K.J.; van der Walt, S.J.; Gommers, R.; Virtanen, P.; Cournapeau, D.; Wieser, E.; Taylor, J.; Berg, S.; Smith, N.J.; et al. Array programming with NumPy. *Nature* **2020**, *585*, 357–362, doi:10.1038/s41586-020-2649-2.
238. Jeff Reback; jbrockmendel; Wes McKinney; Joris Van den Bossche; Tom Augspurger; Phillip Cloud; Simon Hawkins; gfyoung; Sinhrks; Matthew Roeschke; et al. *pandas*: powerful Python data analysis toolkit, 1.3.2; Zenodo, 2020. Available online: https://doi.org/10.5281/zenodo.3509134.
239. Virtanen, P.; Gommers, R.; Oliphant, T.E.; Haberland, M.; Reddy, T.; Cournapeau, D.; Burovski, E.; Peterson, P.; Weckesser, W.; Bright, J.; et al. SciPy 1.0: fundamental algorithms for scientific computing in Python. *Nat Meth* **2020**, *17*, 261–272, doi:10.1038/s41592-019-0686-2.
240. Hunter, J.D. Matplotlib: A 2D Graphics Environment. *Comput. Sci. Eng.* **2007**, *9*, 90–95, doi:10.1109/MCSE.2007.55.
241. Pedregosa, F.; Varoquaux, G.; Gramfort, A.; Michel, V.; Thirion, B.; Grisel, O.; Blondel, M.; Prettenhofer, P.; Weiss, R.; Dubourg, V.; et al. Scikit-learn: Machine Learning in Python. *Journal of Machine Learning Research* **2011**, *12*, 2825–2830.
242. Perez, F.; Granger, B.E. IPython: A System for Interactive Scientific Computing. *Comput. Sci. Eng.* **2007**, *9*, 21–29, doi:10.1109/MCSE.2007.53.
243. LEBIGOT, E.O. *Uncertainties*: a Python package for calculations with uncertainties, 3.1.5. Available online: https://github.com/lebigot/uncertainties.
244. Reeve, A. *npTDMS*: NumPy based Python module for reading TDMS files produced by LabView, 1.3.0. Available online: https://github.com/adamreeve/npTDMS.

245. Harris, S.J.; Timmons, A.; Baker, D.R.; Monroe, C. Direct in situ measurements of Li transport in Li-ion battery negative electrodes. *Chemical Physics Letters* **2010**, *485*, 265–274, doi:10.1016/j.cplett.2009.12.033.
246. Li, W.; Cho, Y.-G.; Yao, W.; Li, Y.; Cronk, A.; Shimizu, R.; Schroeder, M.A.; Fu, Y.; Zou, F.; Battaglia, V.; et al. Enabling high areal capacity for Co-free high voltage spinel materials in next-generation Li-ion batteries. *J. Power Sources* **2020**, *473*, 228579, doi:10.1016/j.jpowsour.2020.228579.
247. An, S.J.; Li, J.; Du, Z.; Daniel, C.; Wood, D.L. Fast formation cycling for lithium ion batteries. *J. Power Sources* **2017**, *342*, 846–852, doi:10.1016/j.jpowsour.2017.01.011.
248. Goodenough, J.B.; Park, K.-S. The Li-Ion Rechargeable Battery: A Perspective. *J. Am. Chem. Soc* **2013**, *135*, 1167–1176, doi:10.1021/ja3091438.
249. Xu, K. Nonaqueous Liquid Electrolytes for Lithium-Based Rechargeable Batteries. *Chem. Rev.* **2004**, *104*, 4303–4418, doi:10.1021/cr030203g.
250. Patil, A.; Patil, V.; Wook Shin, D.; Choi, J.-W.; Paik, D.-S.; Yoon, S.-J. Issue and challenges facing rechargeable thin film lithium batteries. *MRS Bulletin* **2008**, *43*, 1913–1942, doi:10.1016/j.materresbull.2007.08.031.
251. Ohzuku, T. Formation of Lithium-Graphite Intercalation Compounds in Nonaqueous Electrolytes and Their Application as a Negative Electrode for a Lithium Ion (Shuttlecock) Cell. *J. Electrochem. Soc.* **1993**, *140*, 2490, doi:10.1149/1.2220849.
252. Asenbauer, J.; Eisenmann, T.; Kuenzel, M.; Kazzazi, A.; Chen, Z.; Bresser, D. The success story of graphite as a lithium-ion anode material – fundamentals, remaining challenges, and recent developments including silicon (oxide) composites. *Sustainable Energy Fuels* **2020**, *4*, 5387–5416, doi:10.1039/D0SE00175A.
253. REYNIER, Y.; Yazami, R.; Fultz, B. The entropy and enthalpy of lithium intercalation into graphite. *J. Power Sources* **2003**, *119-121*, 850–855, doi:10.1016/S0378-7753(03)00285-4.
254. Aurbach, D. Common Electroanalytical Behavior of Li Intercalation Processes into Graphite and Transition Metal Oxides. *J. Electrochem. Soc.* **1998**, *145*, 3024, doi:10.1149/1.1838758.
255. Levi, M.D.; Aurbach, D. The mechanism of lithium intercalation in graphite film electrodes in aprotic media. Part 1. High resolution slow scan rate cyclic voltammetric studies and modeling. *Journal of Electroanalytical Chemistry* **1997**, *421*, 79–88, doi:10.1016/S0022-0728(96)04832-2.
256. Dahn, J.R.; Fong, R.; Spoon, M.J. Suppression of staging in lithium-intercalated carbon by disorder in the host. *Phys. Rev. B* **1990**, *42*, 6424–6432, doi:10.1103/PhysRevB.42.6424.
257. Van Der Ven, A.; Aydinol, M.K.; Ceder, G.; Kresse, G.; Hafner, J. First-principles investigation of phase stability in LixCoO2. *Phys. Rev. B* **1998**, *58*, 2975–2987, doi:10.1103/PhysRevB.58.2975.
258. Mizushima, K.; Jones, P.C.; Wiseman, P.J.; Goodenough, J.B. LixCoO2 (0<x<-1): A new cathode material for batteries of high energy density. *MRS Bulletin* **1980**, *15*, 783–789, doi:10.1016/0025-5408(80)90012-4.
259. Senyshyn, A.; Dolotko, O.; Muhlbauer, M.J.; Nikolowski, K.; Fuess, H.; Ehrenberg, H. Lithium Intercalation into Graphitic Carbons Revisited:

Experimental Evidence for Twisted Bilayer Behavior. *J. Electrochem. Soc.* **2013**, *160*, 3198–3205, doi:10.1149/2.031305jes.
260. Guerard, D.; Herold, A. Intercalation of lithium into graphite and other carbons. *Carbon* **1975**, *13*, 337–345, doi:10.1016/0008-6223(75)90040-8.
261. Wang, X.; Sone, Y.; Kuwajima, S. In Situ Investigation of the Volume Change in Li-ion Cell with Charging and Discharging. *J. Electrochem. Soc.* **2004**, *151*, A273, doi:10.1149/1.1635827.
262. Direct Plastics Ltd. Acetal Black: POM-C (Polyacetal - Copolymer). Material Data Sheet. Available online: https://www.directplastics.co.uk/pdf/datasheets/Acetal%20Data%20Sheet.pdf (accessed on 14 September 2021).
263. Prusak, K.; Zmywaczyk, J.; Koniorczyk, P.; Godzimirski, J.; Cegła, M. Thermo-Mechanical Analysis of Chosen Epoxy Resins Used in Aviation Technology. *AMR* **2015**, *1126*, 187–193, doi:10.4028/www.scientific.net/AMR.1126.187.
264. Langenberg, K.-J.; Marklein, R.; Mayer, K. *Ultrasonic nondestructive testing of materials*: *Theoretical foundations;* CRC Press: Boca Raton, Fla., 2012, ISBN 9781439855881.
265. Grami, A. Signals, Systems, and Spectral Analysis. *Introduction to Digital Communications*; Elsevier, 2016; pp 41–150, ISBN 9780124076822.
266. Winter, M.; Besenhard, J.O.; Spahr, M.E.; Novák, P. Insertion electrode materials for rechargeable lithium batteries. *Adv. Mater.* **1998**, *10*, 725–763.
267. Pardoe, I.; Simon, L.; Young, D. 2.6 - (Pearson) Correlation Coefficient r. Available online: https://online.stat.psu.edu/stat462/node/96/ (accessed on 10 July 2021).
268. Holmes, A.; Illowsky, B.; Dean, S. Introductory Business Statistics: 68 The Correlation Coefficient r. Available online: https://opentextbc.ca/introbusinessstatopenstax/chapter/the-correlation-coefficient-r/ (accessed on 21 August 2020).

8 Annex A: additional content

8.1 Additional spectra as in Figure 4.25 from the signals displayed in Figure 4.14 to Figure 4.17

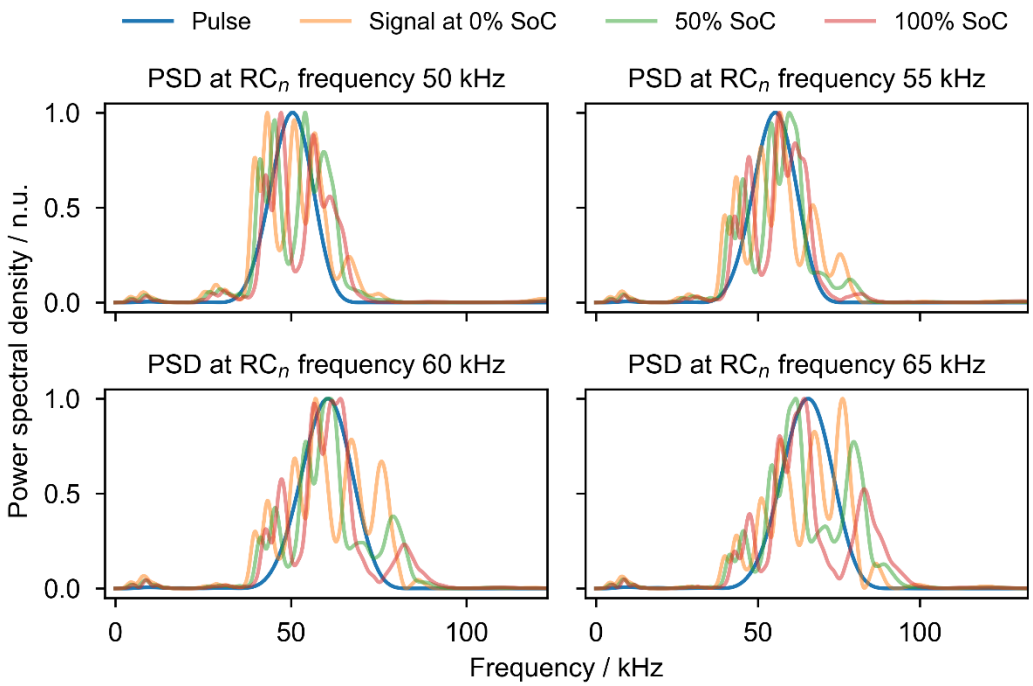

Figure 8.1: PSD of signals displayed in Figure 4.14.

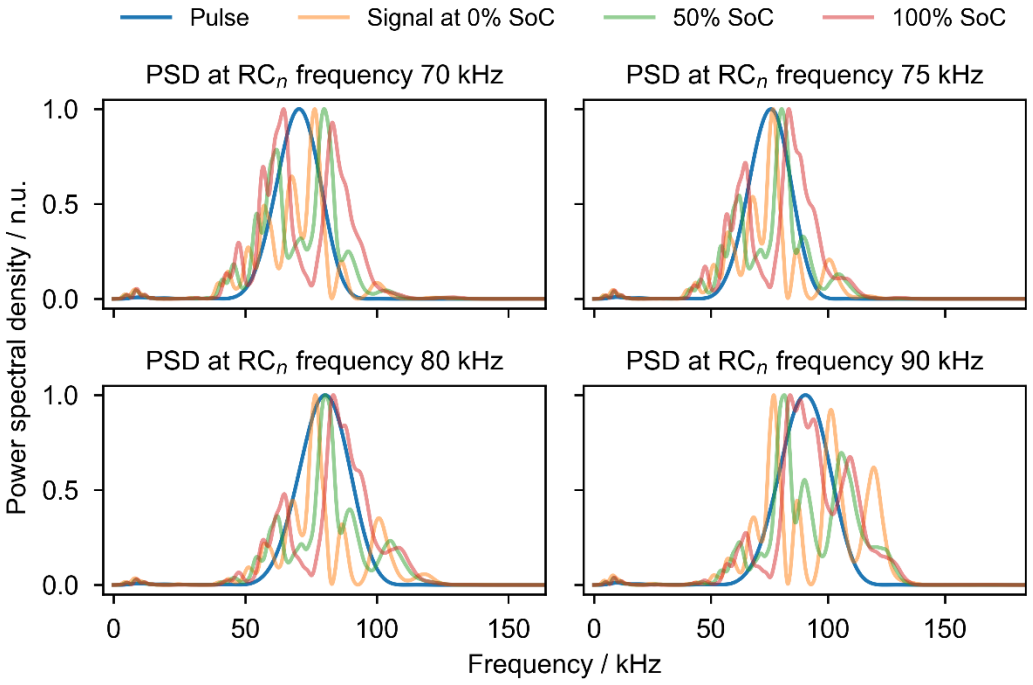

Figure 8.2: PSD of signals displayed in Figure 4.15.

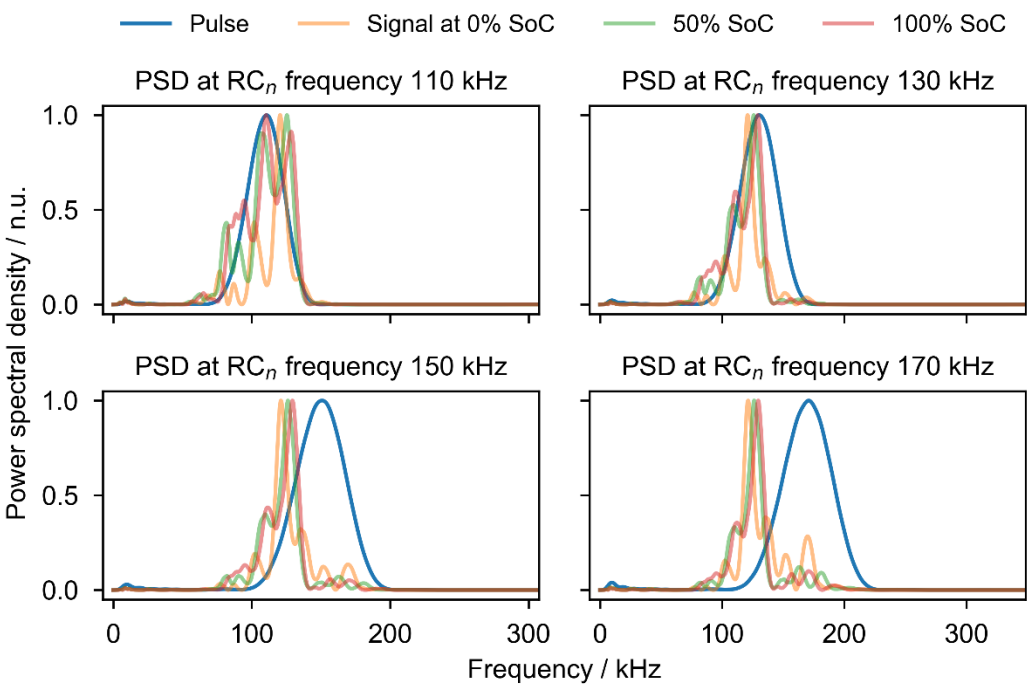

Figure 8.3: PSD of signals displayed in Figure 4.16.

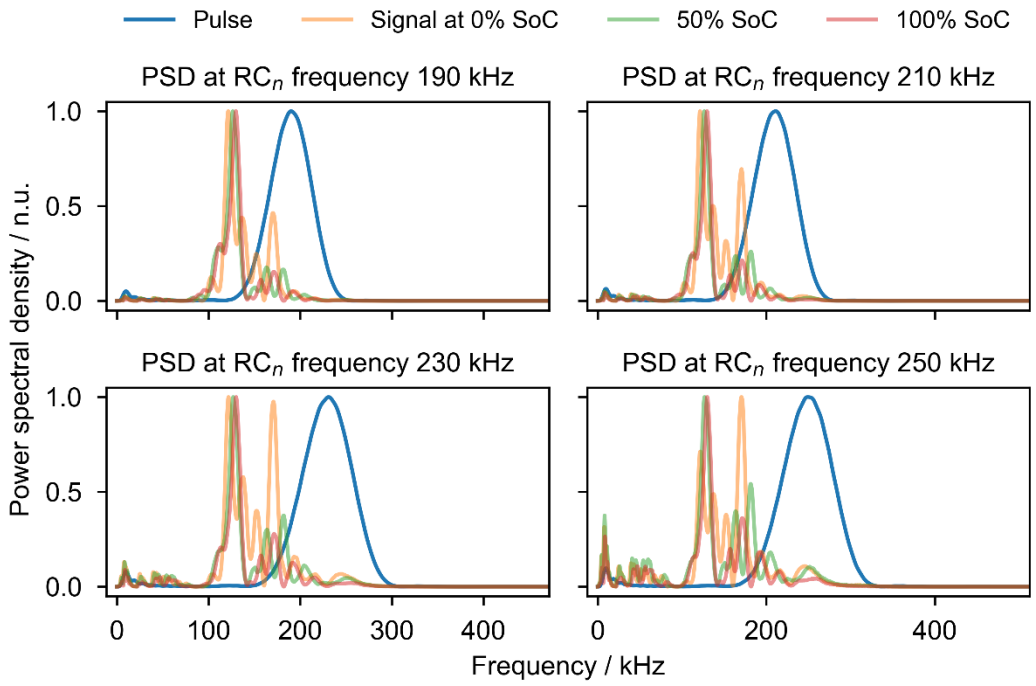

Figure 8.4: PSD of signals displayed in Figure 4.17.

Figure 8.5 shows the result of processing each received signal's PSD according to these equations (Equation (75) and (76)). Here, the expected value or the center of mass of the PSD is plotted as a color value in kHz for different SoCs (y-axis) and RCn frequencies (x-axis). This presentation shows that the CoM shifts towards higher frequencies with increasing RC_n frequency but remains below 150 kHz. For high RC_n frequencies especially, the CoM shifts towards lower frequencies with increasing SoC, being well in accordance with the trends observed in Figure 2.19. Above 100 kHz, the center does not match the exciting RC_n frequency.

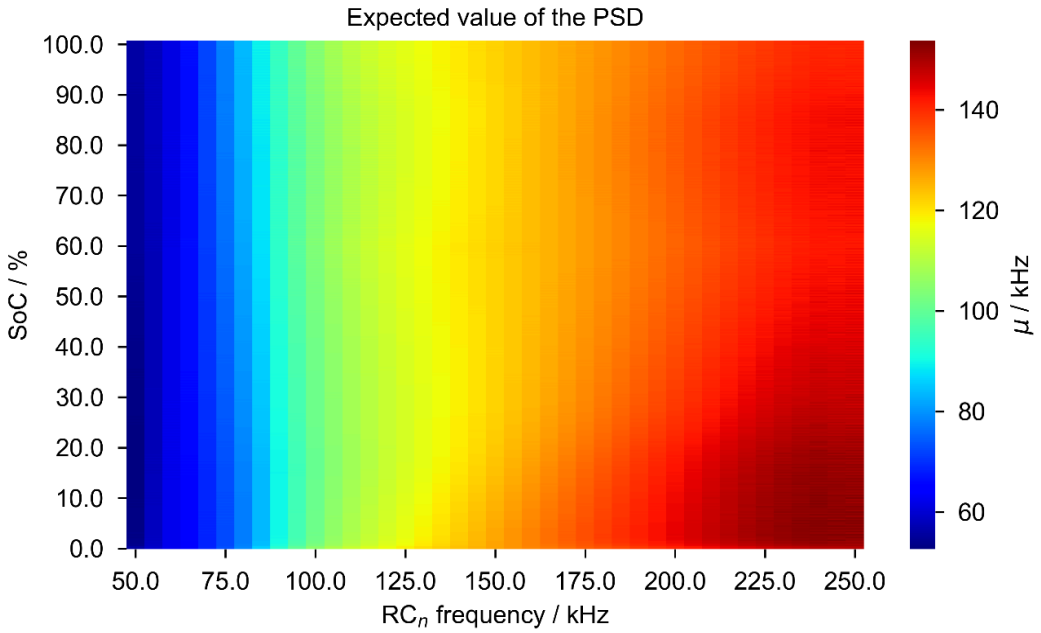

Figure 8.5: Expected value of the power spectral density (PSD) of the transmitted signals, described in Figure 4.27. The expected value describes the center of mass of the PSD and is calculated according to Equations (75) and (76).

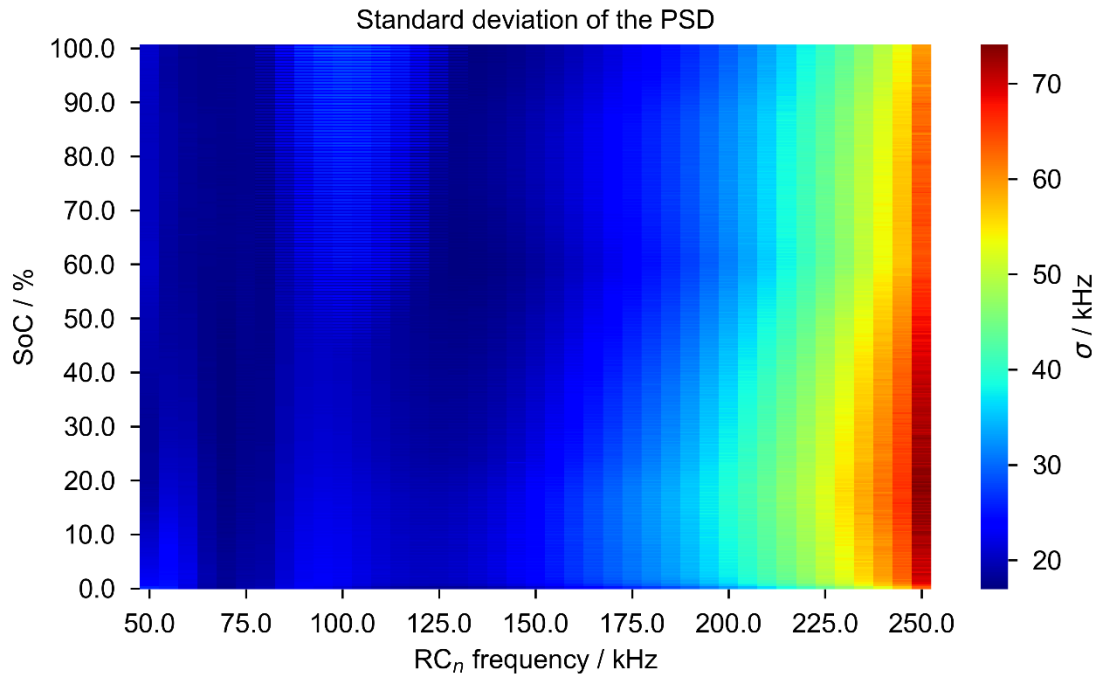

Figure 8.6: Standard deviation of the power spectral density of the transmitted signals described in Figure 4.27.

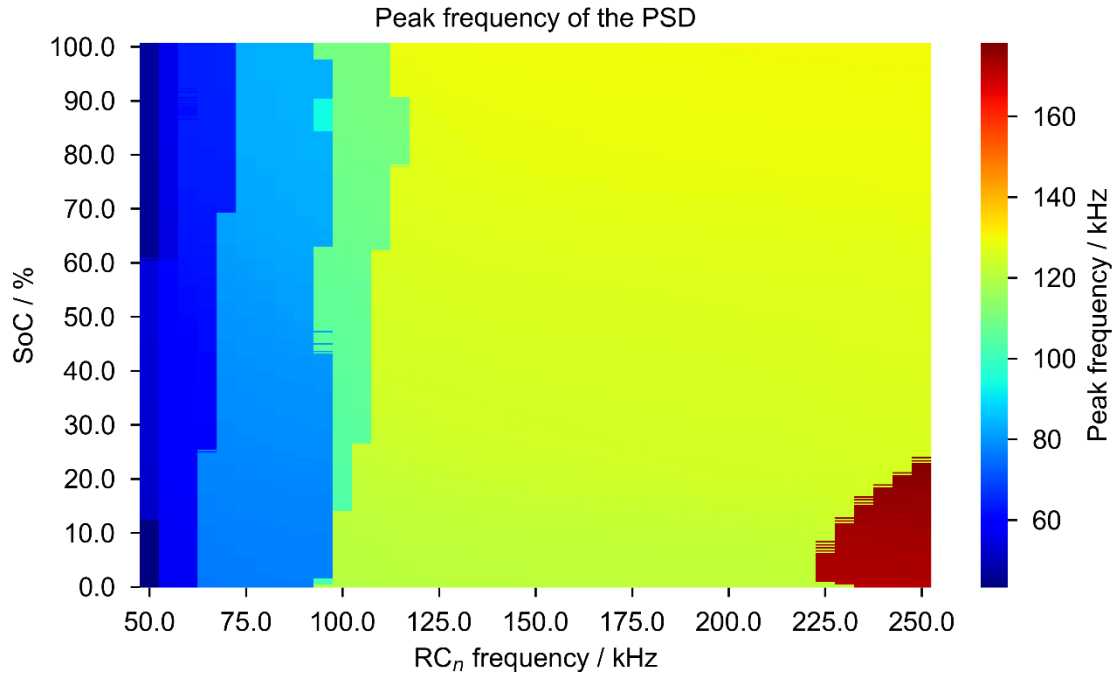

Figure 8.7: Peak frequency of the power spectral density of the transmitted signals described in Figure 4.27.

8.2 Comparison of ToF estimation methods

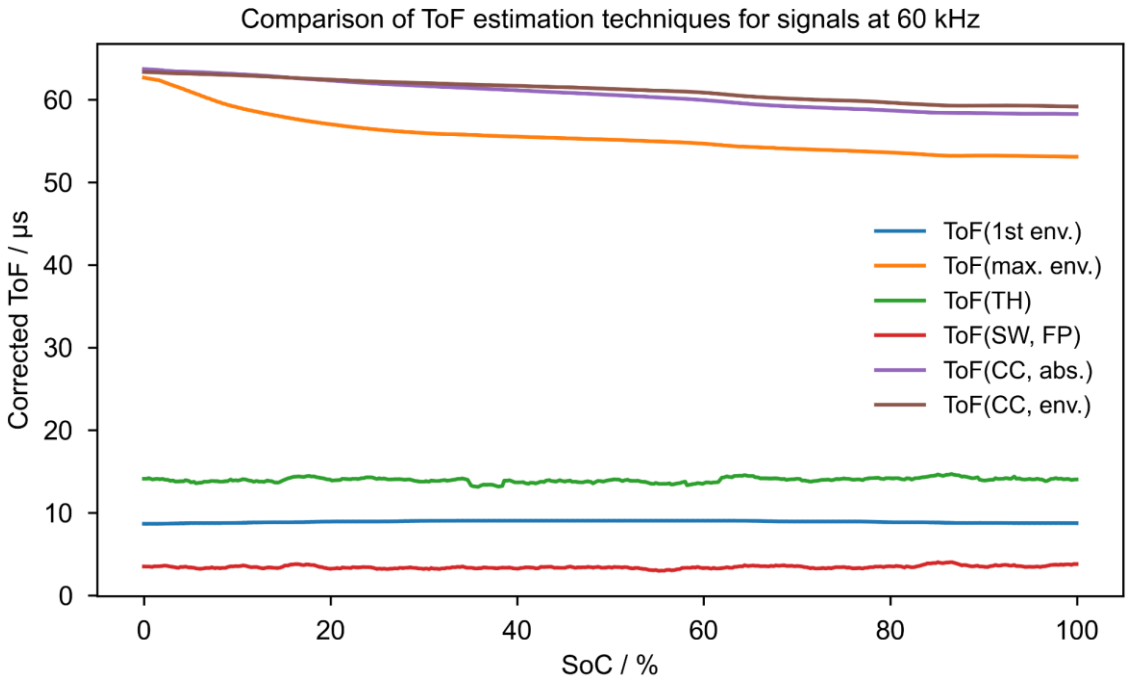

Figure 8.8: Comparison of ToF estimation techniques for signals, transmitted through LDA019, at 60 kHz in an SoC range of 0% to 100%.

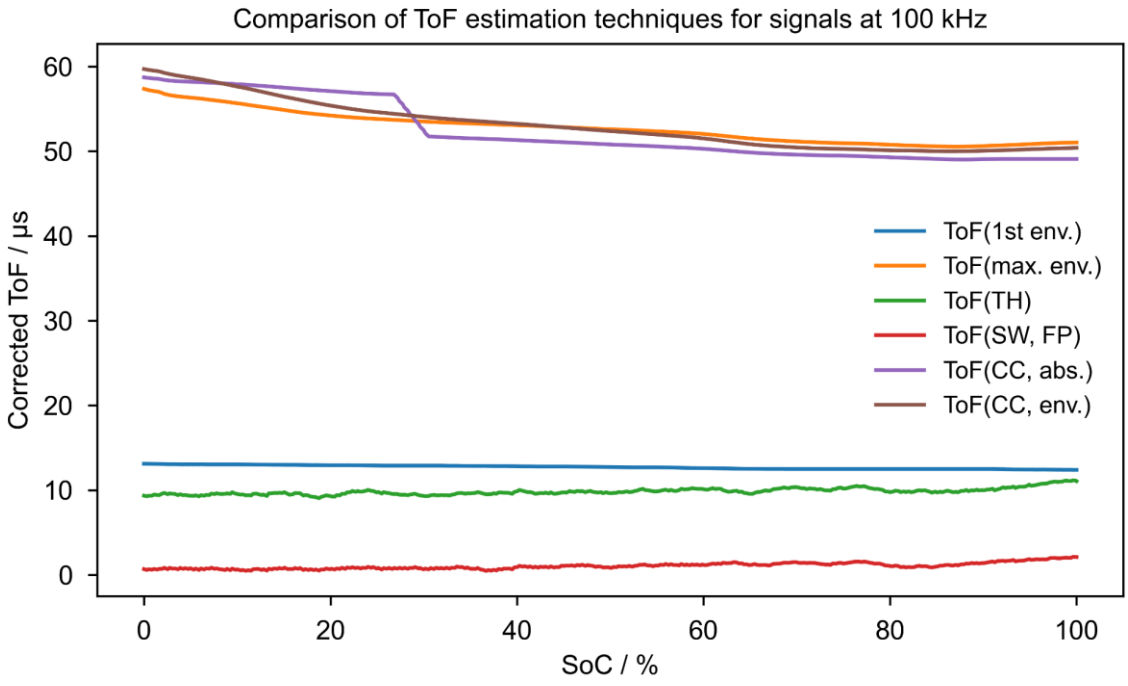

Figure 8.9: Comparison of ToF estimation techniques for signals, transmitted through LDA019, at 100 kHz in an SoC range of 0% to 100%.

8.3 Deviations of prediction and training data

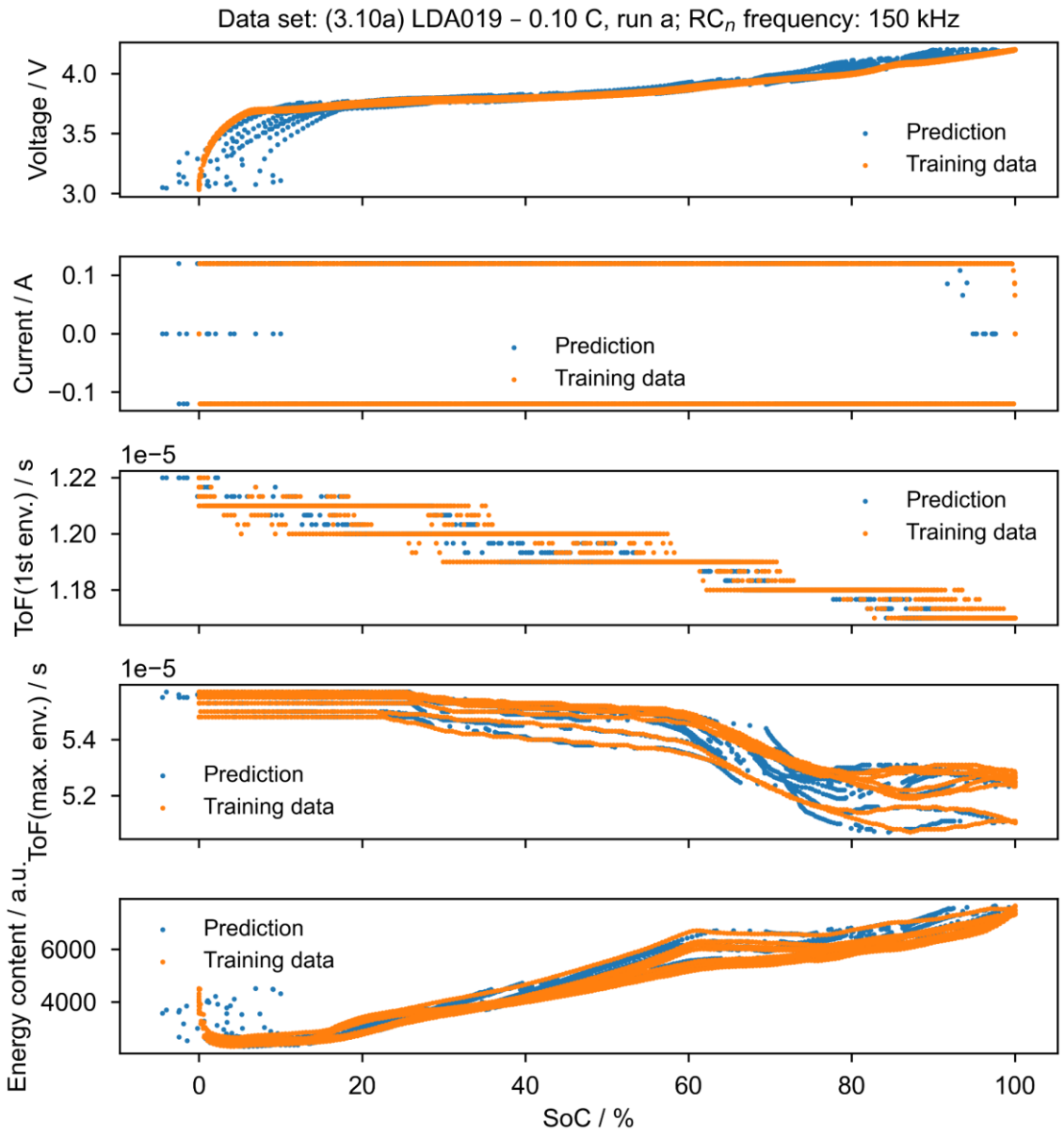

Figure 8.10: Comparison of training data and model prediction. The predicted value SoC is plotted on the x-axis and the features are plotted on the y-axis. Therefore, the deviation of the prediction from the training data can be estimated as the horizontal shift of the blue points against the orange points. Here the training data and prediction of the dataset achieving the best accuracy among the available datasets with different RC_n frequencies is shown. It achieved an R^2 score of 0.978 and an RMSE of 4.4% SoC.

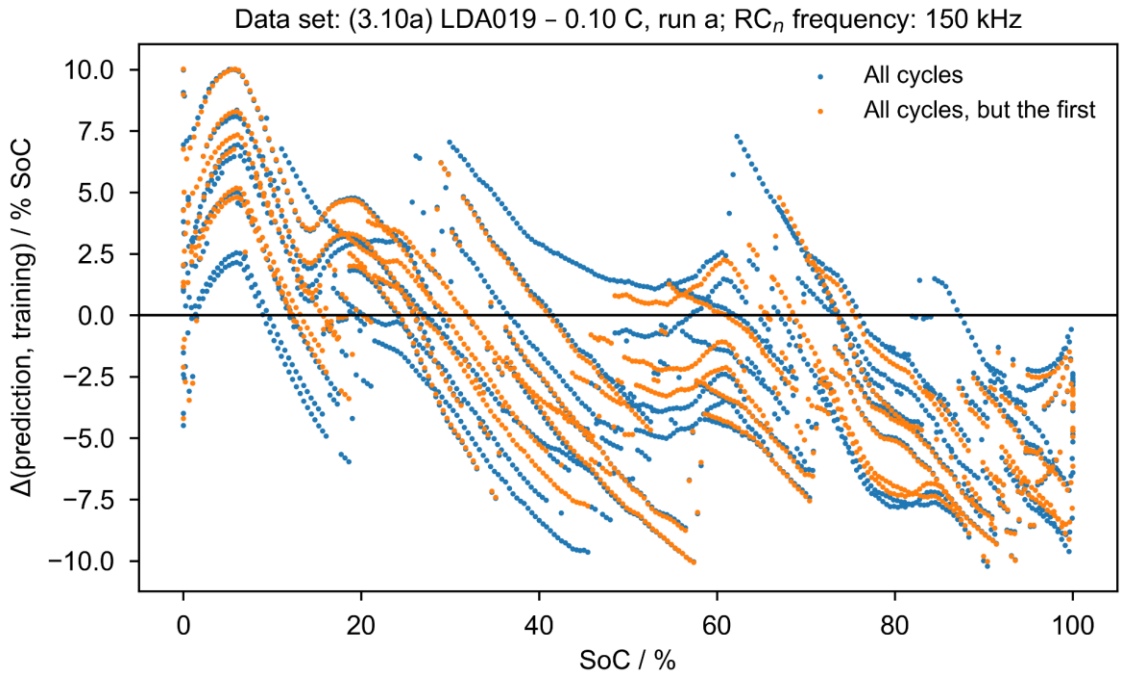

Figure 8.11: Deviation of the predicted value from the training data, plotted vs. the (true) SoC of the training data. Regions of over and under-estimation can be attributed to a misfit of the trained model, as seen in Figure 8.10.

8.4 C-rate dependency of signal properties

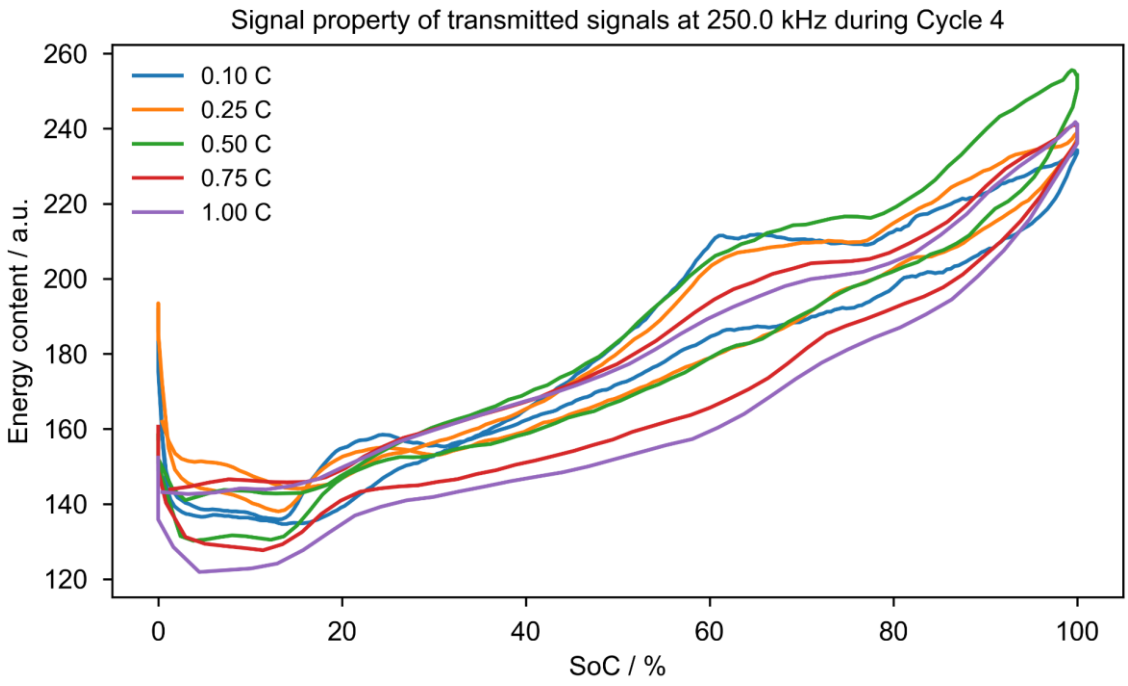

Figure 8.12: Energy content of the signals transmitted in the second cycle out of datasets, recorded at five different C-rates. Especially the curves at low C-rate show distinctive plateaus in their course, which are “smoothed out” at higher C-rates. Here, the data of cell LDA019 is displayed.

8.5 Additional test matrix scores

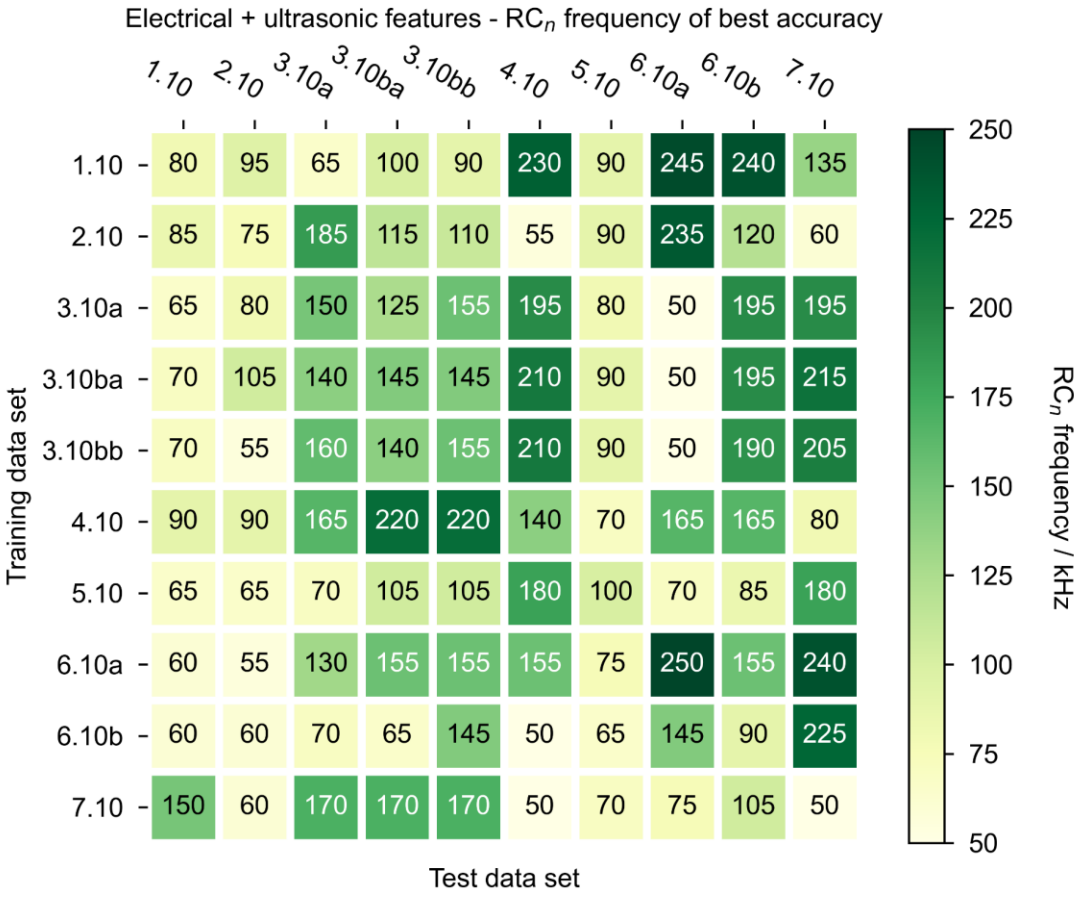

Figure 8.13: RC$_n$ frequency of the dataset achieving the highest accuracy of a support vector regression, estimated by the R² score. The datasets used for training and testing are listed as row labels and column labels, respectively. The diagonal entries represent the average of 10 self-tests of a dataset, where 10% of the data acts as test data and 90% as training data. The best result of the self-tests is achieved by the datasets with RC$_n$ frequencies between 50 kHz and 155 kHz with the exception of one outlier.

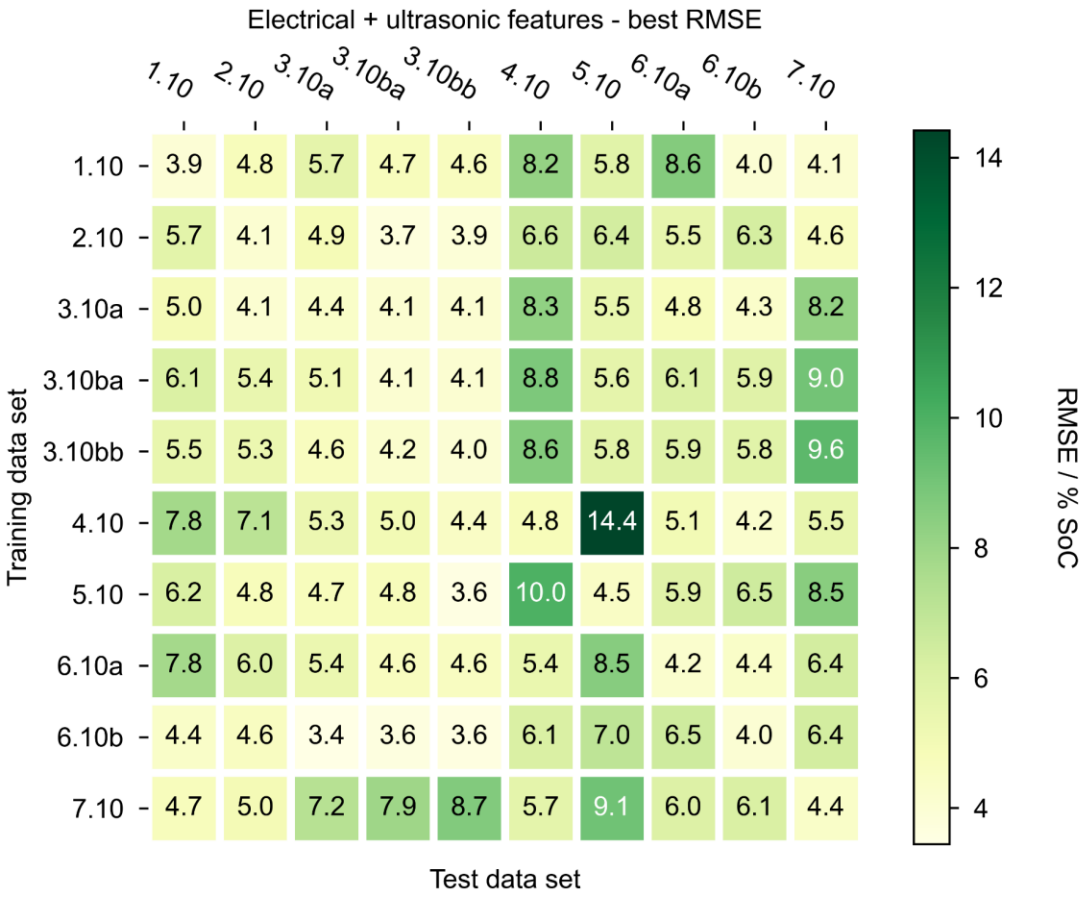

Figure 8.14: Model accuracy of a support vector regression, estimated by the RMSE. The datasets used for training and testing are listed as row labels and column labels, respectively. The diagonal entries represent the average of 10 self-tests of a dataset, where 10% of the data acts as test data and 90% as training data. These tests evaluate to an RMSE as low as 3.4% SoC. The overall accuracy is consistently higher compared to the model trained with electrical or ultrasonic features alone.

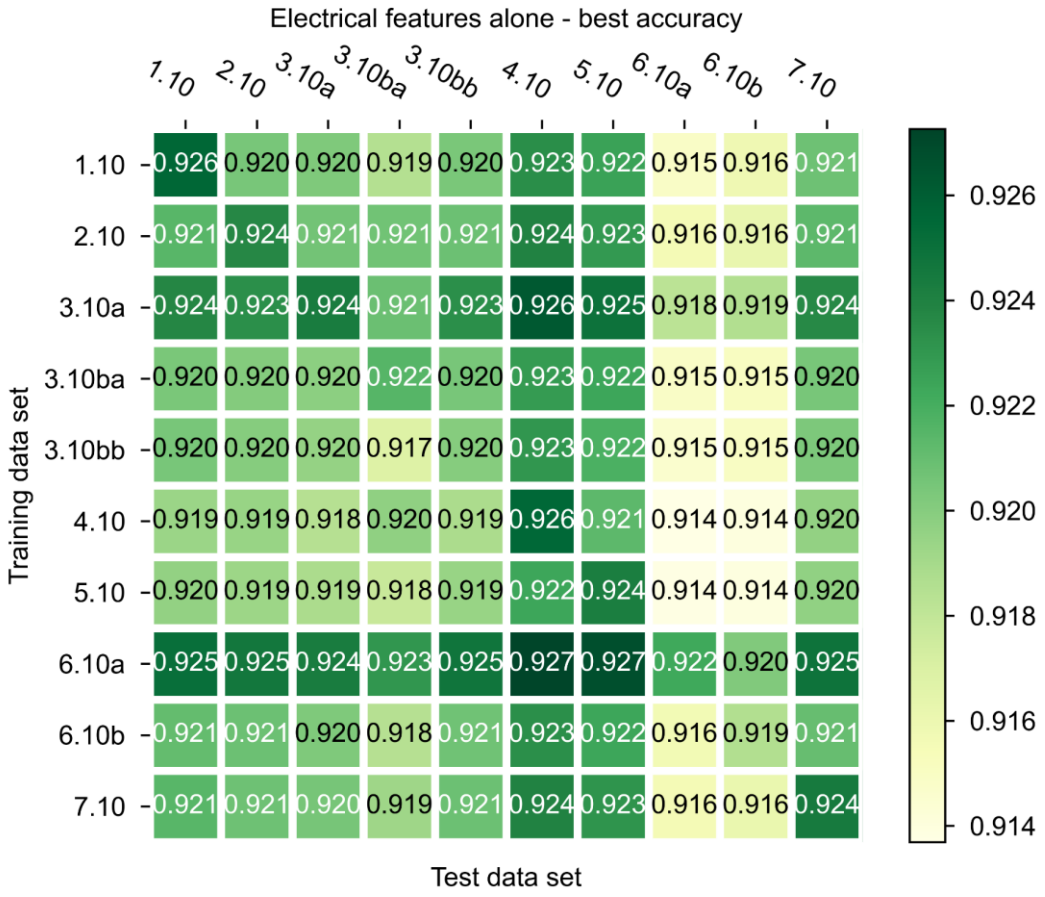

Figure 8.15: Model accuracy of a support vector regression, estimated by the R^2 score. The datasets used for training and testing are listed as row labels and column labels, respectively. The diagonal entries represent the average of 10 self-tests of a dataset, where 10% of the data acts as test data and 90% as training data. Here the electrical quantities cell voltage and current act as features. Overall, an accuracy above 0.93 is achieved. Except for one dataset, the self-test results in an accuracy of 0.94 and above.

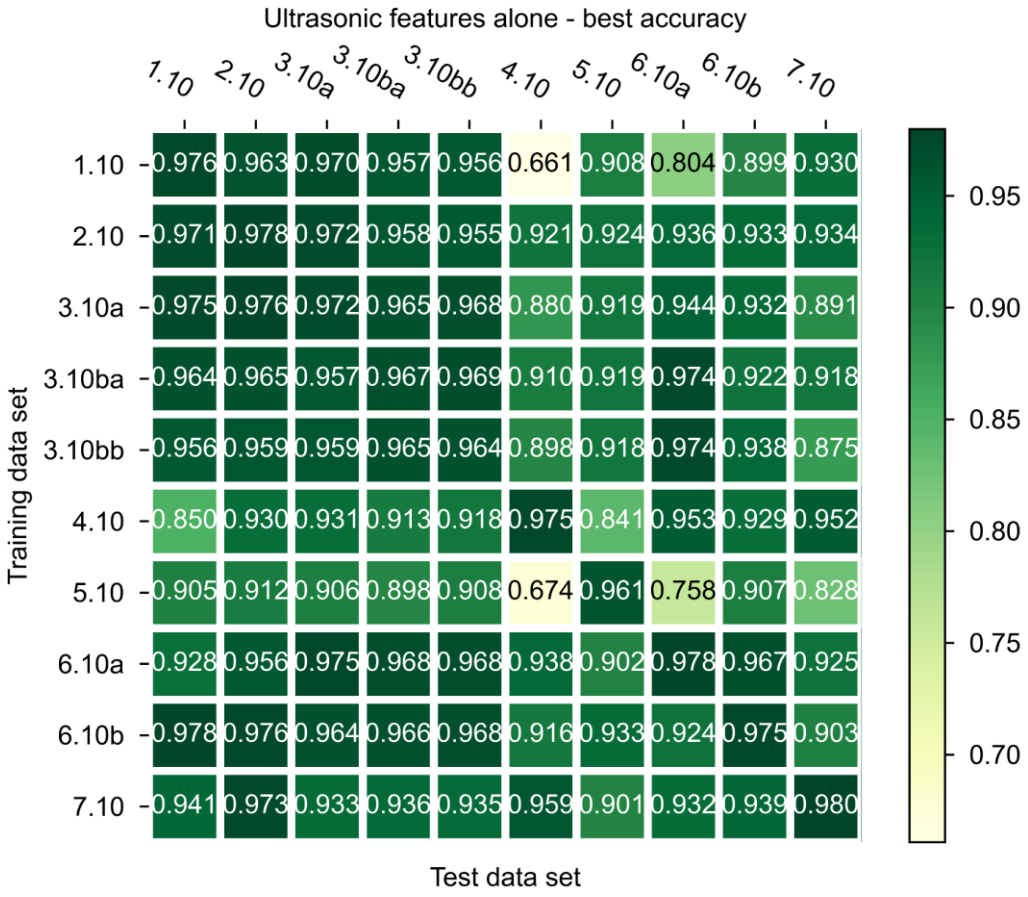

Figure 8.16: Model accuracy of a support vector regression, estimated by the R^2 score. The datasets used for training and testing are listed as row labels and column labels, respectively. The diagonal entries represent the average of 10 self-tests of a dataset, where 10% of the data acts as test data and 90% as training data. Here the time of flight of the wave packages, estimated by the first peak and the maximum of the envelope of the signal, as well as the transmitted energy content are selected as features. The best accuracy varies between 0.67 and 0.98. For the self-test (diagonal entries) an overall high accuracy between 0.96 and 0.98 can be achieved.

9 Annex B: List of publications

9.1 Peer-reviewed journal articles and a patent

Gold, Lukas; Bach, Tobias; Virsik, Wolfgang; Schmitt, Angelika; Müller, Jana; Staab, Torsten E.M.; Sextl, Gerhard (2017): Probing lithium-ion batteries' state-of-charge using ultrasonic transmission – Concept and laboratory testing. In *J. Power Sources* 343, pp. 536–544. doi: 10.1016/j.jpowsour.2017.01.090.

Angeles Cabañero, Maria; Altmann, Johannes; Gold, Lukas; Boaretto, Nicola; Müller, Jana; Hein, Simon; Zausch, Jochen; Kallo, Josef; Latz, Arnulf (2019): Investigation of the temperature dependence of lithium plating onset conditions in commercial Li-ion batteries. In *Energy* 171, pp. 1217–1228. doi: 10.1016/j.energy.2019.01.017.

Gold, Lukas; Heuer, Henning; Herzog, Thomas; Reuber, Sebastian; Lorrmann, Henning (2020): Verfahren zur Überwachung eines oder mehrerer Schritte der Herstellung von Batteriezellen on 22.12.2020. Pat. no. DE102020216517A1.

Wulfert-Holzmann, Paul; Huck, Moritz; Gold, Lukas; Settelein, Jochen; Sauer, Dirk Uwe; Giffin, Guinevere A. (2021): A New In-Situ and Operando Measurement Method to Determine the Electrical Conductivity of the Negative Active Material in Lead-Acid Batteries during Operation. In *J. Electrochem. Soc.* 168 (5), p. 50537. doi: 10.1149/1945-7111/ac00f5.

Zanotto, Franco Martín; Zapata Dominguez, Diana; Ayerbe, Elixabete; Boyano, Iker; Burmeister, Christine; Duquesnoy, Marc; Eisentraeger, Marlene; Florez Montaño, Jonathan; Gallo-Bueno, Alfonso; Gold, Lukas; Hall, Florian; Kaden, Nicolaj; Muerkens, Bernhard; Otaegui, Laida; Reynier, Yvan; Stier, Simon; Thomitzek, Matthias; Turetskyy, Artem; Vallin, Nicolas; Wessel, Jacob; Xu, Xukuan; Abbasov, Jeyhun; Franco, Alejandro A. (2022): Data Specifications for Battery Manufacturing Digitalization: Current Status, Challenges, and Opportunities. In Batteries & Supercaps, Article batt.202200224. doi: 10.1002/batt.202200224.

Gold, Lukas; Herzog, Thomas; Heuer, Henning; Giffin, Guinevere (2022): Ultrasound Propagation in Lithium-Ion Battery Materials – Basis for Developing Monitoring and Imaging Methods. In *Energy Technology*, 2200861, doi:10.1002/ente.202200861.

Feiler, Simon; Daubinger, Philip; Gold, Lukas; Hartmann, Sarah; Giffin, Guinevere (2023): Interplay between Elastic and Electrochemical Properties during Active Material Transitions and Aging of a Lithium-Ion Battery. In *Batteries & Supercaps*, doi:10.1002/batt.202200518.

9.2 Conference contributions

Gold, Lukas; Bach, Tobias C.; Müller, Jana; Lorrmann, Henning; Sextl, Gerhard (2017): State-of-Charge Estimation of Lithium-Ion Batteries using Ultrasonic Transmission. (Poster). Batterieforum Deutschland 2017. Kompetenznetzwerk Lithium-Ionen-Batterien e. V. Berlin, 25.01.2017.

Gold, Lukas; Müller, Jana; Lorrmann, Henning; Sextl, Gerhard (2017): Li-Ion Battery Cell Thickness Change Hysteresis and Link to Aging Behavior. (Poster). Advanced Battery Power 2017. Haus der Technik e.V. Aachen, 29.03.2017.

Gold, Lukas; Hartmann, Sarah; Lorrmann, Henning; Sextl, Gerhard (2019): Ultrasonic Probing of Lithium-Ion Batteries. A new Concept for State of Charge Estimation. (Talk). Advanced Battery Power 2019. Haus der Technik e.V. Aachen, 03.04.2019.

Gold, Lukas; Hartmann, Sarah; Lorrmann, Henning; Sextl, Gerhard (2019): Ultrasonic Probing of Lithium-Ion Batteries. (Talk). German-Israeli Battery School 2019. Justus Liebig University, Gießen. Berlin, 15.05.2019.

10 Acknowledgment

10.1 Funding

The initial research on the topics studied in this work was conducted at Fraunhofer ISC within the project FZEB, funded by the Bavarian State Ministry of Economic Affairs and Media, Energy and Technology (grant number: 43-6629/86). The work conducted within the project Cell-Fill and the associated cooperation with Fraunhofer IKTS, funded by the Federal Ministry of Education and Research (grant number: 03XP0237D), contributed largely to a deeper understanding of the matter at hand.

10.2 University of Alberta

I want to thank Dr. Roberto Henry Herrera, a PostDoc at the University of Alberta, Canada. After reading one of his publications on time of flight estimation and deconvolution, I contacted him via ResearchGate. He kindly pointed me to further reading on the topic, shared his code, and helped generously with the orientation in the field of signal processing.

10.3 Fraunhofer IKTS

The measurement tool US-SBX used to excite and record ultrasonic signals between 20 kHz and 500 kHz, was developed by Fraunhofer IKTS. I want to thank Thomas Klesse and Heiko Neunübel for the patient adaptation of the hardware and the software to the specific needs of the application, discussed in this work.

The cooperation with Fraunhofer IKTS on state estimation and ultrasonic non-destructive testing of lithium-ion battery cells started in 2018. Initiated by Henning Heuer, we started to exchange theories, discuss results and conduct experiments together. For this fruitful and valuable cooperation, I would like to thank the whole team for their plentiful advice. I appreciate the technical and scientific discussions with Henning Heuer, Thomas Herzog, Lars Schubert, Tobias Gaul, Susan Walter, Christian Richter, Hendrik Funke, Kilian Tschöke, Konrad Chwelatiuk.

I want to explicitly thank Thomas Herzog for taking the time to jointly conduct ultrasonic measurements on different battery cells in a water bath that taught me a lot about the ultrasonic wave propagation through battery cells. Furthermore, I acknowledge the experimental contribution of Tobias Gaul to this work. He conducted laser vibrometer

experiments on the studied battery cells that have helped to understand the ultrasonic wave propagation. Further, he and Lars Schubert assisted with the interpretation.

I want to especially thank Henning Heuer for his support in pursuing a PhD by sharing the knowledge resources of his team, creating the often-essential links for a fruitful exchange and by enabling the examination of this thesis.

10.4 Fraunhofer ISC

Since 2013, the Fraunhofer Institute for Silicate Research ISC at Neunerplatz in Würzburg has offered many opportunities to learn and grow in the field of applied research. I have passed through many stations here: I was a scientific assistant with manifold tasks and was thus able to gain insights into many different areas of electrochemistry. Afterwards, the master's thesis period presented the opportunity to develop and test theories on the mechanical properties of lithium-ion batteries. The expert supervision and the many enthusiastic scientific discussions with Tobias Bach during that time motivated me to continue the journey here even further. During the following PhD time, I had many opportunities to explore new and exciting content and to learn the necessary tools of the trade. Over the past six years, there have been many valuable challenges to overcome and grow from. Without the people that I have been privileged to work with, the joy of science would be unthinkable. Therefore, I would like to thank the staff of the different departments of the institute and especially the staff of OE320.

I would like to thank Wolfgang Virsik for his support in all electrical engineering issues and the many lessons, he taught me through the years at his workshop.

I am glad to have worked with Marian Cabanero, Paul Wulfert-Holzmann, Philip Daubinger, Simon Feiler, Tobias Bach and Guinevere Giffin also on topics beyond my PhD thesis and would like to thank them working jointly on several publications.

For their contribution to this work by preparing samples, performing measurements, and discussing the analysis, I especially thank Andreas Gronbach, Annalena Götz, Elena Fleder, Kerstin Heinrich, Martina Kapuschinski, and Vilija Anfimovaite. I also thank Youjin Shin and Simon Feiler for conducting measurements and technical discussions during their respective master's thesis and internships that either became part of this work or contributed to its progress.

For professional exchanges, advice, shared enthusiasm, proofreading and comments on this thesis, I especially thank Bernhard Brunner, Guinevere Giffin, Henning Lorrmann, Philip Daubinger, Sarah Hartmann, Simon Feiler, Simon Stier, and Torsten Staab.

For the supervision of this thesis, in different sections, I would like to thank Henning Lorrmann, Jana Müller, Sarah Hartmann, and Tobias Bach - thank you for your support.

My special thanks go to my doctoral supervisor Gerhard Sextl for the supervision and examination of this thesis, for the interesting and helpful discussions, and for his support in the challenging undertaking of pursuing a PhD – To complete a doctoral thesis indeed means to grow up in many ways.

10.5 Family and Friends

Ich danke den guten Freund:innen, die mich in den vergangenen sieben Jahren mit Rat, Unterstützung, Ablenkung und Aufheiterung begleitet haben.

Ganz besonders danke ich meiner Familie, die mich auf dem Weg bis hierhin immer unterstützt, motiviert und inspiriert hat.